

# **DESEGMENTATION METHOD AND ITS APPLICATIONS TO CIRCULARLY POLARIZED MICROSTRIP ANTENNAS**

A Thesis Submitted  
in Partial Fulfilment of the Requirements  
for the Degree of  
**DOCTOR OF PHILOSOPHY**

*by*  
**PRAMOD CHANDRA SHARMA**

to the  
**DEPARTMENT OF ELECTRICAL ENGINEERING  
INDIAN INSTITUTE OF TECHNOLOGY, KANPUR**  
APRIL, 1982

18258

TO

BELOVED BABU JI - THE DIVINE MASTER

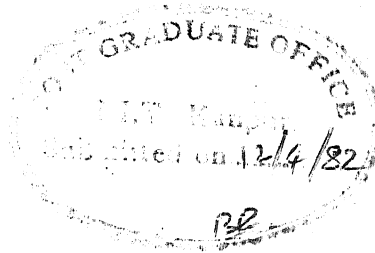


30 MAY 1984

CENTRAL LIBRARY  
Kampur.

Acc. No. **A 82591**

EE-1982-D-SHA-DE



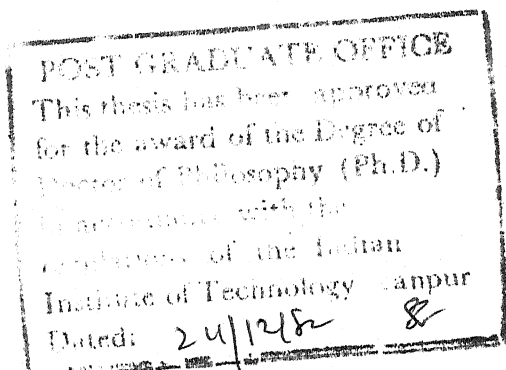
iii

### CERTIFICATE

This is to certify that the work reported in this thesis entitled 'DESEGMENTATION METHOD AND ITS APPLICATIONS TO CIRCULARLY POLARIZED MICROSTRIP ANTENNAS' by Pramod Chandra Sharma has been carried out under my supervision and has not been submitted elsewhere for a degree.

( K.C. GUPTA )  
Professor

Department of Electrical Engineering  
Indian Institute of Technology  
Kanpur 208016,  
India.



## ACKNOWLEDGEMENTS

It is with deep sense of gratitude that I express my indebtedness to Dr. K.C. Gupta for his exemplary guidance and encouragement throughout the course of this work. With no exaggeration at all, I must express that the period of my association with him during the last two and a half years has been the best phase of my life. I have tried my best to learn from him, as much as I could, in all spheres of life. I sincerely feel that my words fail to convey an adequate acknowledgement to him.

I extend my thanks to Dr. N.C. Mathur and Dr. Raghuram who spared time for me whenever I approached them.

I shall be failing in my duty without acknowledging the splendid company and moral support of my friends and fellow research scholars who made my stay here a memorable event of my life. Dr. Rakesh Chadha and Mr. Girish Kumar deserve special word of mention for their help from beginning to the end of this work.

I am thankful to the authorities of S.G.S. Institute of Technology and Science, Indore for sponsoring me under Quality Improvement Programme.

A special word of mention to Mr. C.M. Abraham without whose dedicated and painstaking efforts, the thesis could not have been in its present form.

The tracing work by Mr. J.C. Verma and the cyclostyling work by M/s. T. Tiwari and Gangaram are gratefully acknowledged.

Thanks are also due to M/s. S.K. Kolay and V.S. Yadav for their co-operation and help in fabricating various antennas used in this thesis.

Last, but not the least, I wish to put on record my deepest sense of regard to my parents who have been a constant source of encouragement and inspiration throughout the venture of this work.

P.C. Sharma

## TABLE OF CONTENTS

	Page
LIST OF TABLES	x
LIST OF FIGURES	xi
SYNOPSIS	xxi
Chapter One	
INTRODUCTION	1
1.1 TWO DIMENSIONAL COMPONENTS	1
1.1.1 Applications	3
1.1.2 Methods of analysis of 2-d components	5
1.2 TWO-DIMENSIONAL MICROSTRIP ANTENNAS	9
1.2.1 Special features of microstrip patch antennas	9
1.2.2 Linearly polarized microstrip patch antennas	17
1.2.3 Circularly polarized microstrip patch antennas	17
1.2.4 Methods of analyzing microstrip antennas	28
1.3 OUTLINE OF PRESENT INVESTIGATIONS	33
Chapter Two	
GREEN'S FUNCTION APPROACH AND SEGMENTATION METHOD FOR ANALYSIS OF MICROSTRIP ANTENNAS	38
2.1 GREEN'S FUNCTION APPROACH	41
2.1.1 Input impedance and resonance frequency	41
2.1.2 Voltage around the periphery	44
2.1.3 Evaluation of radiation characteristics	46
2.1.4 Evaluation of axial ratio in broad-side direction	49
2.2 SEGMENTATION METHOD	52
2.2.1 The formulation	52
2.2.2 Application to microstrip antennas	55
2.3 DISCUSSIONS	60

## Chapter Three

## DESEGMENTATION METHOD

66

## 3.1 BASIC CONCEPTS

68

## 3.2 DESEGMENTATION IN TERMS OF Z-MATRICES

72

## 3.2.1 Theoretical formulation

73

3.2.2 Evaluation of  $\underline{Z}_\alpha$  when  $Q \geq D$ 

76

3.2.3 Evaluation of  $\underline{Z}_\alpha$  when  $Q = D$ 

78

## 3.2.4 Number of c-ports and q-ports

79

## 3.2.5 Simplification of formulation

80

## 3.2.6 Computational effort

83

3.2.7 Circuits with  $\underline{Z}_{qq\beta} = \underline{Z}_{qq\gamma}$ 

84

## 3.3 DESEGMENTATION IN TERMS OF S-MATRICES

84

## 3.3.1 Theoretical formulation

84

3.3.2 Evaluation of  $\underline{S}_\alpha$  when  $Q \geq D$ 

89

3.3.3 Evaluation of  $\underline{S}_\alpha$  when  $Q = D$ 

91

## 3.3.4 Incorporation of additional ports and number of q-ports

92

3.3.5 Circuits with  $\underline{S}_{qq\beta} = \underline{S}_{qq\gamma}$ 

93

## 3.4 ILLUSTRATIVE EXAMPLES

93

## 3.4.1 Examples of lumped circuits

94

## 3.4.2 Examples of transmission line circuits

101

## 3.4.3 Planar circuit examples

108

## 3.5 COMPUTATIONAL EFFORT IN DESEGMENTATION AND SEGMENTATION

112

## 3.6 APPLICATION TO DE-EMBEDDING

120

## 3.6.1 De-embedding

120

## 3.6.2 De-embedding using desegmentation method

122

## 3.6.3 Illustrative example

124

## 3.7 DISCUSSIONS

125

Chapter Four	
DIAGONAL FED NEARLY SQUARE PATCH ANTENNA	129
4.1 OPTIMIZATION AND ANALYSIS	129
4.1.1 Optimization of length to width ratio	129
4.1.2 Voltage and magnetic current distribution	135
4.2 ORTHOGONAL MODES	139
4.2.1 Orthogonal modes and their resonance frequencies	139
4.2.2 Superimposition of orthogonal modes	146
4.3 INPUT VSWR AND FEED LOCATION	148
4.4 BANDWIDTH AND BEAMWIDTH	156
4.5 EXPERIMENTAL RESULTS	159
4.6 DISCUSSIONS	171
Chapter Five	
CORNERS CHOPPED NEARLY SQUARE PATCH ANTENNA	173
5.1 ANALYSIS AND OPTIMIZATION	173
5.1.1 Analysis	173
5.1.2 Optimum truncation	178
5.1.3 Voltage and magnetic current distribution	178
5.2 ORTHOGONAL MODES	183
5.3 FEED LOCATION AND INPUT VSWR	189
5.4 BANDWIDTH AND BEAMWIDTH	195
5.4.1 Variation of input VSWR with frequency	195
5.4.2 Variation of axial ratio with frequency	198
5.4.3 Radiation pattern	201
5.5 EXPERIMENTAL RESULTS	204
5.6 DISCUSSIONS	204

Chapter Six	
SQUARE PATCH ANTENNA WITH A DIAGONAL SLOT	212
6.1 ANALYSIS AND OPTIMIZATION	212
6.1.1 Evaluation of Z-matrix for multiport model	214
6.1.2 Voltage along the radiating edges	220
6.1.3 Magnetic current distribution	223
6.1.4 Optimum dimensions of the slot	225
6.2 ORTHOGONAL MODES OF RESONANCE	228
6.3 MINIMUM VSWR AND OPTIMUM FEED LOCATION	240
6.4 BANDWIDTH AND BEAMWIDTH	242
6.4.1 Variation of input VSWR and axial ratio with frequency	242
6.4.2 Radiation pattern and beamwidth	244
6.5 EXPERIMENTAL RESULTS	244
6.6 DISCUSSIONS	248
Chapter Seven	
CONCLUDING REMARKS	252
7.1 ANALYTICAL TECHNIQUES	252
7.1.1 Applications	255
7.2 SUGGESTIONS FOR FURTHER INVESTIGATIONS	258
Appendix A	
CALCULATION OF Q-FACTOR FOR RECTANGULAR PATCH ANTENNA	265
Appendix B	
MEASUREMENT OF DIELECTRIC CONSTANT	266
REFERENCES	268



## LIST OF TABLES

Table No.	Caption	Page
3.1	Orders of the matrices $\underline{Z}_\beta$ and $\underline{Z}_\gamma$ for implementing desegmentation method	101
4.1	Parameters for diagonal fed antennas investigated	169
4.2	Results of investigations on diagonal fed antennas having parameters as in Table 4.1	170
5.1	Summary of results for corners chopped antenna fabricated on a substrate of thickness equal to $1/8"$ with $\epsilon_r = 2.52$	208
5.2	Summary of results for a corners chopped antenna fabricated on a substrate of thickness equal to $1/16"$ with $\epsilon_r = 2.51$	209
6.1	Orders of $\underline{Z}_\beta$ and $\underline{Z}_\gamma$ and total computational effort in evaluating these matrices	219
6.2	Performance of a square patch antenna with a diagonal slot	250
7.1	Performance parameters of three types of antennas (experimental) (substrate thickness = $1/8"$ , $\epsilon_r = 2.52$ )	257

## LIST OF FIGURES

Figure No.	Caption	Page
1.1	Three types of 2-d microwave circuits	2
1.2	A general 2-d microstrip configuration	7
1.3	Examples of circuit configurations where (a) segmentation is applicable (b) segmentation is not applicable	8
1.4(a)	Geometries of some of the microstrip patch antennas	10
1.4(b)	Some more geometries of microstrip patch antennas	11
1.5	Travelling wave antennas	12
1.6(a)	Microstrip slot antenna	13
1.6(b)	Some geometries of microstrip slot antennas	14
1.7	A microstrip dipole antenna	15
1.8	Some of the linearly polarized 2-d microstrip patch antennas	18
1.9	Circularly polarized patch antennas of Category I (a) Square with hybrid (b) square with power divider (c) circular patch with hybrid	20
1.10	Circularly polarized microstrip patch antennas of Category II : (a) corner fed rectangle; (b) Elliptical; (c) square with diagonal slot; (d) corners chopped square; (e) circular with slot; (f) pentagon; (g) and (h) capacitively loaded rectangles	22
1.11	(a) Two orthogonal modes with resonance frequencies $F_{01}$ and $F_{10}$ represented by lumped resonant circuits; (b) reactance variation with frequency. The radiation resistance not shown	23
1.12	(a) Ideal resonant circuits of Fig. 1.11(a) loaded with radiation resistance; (b) Phasor diagram	25

Fig. No.	Caption	Page
1.13	A rectangular patch antenna modelled as transmission line	29
2.1	Planar segments for which eigen-functions are known	39
2.2	Examples of antenna configurations for which modal-expansion or Green's function technique cannot be used directly	40
2.3	Steps involved in microstrip antenna analysis by Green's function approach	42
2.4	Schematic for evaluating the Z-matrix of the combination of the multiport (ideal) cavity and radiation resistance network	45
2.5	(a) Orientation of electric field and magnetic current vectors (b) Coordinate system	47
2.6	Illustrative example of a circuit to be analyzed by segmentation method	53
2.7	(a) The planar model of the antenna structure (b) Radiated power is accounted for by loading effect of $\beta$ -network, the input port is labelled $J_i$	56
2.8	Incorporation of additional ports (shown dotted)	59
2.9	Division of the pentagon shaped antenna, of Fig. 2.2, into five segments for analysis by segmentation method	61
2.10	Division of corners chopped antenna, of Fig. 2.2, into three regular shaped segments for analysis by segmentation method	62
2.11	Two schemes for dividing a square patch antenna with a diagonal slot (Fig. 2.2) into 6 segments	63
2.12	Segmentation of the trapezoidal antenna into three regular shaped segments	64

Fig.N No.	Caption	Page
3.1	Concept of desegmentation. Combination of $\alpha$ - and $\beta$ -segments is (a) regular shaped $\gamma$ -segment (b) combination of regular shaped segments	67
3.2	(a) A 2-dimensional triplate circuit (b) A 2-dimensional microstrip circuit	69
3.3	Planar circuit examples to be analyzed by desegmentation method (a) Given trapezoidal circuit; (b) Desegmentation applied to circuit(a) (c) Given rectangular ring circuit; (d) Desegmentation applied to circuit (c)	71
3.4	(a) Given $\alpha$ -segment with p- and c-ports (b) Addition of $\beta$ -segment to $\alpha$ -segment (c) Additional p-ports incorporated at the locations of given c-ports (d) Given c-ports ignored	81
3.5	Desegmentation in terms of S-matrices (a) $\alpha$ -segment to be analyzed (b) Extension of $\alpha$ -segment to a regular shaped $\gamma$ -segment by addition of a regular shaped $\beta$ -segment	85
3.6	(a) The $\alpha$ -circuit to be analyzed ( $P = 1, C = 1$ ) (b) Extension of $\alpha$ -circuit to $\gamma$ -circuit by addition of $\beta$ -circuit ( $P=1, C=D=1, Q=1$ ) (c) Addition of another $\beta$ -circuit to $\alpha$ -circuit ( $P = 1; C=D=1, Q = 2$ )	95
3.7	(a) Incorporation of an additional p-port (numbered 2) to the $\alpha$ -circuit of Fig.3.6(a) (b) Addition of $\beta$ -circuit to the $\alpha$ -circuit of Fig. (a) ( $P=2, C=D=Q=1$ )	99
3.8	(a) Transmission line circuit ( $\alpha$ ) to be analyzed ( $P=1, C=1$ ) (b) Addition of $\beta$ -circuit to $\alpha$ -circuit ( $P=1, C=D=Q=1$ ) (c) Addition of $\beta$ -circuit to $\alpha$ -circuit ( $P=1, C=D=1, Q=2$ )	102
3.9	Variation of input reactance at port $P_1$ of the trapezoidal 2-d circuit with frequency as evaluated by segmentation and desegmentation methods	110

Fig. No.	Caption	Page
3.10	Variation of input reactance (at port $P_1$ of the rectangular ring 2-d circuit) with frequency as evaluated by segmentation and desegmentation	113
3.11	(a) Given $\alpha$ -segment, $Z_{pp\alpha}$ to be evaluated (b) Segmentation applied to $\alpha$ -segment (c) Desegmentation applied to $\alpha$ -segment	114
3.12	(a) $\alpha$ -segment to be analyzed (b) Segmentation applied to $\alpha$ -segment (c) Desegmentation applied to $\alpha$ -segment	117
3.13	Two dimensional circuit configurations where desegmentation can be more efficient than the segmentation or vice versa depending upon the size of the patch removed from the regular shapes	119
3.14	(a) Single port network embedded in a two-port network (b) Three port network embedded in a $\beta$ -network	121
3.15	(a) Circuit configurations where desegmentation can be used but segmentation is not possible (b) Approximate segmentation of one of the circuits of type (a)	127
4.1	(a) A corner fed nearly square CP microstrip patch antenna (b) The cavity model considered as multiport circuit	130
4.2	Variation of axial ratio with frequency for different values of the ratio (b/a)	133
4.3	Variation of axial ratio with b/a ratio at 3101 MHz	134
4.4	Voltage distribution along periphery for input at $(x/a, y/b) = (0.0, 0.0)$	136
4.5	Magnetic current moment distribution and orientation of resultant moment vectors for the voltage distribution shown in Fig. 4.4	137

Fig. No.	Caption	Page
4.6	Voltage distribution along periphery for input at $(x/a, y/b) = (0.0, 0.5)$	141
4.7	Distribution of magnetic current moments and orientation of resultant moment vectors for voltage distribution of Fig. 4.6	142
4.8	Voltage along periphery of the antenna for input at $(x/a, y/b) = (0.5, 0.0)$	143
4.9	Magnetic current moment distribution and orientation of resultant moment vectors equivalent to voltage distribution of Fig. 4.8	144
4.10	Variation of amplitudes of far-field components (in $\phi = 90^\circ$ plane) with frequency for a diagonal fed antenna	145
4.11	Vector sum of magnetic current moments of Fig. 4.7 and Fig. 4.9. The two resultant vectors are nearly perpendicular to each other	147
4.12	Variation of input VSWR and axial ratio with feed location along the diagonal AC	149
4.13	Variation of input VSWR with frequency	151
4.14	Variation of input VSWR with input port location on the diagonal AC	152
4.15	Variation of input VSWR with feed location on the diagonal AC	154
4.16	Variation of input VSWR with frequency for diagonal fed antenna	155
4.17	Variation of axial ratio with frequency for input port at $r = 0.36$ AC	157
4.18	Variation of axial ratio with frequency for diagonal fed antenna	158
4.19	Antenna configuration and its radiation pattern (theoretical) in $\phi = 90^\circ$ plane for feed located on the diagonal as shown in Fig. 4.13 (inset), substrate thickness = $1/8"$	160

Fig. No.	Caption	Page
4.20	Radiation pattern for the diagonal fed antenna in $\phi = 90^\circ$ plane as obtained theoretically. The feed is on the diagonal as shown in Fig. 4.16 (inset). Substrate thickness=1/16"	161
4.21	Photograph of diagonal fed antennas fabricated on (a) 1/8" thickn substrate with $\epsilon_r = 2.52$ , (b) 1/16" thick substrate with $\epsilon_r = 2.49$	162
4.22	Experimental set up for radiation pattern and axial ratio measurement	164
4.23	Comparison of theoretical and experimental values of $E_\phi$ in $\phi = 90^\circ$ plane for a diagonal fed antenna. Feed location is as shown in Fig. 4.13 (inset)	165
4.24	Comparison of theoretical and experimental values of $E_\phi$ in $\phi = 90^\circ$ plane for a diagonal fed antenna. Feed location as in Fig. 4.13 (inset)	166
4.25	Comparison of theoretical and experimental values of $E_\phi$ for a diagonal fed antenna. Feed location is as in Fig. 4.16 (inset)	167
4.26	Comparison of values of $E_\phi$ as obtained theoretically and experimentally. Feed location is as in Fig. 4.16 (inset)	168
5.1	Corners chopped square patch antenna for circular polarization	174
5.2	(a) The regular square $\gamma$ -segment (b) Removal of $\beta_1$ and $\beta_2$ segments from $\gamma$ -segments from $\gamma$ -segment yields $\alpha$ -segment of Fig. 5.1	175
5.3	(a) The antenna structure considered as multi-port circuit; p-ports:1 to 25; c-ports: 26 to 33; (b) The $\beta$ -segments with 4 d-ports and 4-q ports on each of them	176

Fig. No.	Caption	Page
5.4	Variation of axial ratio with frequency for different values of truncation 'b'	179
5.5	Distribution of voltage along the periphery of the antenna for feed location as shown	180
5.6	Magnetic current moment distribution and orientation of resultant moment vectors for voltage distribution of Fig. 5.5	182
5.7	Variation of voltage along periphery of the antenna for feed location at corner A	184
5.8	Magnetic current moment distribution and orientation of resultant moment vectors for voltage distribution of Fig. 5.7	185
5.9	Variation of amplitudes of the two orthogonal components of far-field with frequency in broad-side direction in planes A-A and B-B.	186
5.10	Voltage distribution along the periphery of the antenna for feed location as shown (inset)	187
5.11	Magnetic current moment distribution and orientation of resultant moment vectors for voltage distribution of Fig. 5.10	188
5.12	Vector addition of magnetic current moment vectors of Fig. 5.8 and of Fig. 5.11	190
5.13	Variation of input VSWR with feed location on $x/a_e = 0.5$ line; substrate thickness = $1/8"$	191
5.14	Variation of input VSWR with feed location on $x/a_e = 0.5$ line for a $1/16"$ substrate antenna	194
5.15	Variation of input VSWR with frequency for a corners chopped square patch antenna; substrate thickness = $1/18"$	196
5.16	Variation of input VSWR with frequency for a $1/16"$ substrate corners chopped antenna. Feed location is as optimized in Fig. 5.14.	197



Fig. No.	Caption	Page
5.17	Variation of axial ratio with frequency for corners chopped antenna on $1/8$ " thick substrate	199
5.18	Variation of axial ratio with frequency for a corners chopped square patch antenna on $1/16$ " thick substrate	200
5.19	The corners chopped square patch antenna and its radiation pattern in $\phi = 90^\circ$ plane at 3.1758 MHz	202
5.20	Radiation pattern (in $\phi = 90^\circ$ plane) for corners chopped antenna on a polystyrene substrate of thickness = $1/16$ "	203
5.21	Photograph of corners chopped antennas (a) Substrate thickness = $1/8$ ", $\epsilon_r = 2.52$ (b) Substrate thickness = $1/16$ ", $\epsilon_r = 2.49$	205
5.22	Theoretical and measured values of $E_\theta$ and $E_\phi$ (in $\phi = 90^\circ$ plane) for corners chopped antenna shown in photograph 5.21 (a). Substrate thickness = $1/8$ " , $\epsilon_r = 2.52$	206
5.23	Radiation pattern for a corners chopped antenna (on $1/16$ " polystyrene substrate with $\epsilon_r = 2.51$ ) shown in photograph 5.21 (b)	207
6.1	(a) A square patch with a diagonal slot; (b) $\gamma$ -segment as combination of $\alpha$ - and $\beta$ -segments	213
6.2	Location of various ports on $\gamma$ - and $\beta$ -segments, $P=25, Q=C=D=27$ ; only a few $q$ -ports are shown for clarity	215
6.3	Incorporation of additional $p$ -ports (26 to 37) around the periphery of the slot; $P=37, Q=27$ . This scheme reduces computational effort and computer storage requirement	218
6.4	Voltage along outer periphery of the antenna	221
6.5	Voltage variation along the periphery of the slot	222

Fig. No.	Caption	Page
6.6	Magnetic current moment distribution and orientation of the two resultant vectors. The two resultant vectors are in space-quadrature	224
6.7	Variation of axial ratio with slot width (w)	226
6.8	Variation of axial ratio with slot length	227
6.9	Variation of voltage along periphery for feed at corner A	230
6.10	Variation of voltage along the periphery of the slot for feed at corner A	231
6.11	Magnetic current moment distributions and orientation of resultant magnetic current moment slot radiation effect cancels out	232
6.12	Voltage distribution along the outer periphery of the antenna for feed at corner B	233
6.13	Distribution of voltage along the periphery of the slot for feed at corner B	234
6.14	Magnetic current moment distributions and orientation of resultant current moments; slot radiation effect is in opposition to that due to peripheral magnetic current	236
6.15	Variation of amplitudes of the two orthogonal components of far-field with frequency for the diagonal slot antenna	237
6.16	Summation of components of magnetic current moments for the two orthogonal modes shown in Fig. 6.11 and Fig. 6.14	239
6.17	Variation of axial ratio and input VSWR with feed location on $x/a_e = 0.5$ line	241
6.18	Variation of input VSWR with frequency for two different locations of input port on $x/a_e = 0.5$ line (coaxial feeding)	243

Fig. No.	Caption	Page
6.19	Variation of axial ratio with frequency	245
6.20	Radiation pattern (in $\phi = 90^\circ$ plane) for a square patch antenna with a diagonal slot	246
6.21	Photograph of the square patch antenna with a diagonal slot	247
6.22	Theoretical and experimental values of far-field components in $\phi = 90^\circ$ plane (a) $E_\theta$ (b) $E_\phi$	249
7.1	(a) Desegmentation applied to pentagon (b) Segmentation and desegmentation applied to pentagon (c) Desegmentation of a square with a corners chopped square removed	259
7.2	Desegmentation applied to three discontinuity configurations	261
7.3	(a) A suspended microstrip circuit and the extension of boundary (b) An inverted microstrip circuit and extension of boundary	264
B.1	A stripline half-wave resonator with upper plane removed	267

## SYNOPSIS

### DESEGMENTATION METHOD AND ITS APPLICATIONS TO CIRCULARLY POLARIZED MICROSTRIP ANTENNAS

A Thesis Submitted

In Partial Fulfilment of the Requirements  
for the Degree of  
DOCTOR OF PHILOSOPHY

by

PRAMOD CHANDRA SHARMA

Department of Electrical Engineering  
Indian Institute of Technology, Kanpur  
January, 1982

Two-dimensional microstrip-like components find applications in microwave integrated circuits (MICs) and in planar microstrip antennas. These components have their lengths and widths comparable to, or greater than, the wavelength at the frequency of operation but the height is much smaller than the wavelength. The methods for analysis and design of two-dimensional components, that have been proposed in the literature, include the Green's function approach, the countour integral method, the spectral domain analysis, and the finite element method. The Green's function approach is based on the availability of the impedance Green's functions for certain regular shapes such as rectangles, circles, annular rings, circular and annular sectors, and three types of triangles, viz., equilateral, right-angled isosceles, and  $30^\circ - 60^\circ$  right-angled. Segmentation method is available for shapes which can be partitioned into

these regular shaped segments. Some of these techniques, namely, the finite element method, the Green's function approach, and the spectral domain technique have been used for the analysis of microstrip patch antennas also.

The use of segmentation method for analysis and design of microstrip patch antennas is proposed in this thesis. A complementary technique called desegmentation method is proposed for analysis of two-dimensional components in MICs and in microstrip antennas. The proposed techniques are used in the design and optimization of three types of singly fed circularly polarized microstrip antennas.

The Green's function approach for analysis and design of planar microstrip antennas, as used in this thesis, employs impedance Green's functions for segments with magnetic wall boundaries. In this method, the antenna is modelled as a multiport resonator with the magnetic wall boundary located slightly outside the physical periphery to compensate for the fringing reactive fields. The periphery of this resonator is divided into a discrete number of sections of small widths. Each of these sections is considered as a port of the multiport network. The Z-matrix for this multiport is evaluated using Green's function(s). For antenna configurations of irregular shapes (i.e. those for which Green's functions are not available), the segmentation and the desegmentation methods are used. The ports on the periphery of the antenna are

terminated by conductances to account for the radiated power. The element  $Z_{ii}$  of the Z-matrix of the resultant loaded multiport network gives the input impedance at the  $i$ th port. The radiation characteristics are evaluated in terms of the magnetic current equivalent to the voltage distribution along the periphery.

In the desegmentation method (proposed in this thesis) one or more regular shaped segments are added to the given irregular shaped segment such that the resultant shape is either a regular shape or a combination of regular shapes. The segment(s) added and the resultant shape are analyzed by Green's function approach and segmentation method. The characterization for the given circuit is obtained in terms of the characterization of the added segment(s) and that of the resultant circuit configuration. This method has been formulated both in terms of Z-parameters and in terms of S-parameters. The validity and applications of the method have been illustrated by several examples of lumped circuits, transmission line circuits, and planar circuits. The desegmentation method has also been used to evolve a generalized method for de-embedding of multiport networks.

Two different design philosophies have been proposed in the literature for obtaining circular polarization from microstrip antennas. In the first case, one uses structures (e.g. squares and circles) with two spatially orthogonal modes which

are excited in phase quadrature by two separate feeds. This arrangement requires a  $90^\circ$ -hybrid for feeding the antenna. The other philosophy makes use of two spatially orthogonal modes which are resonant at slightly different frequencies and the antenna is excited at an intermediate frequency by a single suitably located feed point. In this case the  $90^\circ$ -hybrid is not needed. Several configurations of the latter category have been suggested in the literature. However, detailed analysis and designs have not been reported.

In this thesis, three types of such antennas (viz., a nearly square patch with diagonal feed, a corners chopped square patch, and a square patch with a diagonal slot) have been analyzed and optimized. Desegmentation method outlined above has been used for this purpose. The results are verified experimentally.

A nearly square patch circularly polarized antenna (for which an axial ratio of about 1.4 dB has been reported earlier) is optimized using Green's function approach. The optimum ratio of length to width of the rectangle that gives the best axial ratio is found to depend on the thickness and dielectric constant of the substrate. Antennas on substrates having different thickness and values of dielectric constant have been optimized for axial ratio and input VSWR with respect to a 50 ohm coaxial line. Axial ratio as good as 0.45 dB with input VSWR equal to 1.73 (substrate

thickness =  $1/8$ ",  $\epsilon_r = 2.52$ ), and in another case an axial ratio of 0.17 dB with input VSWR equal to 1.33 (on  $1/16$ " thick substrates with  $\epsilon_r = 2.52$  and 2.49) have been realized in S-band.

A corners chopped square patch antenna has also been analyzed and optimized. The antenna configuration is a square patch with two right-angled isosceles triangular segments from opposite corners removed. The method of desegmentation is used for analysis. The optimum value of truncation for the best axial ratio is determined. Axial ratio of 0.02 dB (input VSWR = 2.2 on  $1/8$ " substrate) and 0.12 dB (input VSWR = 1.6 on  $1/16$ " substrate with  $\epsilon_r = 2.51$ ) have been achieved for S-band operation.

A square patch antenna with a diagonally located slot has also been optimized by desegmentation method. The dimensions of the slot for the best axial ratio and the feed location for the best input VSWR are optimized. An axial ratio equal to 0.2 dB with input VSWR about 2.2 has been obtained.

A comparative study of the three structures, outlined above, reveals that a square antenna with a diagonal slot has the best axial ratio bandwidth whereas a diagonal fed nearly square antenna has best input VSWR values.



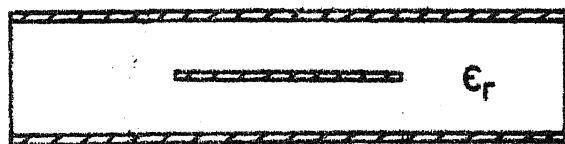
## CHAPTER ONE

### INTRODUCTION

This chapter is a brief review of the two-dimensional (2-d) components used in microwave integrated circuits (MICs) and 2-d microstrip antennas. An outline of the rest of the chapters is also included.

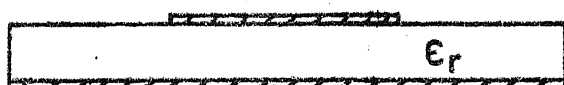
#### 1.1 TWO-DIMENSIONAL COMPONENTS

The use of 2-d components in microwave integrated circuits (MICs) has been proposed about a decade back [1] - [4]. These components have two dimensions comparable to or greater than the wavelength. The third dimension is much smaller than the wavelength and therefore these components are known as 2-d components. The three types of possible configurations of 2-d components are : (i) triplate or stripline-type as shown in Fig. 1.1(a); (ii) open or microstrip-type shown in Fig. 1.1(b) and (c); (iii) waveguide or cavity-type as illustrated in Fig. 1.1(d). The stripline- and microstrip-types of circuits find applications in MICs and can be considered as generalizations of respective one-dimensional (1-d) circuits when the transverse dimension becomes comparable to the wavelength at the frequency of operation. The waveguide-type circuit shown in Fig. 1.1(d) can be regarded as a special case of three-dimensional (3-d)



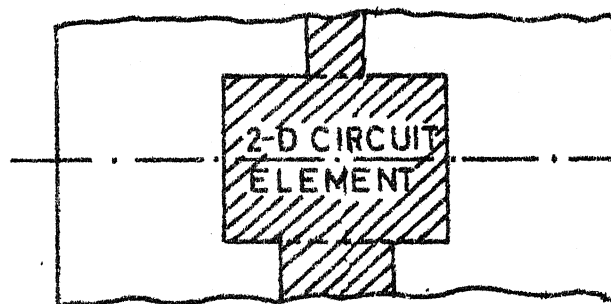
Stripline type

(a)

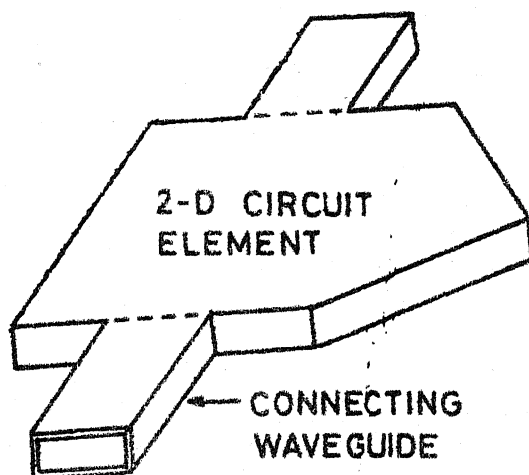


Microstrip type

(b)

Plan view of  
(a) and (b)

(c)



Waveguide type

(d)

FIG.11 THREE TYPES OF 2-d MICROWAVE CIRCUITS

waveguide circuits where the height is much smaller than the wavelength.

### 1.1.1 Applications

The 2-d components find several applications in microwave integrated circuits, waveguide circuits, and ferrite components. Some of the major applications of the 2-d components are listed below.

#### A. Resonators

Two-dimensional components form good resonators compatible with microstrip circuits. Rectangular and circular geometries have been used as resonators for quite some time [1], [5]. The triangular components have been proposed for resonators as well as for use as prototype elements for band-pass and band-stop filters [6], [7]. The gap coupled triangular segments have been proposed for filter circuits [6] and the triangular resonators have been used in the design of three port circulators [7]. More work on triangular resonators has been reported [8], [9] recently. The rhombic and hexagonal resonators have also been proposed [8],[ 9] for use in MICs.

#### B. New Circuit Configurations

Designs of several new circuits have emerged as a result of the development of 2-d circuits. Use of a circular disk resonator as a 3-dB hybrid [5], and as a coupled mode

filter [10] has been reported. T-junctions with triangular geometry have been proposed [8] for use in inphase power dividers and branch line hybrids. It has been shown that the triangular shaped T-junctions exhibit better performance than their counterpart with rectangular geometry [8] in stripline and microstrip circuitry.

#### C. Non-reciprocal elements

Non-reciprocal components may be designed by fabricating 2-d circuits on ferrite substrates [11]. The analysis of such circuits has been carried out using the 2-d approach discussed in the next section. A optimized wide-band 2-d circulator has also been reported in the literature [12].

#### D. Discontinuities as 2-d elements

Equivalent circuits have been reported for several discontinuities in stripline and in microstrip lines [13], [14]. For several discontinuities the equivalent circuits are not available. These discontinuities can, in general, be considered as 2-d components and analyzed by using 2-d approach [8]. Moreover, this approach yields better characterization of the discontinuities than the use of equivalent circuits which are mostly based on quasi-static considerations. Thus the 2-d approach can be considered as a general technique for analyzing stripline and microstrip line discontinuities [15],[8].

Several waveguide discontinuities, when the geometry and the modal fields are uniform along the thickness, can also be analyzed by 2-d approach.

#### 1.1.2 Methods for analysis of 2-d components

The geometry of the 2-d component (i.e. the shape of the central conducting patch in a triplate structure or the upper conducting patch in microstrip type circuit) governs the choice of the method of analysis. A brief review of various methods of analysis of 2-d components is given below.

##### A. Spectral domain analysis [16] - [18]

This technique has been used for quasi-static as well as for full-wave analysis of some of the 2-d configurations. In quasi-static approach, the capacitance for the circuit configuration is evaluated by solving the Poisson's equation in the Fourier transform domain. In full-wave analysis, Galerkin's procedure is employed to deduce a determinantal characteristic equation from the coupled algebraic equations in the Fourier transform domain. This method has been used for rectangular [16], circular [17], triangular [19], and some other composite shapes [19].

##### B. Finite element and contour integral techniques

The finite element method [2] and the contour integral approach [1] have been employed for analyzing 2-d components

of arbitrary geometries such as one shown in Fig. 1.2. In finite element method [20], the conducting patch is divided into several segments and certain basis functions are integrated over each of these segments.

The contour integration approach [1] has been specifically proposed for 2-d component analysis and is based on Green's theorem in cylindrical coordinates. In this approach the voltage at a point on the periphery is evaluated in terms of a line integral along the periphery.

#### C. Green's function approach

When the component, or segment, is of simple (regular) shape, the impedance Green's function [1] technique is the most appropriate method. Green's functions for shapes such as rectangular [1], circular [5], right-angled isosceles triangle, equilateral triangle,  $30^{\circ}$ - $60^{\circ}$  triangle [21], and for circular sectors, annular sectors and annular rings [22] are available. The impedance matrix of 2-d elements with specified locations of ports can be found using these Green's functions.

In more general situations, when the geometry of a 2-d circuit can be considered as combination of regular shapes (i.e. for which Green's functions are available) the segmentation method [3], [4], [23] can be used for evaluating the characteristics of the given circuit in terms of those of the regular shaped segments. Some examples of these shapes are shown in Fig. 1.3(a). There are several situations where the

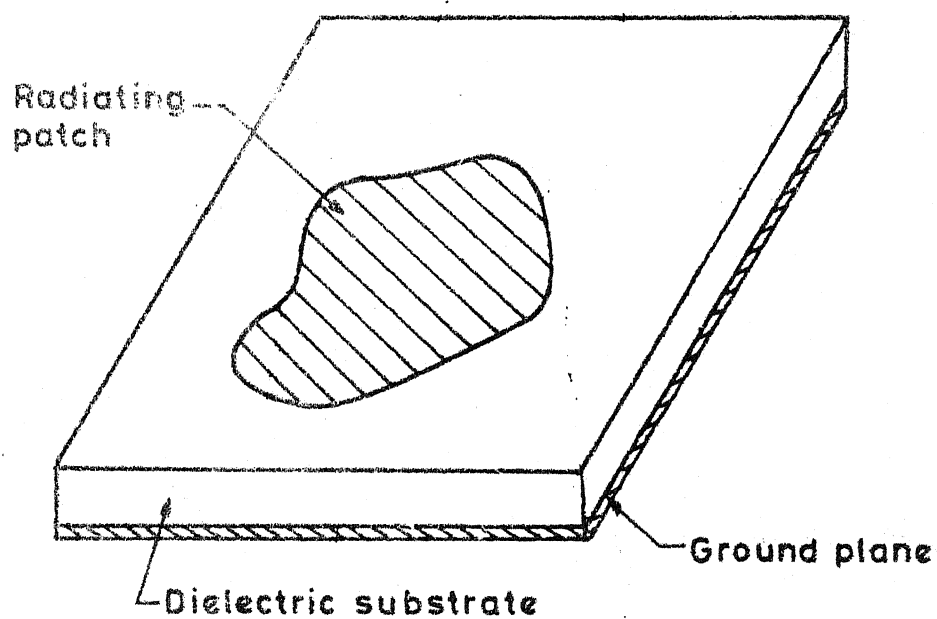
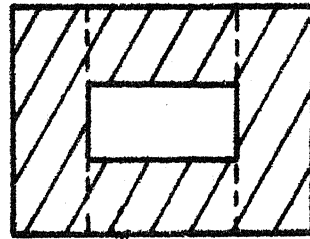
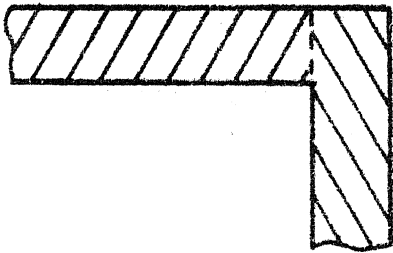
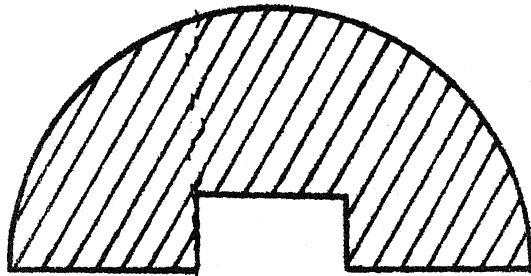
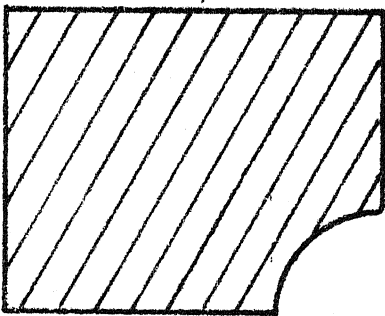


FIG-12 A GENERAL 2-d MICROSTRIP CONFIGURATION



(a)



(b)

**FIG. 1-3 EXAMPLES OF CIRCUIT CONFIGURATIONS WHERE**  
**(a) Segmentation method is applicable ;**  
**(b) Segmentation method is not applicable**



segmentation method is not applicable. Two examples of such circuits are shown in Fig. 1.3(b). No method, other than the numerical methods, of dealing with these shapes has been available so far. Each one of these configurations may be visualized as regular shape from which another smaller regular shape has been removed. A method for analyzing such configurations is proposed in Chapter Three.

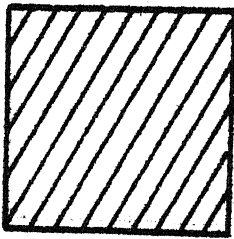
## 1.2 TWO-DIMENSIONAL MICROSTRIP ANTENNAS

The term 'microstrip antennas' is used for a variety of planar radiating structures on dielectric substrates such as shown in Fig. 1.4 to Fig. 1.7. These include patch antennas, travelling wave antennas, slot antennas, dipole antennas and have been discussed in the literature extensively [24] - [41]. More references to work on microstrip antennas may be found in [24] - [41]. Investigations in this thesis are confined to microstrip patch antennas which could be called 2-d microstrip antennas also.

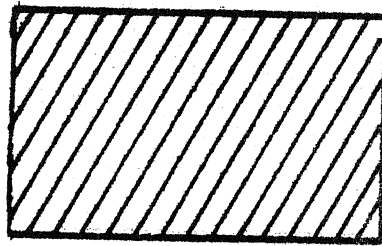
The concept of microstrip antennas was first proposed by Deschamps [24] in 1953. After twenty years since Deschamps proposal, Howel [25] and Munson [26] reported practical microstrip antennas. There are several attractive features of microstrip antennas which have made them very popular in the last decade. Some of these aspects are mentioned below.

### 1.2.1 Special features of microstrip patch antennas

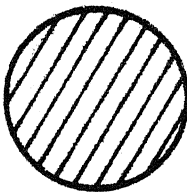
Microstrip patch antennas have several advantages over



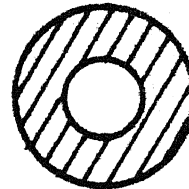
Square



Rectangle



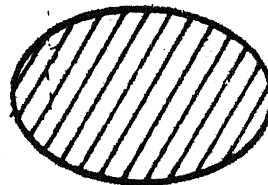
Disk



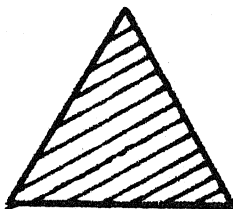
Ring



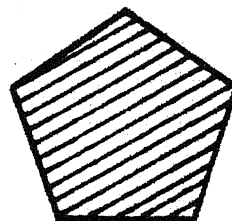
Semidisk



Ellipse

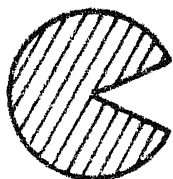


Equilateral triangle

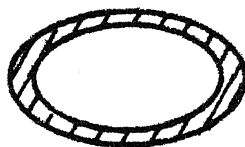


Pentagon

FIG-14(a) GEOMETRIES OF SOME OF THE MICROSTRIP PATCH ANTENNAS



Disk with slot



Elliptical ring



Disk sector



Semi ring



Right angled  
Isosceles triangle



Ring sector

FIG. 1.4(b) SOME MORE GEOMETRIES OF MICROSTRIP  
PATCH ANTENNAS

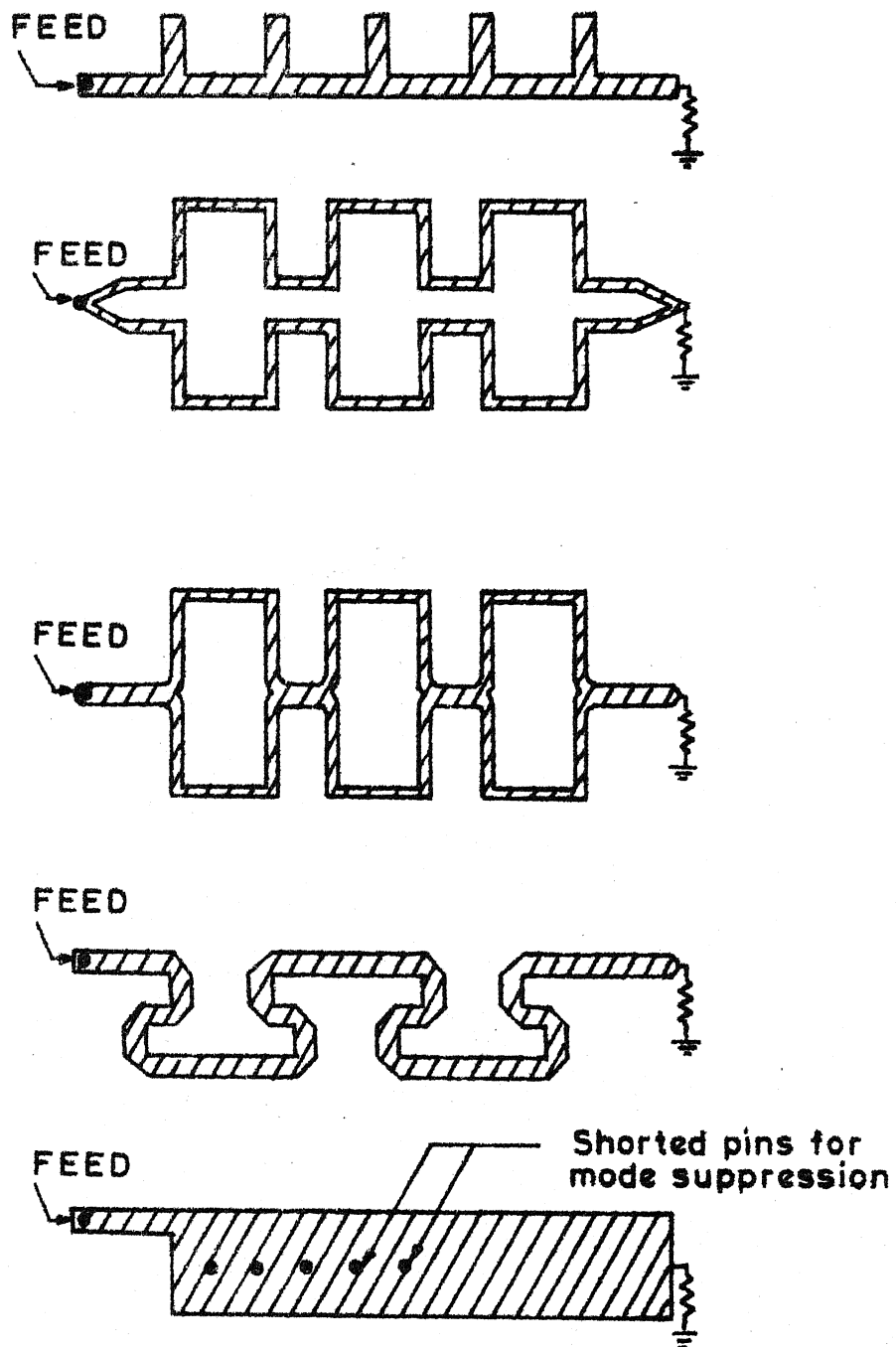


FIG. 1.5 TRAVELLING WAVE ANTENNAS

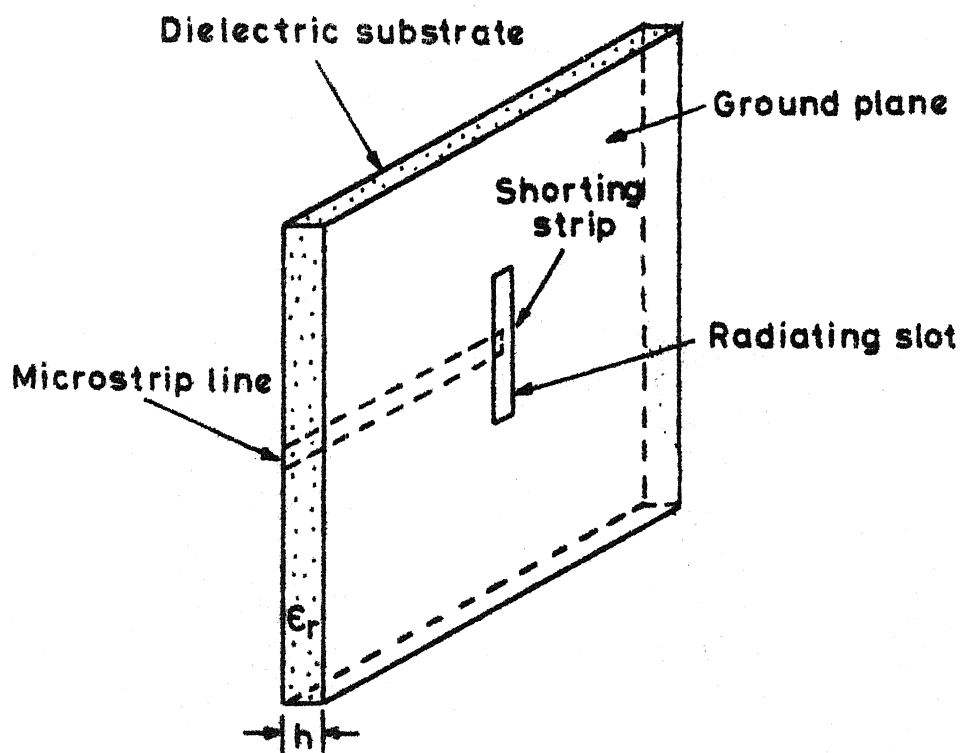
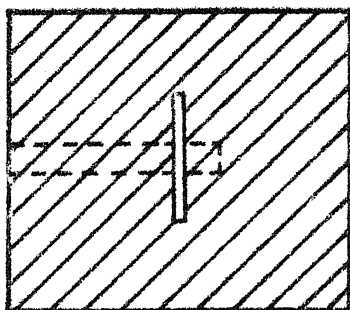
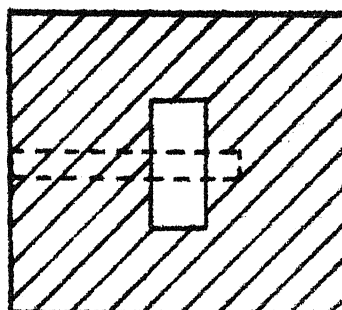


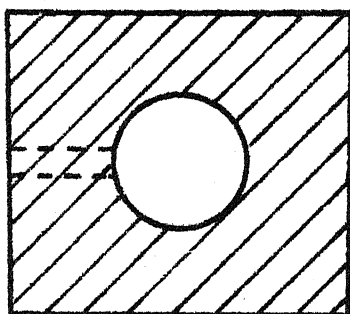
Fig. 16(a) MICROSTRIP SLOT ANTENNA



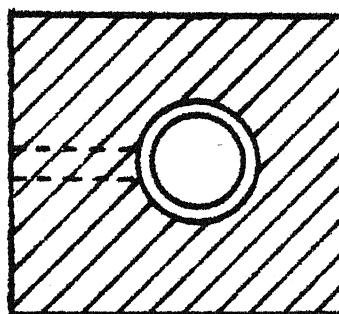
Narrow slot



Wide slot



Circular patch slot



Circular ring slot

FIG.1-6(b) SOME GEOMETRIES OF MICROSTRIP  
SLOT ANTENNAS

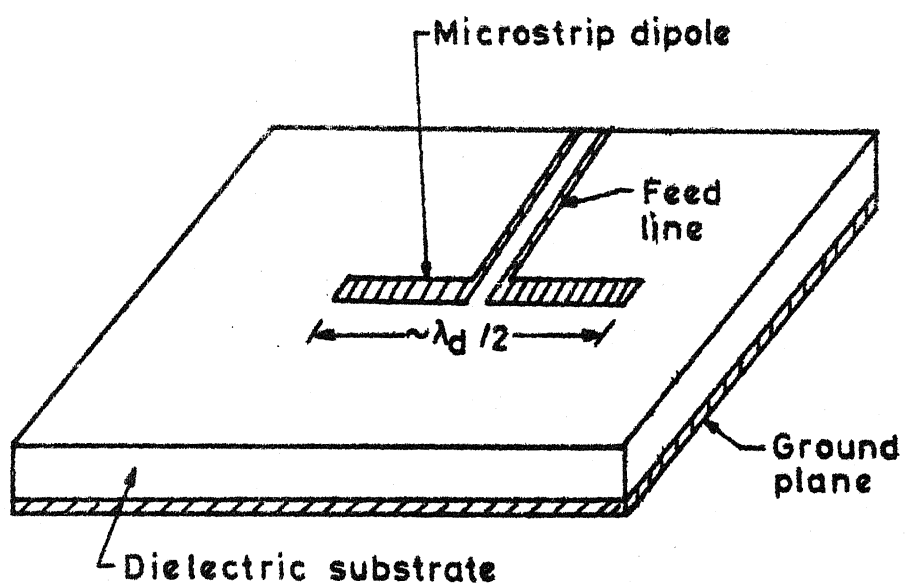


FIG.17 A MICROSTRIP DIPOLE ANTENNA

the conventional antennas [38]. The significant ones are listed below.

- i) Microstrip patch antennas are light in weight, have low volume and low-profile planar configurations which can be made conformal. These features make them suitable for mounting on missiles, rockets, and satellites without perturbing the aerodynamic behaviour of the host vehicles.
- ii) Linear and circular polarizations (right or left handed) are possible.
- iii) Dual frequency antennas can also be designed easily.
- iv) These antennas are compatible with microwave integrated circuits so that solid state devices such as oscillators, amplifiers, variable attenuators, switches, modulators, mixers, phase shifters etc. can be easily fabricated on the antenna substrate itself.
- v) Feed lines and matching networks are fabricated simultaneously with the antenna.

On the other hand, the major shortcoming of microstrip antennas is their narrow bandwidth. Typical antenna bandwidths are of the order of 1 percent to 5 percent. Also, there is a possibility of excitation of surface waves which propagate along the surface of the dielectric substrate used for antenna. These surface waves can cause radiation in undesired directions and produce excessive mutual coupling between elements in antenna arrays.



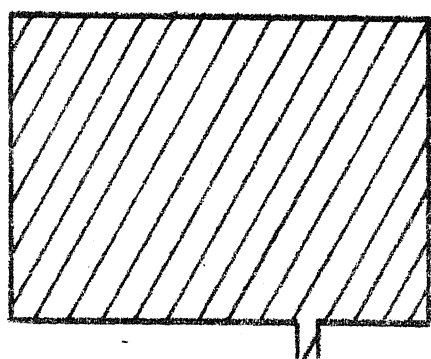
The various linearly and circularly polarized microstrip patch antennas and their methods of analysis are discussed in the following section.

### 1.2.2 Linearly polarized microstrip patch antennas

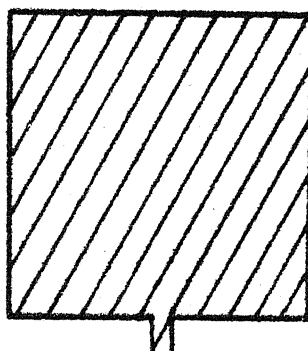
Extensive work on linearly polarized microstrip antennas and antenna arrays has been reported in the literature. Well documented reviews and references are available in [37],[38]. Most of the linearly polarized antennas have simple shapes and are excited in the dominant mode. For these antennas the magnetic currents, equivalent to the voltages at the radiating apertures, are linearly polarized and yield linearly polarized far-field. These antennas can be analyzed by modal-expansion method [32],[34] or by Green's function approach [40]. Some of the shapes used for linearly polarized antennas are shown in Fig. 1.8. The eigen-functions for all these shapes are available [32]. Several other geometries which can be analyzed by modal-expansion method, have been reported in [32]. A detailed account of the linearly polarized antennas is available in [38].

### 1.2.3 Circularly polarized microstrip patch antennas

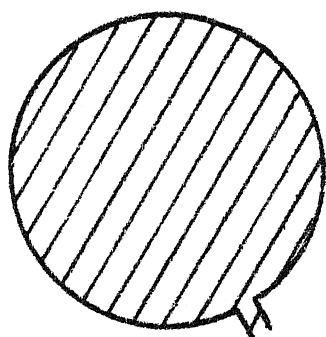
The antennas designed for circular polarization are, generally, more complicated in shapes than those used for linear polarization. As is well known, a circularly polarized field can be decomposed into two components in space- and time-quadrature. If a radiating structure provides



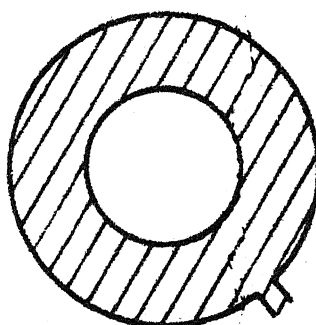
Rectangular



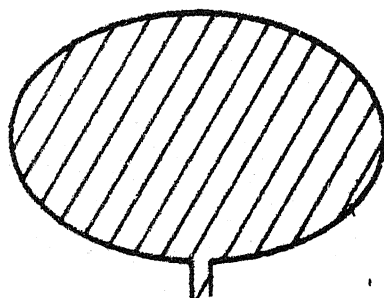
Square



Circular



Circular ring



Elliptical

IG-18 SOME OF THE LINEARLY POLARIZED 2-d  
MICROSTRIP PATCH ANTENNAS

these two components of the wave, circular polarization results. Circularly polarized antennas may be divided into two categories depending upon the mechanism responsible for providing the two components required for producing circular polarization.

A. Category I : Antennas with two separately fed orthogonal modes

These antennas consist of two orthogonal elements or single structure capable of supporting two modes which are excited in phase-quadrature by using an additional phase shifting network such as  $90^\circ$ -hybrid. An example of this type of antennas is the crossed-dipoles with an external  $90^\circ$ -hybrid coupler. This antenna is capable of providing, both, the left-hand and right-hand circular polarizations depending upon the phase relationship between the two inputs. The circularly polarized microstrip patch antennas of this category [27],[37],[39] are shown in Fig. 1.9. The geometries of such antennas are, normally, simple and can be analyzed by using suitable eigen-functions.

B. Category II : Antennas with excitation of two orthogonal modes through a single feed

These antennas yield circular polarization by virtue of the physical configuration of the radiating structure. The space- and time-quadrature relationships are provided by the geometries of the antennas. Various circularly polarized

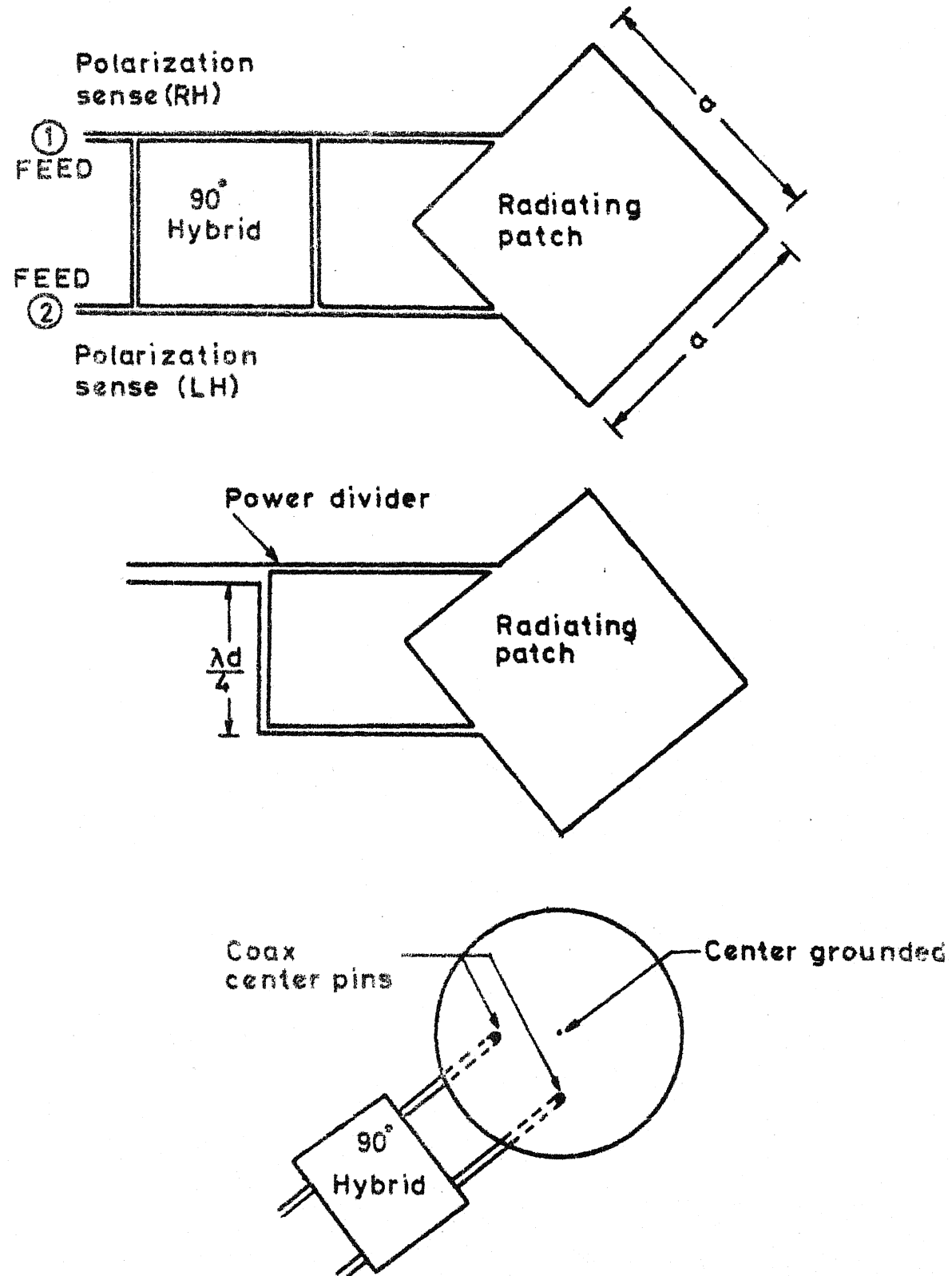
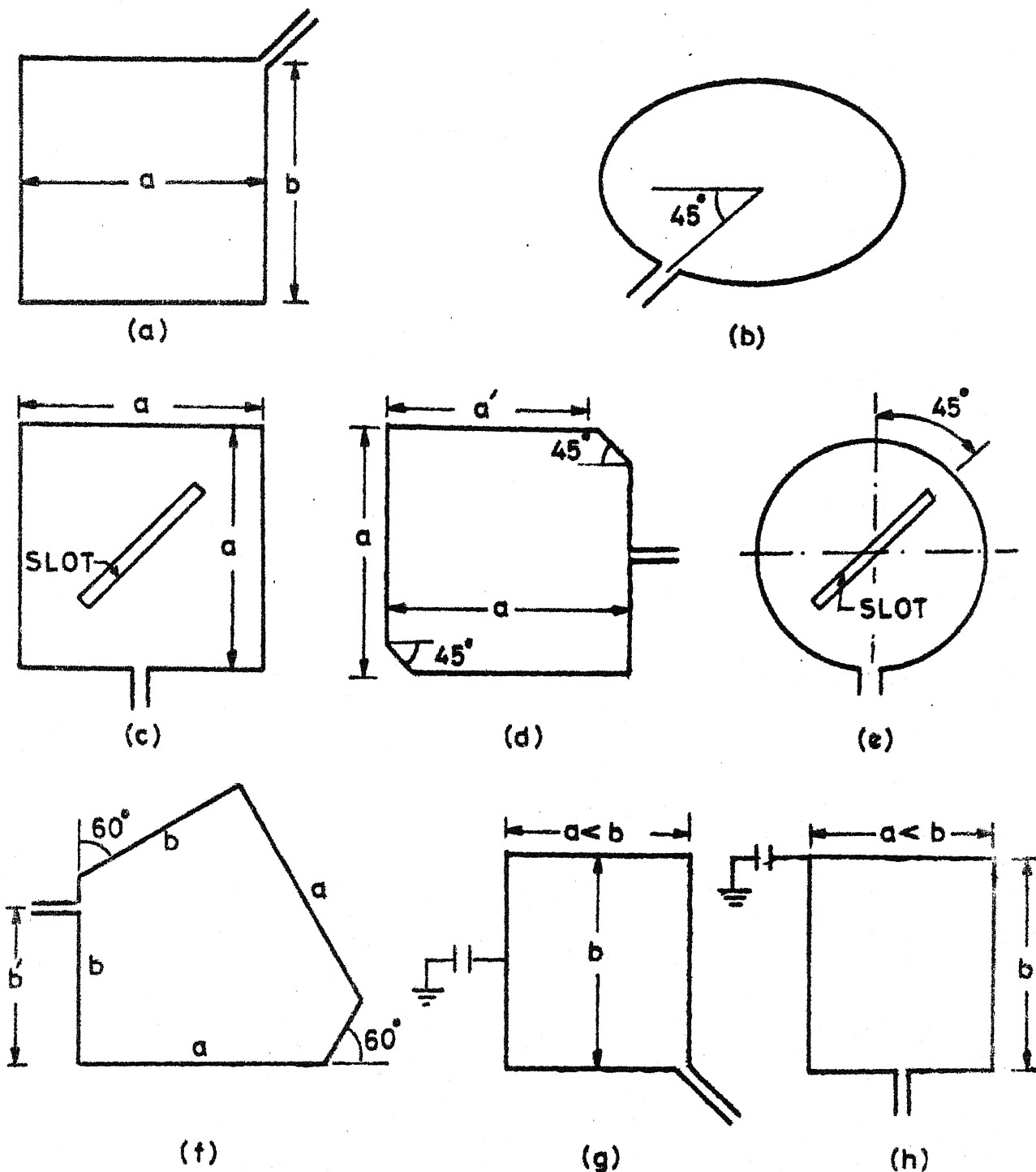


FIG. 19 CIRCULARLY POLARIZED PATCH ANTENNAS OF CATEGORY I (a) Square with hybrid (b) Square with power divider (c) Circular patch with hybrid

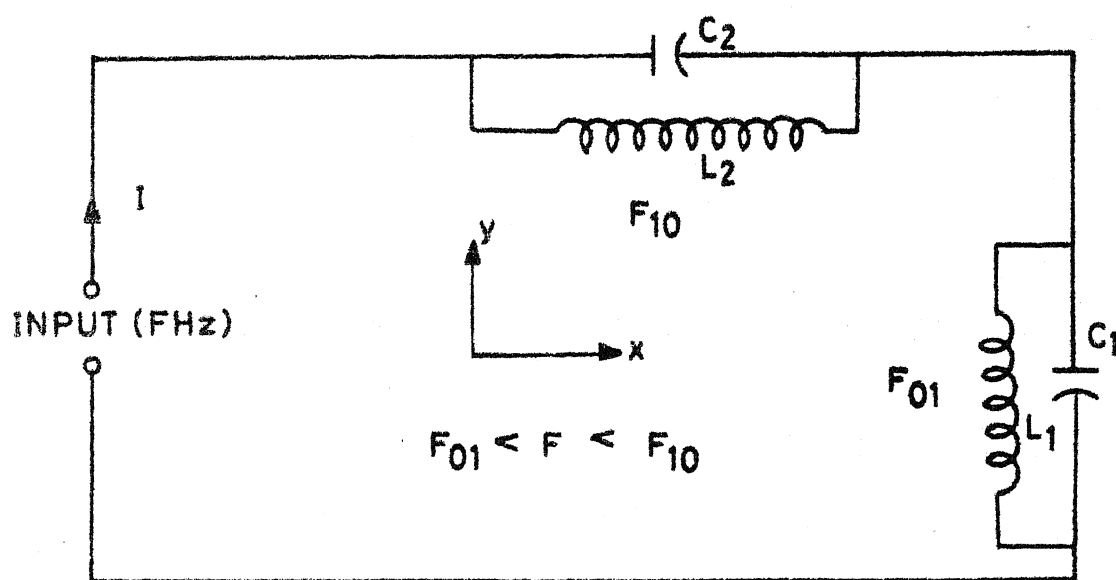
microstrip patch antennas, with single feed, reported in the literature are : the corner fed rectangle [31], [42], the slightly elliptical patch [35], [36], the square patch with diagonal slot [33], corners chopped square patch [33], the circular patch with a slot along the diameter [43],[37], the pentagon shaped patch [28],[44], and the capacitor loaded rectangular shaped patch [39]. The geometries of these antennas are shown in Fig. 1.10.

The key point in operating mechanism of these antennas is the equal excitation of two orthogonal almost degenerate modes. Some asymmetry is introduced to remove the degeneracy of the two modes. With the introduction of the asymmetry, the resonance frequency of one of the modes decreases whereas that of the other (orthogonal) mode increases and the modes are thus decoupled. These two modes are excited by selecting the frequency of operation and the feed point such that one of the mode voltages leads the input current by  $45^\circ$  whereas that of the other mode lags the input current by  $45^\circ$ . When this condition is fulfilled, circular polarization is obtained.

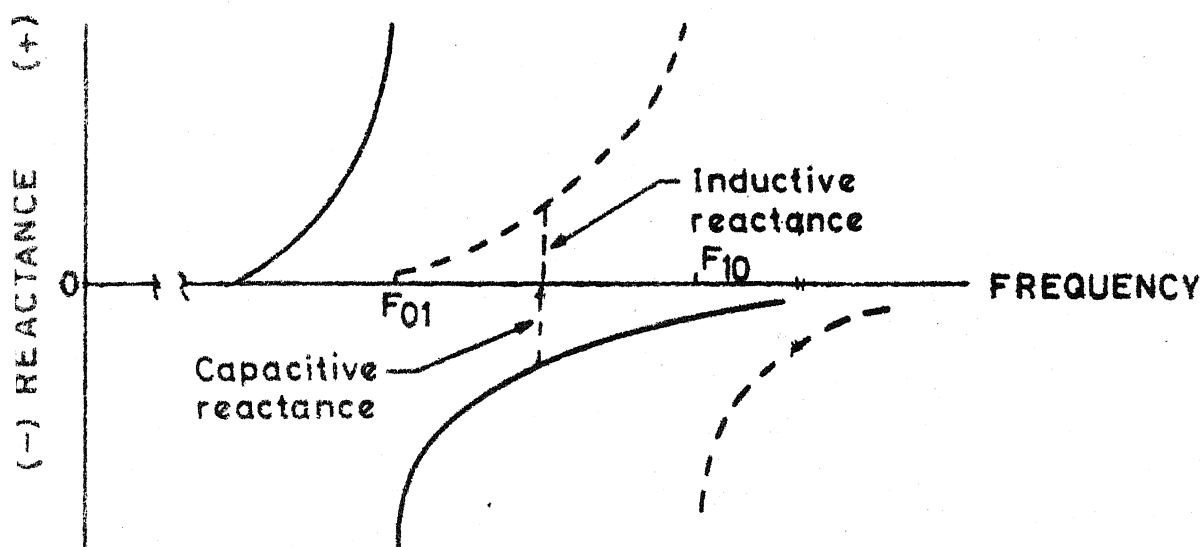
The above discussed mechanism can be illustrated as follows. When the radiation losses are ignored and it is assumed that higher order modes are not excited, the two orthogonal modes can be represented by two resonant circuits as shown in Fig. 1.11(a). The variations of reactances with



**FIG.1-10 CIRCULARLY POLARIZED MICROSTRIP PATCH ANTENNAS OF CATEGORY II**  
 (a) Corner fed rectangle; (b) Elliptical; (c) Square with diagonal slot; (d) Corners chopped square; (e) Circular with slot; (f) Pentagon; (g) and (h)



(a)



(b)

FIG.111 (a) TWO ORTHOGONAL MODES WITH RESONANCE FREQUENCIES  $F_{01}$  AND  $F_{10}$  REPRESENTED BY LUMPED RESONANT CIRCUITS ;(b) REACTANCE VARIATION WITH FREQUENCY. THE RADIATION RESISTANCE NOT SHOWN

frequency for the two circuits of Fig. 1.11(a) are shown in Fig. 1.11(b). When the frequency ( $F$ ) of the input current  $I$  lies between  $F_{01}$  and  $F_{10}$ , the reactance offered by one of the circuits is inductive whereas that offered by the other circuits is capacitive. If  $F_{01}$  and  $F_{10}$  are separated by appropriate amount and  $F$  is chosen suitably, the magnitudes of the two reactances can be made equal. Now consider the two component circuits to be loaded by resistances representing the radiated power as illustrated in Fig. 1.12(a). The phasor diagram for various voltages and input current is shown in Fig. 1.12(b). It may be noted that the voltage across one of the circuits lags behind the current by  $45^\circ$  and that across the other circuits leads the latter by  $45^\circ$ . The two voltages are thus in phase-quadrature. Since the field distributions of the two modes are spatially orthogonal, the voltage vectors  $V_{01}$  and  $V_{10}$  are oriented at right angle to each other. Such a situation can be realized to obtain circular polarization in various microstrip patch antennas of Fig. 1.10 by choosing suitable dimensions, the location of feed and frequency of operation.

In the case of the corner fed rectangular (nearly square) antenna [31] of Fig. 1.11(a) the two dimensions 'a' and 'b' are nearly equal. Two orthogonal modes ( $10$  and  $01$ ) are excited when the feed port is along the diagonal of the rectangle. If the frequency of operation lies between the



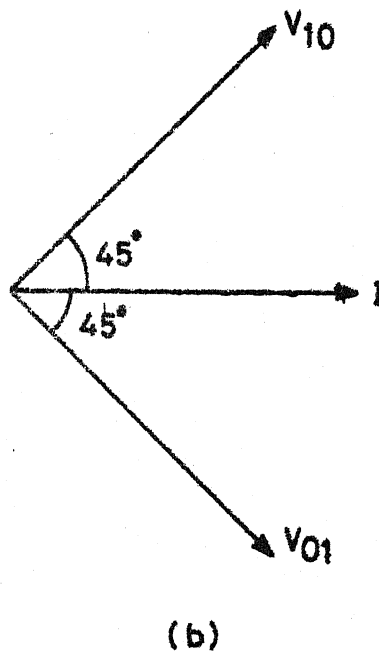
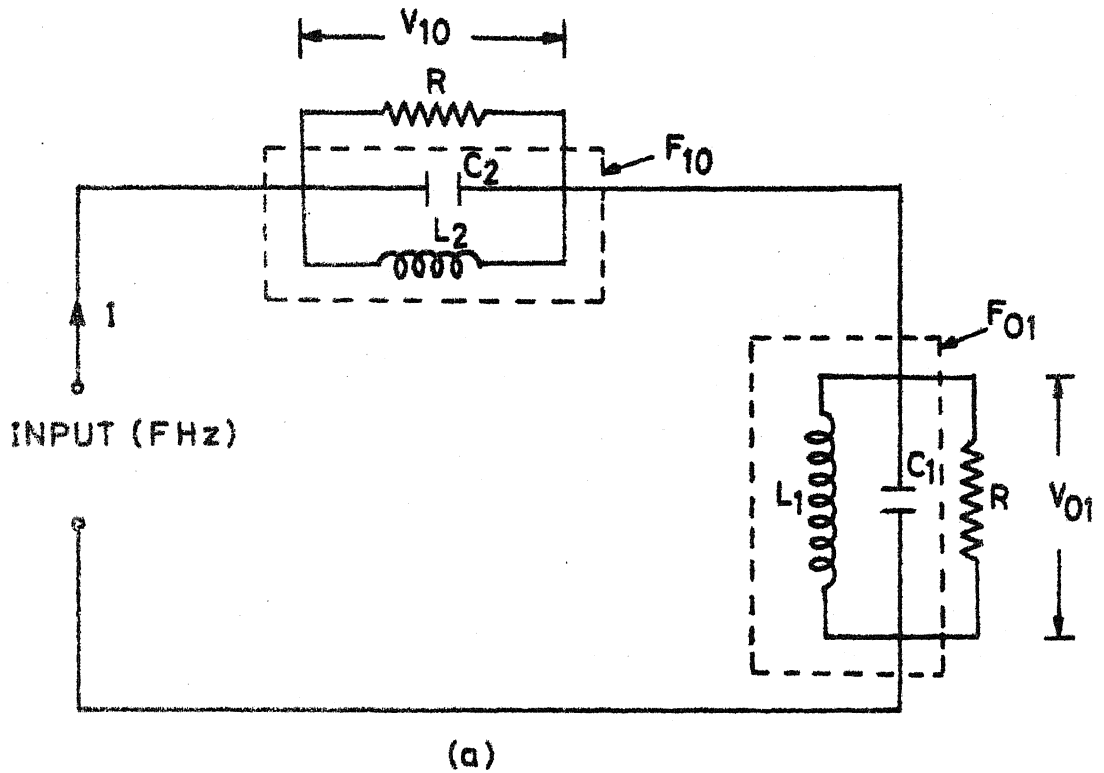


FIG. 1-12 (a) Ideal resonant circuits of Fig. 1-11(a) loaded with radiation resistance;  
(b) Phasor diagram

resonance frequencies of these two orthogonal modes, the respective mode voltages can be made to be in phase quadrature. Lo et al [39] have pointed out that circular polarization is obtained when  $b = a(1 + \frac{1}{Q})$ , where  $Q$  is the quality factor of the antenna. When this condition is satisfied the resonance frequencies of the two modes are separated by a factor  $\frac{1}{Q}$ . This antenna has been studied by Carver and Coffey [42] using the modal-expansion approach.

The elliptical patch antenna of Fig. 1.10(b) has also been studied theoretically as well as experimentally [35],[36]. The asymmetry in the circular shape due to the eccentricity makes the resonance frequencies of the two spatially orthogonal modes slightly different and provides the necessary decoupling of the two orthogonal modes. The feed location suitable for this purpose is found to be at an angle  $45^\circ$  with respect to the semi-major axis. It has been reported [35],[36] that best circular polarization is obtained when the ratio of the minor to major axis is 0.976. The axial ratio remains within 6 dB over a bandwidth of 1.5 percent (1.33 to 1.35 GHz,  $\epsilon_r = 2.41$  and substrate thickness = 0.3175 cm). The theoretical investigations of this antenna have been carried out by Shen [35] using the Mathieu functions to express the modal spectrum and solving the Helmholtz equation in elliptical coordinates.

The antenna configurations of Figs. 1.10(c), (d) and (e) have been studied experimentally by Kerr [43],[33]. Theoretical design and performance results about the slot antennas of Fig. 1.10(c) and (e) are not available. Detailed analysis of a corners chopped square patch antenna of Fig. 1.10(d) has also not been reported.

The pentagon shaped antenna of Fig. 1.10(f) has been experimentally studied by Weinschel [28] and theoretical investigations were carried out by Carver and Coffey [44] using finite element method. It has been pointed out by Weinschel [28] that this antenna exhibits circular polarization over 1 percent bandwidth. It has been explored [44] that in this case also two orthogonal modes, in phase-quadrature, exist for a particular feed location.

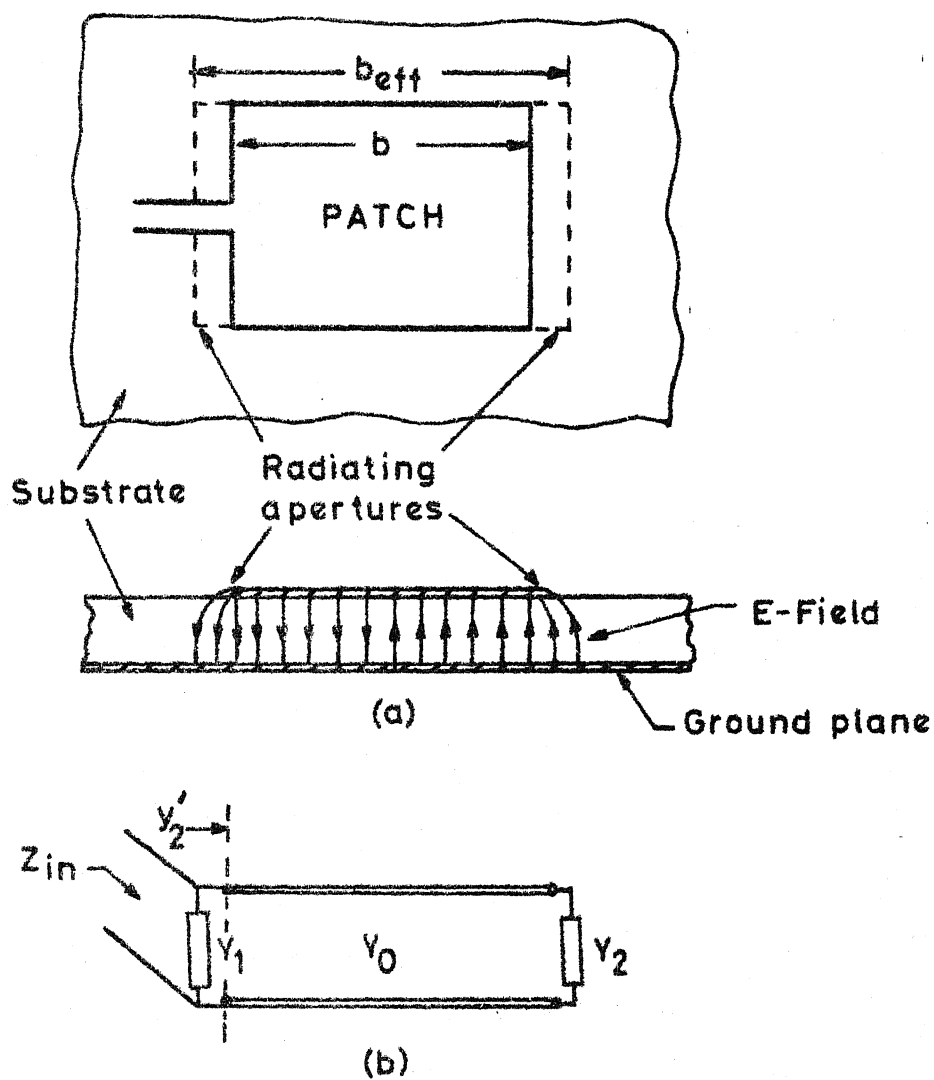
The capacitor loaded antenna [39] of Fig. 1.10(g) and (h) operate on the same principle as the corner fed rectangular antenna of Fig. 1.10(a). The effect of connecting the capacitor at mid-point of side 'b' (Fig. 1.10(g)) is to change the resonance frequency of one of the modes while the other resonance remains unchanged, the capacitor being located at null E-field point of the latter mode. Similar effect is produced for the antenna configuration of Fig. 1.10(h) when the feed is at mid-point of one of the sides as shown in Fig. 1.10(h).

#### 1.2.4 Methods of analyzing microstrip antennas

Several methods of analysis of microstrip patch antennas have been proposed in the literature. Some of these methods are suitable for geometries of simple shapes whereas the others (the numerical techniques) have been used for analyzing antennas with complicated geometries. It may be pointed out here that 2-d resonators and 2-d microstrip antennas differ only in terms of the thickness and dielectric constant of the substrates. Antennas are normally constructed on substrates having  $\epsilon_r$  less than 10 and the thickness larger than those used for resonators. Thus the methods that are used for 2-d component analysis can be used for microstrip antenna analysis also. A brief review of the various techniques, proposed so far, is given below.

##### A. Equivalent transmission-line method [26], [37]

This method is applicable to the analysis of rectangular antennas excited in the dominant mode. In this technique, the radiating element is modelled as a transmission-line. The radiating edges of the antenna are modelled as apertures, radiating into half-space, as shown in Fig. 1.13. The effective dimensions of the antenna are therefore greater than the physical dimensions by an amount equal to the sum of the widths of the two apertures. The physical dimensions 'b' of the antenna is chosen slightly less than half-wavelength ( $\lambda_0/2\sqrt{\epsilon_r}$ ) for the dielectric substrate so that



Transmission line model

FIG. 113 A RECTANGULAR PATCH ANTENNA  
MODELLLED AS TRANSMISSION LINE

due to the fringing field the effective dimension ' $b_{eff}$ ' is equal to half the wavelength and the two apertures are excited  $180^\circ$  out of phase. The aperture admittance [45], input resistance and resonance frequencies are calculated using the slot widths and the effective dimension  $b_{eff}$  [26], [37]. The input impedance is calculated by referring the admittance of one of the apertures to the location of the other aperture as illustrated in Fig. 1.13(b). The field distribution along the radiating edges is considered constant and the radiation characteristics are evaluated. Although this method is the simplest of all the methods, this has a few limitations because of one-dimensional approximations. These are [37] :

- (i) the method is useful for rectangular patches only;
- (ii) the field along the radiating edges is assumed constant which is not strictly true;
- (iii) it is assumed that the extension of the length of the model is same for all sizes of the patches;
- (iv) the effect of the location of the feed port along the transverse dimension is not accounted for.

Another method, which overcomes most of above mentioned shortcomings is the modal-expansion method discussed below.

#### B. Modal-expansion method [32],[34],[37]

In this approach the radiating patch is modelled as

resonator with magnetic walls. The location of magnetic walls is shifted outwards to account for fringing field and further analysis is carried out in terms of effective dimensions [46] which are slightly larger than the physical dimensions of the cavity. The field in the cavity is expanded in series of appropriate eigen-functions. The effect of losses, including those due to radiation, are accounted for by considering an increased effective loss tangent [32] or by employing impedance boundary conditions [34]. This approach has been found to yield accurate results and can be used for analyzing shapes for which eigen-functions are available [32], [34]. Although this method overcomes most of the shortcomings of the equivalent transmission-line method, it cannot be used for analyzing general patch antenna geometries such as shown in Fig. 1.10(c), (d), (e) and (f). In such situations the numerical methods such as finite element method [44] and method of moments [47], [48] are used.

### C. Finite element method [44], [37]

The finite element method has been used by Carver and Coffey [44] for analyzing pentagon shaped patch antenna. The interior region of the microstrip antenna is mathematically decoupled from the exterior region through the use of an equivalent aperture admittance as boundary condition. The inhomogeneous wave equation, satisfied by the interior electric field, with impedance boundary condition along the antenna wall perimeter is solved as variational problem [37].

As in the case of analysis of 2-d circuit components, the antenna geometry is divided into several small segments (such as triangles or rectangles). Trial functions are used to solve variational problem in each segment and the boundary conditions are imposed locally along the edges of segments. The problem is treated as an eigenvalue problem and solved numerically.

D. Method of moments [47], [48], [37]

In this technique the electric surface currents, flowing over the patch and ground planes, and the magnetic currents flowing over the magnetic wall are evaluated by using the Richmond's reaction method [48], [37]. The reaction integral equation is solved using the boundary conditions for the surface currents and the method of moments. Using suitable expansion functions for electric currents, and electric test sources for magnetic surface currents, the integral equations are reduced to algebraic equations. The coefficients of these algebraic equations give the elements of the impedance matrix. Although this method could be used for analyzing patch antennas of arbitrary geometries, it is computationally expensive [37]. Out of all the methods discussed above the modal expansion method has been found to be the simplest and gives good accuracy.



### E. Spectral domain technique [51], [52]

The spectral domain technique proposed earlier [16], [18] for microstrip transmission lines has been extended to analyze microstrip antenna structures [51], [52]. The formulation of the method [51] is based on the spectral domain immittance matrix which is derived from spectral domain equivalent circuits and the solution is obtained using Galerkin's method. In the case of a circular disk antenna, the full wave analysis has been carried out using Hankel transform [52]. In this [52] approach the antenna is considered as a resonator. Since the problem is viewed as a homogeneous one (wherein no excitation is considered) no information about input impedance is obtained.

### F. Green's function approach [40]

The Green's function approach with impedance wall boundary has been used for evaluating the input impedance of a circular disk microstrip patch antenna [40]. The effect of thickness of substrate and of dielectric constant on VSWR bandwidth have been investigated and reported in [40].

## 1.3 OUTLINE OF PRESENT INVESTIGATIONS

The investigations reported in this thesis are aimed at the extension of the applicability of the Green's function approach (with magnetic wall boundary conditions) for design and analysis of 2-d components of more general shapes and of microstrip patch antennas. The emphasis is on the

design and optimization of circularly polarized patch antennas employing the Green's function approach and the desegmentation method developed during these investigations.

The applicability of the Green's function approach [1] has been extended, for analysis and design of 2-d components having shapes that could be considered as combination of simple shapes, by segmentation method [3],[4],[23]. It is proposed in this thesis that the Green's function approach, with magnetic wall boundary conditions, can be used for analysis and design of patch antennas. The proposed technique is developed in Chapter Two. In this approach, the antenna configuration is considered as a planar lossless multiport network obtained by dividing the radiating periphery of the antenna into a discrete number of small sections (so that field variation over width of each section is negligible). Each of these sections is considered as a port. The Z-matrix of the equivalent multiport network is evaluated employing Green's function. For more general shapes the segmentation and/or desegmentation methods are used. The elements of the Z-matrix so obtained are purely reactive since losses in the dielectric, in the conducting planes and the radiated power have not been incorporated. The ports of this multiport network are loaded with radiation resistances to account for the radiated power.

The input impedance and voltage around the periphery of the antenna (and therefrom the radiation characteristics) are evaluated from the Z-matrix of the loaded network. This approach is applicable to antennas of more general shapes than those which could be analyzed by modal-expansion method.

The formulation of the desegmentation method is developed in Chapter Three. In this method, a 2-d configuration (an irregular shape for which Green's function is not available) is considered as obtained by removal of one or more regular shapes from a larger segment which is either regular shaped or a combination of regular-shapes. The Z- or S-parameters for the regular shaped segments are evaluated employing Green's function approach. The Z- and S-parameters for the given segment can be evaluated in terms of those of the segments removed and those of the larger segment from which the segments are removed. The validity of the formulation is illustrated by several examples of lumped-circuits, transmission line networks, and planar circuits. The S-matrix formulation is used to evolve a generalized method for de-embedding of multiport networks. An illustrative example is given.

In the next three chapters the Green's function approach and the desegmentation method have been used to analyze and to optimize three types of circularly polarized microstrip antennas with single feed. These include three diagonal fed

nearly square patch antennas, two corners-chopped square patch antennas, and a square patch antenna with a diagonal slot discussed in Chapters Four, Five and Six respectively.

The modal-expansion method has been used by Carver and Coffey [42] for analysis and design of a corner-fed (called diagonal-fed in this thesis) rectangular patch antenna and experimental value of axial ratio of about 1.4 dB has been reported. In the present investigations, the Green's function approach has been used to optimize the antenna polarization characteristics. Axial ratio as low as 0.17 dB has been achieved, and experimentally verified. Axial ratio limited bandwidth and VSWR bandwidth are evaluated. Optimization is also carried out for input VSWR with coaxial feed so that no external impedance matching network is needed. Three S-band antennas on different substrates are investigated. These results are reported in Chapter Four.

Chapter Five gives the details of investigations carried out on a corners chopped square patch antenna which has been studied experimentally by Kerr [33], [43]. The desegmentation method and the Green's function approach are used for optimizing the axial ratio and the optimum value of the truncation of two opposite corners of a square patch is arrived at. Axial ratio as low as 0.02 dB has been obtained in the analytical design and also verified experimentally by fabricating antennas on  $1/8$ " and  $1/16$ " thick substrates.

Axial ratio and input VSWR are studied as functions of frequency and the optimum location of the feed point is arrived at.

Some experimental results on a square patch antenna with a diagonal slot have been reported earlier by Kerr [33], [43]. However, no procedure for theoretical analysis and design of this type of antenna have been reported as yet. In the present investigations, reported in Chapter Six, desegmentation method is used to optimize the antenna performance. The axial ratio equal to 0.2 dB has been obtained theoretically and confirmed experimentally. Variations of axial ratio and input VSWR with feed location are investigated. The axial ratio bandwidth and input VSWR bandwidth are evaluated.

The mechanism of operation of all the three types of circularly polarized antennas is explained in terms of two orthogonal modes in phase-quadrature. The voltage distribution for a single feed that results in circular polarization (CP) is shown to be a linear combination of the voltage distributions of the two orthogonal modes. The resonance frequencies of the two orthogonal modes are evaluated theoretically and are measured.

The thesis concludes with Chapter Seven which contains comparison of three types of antennas, a summary of the present work and some suggestions for further investigations.

## CHAPTER TWO

### GREEN'S FUNCTION APPROACH AND SEGMENTATION METHOD FOR ANALYSIS OF MICROSTRIP ANTENNAS

As pointed out in the previous chapter, methods suitable for analysis of two-dimensional circuits may be used for analyzing microstrip patch antennas also. Analysis of microstrip patch antennas by modal-expansion of the field and the use of eigen-functions for magnetic wall boundary conditions has been proposed, and used successfully [32]. Coffey and Carver [42] have also used similar technique with impedance wall boundary conditions to analyze the corner fed rectangular patch circularly polarized antenna. The eigen-functions are known only for certain regular shapes. Some such configurations are shown in Fig. 2.1. When the antenna shapes are more complicated, such as shown in Fig. 2.2, alternative methods of analysis are needed. Carver and Coffey have used the finite element method for analyzing the pentagon shaped antenna [29]. The Green's function approach with impedance wall boundary [40] has also been used to compute input impedance of a circular disk antenna.

In this chapter it is proposed that the Green's function approach [1], which is frequently used for analyzing two-dimensional microwave circuits, can be employed for analyzing microstrip antennas also. Green's functions for

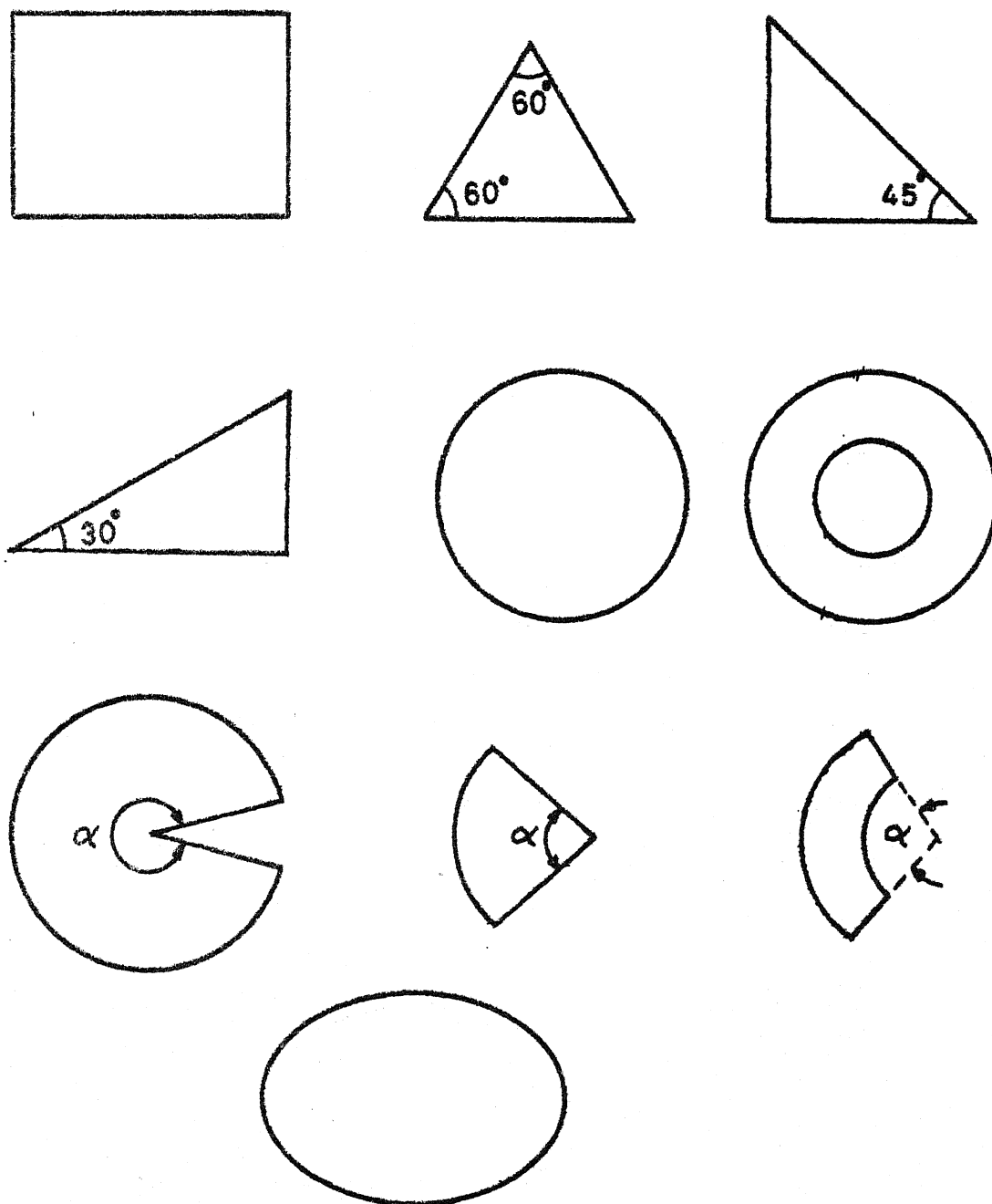
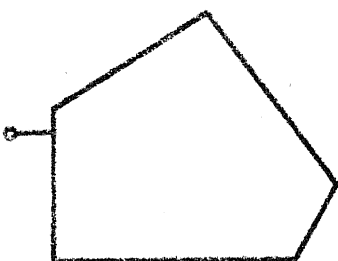
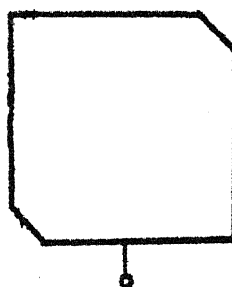


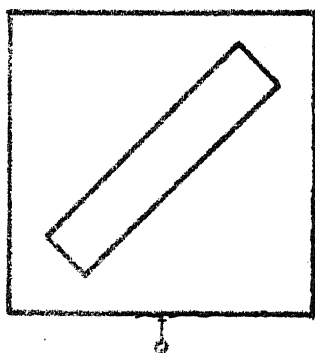
FIG.2.1 PLANAR SEGMENTS FOR WHICH EIGEN-FUNCTIONS ARE KNOWN



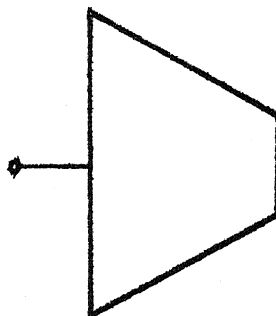
Pentagon shape



Corners chopped  
square



Square with diagonal



Trapezoidal antenna

**FIG.2-2 EXAMPLES OF ANTENNA CONFIGURATIONS  
FOR WHICH MODEL EXPANSION OR GREENS  
FUNCTION TECHNIQUE CAN NOT BE USED  
DIRECTLY**



segments with magnetic wall boundaries are used. The method may be extended by using the segmentation method [23] and the desegmentation method, proposed in Chapter Three, to analyze antenna configurations of more complicated shapes of the type shown in Fig. 2.2.

## 2.1 GREEN'S FUNCTION APPROACH

### 2.1.1 Input impedance and resonance frequency

The given antenna structure is analyzed in terms of a planar model with magnetic wall boundary. The procedure is illustrated in Fig. 2.3. The physical boundary of the antenna is extended outward [6], [46] to take into account the effect of fringing field around the edge. The periphery of the magnetic wall model is divided into several sections and each section is considered as a port. The width of each of these sections is considered small enough so that the field variation over a portwidth is negligibly small. The impedance matrix of such a multiport network model is calculated using the relevant Green's function. For shapes such as shown in Fig. 2.2 the methods of segmentation and/or desegmentation are used. When the losses in the conducting plane and in the dielectric substrate are ignored, the elements of the impedance matrix, thus obtained, are purely reactive. Until this step of computations the elements of the Z-matrix are treated as real, which results in saving in computer memory requirement and computation time. When the elements

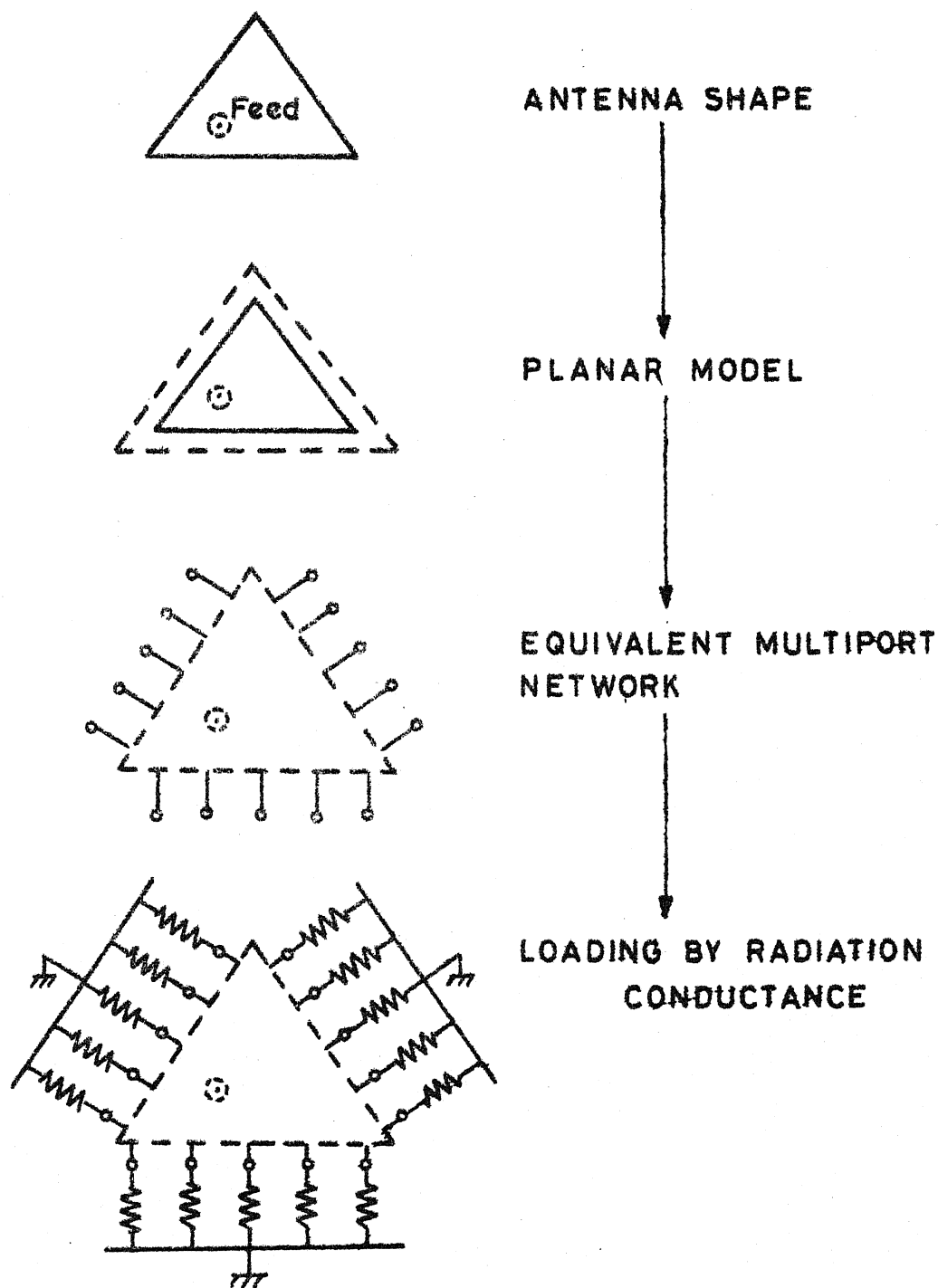


FIG.2.3 STEPS INVOLVED IN MICROSTRIP ANTENNA ANALYSIS BY GREEN'S FUNCTION APPROACH

of the Z-matrix are used further in calculations on antenna characteristics, each element is treated as complex with real part equal to zero. The poles of the input reactance yield the resonance frequencies of the planar structure (the losses in the structure and the radiated power having been ignored for the time being). At resonance frequencies of the antenna the radiations from an antenna become maximum. Also, a circularly polarized antenna excited with a single feed exhibits linear polarization at resonance frequencies because only one mode is excited dominantly. This property has been employed, in Chapters Four, Five and Six, to measure the resonance frequencies of the antennas and are found to be in good agreement with those calculated theoretically.

The losses due to radiation effect of the antenna are accounted for by loading the ports of the ideal multiport network model by radiation resistances [49], [50] as illustrated in Fig. 2.3. The values of the resistive elements (which terminate the ports) are calculated as follows :

(i) calculate the radiation conductance for each of the straight sides, for viz. that for each of the three sides of the planar model of Fig. 2.3; (ii) distribute the radiation conductance to each of the ports, the values of the radiation conductance being proportional to the respective portwidths; (iii) consider the radiation resistances so calculated

( $R_i = 1/G_i$  where  $G_i$  is the radiation conductance value at the

ith port) to be connected at the mid-point of the respective ports. The radiation resistance multiport network is considered as one multiport network ( $\beta$ ) and the multiport network representing the planar element as another network ( $\alpha$ ). This is illustrated in Fig. 2.4. The entries in the Z-matrix of  $\beta$ -network are all zeros except the diagonal elements  $Z_{ii}(= R_{ii})$  which correspond to the radiation resistance values. The impedance matrix for the combination of  $\alpha$ - and  $\beta$ -networks is evaluated using the segmentation method [8], [23] discussed in Section 2.2. The diagonal element  $Z_{ii}$  of the impedance matrix gives the input impedance at the ith port. If an input port location is already specified, this port can be considered as an additional port (in addition to those already considered around the periphery of the patch) which remains unterminated by the radiation resistance. One such input port, labelled as j port, is shown in Fig. 2.4. The necessity of adding the additional port is discussed later in Section 2.2.2.

### 2.1.2 Voltage around the periphery

The element  $Z_{ij}$  of the Z-matrix, evaluated as discussed in the preceeding section, gives the voltage at the ith port for a unit input current into the jth port. The voltage distribution around the periphery of the antenna, for any arbitrary location of the input port, is thus evaluated. It may be noted that the voltage around the periphery is a

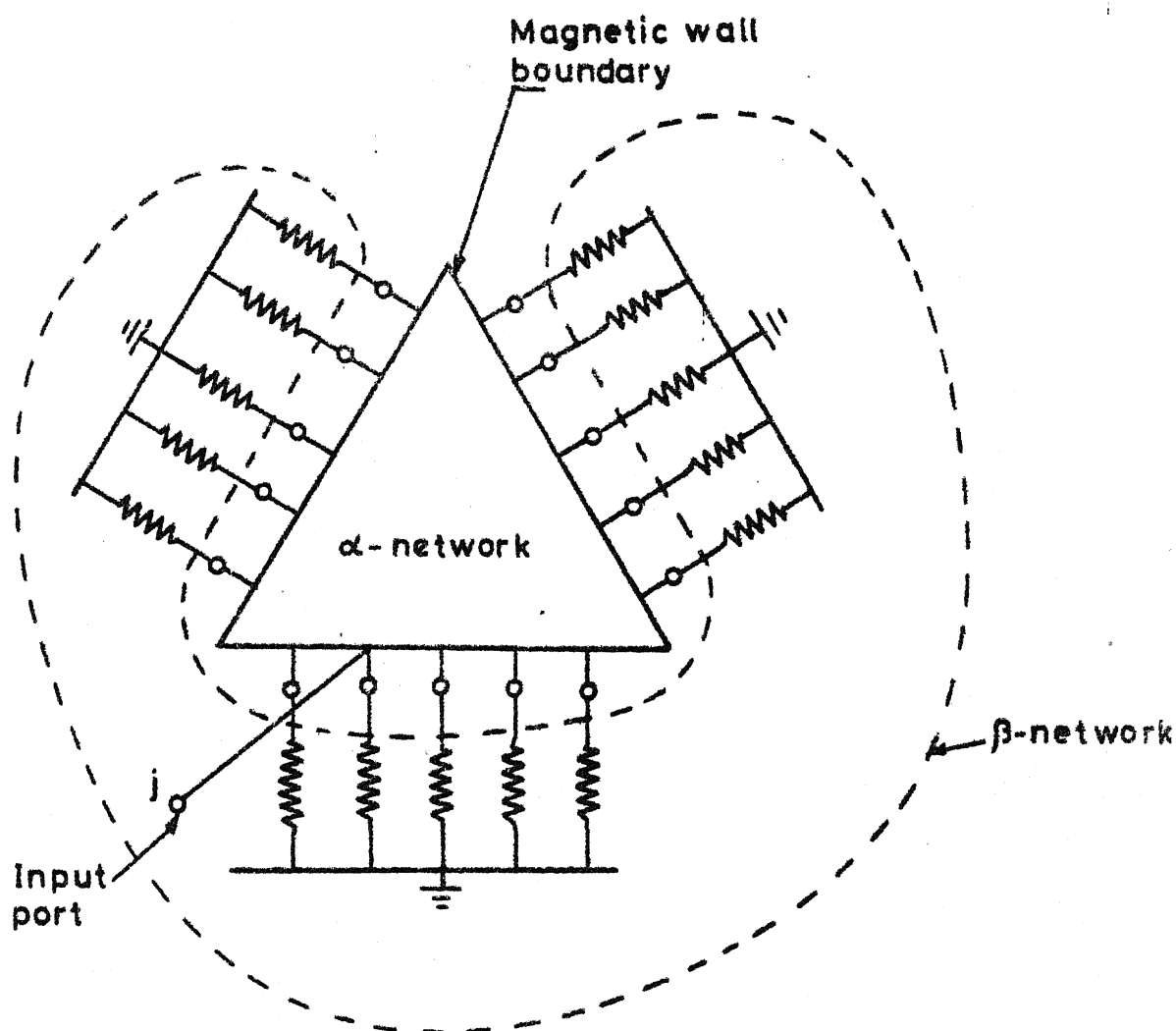


FIG.2.4 SCHEMETIC FOR EVALUATING THE Z MATRIX OF THE COMBINATION OF THE MULTIPORT(ideal) CAVITY AND RADIATION RESISTANCE NETWORK

complex variable having real and imaginary components which are in phase-quadrature. A graphical representation of the voltage variation along the periphery of the antenna can be used to predict radiation characteristics and polarization of the antenna. This aspect has been discussed later in Chapters Four to Six. The numerical evaluation of the radiation characteristics, from the voltage distribution around the periphery, is discussed in the following section.

### 2.1.3 Evaluation of radiation characteristics

The voltage at any port (small section of the periphery) can be expressed as equivalent Huygen's magnetic current source [32],

$$\bar{K}' = -2(\hat{n} \times \hat{z}) E_z, \quad (2.1)$$

where  $\bar{K}'$  is the surface magnetic current density,  $E_z$  the electric field at the respective port location directed along Z-axis,  $\hat{z}$  the unit vector directed along Z-axis, and  $\hat{n}$  is the unit outward normal to the magnetic wall. The relative orientation of  $\bar{K}'$ ,  $\hat{n}$  and  $E_z$  are shown in Fig. 2.5(a). The factor of 2 in (2.1) takes care of the image of the magnetic current with respect to the ground plane. As the thickness of the dielectric substrate, in case of planar microstrip antennas, is small and consequently there is no field variation along the Z-axis, eqn. (2.1) can be expressed as,

$$\bar{K} = 2(\hat{n} \times \hat{z}) V_z, \quad (2.2)$$

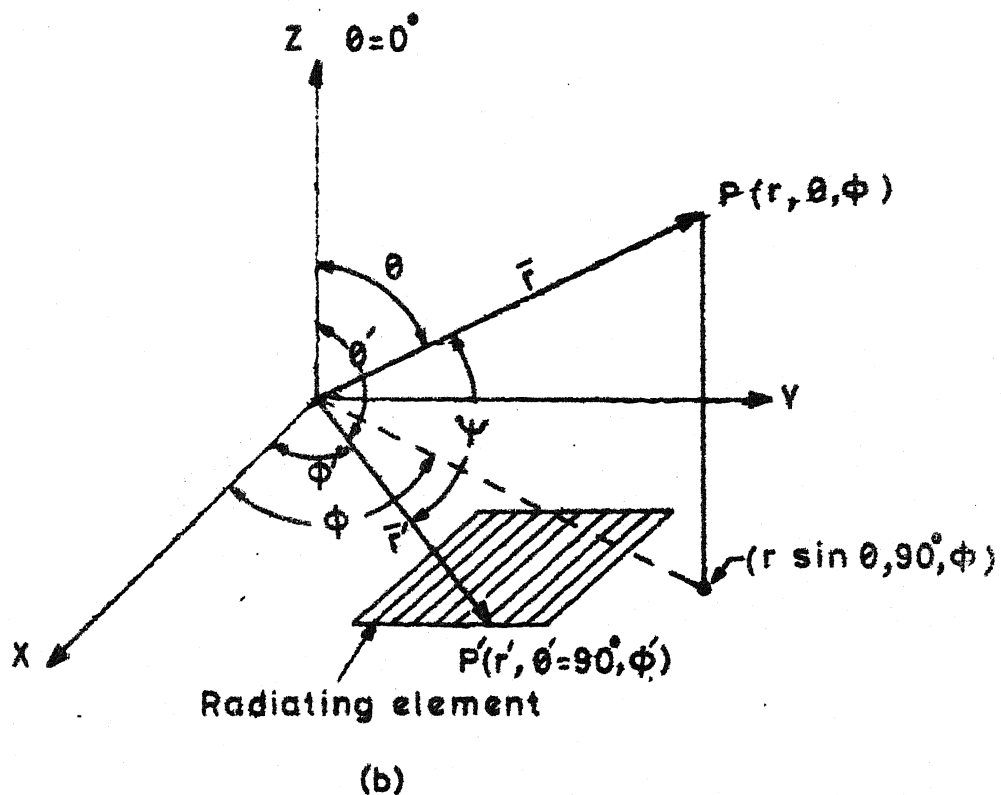
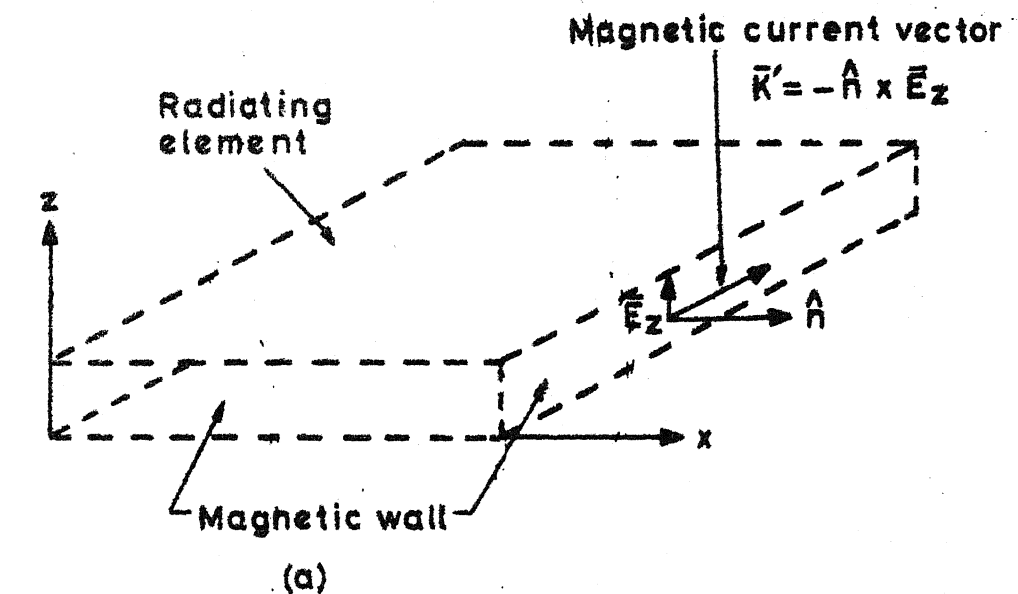


FIG. 2-5 (a) ORIENTATION OF ELECTRIC FIELD AND  
MAGNETIC CURRENT VECTORS  
(b) COORDINATE SYSTEM

where  $V_z$  is the voltage at the respective port location and  $\bar{K}$  represent the equivalent magnetic line current source (V) which corresponds to the integration of (2.1) over the thickness of the substrate. The electric vector potential for the magnetic current given by (2.2), in general, is [32],

$$\bar{F}(\bar{r}) = \epsilon_0 \int_c \frac{\bar{K}(\bar{r})}{4\pi |\bar{r}-\bar{r}'|} e^{-jk_0 |\bar{r}-\bar{r}'|} dl(\bar{r}') \quad (2.3)$$

where  $k_0$  is the free-space propagation constant and  $\bar{r}$  and  $\bar{r}'$  are the distance vectors of the field point and source point respectively as shown in Fig. 2.5(b). The integration is performed along the periphery of the antenna. When the voltage over a portwidth is considered to be constant in magnitude, (2.3) reduces to

$$\bar{F}(\bar{r}) = \frac{\epsilon_0}{4\pi} \sum_{i=1}^m \bar{K}_i(\bar{r}') \int_{c_i} \frac{1}{|\bar{r}-\bar{r}'|} e^{-jk_0 |\bar{r}-\bar{r}'|} dl(r') \quad (2.4)$$

where  $m$  is the number of ports considered around the boundary and is equal to the number of sections the periphery is divided in. The integration is thus performed over each portwidth and summed up to evaluate the electric vector potential. The far-field at a distance  $\bar{r}$  from the origin is then given by

$$\bar{E}_\theta = \eta \bar{H}_\phi = jk_0 \bar{F}_\phi = jk_0 (-\bar{F}_x \sin\phi + \bar{F}_y \cos\phi) \quad (2.5a)$$

$$\bar{E}_\phi = -\eta \bar{H}_\theta = -jk_0 \bar{F}_\theta = -jk_0 (\bar{F}_x \cos\theta \cos\phi + \bar{F}_y \cos\theta \sin\phi), \quad (2.5b)$$



where  $\bar{F}_x$  and  $\bar{F}_y$  are x and y components of the electric vector potential  $\bar{F}(\bar{r})$ . It may be noted that the magnetic current vectors have no component along Z-direction (Fig. 2.5(a)) and therefore the Z-component of  $\bar{F}(\bar{r})$  is zero. The radiation field is given by (2.5a) and (2.5b).  $E_\theta$  and  $E_\phi$  are the two vectors in space-quadrature, and knowing amplitudes and the phases of  $E_\theta$  and  $E_\phi$ , from (2.5), the polarization pattern and axial ratio, in any direction and plane, can be evaluated.

#### 2.1.4 Evaluation of axial ratio in broad-side direction

As pointed out in the preceeding section, the axial ratio in any direction can be evaluated using the information obtained from (2.5). However, the axial ratio in broad-side direction can be evaluated from the directions and magnitudes of the magnetic current vectors (each vector being a complex quantity having two components which are in phase-quadrature with each other) rather than evaluating it from the far-field. This procedure is described below.

The magnetic current distribution along the periphery is resolved into x- and y-components. Using (2.4), the x- and y-components of the electric vector potential, for far-field evaluation, can be expressed as

$$\bar{F}_x(\bar{r}') = \frac{\epsilon_0}{4\pi r} e^{-jk_0 r} \sum_{i=1}^m \bar{K}_{ix}(\bar{r}') \int_{c_i} e^{+jk_0 r' \cos \psi} dl(\bar{r}') \quad (2.6a)$$

$$\bar{F}_y(\bar{r}') = \frac{\epsilon_0}{4\pi r} e^{-jk_0 r} \sum_{i=1}^m \bar{K}_{iy}(\bar{r}') \int_{c_i} e^{+jk_0 r' \cos \psi} dl(\bar{r}') \quad (2.6b)$$

where  $\bar{K}_{ix}$  and  $\bar{K}_{iy}$  are the components of magnetic current vectors along x- and y-directions, evaluated from (2.2), and  $\psi$  is the angle, between the vectors  $\bar{r}$  and  $\bar{r}'$  as in Fig. 2.5(b), given by

$$\cos \psi = \cos \theta \cos \theta' + \sin \theta \sin \theta' \cos(\varphi - \varphi') \quad (2.7)$$

As pointed out in the last paragraph of Section 2.1.3, the magnetic current has only x- and y-components. Hence, we have  $\theta' = 90^\circ$ . This reduces (2.7) to

$$\cos \psi = \sin \theta \cos(\varphi - \varphi') \quad (2.8)$$

In  $\theta = 0$  direction we have  $\sin \theta = 0$ , which makes  $\cos \psi = 0$ . Using this condition in equations (2.6a) and (2.6b) we obtain

$$\bar{F}_x = \frac{\epsilon_0}{4\pi r} e^{-jk_0 r} \sum_{i=1}^m \bar{K}_{ix} W_{ix} \quad (2.9a)$$

$$\bar{F}_y = \frac{\epsilon_0}{4\pi r} e^{-jk_0 r} \sum_{i=1}^m \bar{K}_{iy} W_{iy} \quad (2.9b)$$

where  $W_{ix}$  and  $W_{iy}$  are the port widths along x and y directions.

Using equations (2.9) in equations (2.5), for  $\theta = 0$ , we obtain

$$\bar{E}_\theta = jk_0(-\bar{F}_x \sin\varphi + \bar{F}_y \cos\varphi) \quad (2.10a)$$

$$\bar{E}_\varphi = -jk_0(\bar{F}_x \cos\varphi + \bar{F}_y \sin\varphi) \quad (2.10b)$$

In  $\varphi = 0$  plane, we have, from (2.9) and (2.10),

$$\bar{E}_\theta = jk_0 \bar{F}_y = jk_0 \frac{\epsilon_0}{4\pi r} e^{-jk_0 r} \sum_{i=1}^m \bar{K}_{iy} W_{iy} \quad (2.11a)$$

$$\bar{E}_\varphi = -jk_0 \bar{F}_x = -jk_0 \frac{\epsilon_0}{4\pi r} e^{-jk_0 r} \sum_{i=1}^m \bar{K}_{ix} W_{ix} \quad (2.11b)$$

On the other hand in  $\varphi = 90^\circ$  plane, the far field components can be expressed as

$$\bar{E}_\theta = -jk_0 \bar{F}_x = -jk_0 \frac{\epsilon_0}{4\pi r} e^{-jk_0 r} \sum_{i=1}^m \bar{K}_{ix} W_{ix} \quad (2.12a)$$

$$\bar{E}_\varphi = -jk_0 \bar{F}_y = -jk_0 \frac{\epsilon_0}{4\pi r} e^{jk_0 r} \sum_{i=1}^m \bar{K}_{iy} W_{iy} \quad (2.12b)$$

Since  $E_\theta$  and  $E_\varphi$  are proportional to  $K_{ix} W_{ix}$  and  $K_{iy} W_{iy}$  the polarization ellipse of the far-field can be evaluated from the summation of magnetic current at various sections. These summations of the magnetic current components in equations (2.6), (2.9), (2.11), and (2.12) are the vector additions of complex quantities.

CENTRAL LIBRARY  
K. J. S. S.

Acc. No. 82594-

## 2.2 SEGMENTATION METHOD [8], [23]

### 2.2.1 The formulation

Consider a 2-d segment ( $\alpha$ ) shown in Fig. 2.6(a), for which the impedance Green's function is not known. The given segment can be divided into two segments,  $\beta$  and  $\gamma$ , which are interconnected by several discrete number of ports. The number of interconnected ports is decided by the nature of the field variation along the common interface between the segments. The segments  $\beta$  and  $\gamma$  are regular shapes for which Green's functions [1], [8], [21] are available. The impedance matrices for  $\beta$ - and  $\gamma$ -segments can therefore be evaluated. By segmentation method the Z-matrix of the  $\alpha$ -segment can be evaluated in terms of those of the constituent  $\beta$ - and  $\gamma$ -segments. The ports on the periphery of the  $\alpha$ -segment are named as  $j$  ports. These constitute unconnected ports of  $\beta$ - and  $\gamma$ -segments as illustrated in Fig. 2.6. The interconnected ports at the interface of  $\beta$ - and  $\gamma$ -segments are named as  $m$ -ports on the  $\beta$ -segment side and  $n$  ports on the  $\gamma$ -segment. These ports are numbered such that  $i$ th port on  $\beta$ -segment (i.e.  $i$ th from amongst the  $m$ -ports) is connected to the  $i$ th port on  $\gamma$ -segment (i.e.  $i$ th from amongst the  $n$ -ports). The impedance matrices of  $\beta$ - and  $\gamma$ -segments can be expressed as

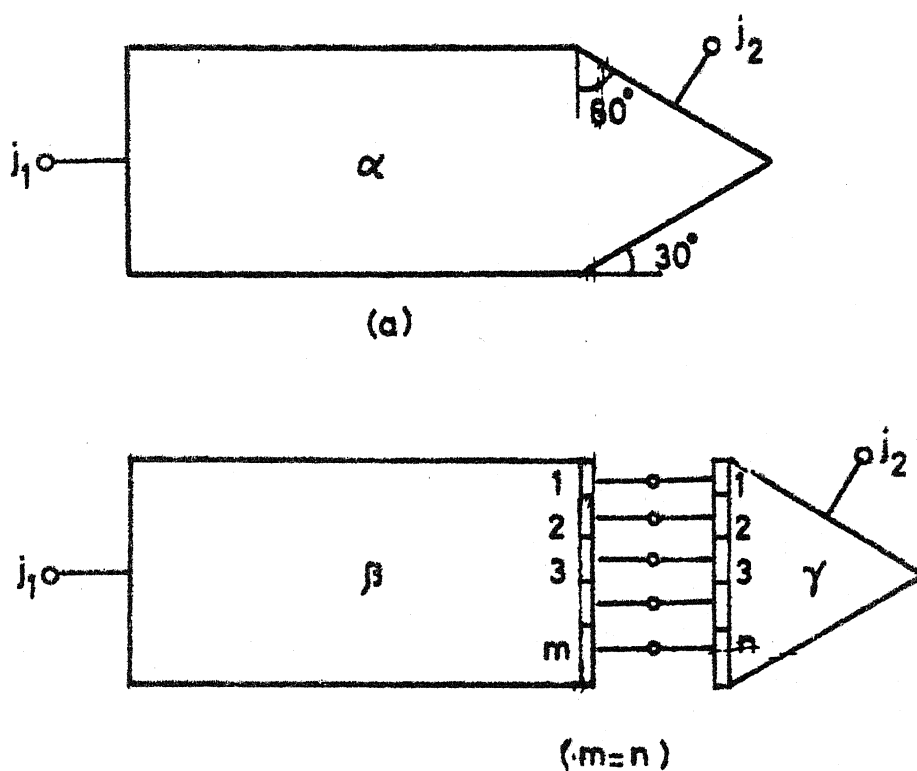


FIG.2-6 ILLUSTRATIVE EXAMPLE OF A CIRCUIT  
TO BE ANALYSED BY SEGMENTATION  
METHOD

$$\begin{aligned}
 \begin{bmatrix} \underline{V}_{j\beta} \\ \underline{V}_m \end{bmatrix} &= \underline{Z}_\beta \begin{bmatrix} \underline{I}_{j\beta} \\ \underline{I}_m \end{bmatrix} \\
 &= \begin{bmatrix} \underline{Z}_{jj\beta} & \underline{Z}_{jm} \\ \underline{Z}_{mj} & \underline{Z}_{mm} \end{bmatrix} \begin{bmatrix} \underline{I}_{j\beta} \\ \underline{I}_m \end{bmatrix}
 \end{aligned} \tag{2.13}$$

$$\begin{aligned}
 \begin{bmatrix} \underline{V}_{j\gamma} \\ \underline{V}_n \end{bmatrix} &= \underline{Z}_\gamma \begin{bmatrix} \underline{I}_{j\gamma} \\ \underline{I}_n \end{bmatrix} \\
 &= \begin{bmatrix} \underline{Z}_{jj\gamma} & \underline{Z}_{jn} \\ \underline{Z}_{nj} & \underline{Z}_{nn} \end{bmatrix} \begin{bmatrix} \underline{I}_{j\gamma} \\ \underline{I}_n \end{bmatrix}
 \end{aligned} \tag{2.14}$$

where the bar (-) below the letters indicates a matrix or a multidimensional vector. At the interface between  $\beta$ - and  $\gamma$ -segments we have

$$\underline{V}_m = \underline{V}_n, \quad \underline{I}_m = -\underline{I}_n \tag{2.15}$$

The matrices  $\underline{Z}_\beta$  and  $\underline{Z}_\gamma$  can be grouped together, after partitioning with respect to the unconnected and the connected ports, as

$$\begin{bmatrix} \underline{V}_j \\ \underline{V}_m \\ \underline{V}_n \end{bmatrix} = \begin{bmatrix} \underline{Z}_{jj} & \underline{Z}_{jm} & \underline{Z}_{jn} \\ \underline{Z}_{mj} & \underline{Z}_{mm} & \underline{Z}_{mn} \\ \underline{Z}_{nj} & \underline{Z}_{nm} & \underline{Z}_{nn} \end{bmatrix} \begin{bmatrix} \underline{I}_j \\ \underline{I}_m \\ \underline{I}_n \end{bmatrix} \tag{2.16}$$

Substituting (2.15) in the last two equations of (2.16) and eliminating  $\underline{V}_m$ ,  $\underline{V}_n$ , and  $\underline{I}_n$  we obtain

$$[\underline{Z}_{mm} + \underline{Z}_{nn} - \underline{Z}_{mn} - \underline{Z}_{nm}] \underline{I}_m = [\underline{Z}_{nj} - \underline{Z}_{mj}] \underline{I}_j$$

or

$$\underline{I}_m = [\underline{Z}_{mm} + \underline{Z}_{nn} - \underline{Z}_{mn} - \underline{Z}_{nm}]^{-1} [\underline{Z}_{nj} - \underline{Z}_{mj}] \underline{I}_j \quad (2.17)$$

Substituting (2.17) into the first equation of (2.16) and using  $\underline{I}_m = -\underline{I}_n$ , the Z-matrix of the  $\alpha$ -segment is obtained as

$$\underline{Z}_{j\alpha} = \underline{Z}_{jj} - [\underline{Z}_{jm} - \underline{Z}_{jn}] \underline{Z}'_{mj}, \quad (2.18a)$$

where

$$\underline{Z}'_{mj} = [\underline{Z}_{mm} + \underline{Z}_{nn} - \underline{Z}_{mn} - \underline{Z}_{nm}]^{-1} [\underline{Z}_{mj} - \underline{Z}_{nj}] \quad (2.18b)$$

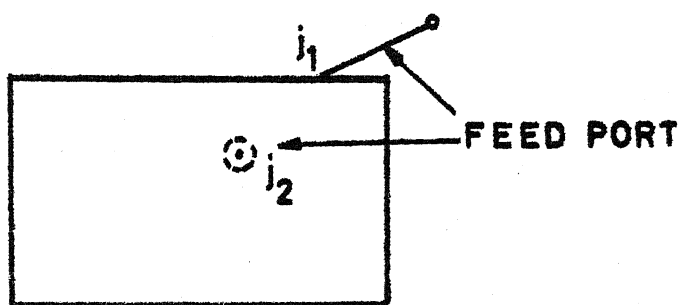
The relation between  $\underline{I}_j$  and  $\underline{V}_m (= \underline{V}_n)$  is obtained by substituting (2.17) into the second equation of (2.16), and is given by

$$\underline{V}_m = [\underline{Z}_{mj} - [\underline{Z}_{mm} - \underline{Z}_{mn}] \underline{Z}'_{mj}] \underline{I}_j. \quad (2.19)$$

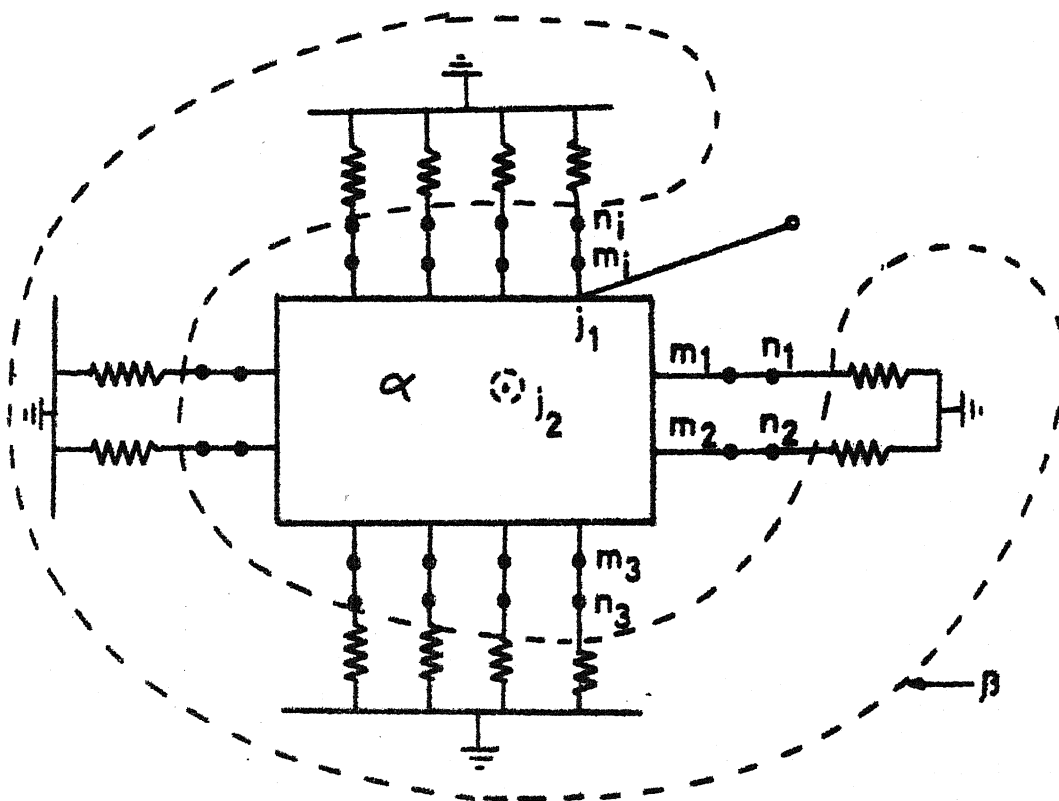
Equations (2.18) and (2.19) are used in antenna analysis by Green's function approach as discussed in the following section.

### 2.2.2 Application to microstrip antennas

Consider a microstrip patch antenna configuration, with a feed port  $j_1$  or  $j_2$  shown in Fig. 2.7(a). The Z-matrix of the multiport network, with loading effect of the radiation



(a)



(b)

FIG.2-7 (a) THE PLANAR MODEL OF THE ANTENNA STRUCTURE

(b) RADIATED POWER IS ACCOUNTED FOR BY LOADING EFFECT OF  $\beta$ -NETWORK, THE INPUT PORT IS LABELED  $j_i$



resistances to account for the radiated power, is evaluated using the segmentation method discussed in the preceeding section. In Fig. 2.7(b), the multiport network representing the planar element and the radiation resistance multiport network are represented by two networks  $\alpha$  and  $\beta$  respectively. Note that the input port (even when on the periphery) is considered unterminated and corresponds to a  $j$  port in the segmentation method discussed in Section 2.2.1. Since usually there is only one feed port, the input impedance of the antenna is given by the equation (2.18), for  $j = 1$ . For a unit electric current input at the port  $j$ , the voltages at the interconnected ports are given by (2.19). This holds even when a feed port, such as  $j_2$  in Fig. 2.7, is located on the surface (inside the periphery) of the radiating element, as is the case in back feeding through a coaxial connector.

When it is desired to find a suitable feed port location for obtaining the best antenna performance, for example the circular polarization and/or impedance matching, additional ports are incorporated at the possible feed locations all around the periphery and/or on the surface within the periphery of the radiating element. The consideration of additional unconnected ports on the periphery of the antenna needs no extra computational effort in evaluating the Z-matrix of the planar multiport model. Contrary to the scheme shown in Fig. 2.7, now we consider each of the elements of the

radiation resistance network as two port network (Fig. 2.8) rather than as a single port network as in Fig. 2.7. This is equivalent to taking out one terminal from each of the junctions of the radiation resistances and the mid-points of the ports of the multiport network representing planar model. One of these two terminals remains unterminated (named  $j$ ) and the other port (named  $m$ ) is connected to the respective port (named  $n$ ) of the ideal multiport network. For the sake of clarity only four ports of the multiport network, representing the radiating element, have been shown (Fig. 2.8) as terminated by two-port radiation resistances. When these additional ports (shown in Fig. 2.8) are considered only equation (2.18) is needed for evaluation of the  $Z$ -matrix (of order  $j \times j$ ) and of the voltage distribution around the periphery for any of the  $j$  ports as feed port. The advantage of incorporating a large number of additional ports is that the voltage distribution for any of the input port locations can be evaluated by choosing the appropriate column of the  $Z$ -matrix which is to be evaluated only once. It may be pointed out here that incorporation of additional ports does not increase the order of the matrix ( $m \times m$ ) to be inverted in equation (2.18). The arrangement of Fig. 2.7(b) is employed when feed port location is specified whereas that of Fig. 2.8 is used when feed port location is being searched.

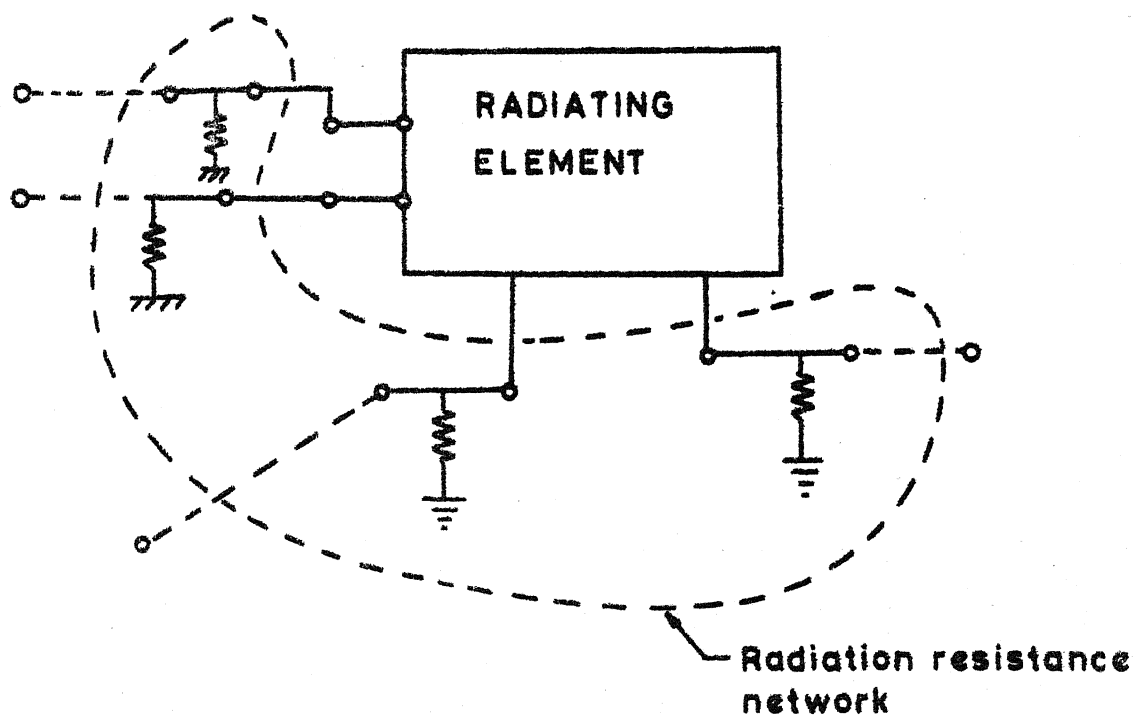


**FIG.2-8 INCORPORATION OF ADDITIONAL PORTS  
(Shown dotted)**

When the antenna configuration is a nonregular shape such that it can be divided into segments having regular shapes, the segmentation method is used to evaluate the Z-matrix of the equivalent multiport network of the planar model. The segmentation procedure for various shapes shown in Fig. 2.2 is illustrated in Figs. 2.9 to 2.12. The Z-matrix of the individual segments is evaluated using the respective Green's functions. The radiated power is accounted for by loading effect of radiation resistance network employing the technique as discussed in the preceding paragraphs.

### 2.3 DISCUSSIONS

The use of the Green's function approach, which is used often for analyzing 2-d components, is applicable for analysis of microstrip antennas. Green's functions with magnetic wall boundary conditions are used. This approach requires the segmentation method in terms of Z-matrices, for taking into account the effect of radiation resistance. The advantage of the method outlined above is that antennas of general shapes can be analyzed by employing segmentation and desegmentation methods. Also during the process of evaluation of radiation characteristics the input impedance of the antenna is obtained. At resonance frequencies of the antenna the polarization is linear and the corresponding far-field components become maximum. The approach described

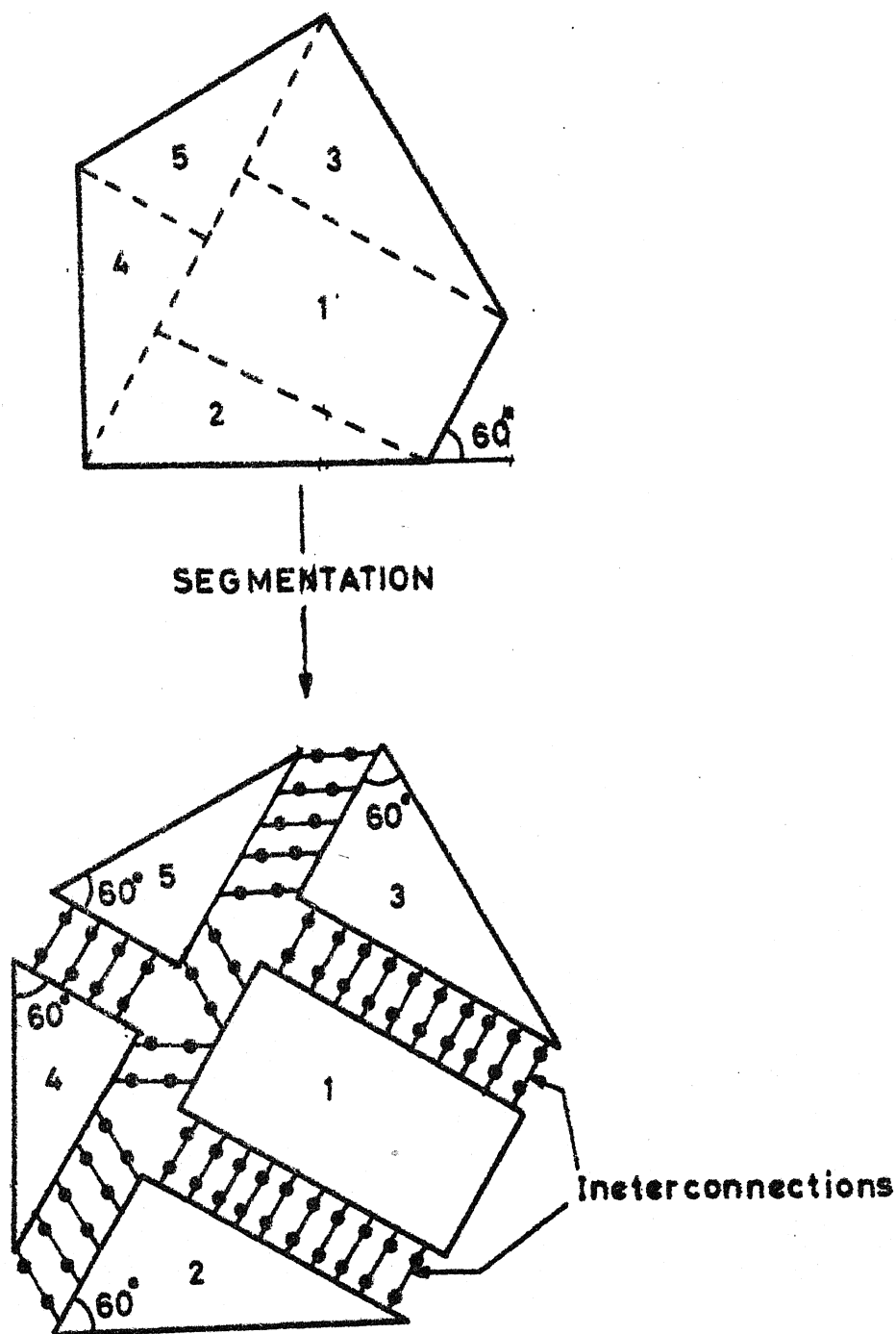


**FIG. 2.9 DIVISION OF THE PENTAGON SHAPED ANTENNA OF FIG. 2.2, INTO FIVE SEGMENTS FOR ANALYSIS BY SEGMENTATION METHOD**

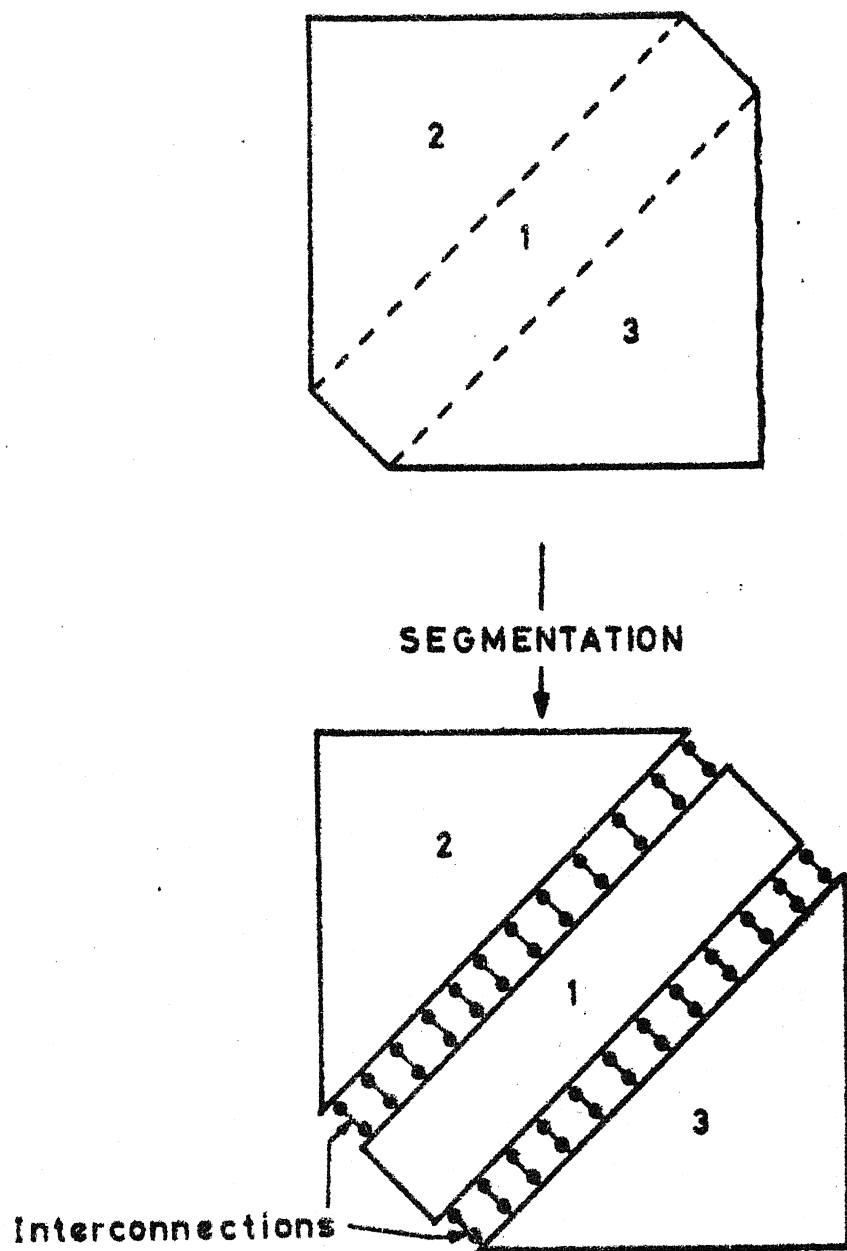
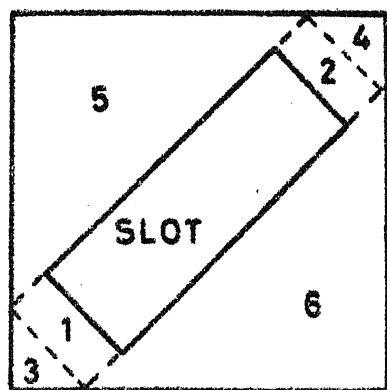
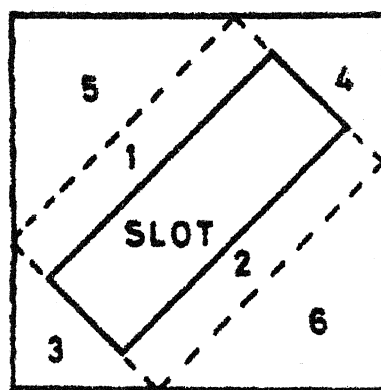
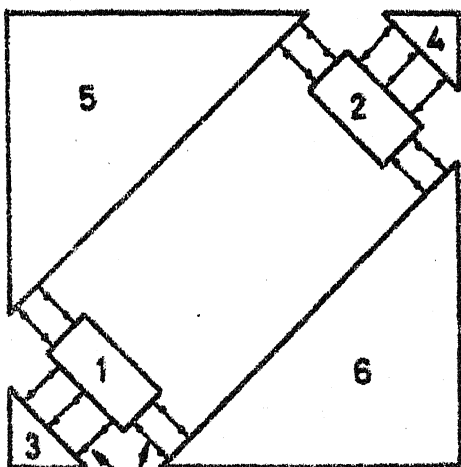


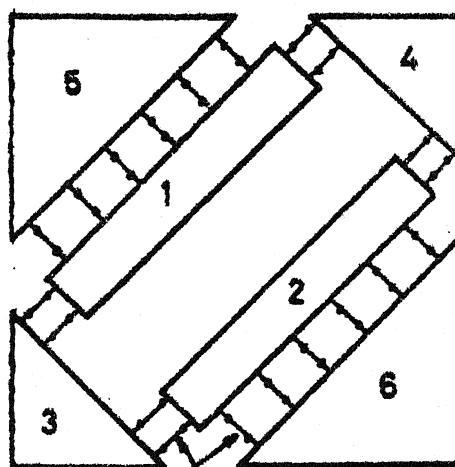
**FIG. 2.10 DIVISION OF CORNERS CHOPPED ANTENNA, OF FIG. 2.2, INTO THREE REGULAR SHAPED SEGMENTS FOR ANALYSIS BY SEGMENTATION METHOD**



SEGMENTATION



SEGMENTATION



INTER CONNECTIONS

FIG.2.11 TWO SCHEMES FOR DIVIDING A SQUARE ANTENNA WITH A DIAGONAL SLOT (FIG.2.2) INTO 6 SEGMENTS

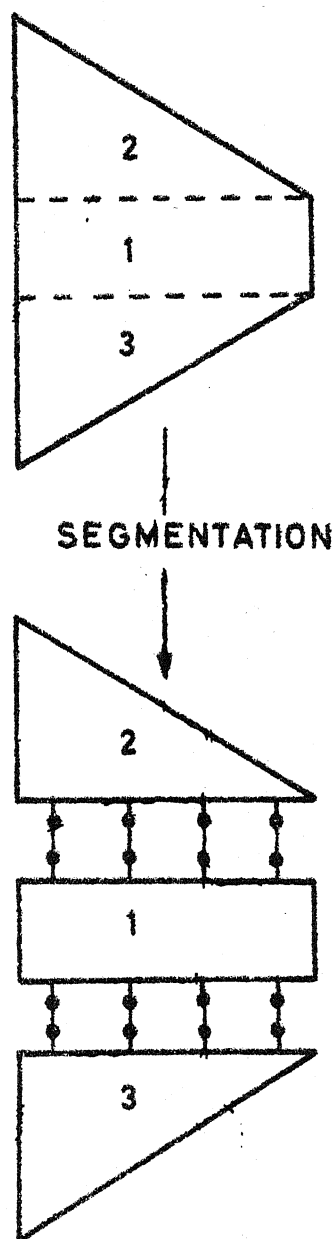


**FIG. 2.12 SEGMENTATION OF THE TRAPEZOIDAL ANTENNA INTO THREE REGULAR SHAPED SEGMENTS**



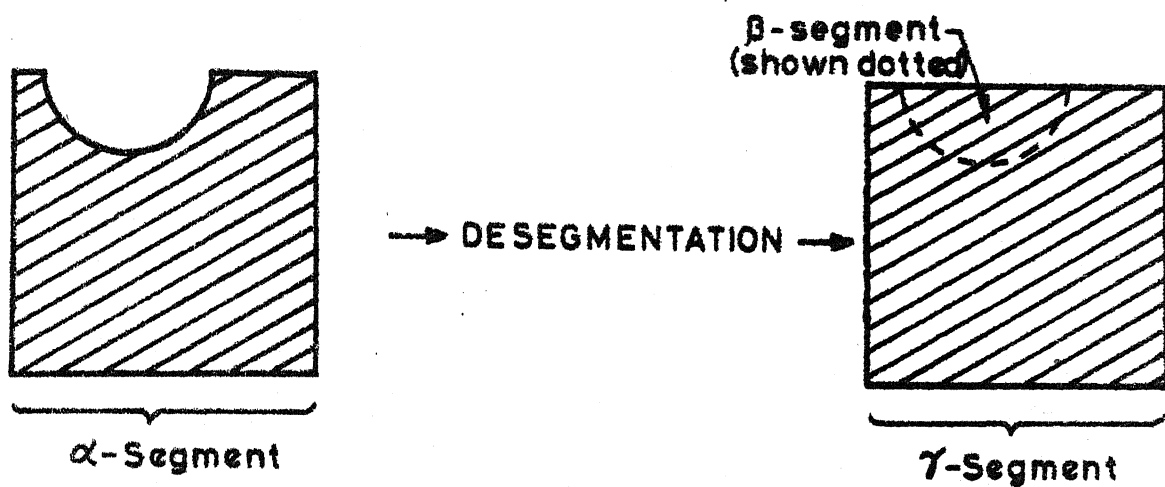
above is illustrated by the analysis of a corner-fed rectangular (nearly square), circularly-polarized, antenna in Chapter Four.

It may be noted that for antenna shapes such as those of Fig. 2.2, the number of segments and therefore the number of interconnections become large (Figs. 2.9 to 2.12). In segmentation method one is therefore required to deal with matrices of large sizes. For such situations, an alternative method called 'desegmentation' is proposed in the next chapter. This method is used for analysis and design of corners chopped square patch antennas and a square patch antenna with a diagonal slot in Chapters Five and Six respectively.

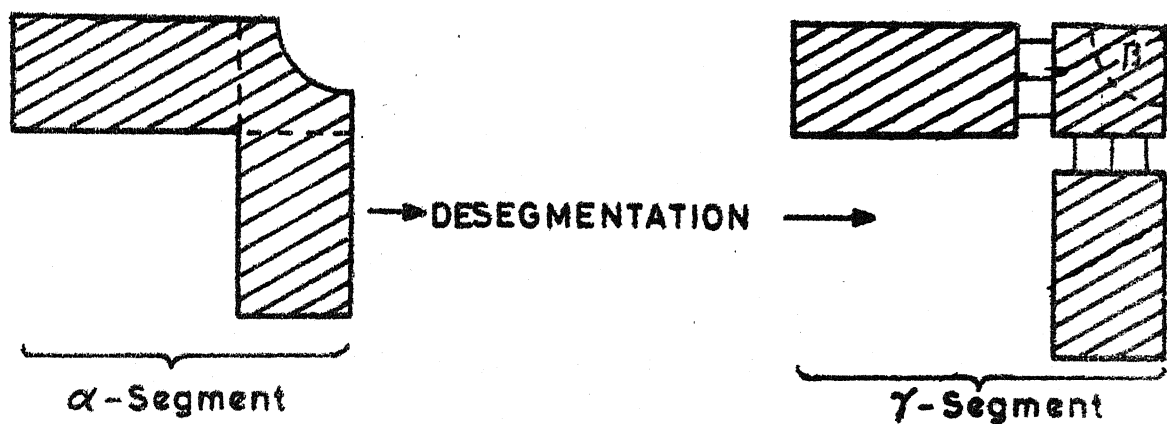
## CHAPTER THREE

### DESEGMENTATION METHOD

There are several two-dimensional configurations (such as one shown in Fig. 3.1(a)) for which neither the impedance Green's function is available nor can such a configuration be analyzed by segmentation method. Such a geometry can be considered as obtained by removal of a circular sector ( $\beta$ ) from a rectangular geometry ( $\gamma$ ) as shown in Fig. 3.1(a). In other words, if a circular sector ( $\beta$ ) is added to the given segment  $\alpha$ , the combination is a regular rectangle  $\gamma$ . The concept of removal of one or more regular shapes from a larger segment which is either a regular shape (Fig. 3.1(a)) or a combination of regular shapes (Fig. 3.1(b)) has been termed as desegmentation in the following discussion. In this chapter, it is shown that Z- and S-parameters of the  $\alpha$ -segment can be evaluated in terms of those of the  $\beta$ - and  $\gamma$ -segments using the desegmentation method developed for this purpose. Since the  $\beta$ - and  $\gamma$ -segments (Fig. 3.1(a)) are regular shapes, the Z-parameters, and therefrom the S-parameters, of these segments are evaluated employing the Green's functions. In general,  $\beta$  and  $\gamma$  can themselves be combinations of regular shapes (such as  $\gamma$ -segment in Fig. 3.1(b)) and the segmentation method discussed in Chapter Two can be used for evaluating their characteristics.



(a)



(b)

FIG. 3-1 CONCEPT OF DESEGMENTATION. COMBINATION OF  $\alpha$ - AND  $\beta$ -SEGMENT IS (a) REGULAR SHAPED  $\gamma$ -SEGMENT (b) COMBINATION OF REGULAR SHAPED SEGMENTS

The theoretical formulation of the desegmentation method in terms of Z- and S-parameters is discussed in the following sections. The validity and applications of the method are illustrated by examples of lumped, 1-dimensional and 2-dimensional circuits.

### 3.1 BASIC CONCEPTS

A general triplate planar circuit is shown in Fig.

3.2(a). The basic equation governing the electromagnetic field in a triplate circuit, with magnetic wall boundary, is the two-dimensional equation [1]

$$(\nabla_T^2 + K^2)V = 0 \quad (3.1)$$

with

$$\frac{\partial V}{\partial n} = 0, \quad \text{where}$$

$$\nabla_T^2 = \frac{\partial^2}{\partial x^2} + \frac{\partial^2}{\partial y^2},$$

$$V = E_z d, \quad K^2 = \omega^2 \mu \epsilon,$$

$\mu$  and  $\epsilon$  denote the permeability and permittivity of the dielectric material,  $\omega$  the angular frequency,  $d$  the spacing between the planar element and the ground planes, and  $E_z$  denotes the electric field normal to the conductors. It may be pointed out here that the eqn. (3.1) holds good for a microstrip planar circuits (Fig. 3.2(b)) also.

The analysis of such a circuit involves determination of the circuit parameters of its equivalent n-port network

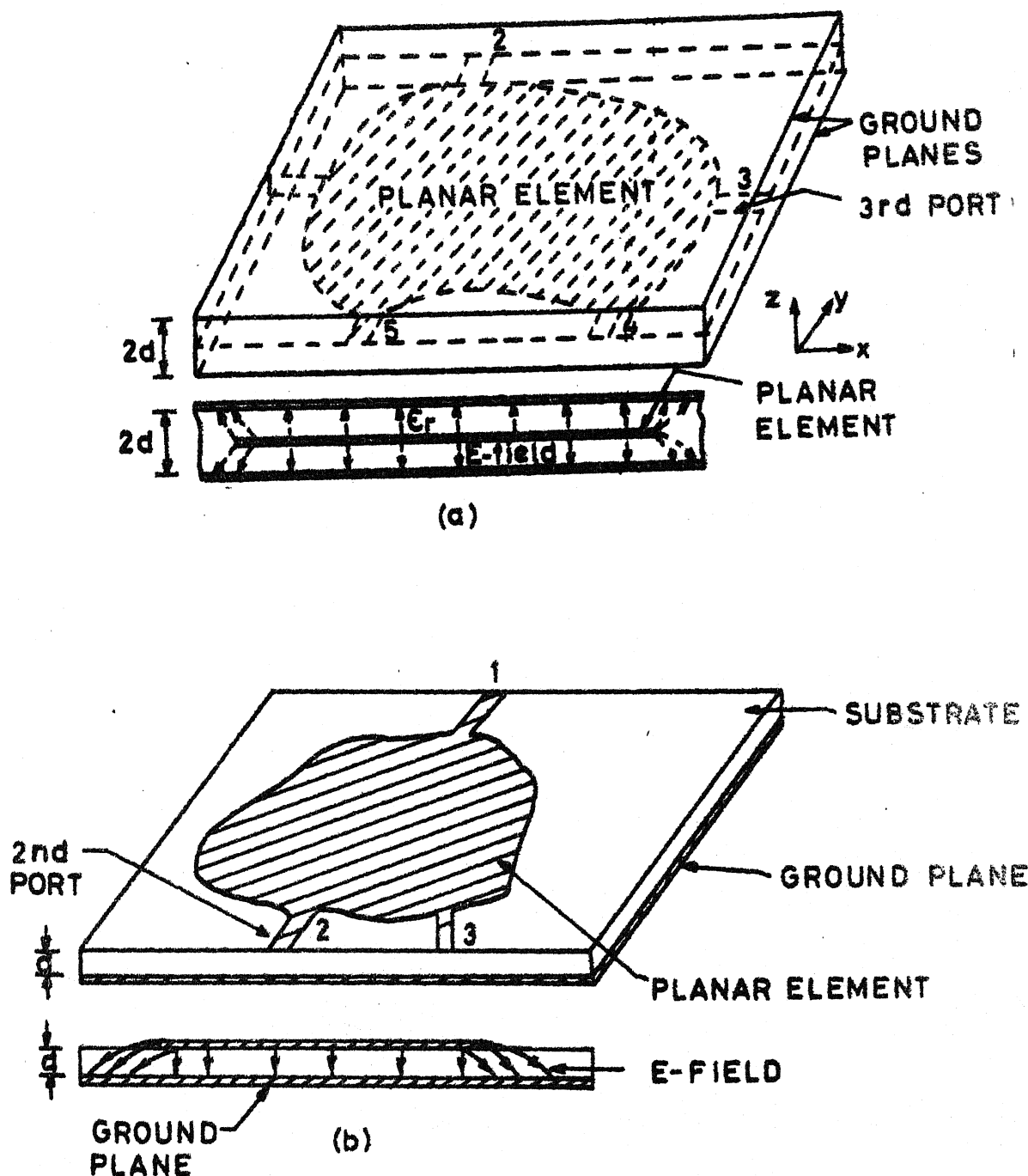
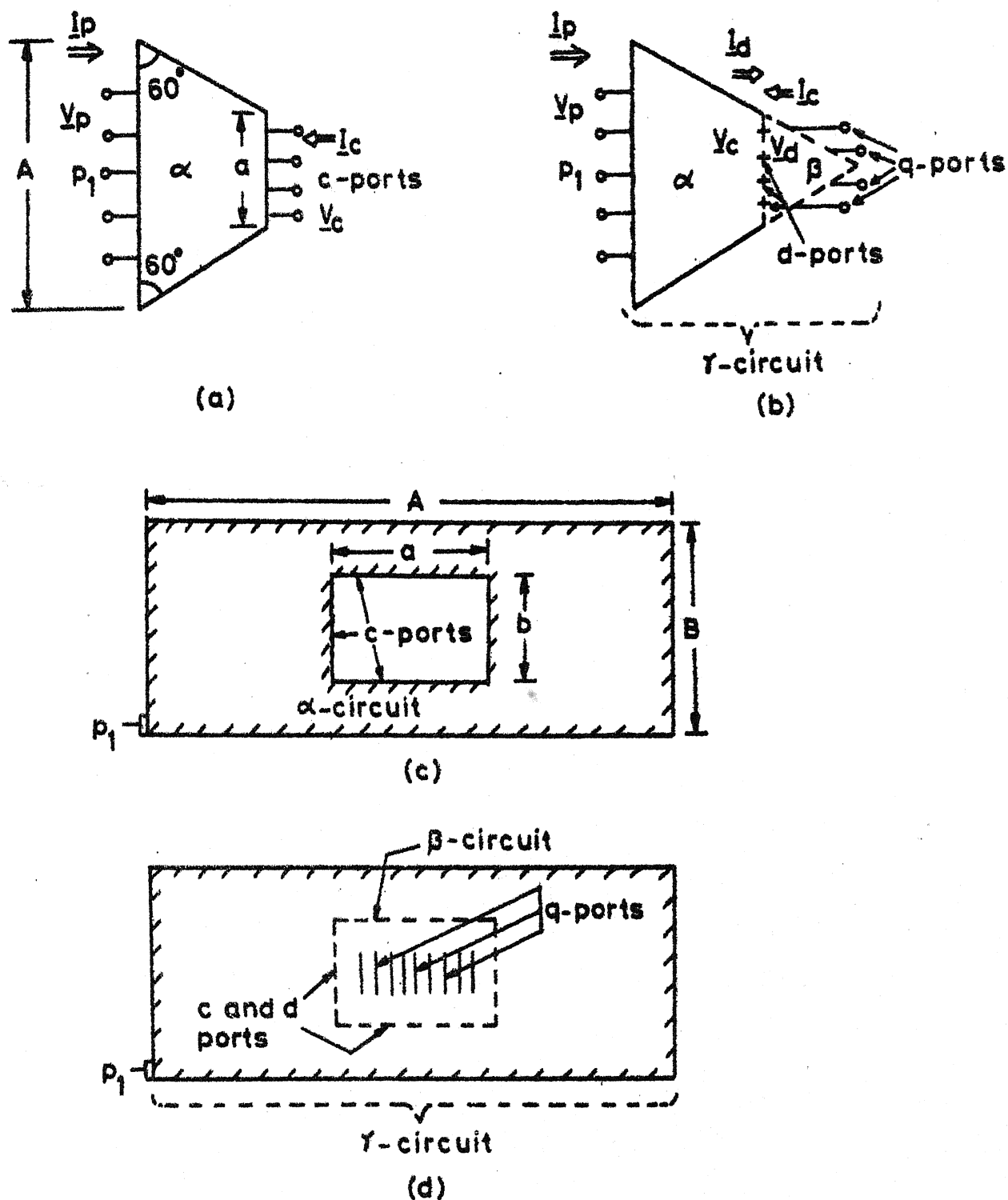


FIG. 3.2 (a) A 2-DIMENSIONAL TRIPLATE CIRCUIT  
(b) A 2-DIMENSIONAL MICROSTRIP CIRCUIT

as a function of frequency by solving (3.1). When the circuit pattern is of a regular shape (namely rectangular, circular, equilateral triangular, isosceles right-angled triangular etc.) the Green's function technique can be used to find the solution analytically [1]. Also if the pattern can be divided into segments having regular shapes, such as for some circuits shown in Figs. 2.9 - 2.12, the segmentation methods [3],[4],[23] can be used for analysis. Some times a planar circuit can be extended to a regular shape by adding another segment (or segments) of regular shape to it. Two examples of this kind are shown in Fig. 3.3. The trapezoidal planar circuit of Fig. 3.3(a) can be converted into an equilateral triangular circuit of Fig. 3.3(b) by adding a triangular segment to it. Similarly, the rectangular circuit with a slot (Fig. 3.3(c)) can be converted into a complete rectangle by addition of a rectangular patch to it as illustrated in Fig. 3.3(d). This process of adding a segment (or segments) in order to convert the original configuration into a regular segment (or a combination of regular segments) has been termed as 'desegmentation'. In general, in the desegmentation method a regular pattern  $\beta$  is added to a non-regular pattern  $\alpha$  (for which Green's function is not available) such that the resulting combination of  $\alpha$ - and  $\beta$ -segments is also a regular pattern  $\gamma$  or a combination of regular patterns. Characteristics of  $\beta$ - and  $\gamma$ -segments can be computed using Green's function approach [1] and employing the segmentation



**FIG.3.3 PLANAR CIRCUIT EXAMPLES TO BE ANALYZED BY DESEGMENTATION METHOD** (a) Given trapezoidal circuit;(b) Desegmentation method applied to circuit (a);(c) Given rectangular ring circuit;(d) Desegmentation applied to circuit (c)

methods [4],[23], if needed. The characteristics of the  $\alpha$ -segment can be calculated by the method of desegmentation developed in this chapter.

The desegmentation method can be formulated to evaluate either the S-matrix or Z-matrix for the  $\alpha$ -segment, in terms of S- or Z-matrices for  $\beta$ - and  $\gamma$ -segments. However, for the segmentation method, it has been shown [23] that the use of the Z-matrices is more efficient than that of the S-matrices [4]. S-matrix for the  $\alpha$ -segment can be evaluated once the Z-matrix has been found using the segmentation method. These arguments are extendible to 'desegmentation' also. This is illustrated later in this chapter. Also the Z-matrix formulation can be used conveniently for analysis and design of microstrip antennas because Z-matrices lead directly to voltages at various ports along the periphery of the antennas. This aspect has been dealt with in Chapters Five and Six.

The formulation of the desegmentation method in terms of S-matrices has been used to evolve a generalized method for de-embedding of multiport networks. This has been illustrated in the Section 3.6.

### 3.2 DESEGMENTATION IN TERMS OF Z-MATRICES

The theoretical formulation of the desegmentation method using Z-matrices is discussed in this section. The application and validity of the method are illustrated by examples



of lumped, transmission line and two-dimensional circuits.

### 3.2.1 Theoretical formulation

Consider the example of a trapezoidal circuit shown in Fig. 3.3(a) and its extension by desegmentation as illustrated in Fig. 3.3(b). As in the segmentation method, discussed in Chapter Two, the continuous interconnection between  $\alpha$ - and  $\beta$ -segments is replaced by a discrete number of interconnected ports, named as c-ports on the  $\alpha$ -segment and d-ports on the  $\beta$ -segment. Their number ( $= C = D$ ) depends on the nature of variation of the field along the interface and is found by an iterative process in numerical computations. Ports p and q are the external (unconnected) ports of  $\alpha$ - and  $\beta$ -segments, respectively.

We define  $\underline{I}_p$ ,  $\underline{I}_c$ ,  $\underline{I}_d$  and  $\underline{I}_q$  as the current vectors and  $\underline{V}_p$ ,  $\underline{V}_c$ ,  $\underline{V}_d$  and  $\underline{V}_q$  as the voltage vectors at the ports p, c, d, and q, respectively, where  $p = 1, 2, \dots, P$ ;  $c = 1, 2, \dots, C$ ;  $d = 1, 2, \dots, D$ ;  $q = 1, 2, \dots, Q$ . Since the c-ports are connected to respective d-ports, we have  $C = D$  and

$$\underline{V}_c = \underline{V}_d, \quad \underline{I}_c = -\underline{I}_d. \quad (3.2)$$

The Z-matrices for  $\alpha$ -,  $\beta$ - and  $\gamma$ -segments, namely  $\underline{Z}_\alpha$ ,  $\underline{Z}_\beta$  and  $\underline{Z}_\gamma$ , respectively, can be partitioned into submatrices corresponding to the external (unconnected) and connected

ports as follows :

$$\underline{Z}_{\alpha} = \begin{bmatrix} \underline{Z}_{pp\alpha} & \underline{Z}_{pc} \\ \underline{Z}_{cp} & \underline{Z}_{cc} \end{bmatrix} \quad (3.3)$$

$$\underline{Z}_{\beta} = \begin{bmatrix} \underline{Z}_{dd} & \underline{Z}_{dq} \\ \underline{Z}_{qd} & \underline{Z}_{qq\beta} \end{bmatrix} \quad (3.4)$$

$$\underline{Z}_{\gamma} = \begin{bmatrix} \underline{Z}_{pp\gamma} & \underline{Z}_{pq} \\ \underline{Z}_{qp} & \underline{Z}_{qq\gamma} \end{bmatrix} \quad (3.5)$$

where a bar (-) below a letter 'Z' indicates a matrix or submatrix. The third subscript with submatrices in (3.3) - (3.5) is used to distinguish the submatrices of the same order in  $\underline{Z}_{\alpha}$ ,  $\underline{Z}_{\beta}$  and  $\underline{Z}_{\gamma}$ . If  $\underline{Z}_{\alpha}$  and  $\underline{Z}_{\beta}$  are known,  $\underline{Z}_{\gamma}$  can be computed using the segmentation method [23].

Using (3.2), (3.3), and (3.4), the Z-matrix for the  $\gamma$ -segment can be expressed as

$$\underline{Z}_{\gamma} = \begin{bmatrix} \underline{Z}_{pp\alpha} - \underline{Z}_{pc} \underline{Z}'_{dp} & \underline{Z}_{pc} \underline{Z}'_{dq} \\ \underline{Z}_{qd} & \underline{Z}_{qq\beta} - \underline{Z}_{qd} \underline{Z}'_{dq} \end{bmatrix} \quad (3.6)$$

where

$$\underline{Z}'_{dp} = [\underline{Z}_{cc} + \underline{Z}_{dd}]^{-1} \underline{Z}_{cp}, \quad \underline{Z}'_{dq} = [\underline{Z}_{cc} + \underline{Z}_{dd}]^{-1} \underline{Z}_{dq}.$$

In the desegmentation method we express  $\underline{Z}_\alpha$  in terms of  $\underline{Z}_\beta$  and  $\underline{Z}_\gamma$  using (3.5) and (3.6). This is equivalent to obtaining  $\underline{Z}_\alpha$  in terms of  $\underline{Z}_\beta$  and  $\underline{Z}_\gamma$  by employing the interconnection relations given in (3.2). If the currents at p- and q-ports are considered as known excitations and other variables, namely the voltages at p-, c-, d- and q-ports, and the currents at c- and d-ports, are determined, the impedance matrix  $\underline{Z}_\alpha$  can be evaluated. In this formulation the unknowns, P voltages at p-ports, Q voltages at q-ports, C voltages and C currents at c-ports, and D voltages and D currents at d-ports, add to  $(P+Q+4D)$  variables. On the other hand, we have only  $(D+Q)$  equations from the definition of  $\underline{Z}_\beta$ ,  $P+Q$  equations from the definition of  $\underline{Z}_\gamma$  and  $2D$  equations from the interconnection relations in (3.2). These add up to only  $(P+2Q+3D)$  equations. In order that  $\underline{Z}_\alpha$  obtained be unique, it is necessary and sufficient that

$$(p+2Q+3D) \geq (P+Q+4D) \quad (3.7)$$

which implies  $Q \geq D$ . Therefore, in the desegmentation method the number of q-ports ( $= Q$ ) on the periphery common to  $\beta$ - and  $\gamma$ -segments should be at least equal to the number of inter-connected ports ( $= C = D$ ). Since  $\beta$ - and  $\gamma$ -segments are regular shapes (or combinations their of), the submatrices of  $\underline{Z}_\beta$  and  $\underline{Z}_\gamma$  can be computed using the corresponding Green's functions (and segmentation method if needed). Therefore,

the submatrices in (3.5), that is the left hand side of (3.6), are known. It may be noted that on the right-hand side of (3.6), only the submatrices corresponding  $\underline{Z}_\beta$  are known. Thus  $\underline{Z}_\alpha$  can be computed from (3.6), provided  $Q \geq D$ , as discussed in the following.

### 3.2.2 Evaluation of $\underline{Z}_\alpha$ when $Q \geq D$

Comparing sub-matrix  $\underline{Z}_{qq\gamma}$  in (3.5) with the corresponding submatrix in (3.6), we have

$$\begin{aligned}\underline{Z}_{qq\gamma} &= \underline{Z}_{qq\beta} - \underline{Z}_{qd} \underline{Z}_{dq}^t \\ &= \underline{Z}_{qq\beta} - \underline{Z}_{qd} [\underline{Z}_{cc} + \underline{Z}_{dd}]^{-1} \underline{Z}_{dq}.\end{aligned}\quad (3.8)$$

This equation can be solved for  $\underline{Z}_{cc}$  to give

$$\underline{Z}_{cc} = -\underline{Z}_{dd} - \underline{Z}_1 \quad (3.9)$$

where

$$\underline{Z}_1 = \underline{Z}_{dq} \underline{Z}_{dq}^t [\underline{Z}_{qd} [\underline{Z}_{qq\gamma} - \underline{Z}_{qq\beta}] \underline{Z}_{dq}^t]^{-1} \underline{Z}_{qd} \underline{Z}_{qd}^t. \quad (3.9a)$$

Employing (3.5), (3.6) and (3.9), other submatrices of  $\underline{Z}_\gamma$  can be expressed as,

$$\underline{Z}_{pq} = -\underline{Z}_{pc} \underline{Z}_1^{-1} \underline{Z}_{dq} \quad (3.10a)$$

$$\underline{Z}_{qp} = -\underline{Z}_{qd} \underline{Z}_1^{-1} \underline{Z}_{cp} \quad (3.10b)$$

$$\underline{Z}_{pp\gamma} = \underline{Z}_{pp\alpha} + \underline{Z}_{pc} \underline{Z}_1^{-1} \underline{Z}_{cp} \quad (3.10c)$$

Equations (3.10a) - (3.10c) can be rearranged to give other sub-matrices of  $\underline{Z}_\alpha$  as,

$$\underline{Z}_{pc} = -\underline{Z}_{pq} \underline{Z}_{dq}^t [\underline{Z}_{dq} \underline{Z}_{dq}^t]^{-1} \underline{Z}_1 \quad (3.11a)$$

$$\underline{Z}_{cp} = -\underline{Z}_1 [\underline{Z}_{qd}^t \underline{Z}_{qd}]^{-1} \underline{Z}_{qd}^t \underline{Z}_{qp} \quad (3.11b)$$

$$\underline{Z}_{pp\alpha} = \underline{Z}_{pp\gamma} - \underline{Z}_{pc} \underline{Z}_1^{-1} \underline{Z}_{cp} \quad (3.11c)$$

From (3.9) and (3.11a) - (3.11c)  $\underline{Z}_\alpha$  can be expressed as

$$\underline{Z}_\alpha = \begin{bmatrix} \underline{Z}_{pp\gamma} - \underline{Z}_{pc} \underline{Z}_1^{-1} \underline{Z}_{cp} & -\underline{Z}_{pq} \underline{Z}_{dq}^t [\underline{Z}_{dq} \underline{Z}_{dq}^t]^{-1} \underline{Z}_1 \\ -\underline{Z}_1 [\underline{Z}_{qd}^t \underline{Z}_{qd}]^{-1} \underline{Z}_{qd}^t \underline{Z}_{qp} & -\underline{Z}_{dd} - \underline{Z}_1 \end{bmatrix} \quad (3.12)$$

where  $\underline{Z}_1$  is given by (3.9a).

The Z-matrix of  $\alpha$ -segment, as partitioned in (3.3), is thus given by (3.12). The procedure for computing  $\underline{Z}_\alpha$  is, therefore, to compute  $\underline{Z}_1$ ,  $\underline{Z}_{cc}$  from (3.9),  $\underline{Z}_{pc}$  and  $\underline{Z}_{cp}$  from (3.11a) and (3.11b), and finally  $\underline{Z}_{pp\alpha}$  from (3.11c).

The expressions for  $\underline{Z}_\alpha$  obtained above hold good, as mentioned earlier, for  $Q \geq D$ . The computations get simplified if  $D$  can be made equal to  $Q$ . In planar circuits this condition can always be met, since the number of interconnected ports can always be made greater than the minimum needed for convergence of the results and also the number of  $q$ -ports ( $= Q$ ) on  $\beta$ -segment can be increased by considering additional ports.

### 3.2.3 Evaluation of $\underline{Z}_\alpha$ when $Q = D$

When  $D = Q$  we have

$$\underline{Z}_1 = \underline{Z}_{dq} [\underline{Z}_{qq\gamma} - \underline{Z}_{qq\beta}]^{-1} \underline{Z}_{qd} \quad (3.13)$$

and  $\underline{Z}_\alpha$ , partitioned as in (3.3), can be expressed as

$$\underline{Z}_\alpha = \begin{bmatrix} \underline{Z}_{pp\gamma} - \underline{Z}_{pq} \underline{Z}'_{qp} & -\underline{Z}_{pq} \underline{Z}'_{qd} \\ -\underline{Z}_{dq} \underline{Z}'_{qp} & -\underline{Z}_{dd} - \underline{Z}_{dq} \underline{Z}'_{qd} \end{bmatrix} \quad (3.14)$$

where

$$\underline{Z}'_{qp} = [\underline{Z}_{qq\gamma} - \underline{Z}_{qq\beta}]^{-1} \underline{Z}_{qp} \quad (3.14a)$$

$$\underline{Z}'_{qd} = [\underline{Z}_{qq\gamma} - \underline{Z}_{qq\beta}]^{-1} \underline{Z}_{qd} \quad (3.14b)$$

It can be seen from (3.14) that it is not necessary to follow any sequence, as is required in the general case, for computing the submatrices of  $\underline{Z}_\alpha$  when  $D = Q$ . This makes computational procedure simpler. For example, if only p-ports are given on the  $\alpha$ -segment, corresponding to which the Z-parameters are to be evaluated, the Z-parameters of the  $\beta$ -segment corresponding to the d-ports need not be calculated if equation (3.14) is employed. In such situations, the matrix  $\underline{Z}_\alpha$  can be rewritten, from (3.14), as

$$\begin{aligned} \underline{Z}_\alpha &= \underline{Z}_{pp\alpha} \\ &= \underline{Z}_{pp\gamma} - \underline{Z}_{pq} [\underline{Z}_{qq\gamma} - \underline{Z}_{qq\beta}]^{-1} \underline{Z}_{qp} \end{aligned} \quad (3.15)$$

Thus in computing  $\underline{Z}_{pp\alpha}$ , it is required to evaluate only  $\underline{Z}_\gamma$  and the submatrix  $\underline{Z}_{qq\beta}$  of  $\underline{Z}_\beta$ . On the otherhand if (3.12) is employed evaluations of all the submatrices of  $\underline{Z}_\gamma$  and  $\underline{Z}_\beta$  will be needed. Moreover while using (3.12) for evaluating  $\underline{Z}_{pp\alpha}$  one has to evaluate  $\underline{Z}_{pc}$ ,  $\underline{Z}_{cp}$  and  $\underline{Z}_{cc}$ , as is obvious from (3.11c). Thus the use of (3.14) is computationally more efficient than that of the equation (3.12).

#### 3.2.4 Number of c-ports and q-ports

The matrix  $\underline{Z}_\alpha$ , obtained in any of the two cases discussed above, is the Z-matrix of the  $\alpha$ -segment to which several c-ports may have been added at the interface between  $\alpha$ - and  $\beta$ -segments. Some c-ports may be the original c-ports of the  $\alpha$ -segment for which the Z-parameters are required. Other c-ports are the ports added for computations in the desegmentation method outlined above so that the condition  $Q > D$  or  $Q = D$  is satisfied. The Z-matrix  $\underline{Z}_\alpha$  (with the originally given c-ports only) can be deduced from the Z-matrix, obtained from (3.12) or from (3.14), by deleting the rows and columns corresponding to the additionally incorporated c-ports.

One of the methods of selecting the number of c-ports and q-ports, which has been used successfully in several cases, is as follows. A special case with  $P = 1$  is considered. Starting with an assumed value of  $Q = 1$ , the submatrix  $\underline{Z}_{pp\alpha}$  is evaluated by using (3.15). As pointed out in the preceding section, for computing  $\underline{Z}_{pp\alpha}$  we do not need to evaluate

$\underline{Z}_{dd}$ ,  $\underline{Z}_{dq}$  and  $\underline{Z}_{qd}$ . Only the computations of  $\underline{Z}_\gamma$  and  $\underline{Z}_{qq\beta}$  are required which do not involve the Z-parameters corresponding to c- and d-ports. The value of the number Q is increased iteratively until the value of  $\underline{Z}_{pp\alpha}$ , calculated from (3.15), converges. This gives the minimum number of q-ports, that is Q, needed. The number of c- and d-ports should be at least equal to this value. In the number of examples that have been studied, it is found that this is also the sufficient number of c-ports required for convergence of  $\underline{Z}_\alpha$ .

### 3.2.5 Simplification of formulation

As discussed in Section 3.2.3, the equation (3.14) leads to efficient computational procedure as compared to that when (3.12) is used. Also it has been pointed out that (3.15) can be used when only p-ports, on the  $\alpha$ -segment, are specified (i.e. when there are no port on the portion of periphery of  $\alpha$  segment which is connected to the  $\beta$ -segment). It is proposed in this section that (3.15) can be used in all the situations whether or not the c-ports are specified. This scheme sometimes leads to more economical computation of  $\underline{Z}_\beta$  and  $\underline{Z}_\gamma$ , and consequently an efficient evaluation of  $\underline{Z}_\alpha$ .

Consider the  $\alpha$ -segment of Fig. 3.4(a) wherein some p-ports ( $P_1$  in number) and some c-ports ( $C_2$  in number), at which Z-parameters are to be evaluated, are specified. When (3.14) is used for evaluating  $\underline{Z}_\alpha$ , incorporation of additional c-ports (Fig. 3.4(b)) would be required so that the condition



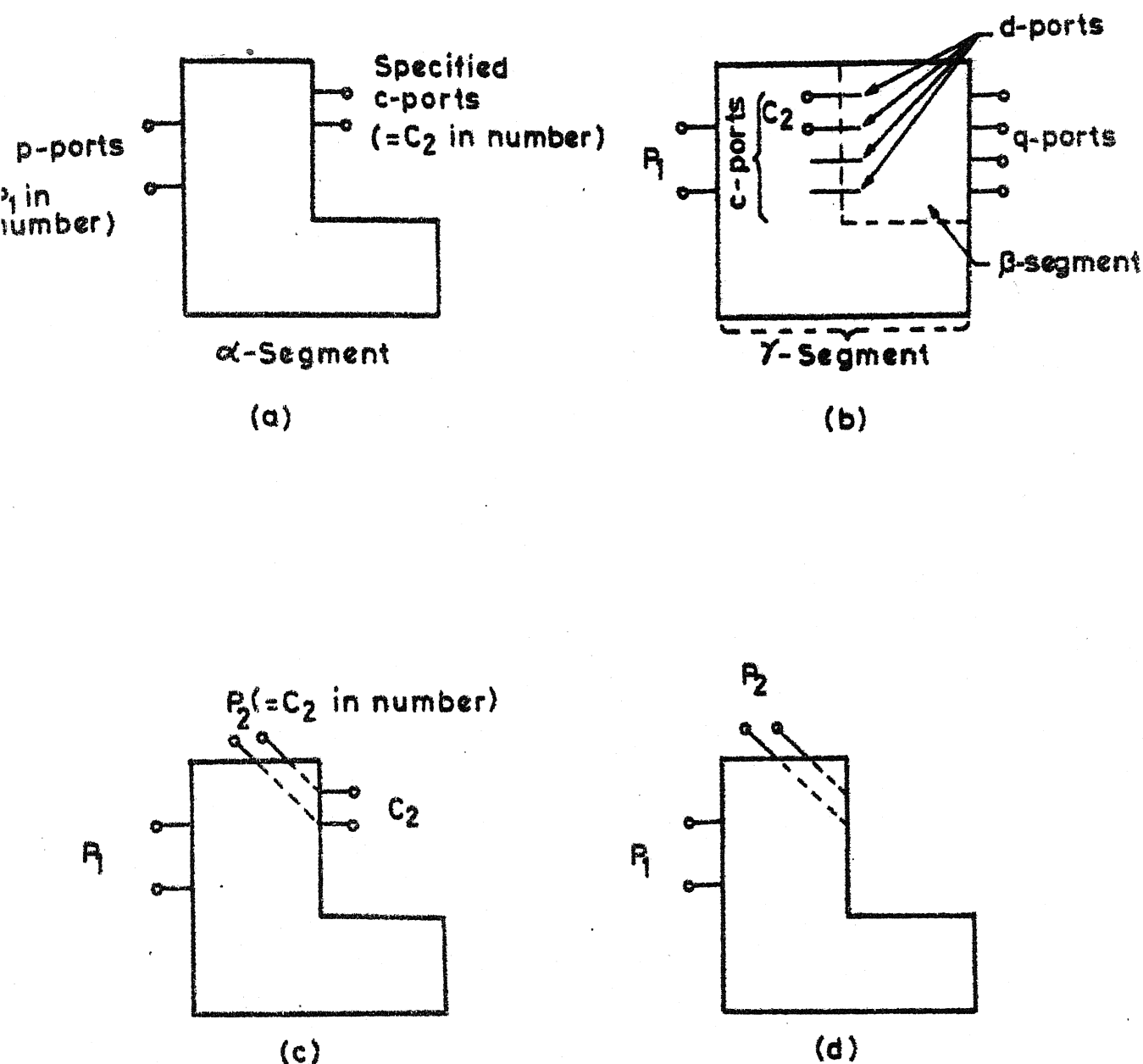


FIG. 3-4 (a) GIVEN  $\alpha$ -SEGMENT WITH  $p$ -AND  $c$ -PORTS ;  
 (b) ADDITION OF  $\beta$ -SEGMENT TO  $\alpha$ -SEGMENT  
 (c) ADDITIONAL  $p$ -PORTS INCORPORATED AT THE  
 LOCATIONS OF GIVEN  $c$ -PORTS;  
 (d) GIVEN  $c$ -PORTS IGNORED

$C = D = Q$  is satisfied. In this case the order of the matrix  $\underline{Z}_\beta$  would be  $(D+Q) \times (D+Q) = 2Q \times 2Q$  and that of the matrix  $\underline{Z}_\gamma$  would be  $(P_1+Q) \times (P_1+Q)$ .

Now consider the configuration of Fig. 3.4(c) wherein additional p-ports ( $= C_2 = P_2$ ), which are situated at the same locations as those of  $c_2$ -ports, have been incorporated. These ports are treated as the additional unconnected ports and are therefore named as p-ports. It is evident from Fig. 3.4(c) that the Z-parameters with these additional p-ports are identical to those with the specified c-ports. If the  $c_2$ -ports in Fig. 3.4(c) are now ignored, the configuration of Fig. 3.4(d) is obtained. The Z-parameters of the  $\alpha$ -segment of Fig. 3.4(a) and those of the circuit configuration of Fig. 3.4(d) are identical. Since there are only p-ports and no specified c-ports in the configuration of Fig. 3.4(d), one can use equation (3.15) to evaluate the Z-parameters. The total number of p-ports now add up to  $P_1+C_2 = P_1+P_2 = P$  (say). As has been pointed out earlier, in Section 3.2.3, the evaluation of  $\underline{Z}_{pp\alpha}$  now requires  $\underline{Z}_{qq\beta}$  and  $\underline{Z}_\gamma$  since (3.15) can be used. The matrices  $\underline{Z}_\gamma$  and  $\underline{Z}_{qq\beta}$  are of order  $(P_1+P_2+Q) \times (P_1+P_2+Q)$  and  $Q \times Q$  respectively. Depending upon the computational effort required in evaluating  $\underline{Z}_\beta$  and  $\underline{Z}_\gamma$ , one may choose to use either the procedure outlined in Section 3.2.3 or the procedure discussed in this section. A criterion for comparing the computational efforts in the two cases, discussed above, is developed in the following section.

### 3.2.6 Computational effort

As pointed out in the preceeding section, use of (3.14) for evaluating  $\underline{Z}_\alpha$  requires all the submatrices of  $\underline{Z}_\beta$  and of  $\underline{Z}_\gamma$ ; the orders of the matrices  $\underline{Z}_\beta$  and  $\underline{Z}_\gamma$  being  $(D+Q) \times (D+Q) = 2Q \times 2Q$  and  $(P_1+Q) \times (P_1+Q)$  respectively. When (3.15) is used and the procedure outlined in Section 3.2.5 is employed, evaluation of the matrices  $\underline{Z}_{qq\beta}$  (of order  $Q \times Q$ ) and  $\underline{Z}_\gamma$  (of order  $(P_1+P_2+Q) \times (P_1+P_2+Q)$ ) is needed.

In 2-d circuit analysis, evaluation of Z-matrix of order  $n \times n$  requires evaluation of integrals of eigen functions (in Green's function expressions) at  $n$ -ports only. This step is most expensive as compared to the other mathematical operations involved in evaluating the elements of the Z-matrix once the integrals have been evaluated. Therefore, the computational effort in evaluating a Z-matrix of order  $n \times n$  from Green's function is, to a good approximation, proportional to the number of ports ' $n$ '. Let  $E(\beta)$  and  $E(\gamma)$  be the computational efforts in evaluating the integral functions at one port of  $\beta$ -segment and of  $\gamma$ -segment respectively. The computational efforts in evaluating  $\underline{Z}_\beta$  and  $\underline{Z}_\gamma$  for procedures of Sections 3.2.3 and 3.2.5, respectively, are

$$E_1 = 2QE(\beta) + (P_1+Q) E(\gamma) \quad (3.16)$$

$$E_2 = QE(\beta) + (P_1+P_2+Q) E(\gamma) \quad (3.17)$$

For equal efforts in the two procedures we have

$$P_2 E(\gamma) = QE(\beta) \quad (3.18)$$

The choice of the procedure, therefore, depends upon  $P_2, Q$ ,  $E(\beta)$  and  $E(\gamma)$ .

### 3.2.7 Circuits with $Z_{qq\beta} = Z_{qq\gamma}$

It may be noted that if  $Z_{qq\gamma} = Z_{qq\beta}$ , both (3.9a) and (3.13) become indeterminate and the Z-matrix formulation of the desegmentation method cannot be used. However, such a situation is unlikely to occur in case of planar circuits. As pointed out later, S-matrix formulation of the desegmentation method can still be used.

The formulation of the desegmentation method in terms of scattering-parameters is developed in the next section.

## 3.3 DESEGMENTATION IN TERMS OF S-MATRICES

### 3.3.1 Theoretical formulation

Consider the 2-d  $\alpha$ -segment of Fig. 3.5(a) and its extension to  $\gamma$ -segment by addition of a  $\beta$ -segment as shown in Fig. 3.5(b). The various ports, in Fig. 3.5, are named as p, c, d and q, as explained in Section 3.2.1.  $\underline{a}_p$ ,  $\underline{a}_c$ ,  $\underline{a}_d$ ,  $\underline{a}_q$  are the normalized wave variables at p-, c-, d- and q-ports for the incoming waves, and  $\underline{b}_p$ ,  $\underline{b}_c$ ,  $\underline{b}_d$  and  $\underline{b}_q$  represent the normalized wave variables for the outgoing waves at the corresponding ports.

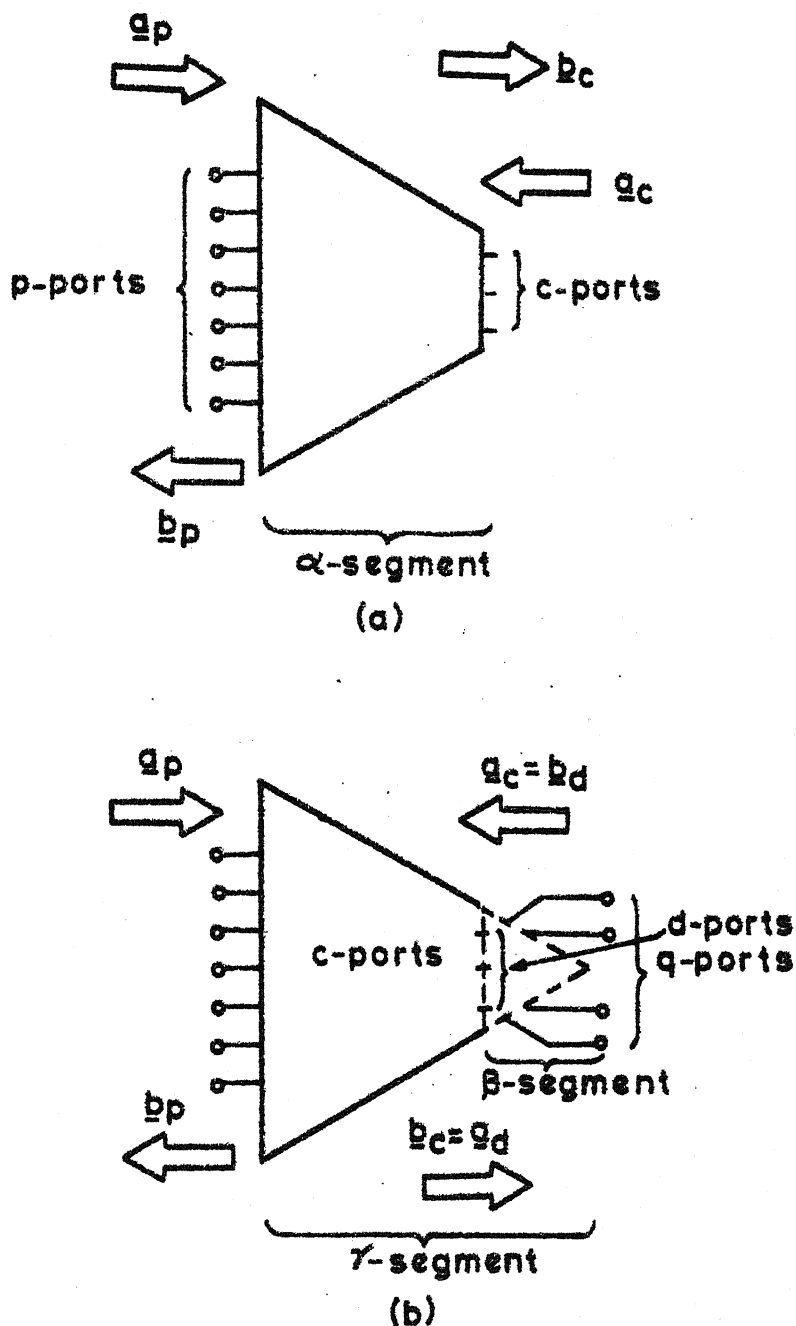


FIG. 3.5 DESEGMENTATION IN TERMS OF S-MATRICES

(a)  $\alpha$ -Segment to be analyzed

(b) Extension of  $\alpha$ -segment to a regular shaped  $\gamma$ -segment by addition of a regular shaped  $\beta$ -segment

The scattering matrices of  $\alpha$ -,  $\beta$ - and  $\gamma$ -segments, namely,  $S_\alpha$ ,  $S_\beta$  and  $S_\gamma$  respectively, satisfy the following relations :

$$\begin{bmatrix} \underline{b}_p \\ \underline{b}_c \end{bmatrix} = \underline{S}_\alpha \begin{bmatrix} \underline{a}_p \\ \underline{a}_c \end{bmatrix} = \begin{bmatrix} \underline{S}_{pp\alpha} & \underline{S}_{pc} \\ \underline{S}_{cp} & \underline{S}_{cc} \end{bmatrix} \begin{bmatrix} \underline{a}_p \\ \underline{a}_c \end{bmatrix} \quad (3.19)$$

$$\begin{bmatrix} \underline{b}_d \\ \underline{b}_q \end{bmatrix} = \underline{S}_\beta \begin{bmatrix} \underline{a}_d \\ \underline{a}_q \end{bmatrix} = \begin{bmatrix} \underline{S}_{dd} & \underline{S}_{dq} \\ \underline{S}_{qd} & \underline{S}_{qq\beta} \end{bmatrix} \begin{bmatrix} \underline{a}_d \\ \underline{a}_q \end{bmatrix} \quad (3.20)$$

and

$$\begin{bmatrix} \underline{b}_p \\ \underline{b}_q \end{bmatrix} = \underline{S}_\gamma \begin{bmatrix} \underline{a}_p \\ \underline{a}_q \end{bmatrix} = \begin{bmatrix} \underline{S}_{pp\gamma} & \underline{S}_{pq} \\ \underline{S}_{qp} & \underline{S}_{qq\gamma} \end{bmatrix} \begin{bmatrix} \underline{a}_p \\ \underline{a}_q \end{bmatrix} \quad (3.21)$$

The third subscript with submatrices in (3.19) - (3.21) is used to distinguish the submatrices of the same order in  $\underline{S}_\alpha$ ,  $\underline{S}_\beta$  and  $\underline{S}_\gamma$ . As the common interface between  $\alpha$ - and  $\beta$ -segments is considered to be connected by discrete number of ports, we have

$$\underline{a}_c = \underline{b}_d \quad ; \quad \underline{a}_d = \underline{b}_c \quad (3.22)$$

Using the segmentation method in terms of S-matrices [4],  $S_\gamma$  can be expressed in terms of  $S_\alpha$  and  $S_\beta$ , as

$$\underline{S}_\gamma = \underline{S}_{jj} + \underline{S}_{ji} [\underline{\Gamma} - \underline{S}_{ii}]^{-1} \underline{S}_{ij}, \quad (3.23)$$

where  $j = P+Q$  (i.e., the number of unconnected ports  $p$  and  $q$ );

$i = C+D$  (i.e., the total number interconnected ports  $c$  and  $d$ ); and

$\underline{\Gamma}$  = the interconnection matrix specified as

$$\underline{b}_1 = \underline{\Gamma} \underline{a}_1 \quad (3.24)$$

The submatrices in (3.23), when expressed explicitly, in terms of the submatrices of  $S_\alpha$  and  $S_\beta$ , can be written as follows :

$$\underline{S}_{jj} = \begin{bmatrix} \underline{S}_{pp\alpha} & \underline{0} \\ \underline{0} & \underline{S}_{qq\beta} \end{bmatrix} \quad (3.25)$$

$$\underline{S}_{ji} = \begin{bmatrix} \underline{S}_{pc} & \underline{0} \\ \underline{0} & \underline{S}_{qd} \end{bmatrix} \quad (3.26)$$

$$\underline{S}_{ij} = \begin{bmatrix} \underline{S}_{cp} & \underline{0} \\ \underline{0} & \underline{S}_{dq} \end{bmatrix} \quad (3.27)$$

When  $\underline{\Gamma}$  and  $\underline{S}_{ii}$  are arranged as in [58], we obtain

$$\begin{aligned}
 [\underline{r} - \underline{s}_{ii}]^{-1} &= \left[ \begin{bmatrix} \underline{0} & \underline{U} \\ \underline{U} & \underline{0} \end{bmatrix} - \begin{bmatrix} \underline{s}_{cc} & \underline{0} \\ \underline{0} & \underline{s}_{dd} \end{bmatrix} \right]^{-1} \\
 &= \begin{bmatrix} -\underline{s}_{cc} & \underline{U} \\ \underline{U} & -\underline{s}_{dd} \end{bmatrix}^{-1} = \begin{bmatrix} \underline{M}_{11} & \underline{M}_{12} \\ \underline{M}_{21} & \underline{M}_{22} \end{bmatrix} \quad (3.28)
 \end{aligned}$$

where

$$\left. \begin{aligned}
 \underline{M}_{12} &= [\underline{U} - \underline{s}_{dd} \underline{s}_{cc}]^{-1} \\
 \underline{M}_{21} &= [\underline{U} - \underline{s}_{cc} \underline{s}_{dd}]^{-1} \\
 \underline{M}_{11} &= \underline{s}_{dd} \underline{M}_{21} \\
 \underline{M}_{22} &= \underline{s}_{cc} \underline{M}_{12}
 \end{aligned} \right\} \quad (3.29)$$

and  $\underline{U}$  denotes identity matrix of appropriate dimensions.

Substitution of (3.25) - (3.29) in (3.23) yields

$$\underline{S}_\gamma = \begin{bmatrix} \underline{s}_{pp\alpha} + \underline{s}_{pc} \underline{M}_{11} \underline{s}_{cp} & \underline{s}_{pc} \underline{M}_{12} \underline{s}_{dq} \\ \underline{s}_{qd} \underline{M}_{21} \underline{s}_{cp} & \underline{s}_{qq\beta} + \underline{s}_{qd} \underline{M}_{22} \underline{s}_{dq} \end{bmatrix} \quad (3.30)$$

Comparing (3.21) and (3.30), the submatrices of  $\underline{S}_\gamma$  in terms of those of  $\underline{S}_\alpha$  and  $\underline{S}_\beta$  can be, explicitly, written as



$$\underline{S}_{pp\gamma} = \underline{S}_{pp\alpha} + \underline{S}_{pc} \underline{S}_{dd} [\underline{U} - \underline{S}_{cc} \underline{S}_{dd}]^{-1} \underline{S}_{cp} \quad (3.31)$$

$$\underline{S}_{pq} = \underline{S}_{pc} [\underline{U} - \underline{S}_{dd} \underline{S}_{cc}]^{-1} \underline{S}_{dq} \quad (3.32)$$

$$\underline{S}_{qp} = \underline{S}_{qd} [\underline{U} - \underline{S}_{cc} \underline{S}_{dd}]^{-1} \underline{S}_{cp} \quad (3.33)$$

$$\underline{S}_{qq\gamma} = \underline{S}_{qq\beta} + \underline{S}_{qd} \underline{S}_{cc} [\underline{U} - \underline{S}_{dd} \underline{S}_{cc}]^{-1} \underline{S}_{dq} \quad (3.34)$$

As explained in the formulation of the desegmentation method in terms of Z-matrices, in Section 3.2, the aim is to express  $\underline{S}_{\alpha}$  in terms of  $\underline{S}_{\beta}$  and  $\underline{S}_{\gamma}$  by using (3.31) - (3.34). This is equivalent to obtaining  $\underline{S}_{\alpha}$  in terms of  $\underline{S}_{\beta}$  and  $\underline{S}_{\gamma}$  employing equations (3.20) - (3.22). If for a set of given excitations  $\underline{a}_p$  and  $\underline{a}_q$  (inputs to the  $\gamma$ -segment), other wave variables  $\underline{b}_p$ ,  $\underline{b}_q$ ,  $\underline{a}_c$ ,  $\underline{a}_d$ ,  $\underline{b}_c$  and  $\underline{b}_d$  are determined, the S-matrix  $\underline{S}_{\alpha}$  can be characterized. Thus, as in the case of formulation in terms of Z-matrices, there are  $(P+Q+4D)$  unknowns and  $(P+2Q+3D)$  available equations. As before, in order that  $\underline{S}_{\alpha}$  thus obtained from (3.20) - (3.22) be unique, the necessary and sufficient condition is still given by (3.7). Cases where  $Q \geq D$  and where  $Q = D$  are discussed separately.

### 3.3.2 Evaluation of $\underline{S}_{\alpha}$ when $Q \geq D$

It may be noted from (3.31) - (3.34) that, equation (3.31) contains all the four submatrices of  $\underline{S}_{\alpha}$  as in (3.19); (3.32) contains the submatrices  $\underline{S}_{pc}$  and  $\underline{S}_{cc}$ ; (3.33) contains submatrices  $\underline{S}_{cp}$  and  $\underline{S}_{cc}$ ; and the equation (3.34) contains the

submatrix  $\underline{S}_{cc}$  only. Hence, to solve for  $\underline{S}_\alpha$  from (3.31) - (3.34), equation (3.34) should be solved first, then (3.33) and (3.32) should be solved for  $\underline{S}_{cp}$  and  $\underline{S}_{pc}$ . Alternatively equation (3.32) may be solved first for  $\underline{S}_{pc}$  and then  $\underline{S}_{cp}$  can be obtained from (3.33). Finally,  $\underline{S}_{pp\alpha}$  is evaluated by substitution of  $\underline{S}_{cc}$ ,  $\underline{S}_{pc}$ , and  $\underline{S}_{cp}$  in (3.31). From (3.34) we obtain

$$\underline{S}_{qd} \underline{S}_{cc} [\underline{U} - \underline{S}_{dd} \underline{S}_{cc}]^{-1} \underline{S}_{dq} = [\underline{S}_{qq\gamma} - \underline{S}_{qq\beta}] \quad (3.35)$$

Since  $Q \geq D$ , the preceding equation can be premultiplied by  $\underline{S}_{qd}^t$  and postmultiplied by  $\underline{S}_{dq}^t$ , so that  $[\underline{S}_{qd}^t \underline{S}_{qd}]$  and  $[\underline{S}_{dq} \underline{S}_{dq}^t]$  are nonsingular square matrices, and rearranged to give

$$\underline{S}_{cc} = \underline{S}_1 [\underline{U} - \underline{S}_{dd} \underline{S}_{cc}] \quad (3.36)$$

where

$$\underline{S}_1 = [\underline{S}_{qd}^t \underline{S}_{qd}]^{-1} [\underline{S}_{qd}^t [\underline{S}_{qq\gamma} - \underline{S}_{qq\beta}] \underline{S}_{dq}^t] [\underline{S}_{dq} \underline{S}_{dq}^t]^{-1} \quad (3.36a)$$

and the superscript  $t$  indicates the transpose.

The matrix  $\underline{S}_{cc}$  can be obtained from (3.36), in the following form :

$$\underline{S}_{cc} = [\underline{U} + \underline{S}_1 \underline{S}_{dd}]^{-1} \underline{S}_1 \quad (3.37)$$

Since  $\beta$ -segment is of regular shape the submatrices of  $\underline{S}_\beta$  are known. Having evaluated  $\underline{S}_{cc}$  from (3.37), we therefore can evaluate  $\underline{M}_{12}$ ,  $\underline{M}_{21}$ ,  $\underline{M}_{11}$  and  $\underline{M}_{22}$  from (3.29). Premultiplying (3.33) by  $\underline{S}_{qd}^t$  and solving for  $\underline{S}_{cp}$  yields

$$\underline{S}_{cp} = \underline{M}_{21}^{-1} [\underline{S}_{qd}^t \underline{S}_{qd}]^{-1} [\underline{S}_{qd}^t \underline{S}_{qp}] \quad (3.38)$$

Equation (3.32) can be postmultiplied by  $\underline{S}_{dq}^t$  and, rearranged to express  $\underline{S}_{pc}$  as,

$$\underline{S}_{pc} = [\underline{S}_{pq} \quad \underline{S}_{dq}^t] [\underline{S}_{dq} \quad \underline{S}_{dq}^t]^{-1} \underline{M}_{12}^{-1} . \quad (3.39)$$

Finally  $\underline{S}_{pp\alpha}$  can be obtained from (3.31) in the form

$$\underline{S}_{pp\alpha} = \underline{S}_{pp\gamma} - \underline{S}_{pc} \underline{M}_{11} \underline{S}_{cp} . \quad (3.40)$$

Comparing the submatrices of  $\underline{S}_{\alpha}$  in (3.19) with the corresponding submatrices in (3.37) - (3.40), we obtain

$$\underline{S}_{\alpha} = \begin{bmatrix} \underline{S}_{pp\gamma} - \underline{S}_{pc} \underline{M}_{11} \underline{S}_{cp} & [\underline{S}_{pq} \underline{S}_{dq}^t] [\underline{S}_{dq} \underline{S}_{dq}^t]^{-1} \underline{M}_{12}^{-1} \\ \underline{M}_{21}^{-1} [\underline{S}_{qd}^t \underline{S}_{qd}]^{-1} \underline{S}_{qd}^t \underline{S}_{qd} & [\underline{U} + \underline{S}_1 \underline{S}_{dd}]^{-1} \underline{S}_1 \end{bmatrix} \quad (3.41)$$

It may be noted that even if there is only one specified p-port of the  $\alpha$ -segment, it is necessary to consider sufficient number of c-ports for computations of  $\underline{S}_{pp\alpha}$ . In this case also, as explained in the case of formulation of the desegmentation method in terms of Z-matrices, the computations get simplified if number of q-ports ( $=Q$ ) can be made equal to that of d-ports ( $=D$ ). This formulation is discussed in the following subsection.

### 3.3.3 Evaluation of $\underline{S}_{\alpha}$ when $Q = D$

In this case the matrix  $\underline{S}_1$  in equation (3.36a) reduces to  $\underline{S}_2$  given by

$$\underline{S}_2 = \underline{S}_{qd}^{-1} [\underline{S}_{qq\gamma} - \underline{S}_{qq\beta}] \underline{S}_{dq}^{-1} . \quad (3.42)$$

The preceding equation can be used in (3.36) to write

$$\underline{S}_{cc} = [\underline{U} + \underline{S}_2 \underline{S}_{dd}]^{-1} \underline{S}_2 . \quad (3.43)$$

Knowing  $\underline{S}_{cc}$  and  $\underline{S}_\beta$ ,  $\underline{M}_{ij}$  can be evaluated from (3.29). Using (3.31) - (3.34), the S-matrix of  $\alpha$ -segment, i.e.,  $\underline{S}_\alpha$ , can be expressed as

$$\underline{S}_\alpha = \begin{bmatrix} \underline{S}_{pp} - \underline{S}_{pc} \underline{M}_{11}^{-1} \underline{S}_{cp} & \underline{S}_{pq} \underline{S}_{dq} \underline{M}_{12}^{-1} \\ \underline{M}_{21} \underline{S}_{qd}^{-1} \underline{S}_{qp} & [\underline{U} + \underline{S}_2 \underline{S}_{dd}]^{-1} \underline{S}_2 \end{bmatrix} \quad (3.44)$$

The sequence of computations of the submatrices of  $\underline{S}_\alpha$  from (3.44) is the same as that while using (3.41).

### 3.3.4 Incorporation of additional ports and numbers of q-ports

The  $\underline{S}_\alpha$  obtained in both the cases discussed above is the S-matrix of the  $\alpha$ -segment to which several c-ports have been added at the interface between  $\alpha$ - and  $\beta$ -segments. As discussed in section 3.2.4 some of these c-ports may be the original c-ports of the  $\alpha$ -segment at which S-parameters are required. Others are the c-ports incorporated additionally so as to satisfy the relation  $Q \geq D$  and also for the convergence of the results. For evaluating  $\underline{S}_\alpha$  (with the originally given c-ports only) these additionally incorporated c-ports are considered to be open circuited and the S-matrix as obtained from (3.41) or (3.44) is reduced to the required  $\underline{S}_\alpha$  by putting  $a_i = b_i$  at the additionally incorporated ports.

The selection of number of q-ports (that is = D) is made by following the procedure as outlined in section 3.2.4. For this purpose only one p-port is considered first. It may be noted that, in this formulation all the submatrices of  $\underline{S}_\gamma$  and  $\underline{S}_\beta$  are needed for computation of  $\underline{S}_{pp\alpha}$ . Moreover, for evaluating  $\underline{S}_{pp\alpha}$ , other submatrices of  $\underline{S}_\alpha$  are also required. This feature makes the formulation in terms of S-matrices less efficient than that in terms of Z-matrices.

### 3.3.5 Circuits with $\underline{S}_{qq\beta} = \underline{S}_{qq\gamma}$

As pointed out in Section 3.2.7, the formulation of the desegmentation method in terms of Z-matrices cannot be used if  $\underline{Z}_{qq\beta} = \underline{Z}_{qq\gamma}$ . However, the formulation in terms of S-matrices can be used even in such situations. When  $\underline{S}_{qq\beta} = \underline{S}_{qq\gamma}$ , the matrices  $\underline{S}_1$  in (3.36a) and  $\underline{S}_2$  in (3.42) become null matrices. This makes  $\underline{S}_{cc}$ , in (3.37) and in (3.43), a null matrix. The matrices  $\underline{M}_{ij}$  in (3.29), therefore, reduce to  $\underline{M}_{12} = \underline{U}$ ;  $\underline{M}_{21} = \underline{U}$ ;  $\underline{M}_{11} = \underline{S}_{dd}$ ; and  $\underline{M}_{22} = \underline{0}$ . These values of  $\underline{M}_{ij}$  are substituted in (3.41) or (3.44) to obtain  $\underline{S}_\alpha$ .

## 3.4 ILLUSTRATIVE EXAMPLES

For illustrating the validity and applications of the desegmentation method, a few examples of lumped circuits, of transmission-line circuits, and of planar circuits are presented in this section.

### 3.4.1 Examples of lumped circuits

#### A. Example 1

Consider the  $\alpha$ -circuit of Fig. 3.6(a) and its extension by addition of  $\beta$ -circuit as shown in Fig. 3.6(b). The Z-matrix formulation of the desegmentation method is used in this case. The impedance matrices of  $\beta$ -circuit and  $\gamma$ -circuit (combination of  $\alpha$ - and  $\beta$ -circuits) are

$$\underline{Z}_{\beta} = \begin{bmatrix} \underline{Z}_{dd} & \underline{Z}_{dq} \\ \underline{Z}_{qd} & \underline{Z}_{qq\beta} \end{bmatrix} = \begin{bmatrix} 2 & 1 \\ 1 & 2 \end{bmatrix} \text{ ohm} \quad (3.45)$$

$$\underline{Z}_{\gamma} = \begin{bmatrix} \underline{Z}_{pp\gamma} & \underline{Z}_{pq} \\ \underline{Z}_{qp} & \underline{Z}_{qq\gamma} \end{bmatrix} = \begin{bmatrix} 11/5 & 2/5 \\ 2/5 & 9/5 \end{bmatrix} \text{ ohm} \quad (3.46)$$

For this example,  $P = 1$ ,  $C = D = 1$  and  $Q = 1$ . Also in this case  $D = Q$ , therefore, equation (3.14) can be employed to evaluate  $\underline{Z}_{\alpha}$ . The various submatrices in (3.14) are,

$$\underline{Z}'_{qp} = \left[ \frac{9}{5} - 2 \right]^{-1} \frac{2}{5} = -2$$

$$\underline{Z}'_{qd} = \left[ \frac{9}{5} - 2 \right]^{-1} 1 = -5$$

$$\underline{Z}_{pp\alpha} = \frac{11}{5} - \frac{2}{5} (-2) = 3$$

$$\underline{Z}_{pc} = -\frac{2}{5} (-5) = 2$$

$$\underline{Z}_{cp} = -1 (-2) = 2$$

$$\underline{Z}_{cc} = -2 - 1 (-5) = 3.$$

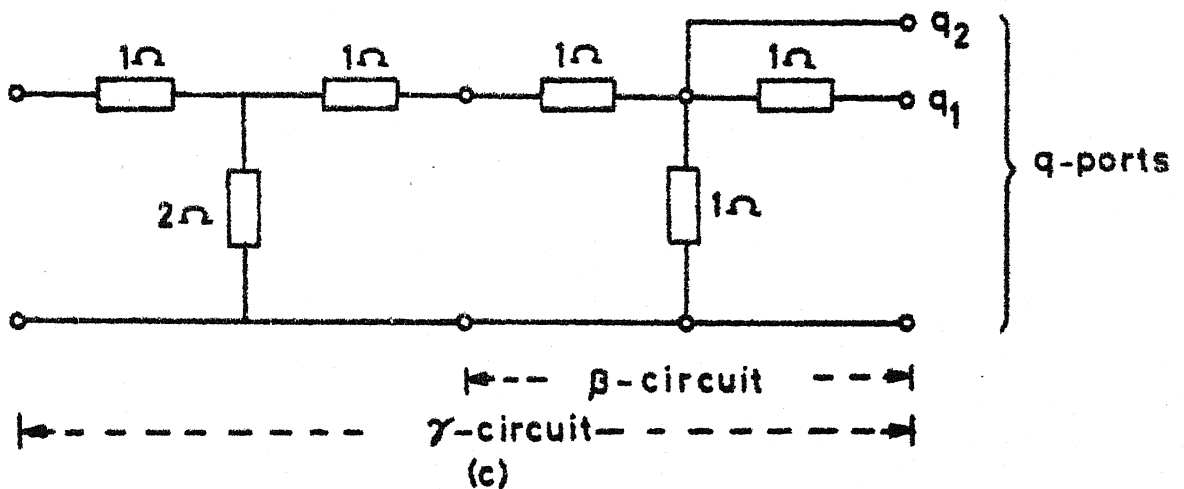
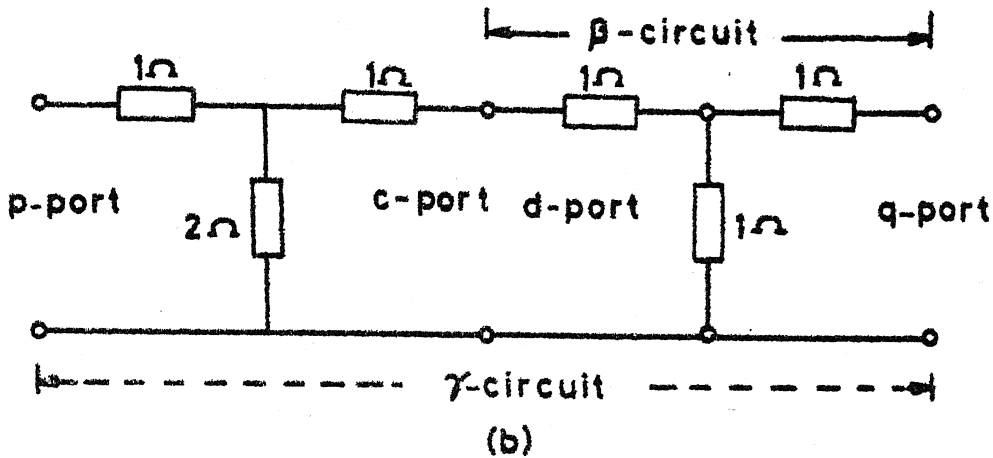
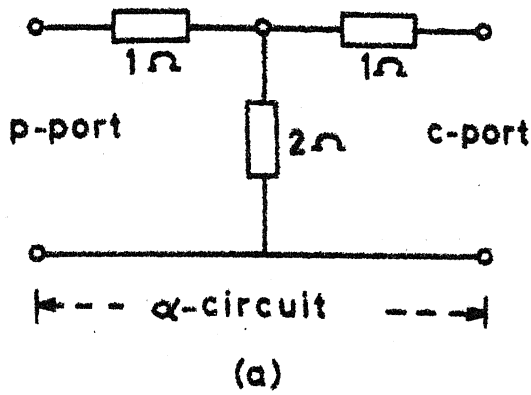


FIG. 3-6 (a) THE  $\alpha$ -CIRCUIT TO BE ANALYZED ( $P=1, C=1$ )

(b) EXTENSION OF  $\alpha$ -CIRCUIT TO  $\gamma$ -CIRCUIT BY ADDITION OF  $\beta$ -CIRCUIT ( $P=1, C=D=1, Q=1$ )

(c) ADDITION OF ANOTHER  $\beta$ -CIRCUIT TO  $\alpha$ -CIRCUIT ( $P=1, C=D=1, Q=2$ )

Hence  $\underline{Z}_\alpha$  can be expressed as

$$\underline{Z}_\alpha = \begin{bmatrix} \underline{Z}_{pp\alpha} & \underline{Z}_{pc} \\ \underline{Z}_{cp} & \underline{Z}_{cc} \end{bmatrix} = \begin{bmatrix} 3 & 2 \\ 2 & 3 \end{bmatrix} \quad (3.47)$$

which can be easily verified by direct calculations of  $\underline{Z}_\alpha$  for the  $\alpha$ -circuit of Fig. 3.6(a).

As mentioned earlier the formulation (3.12) is valid for  $Q > D$ , and can be used in the present case also. Using (3.9a) and (3.9) we have

$$\begin{aligned} \underline{Z}_1 &= 1 \left[ 1 \quad \left[ \frac{9}{5} - 2 \right] \quad 1 \right]^{-1} 1 \\ &= -5, \end{aligned}$$

$$\underline{Z}_{cc} = -2 - (-5) = 3.$$

Using (3.11a) - (3.11c), (3.45) - (3.46) and the values of  $\underline{Z}_1$  and  $\underline{Z}_{cc}$ , as obtained above, we obtain

$$\underline{Z}_{pc} = -\frac{2}{5} \cdot 1 \cdot 1 \cdot (-5) = 2$$

$$\underline{Z}_{cp} = -(-5) \cdot 1 \cdot 1 \cdot \left(\frac{2}{5}\right) = 2$$

$$\underline{Z}_{pp\alpha} = \frac{11}{5} - 2 \left(-\frac{1}{5}\right) 2 = 3.$$

Hence  $\underline{Z}_\alpha$  can be expressed as,

$$\underline{Z}_\alpha = \begin{bmatrix} 3 & 2 \\ 2 & 3 \end{bmatrix} \text{ ohm ,} \quad (3.48)$$



which is same as that given by (3.47).

The case when  $Q > D$  is illustrated by the example that follows.

### B. Example 2

The circuit in example 1 may be modified to illustrate the validity of the case when  $Q > D$  and (3.12) (that is the set of equations (3.9) and (3.11a) - (3.11c)) is employed for computing  $\underline{Z}_\alpha$  from the known  $\underline{Z}_\beta$  and  $\underline{Z}_\gamma$ .

The  $\alpha$ -circuit is the same as shown in the Fig. 3.6(a). The  $\beta$ -circuit selected has  $D = 1$  and  $Q = 2$ , and the combination of  $\alpha$ - and  $\beta$ -circuits is the  $\gamma$ -circuit with  $P = 1$ , and  $Q = 2$  as illustrated in Fig. 3.6(c). The Z-matrices for  $\beta$ - and  $\gamma$ -circuits, with appropriate partitioning into submatrices, can be written as,

$$\underline{Z}_\beta = \begin{bmatrix} \underline{Z}_{dd} & \underline{Z}_{dq} \\ \underline{Z}_{qd} & \underline{Z}_{qq} \end{bmatrix} = \begin{bmatrix} 2 & 1 & 1 \\ 1 & 2 & 1 \\ 1 & 1 & 1 \end{bmatrix} \text{ ohm} \quad (3.49)$$

and

$$\underline{Z}_\gamma = \begin{bmatrix} \underline{Z}_{pp\gamma} & \underline{Z}_{pq} \\ \underline{Z}_{qp} & \underline{Z}_{qq\gamma} \end{bmatrix} = \begin{bmatrix} 11/5 & 2/5 & 2/5 \\ 2/5 & 9/5 & 4/5 \\ 2/5 & 4/5 & 4/5 \end{bmatrix} \text{ ohm} \quad (3.50)$$

Using (3.9) we have,

$$\underline{Z}_1 = [1 \quad 1] \begin{bmatrix} 1 \\ 1 \end{bmatrix} \left[ [1 \quad 1] \begin{bmatrix} -\frac{1}{5} & -\frac{1}{5} \\ -\frac{1}{5} & -\frac{1}{5} \end{bmatrix} \begin{bmatrix} 1 \\ 1 \end{bmatrix} \right]^{-1} [1 \quad 1] \begin{bmatrix} 1 \\ 1 \end{bmatrix}$$

$$= -5 \quad (3.51a)$$

$$\text{and } \underline{Z}_{cc} = -\underline{Z}_{dd} - \underline{Z}_1 = -2 + 5 = 3. \quad (3.51b)$$

Substitution of  $\underline{Z}_1$  and  $\underline{Z}_{cc}$ , from (3.51a) and (3.51b), in (3.11a) - (3.11c) yields

$$\underline{Z}_{pc} = 2; \quad \underline{Z}_{cp} = 2; \quad \underline{Z}_{pp\alpha} = 3. \quad (3.52)$$

From (3.51b) and (3.52) we obtain

$$\underline{Z}_\alpha = \begin{bmatrix} 3 & 2 \\ 2 & 3 \end{bmatrix} \text{ ohm} \quad (3.53)$$

which is identical to  $\underline{Z}_\alpha$  given by (3.47).

### c. Example 3

This example illustrates the fact that (3.15) can be used for evaluating  $\underline{Z}_\alpha$  by incorporation of an additional port at the location of the c-port as discussed in Section 3.2.5.

Consider again the  $\alpha$ -circuit shown in Fig. 3.6(a). When additional port is incorporated at the location of the c-port, the  $\alpha$ -circuit modifies itself to that shown in Fig. 3.7(a). A  $\beta$ -circuit, with  $D = Q = 1$ , is added to the  $\alpha$ -circuit to obtain a  $\gamma$ -circuit as illustrated in Fig. 3.7(b). We now have,  $P = 2$ ,  $C = D = Q = 1$ . Since we are now interested in evaluating

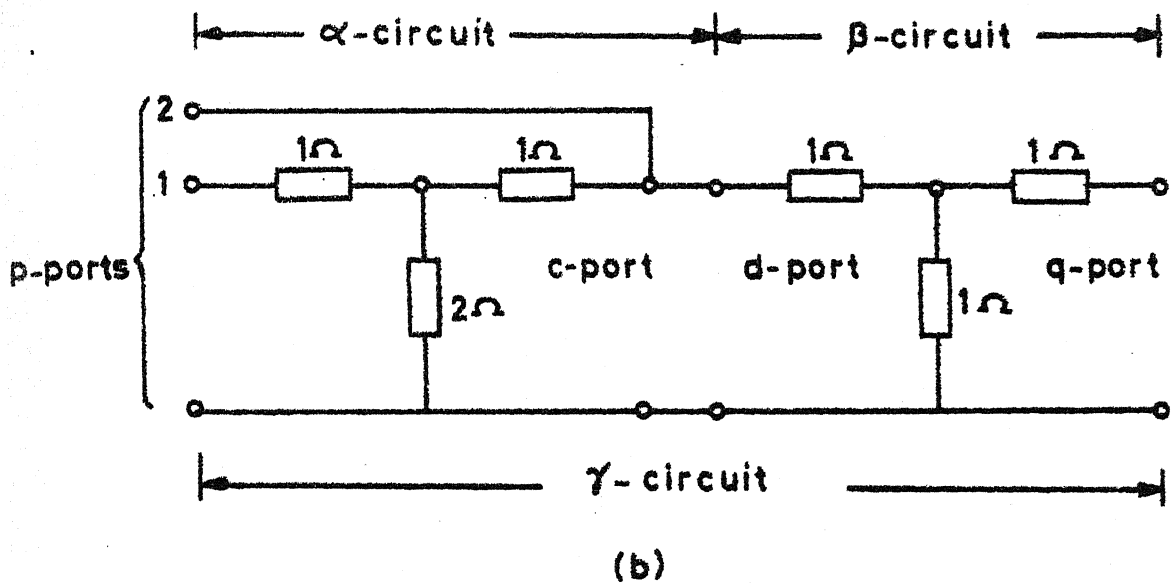
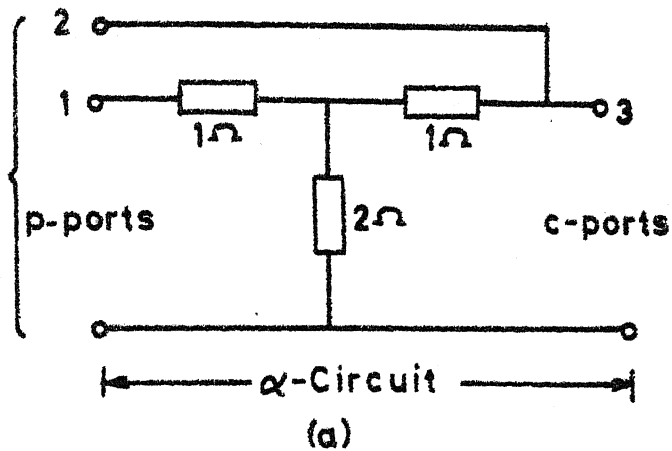


**FIG.3.7 (a) INCORPORATION OF AN ADDITIONAL p-PORT  
(numbered 2) TO THE  $\alpha$ -CIRCUIT OF FIG.3.6(a)**

**(b) ADDITION OF  $\beta$ -CIRCUIT TO THE  $\alpha$ -CIRCUIT  
OF FIGURE(a) ( $P=2, C=D=Q=1$ )**

$\underline{Z}_{pp\alpha}$  of the circuit of Fig. 3.7(a), which is identical to  $\underline{Z}_{\alpha}$  of the circuit shown in Fig. 3.6(a), we need to evaluate  $\underline{Z}_{qq\beta}$  and  $\underline{Z}_{qq\gamma}$ . These matrices for the  $\beta$ - and  $\gamma$ -circuits of Fig. 3.7(b) can be expressed as,

$$\underline{Z}_{qq\beta} = 2 \text{ ohm} \quad (3.54)$$

$$\underline{Z}_{\gamma} = \begin{bmatrix} \underline{Z}_{pp\gamma} & \underline{Z}_{pq} \\ \underline{Z}_{qp} & \underline{Z}_{qq\gamma} \end{bmatrix} = \begin{bmatrix} 11/5 & 4/5 & 2/5 \\ 4/5 & 6/5 & 3/5 \\ 2/5 & 3/5 & 9/5 \end{bmatrix} \text{ ohm} \quad (3.55)$$

The matrix  $\underline{Z}_{pp\alpha}$  is then given by, from (3.15),

$$\begin{aligned} \underline{Z}_{pp\alpha} &= \underline{Z}_{pp\gamma} - \underline{Z}_{pq} [\underline{Z}_{qq\gamma} - \underline{Z}_{qq\beta}]^{-1} \underline{Z}_{qp} \\ &= \begin{bmatrix} 11/5 & 4/5 \\ 4/5 & 6/5 \end{bmatrix} - \begin{bmatrix} 2/5 \\ 3/5 \end{bmatrix} \begin{bmatrix} -5 & 2/5 & 3/5 \end{bmatrix} \\ &= \begin{bmatrix} 3 & 2 \\ 2 & 3 \end{bmatrix} \text{ ohm} \end{aligned} \quad (3.56)$$

which is identical to the  $\underline{Z}_{\alpha}$  given by (3.48) and (3.53).

This solution proves the validity of the procedure outlined in Section 3.2.5.

Next, we compare the computational efficiency of the two procedures, discussed in Section 3.2.3 and 3.2.5, in evaluating  $\underline{Z}_{\alpha}$  of the  $\alpha$ -circuit configuration of Fig. 3.6(a) and in evaluating  $\underline{Z}_{pp\alpha}$  ( $= \underline{Z}_{\alpha}$  for  $\alpha$ -circuit of Fig. 3.6(a)) of the modified

$\alpha$ -circuit as shown in Fig. 3.7(a). The orders of the matrices to be evaluated in the two procedures are given in Table 3.1.

Table 3.1 Orders of the matrices  $\underline{Z}_\beta$  and  $\underline{Z}_\gamma$  for implementing desegmentation method

	$\alpha$ -circuit of Fig. 3.6(a)	Modified $\alpha$ -circuit of Fig. 3.7(a)
Procedure employed	Section 3.2.3	Section 3.2.5
Order of the matrix :		
i) $\underline{Z}_\beta$	2x2	1x1
ii) $\underline{Z}_\gamma$	2x2	3x3

Thus for the example choosen the procedure discussed in Section 3.2.3 is more efficient than that discussed in Section 3.2.5.

### 3.4.2 Examples of transmission line circuits

#### A. Example 1

Consider the transmission line circuit  $\alpha$ , shown in Fig. 3.8(a), with  $P = 1$ , and  $C = 1$ . When a  $\beta$ -circuit, with  $D = 1$  and  $Q = 1$ , is added to the  $\alpha$ -circuit, we have a  $\gamma$ -circuit with  $P = 1$  and  $Q = 1$  as illustrated in Fig. 3.8(b). For the sake of simplicity in the illustration, both the transmission lines are considered to have equal characteristic impedance  $Z_0$ . In the present case, the Z-matrix formulation is used and only the case  $Q = D$  is being illustrated.

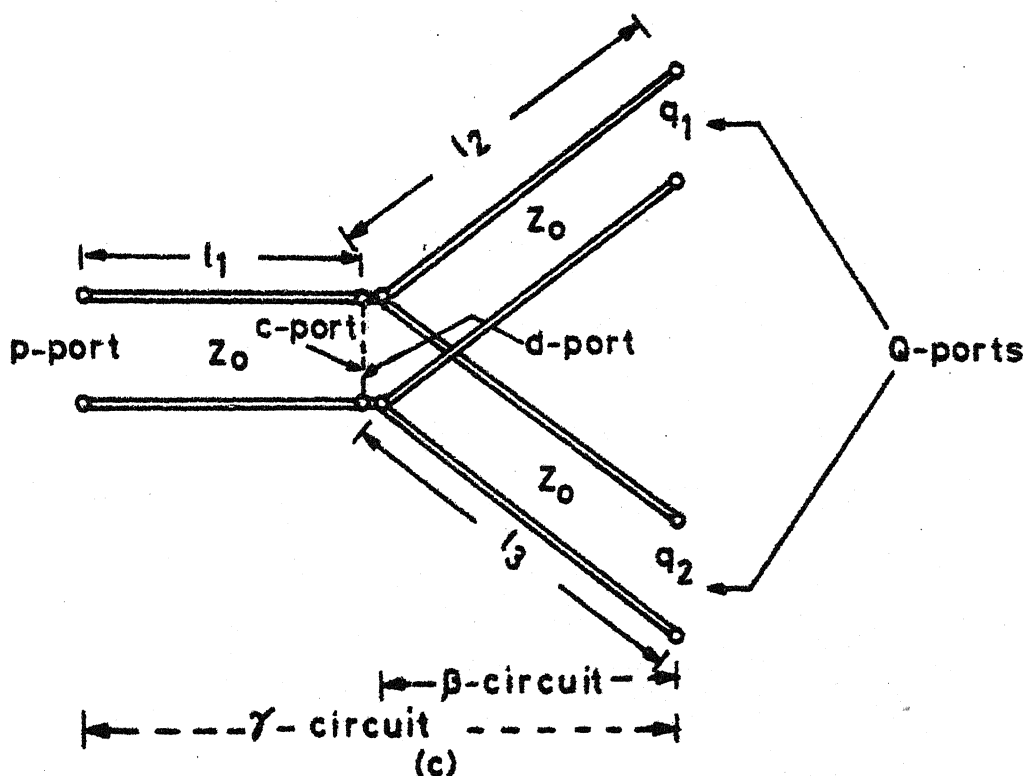
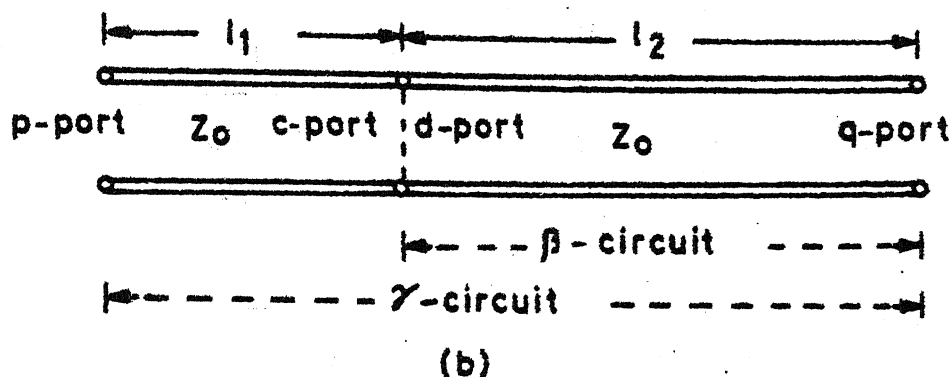
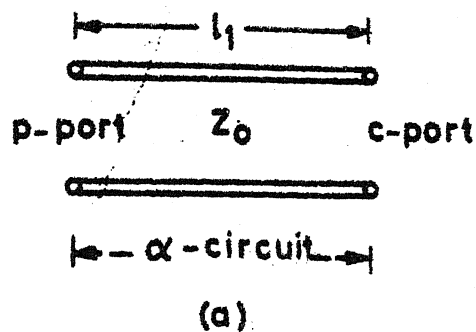


FIG. 3-8 (a) TRANSMISSION LINE CIRCUIT ( $\alpha$ ) TO BE ANALYZED ( $P=1, C=1$ )  
 (b) ADDITION OF  $\beta$ -CIRCUIT TO  $\alpha$ -CIRCUIT ( $P=1, C=D=Q=1$ )  
 (c) ADDITION OF  $\beta$ -CIRCUIT TO  $\alpha$ -CIRCUIT ( $P=1, C=D=1, Q=2$ )

The Z-matrices of  $\beta$ - and  $\gamma$ -circuits configurations of Fig. 3.8(b) are given by

$$\underline{Z}_{\beta} = \begin{bmatrix} Z_0 \coth(\gamma_1 l_2) & Z_0 / \sinh(\gamma_1 l_2) \\ Z_0 / \sinh(\gamma_1 l_2) & Z_0 \coth(\gamma_1 l_2) \end{bmatrix} \text{ ohm} \quad (3.57)$$

$$\underline{Z}_{\gamma} = \begin{bmatrix} Z_0 \coth(\gamma_1 l_3) & Z_0 / \sinh(\gamma_1 l_3) \\ Z_0 / \sinh(\gamma_1 l_3) & Z_0 \coth(\gamma_1 l_3) \end{bmatrix} \text{ ohm} \quad (3.58)$$

where  $Z_0$  is the characteristic impedance of the lines and  $\gamma_1$  is the propagation constant .

Employing (3.14), (3.57) and (3.58) we have

$$\begin{aligned} \underline{Z}_{qq\gamma} - \underline{Z}_{qq\beta} &= Z_0 (\coth(\gamma_1 l_3) - \coth(\gamma_1 l_2)) \\ &= -Z_0 \frac{\sinh(\gamma_1 (l_3 - l_2))}{\sinh(\gamma_1 l_3) \sinh(\gamma_1 l_2)} \\ &= -Z_0 \frac{\sinh(\gamma_1 l_1)}{\sinh(\gamma_1 l_3) \sinh(\gamma_1 l_2)} \end{aligned} \quad (3.59)$$

$$\begin{aligned} \underline{Z}'_{qd} &= [\underline{Z}_{qq\gamma} - \underline{Z}_{qq\beta}]^{-1} \underline{Z}_{qd} \\ &= - \frac{\sinh(\gamma_1 l_3) \sinh(\gamma_1 l_2)}{Z_0 \sinh(\gamma_1 l_1)} \cdot \frac{Z_0}{\sinh(\gamma_1 l_2)} = - \frac{\sinh(\gamma_1 l_3)}{\sinh(\gamma_1 l_1)} \end{aligned} \quad (3.60)$$

$$\begin{aligned}
 \underline{Z}'_{qp} &= [\underline{Z}_{qq\gamma} - \underline{Z}_{qq\beta}]^{-1} \underline{Z}_{qp} \\
 &= - \frac{\sinh(\gamma_1 l_3) \sinh(\gamma_1 l_2)}{Z_0 \sinh(\gamma_1 l_1)} \cdot \frac{Z_0}{\sinh(\gamma_1 l_3)} = - \frac{\sinh(\gamma_1 l_2)}{\sinh(\gamma_1 l_1)} \quad (3.61)
 \end{aligned}$$

Use of (3.57) - (3.61) in (3.14) yields

$$\begin{aligned}
 \underline{Z}_{pp\alpha} &= \underline{Z}_{pp\gamma} - \underline{Z}_{pq} \underline{Z}'_{qp} \\
 &= Z_0 \left[ \coth(\gamma_1 l_3) - \frac{\operatorname{cosech}^2(\gamma_1 l_3)}{\coth(\gamma_1 l_3) - \coth(\gamma_1 l_2)} \right] \\
 &= Z_0 \left[ \frac{1 - \coth(\gamma_1 l_3) \coth(\gamma_1 l_2)}{\coth(\gamma_1 l_3) - \coth(\gamma_1 l_2)} \right] \\
 &= Z_0 \coth(\gamma_1 (l_3 - l_2)) = Z_0 \coth(\gamma_1 l_1) \quad (3.62)
 \end{aligned}$$

$$\begin{aligned}
 \underline{Z}_{pc} &= -\underline{Z}_{pq} \underline{Z}'_{qd} \\
 &= - \frac{Z_0}{\sinh(\gamma_1 l_3)} \cdot \frac{-\sinh(\gamma_1 l_3)}{\sinh(\gamma_1 l_1)} = \frac{Z_0}{\sinh(\gamma_1 l_1)} \quad (3.63)
 \end{aligned}$$

$$\begin{aligned}
 \underline{Z}_{cp} &= -\underline{Z}_{dq} \underline{Z}'_{qp} \\
 &= - \frac{Z_0}{\sinh(\gamma_1 l_2)} \cdot \frac{-\sinh(\gamma_1 l_2)}{\sinh(\gamma_1 l_1)} = \frac{Z_0}{\sinh(\gamma_1 l_1)} \quad (3.64)
 \end{aligned}$$

and

$$\begin{aligned}
 \underline{Z}_{cc} &= -\underline{Z}_{dd} - \underline{Z}_{dq} \underline{Z}'_{qd} \\
 &= - \left[ Z_0 \coth(\gamma_1 l_2) + \frac{\operatorname{cosech}^2(\gamma_1 l_2)}{\coth(\gamma_1 l_3) - \coth(\gamma_1 l_2)} \right] \\
 &= Z_0 \frac{1 - \coth(\gamma_1 l_3) \coth(\gamma_1 l_2)}{\coth(\gamma_1 l_3) - \coth(\gamma_1 l_2)} \\
 &= Z_0 \coth(\gamma_1 (l_3 - l_2)) = Z_0 \coth(\gamma_1 l_1) \quad (3.65)
 \end{aligned}$$



From (3.62) - (3.65) we have

$$\underline{Z}_\alpha = \begin{bmatrix} Z_0 \coth(\gamma_1 l_1) & Z_0 / \sinh(\gamma_1 l_1) \\ Z_0 / \sinh(\gamma_1 l_1) & Z_0 \coth(\gamma_1 l_1) \end{bmatrix} \text{ ohm} \quad (3.66)$$

It can be easily verified that (3.66) represents the Z-matrix for the circuit of Fig. 3.8(a).

In the next two examples, the S-matrix formulation of the desegmentation method is illustrated.

### B. Example 2

Consider again the  $\alpha$ -,  $\beta$ - and  $\gamma$ -transmission line circuits shown in Figs. 3.8(a) and 3.8(b). As in the example 1, discussed in the preceeding paragraphs, we have  $P = C = D = Q = 1$ . The S-matrices of  $\beta$ - and  $\gamma$ -circuits can be written as,

$$\underline{S}_\beta = \begin{bmatrix} S_{dd} & S_{dq} \\ S_{qd} & S_{qq\beta} \end{bmatrix} = \begin{bmatrix} 0 & e^{-\gamma_1 l_2} \\ e^{-\gamma_1 l_2} & 0 \end{bmatrix} \quad (3.67)$$

$$\underline{S}_\gamma = \begin{bmatrix} S_{pp\gamma} & S_{pq} \\ S_{qp} & S_{qq\gamma} \end{bmatrix} = \begin{bmatrix} 0 & e^{-\gamma_1 (l_1 + l_2)} \\ e^{-\gamma_1 (l_1 + l_2)} & 0 \end{bmatrix} \quad (3.68)$$

Since for this example  $D = Q$ , using (3.44) with (3.29), (3.42), (3.67), and (3.68), we obtain

$$\underline{S}_2 = 0 ; \quad \underline{S}_{cc} = 0 ;$$

$$\underline{M}_{12} = [\underline{U} - \underline{S}_{dd} \underline{S}_{cc}]^{-1} = 1 ;$$

$$\underline{M}_{21} = [\underline{U} - \underline{S}_{cc} \underline{S}_{dd}]^{-1} = 1 ;$$

$$\underline{M}_{11} = \underline{S}_{dd} \underline{M}_{21} = 0 ;$$

$$\underline{M}_{22} = \underline{S}_{cc} \underline{M}_{12} = 0 ,$$

and the S-matrix for the  $\alpha$ -circuit

$$\underline{S}_\alpha = \begin{bmatrix} 0 & e^{-\gamma_1 l_1} \\ e^{-\gamma_1 l_1} & 0 \end{bmatrix} \quad (3.69)$$

which is known to be the correct result.

### B. Example 3

To illustrate the validity of the equation (3.41), when  $Q \geq D$ , we again consider the  $\alpha$ -circuit (with  $P = C = 1$ ) of Fig. 3.8(a). When a  $\beta$ -circuit with two q-ports and one d-port (i.e.  $Q = 2$ ,  $D = 1$ ) is added to the  $\alpha$ -circuit, the resultant combination is the  $\gamma$ -circuit with  $P = 1$  and  $Q = 2$ . This is illustrated in Fig. 3.8(c).

In this case the S-matrix for the  $\beta$ - and  $\gamma$ -circuits can be expressed as

$$\underline{S}_\beta = \begin{bmatrix} \underline{S}_{dd} & \underline{S}_{dq} \\ \underline{S}_{qd} & \underline{S}_{qq\beta} \end{bmatrix}$$

$$= \left[ \begin{array}{c|cc} -\frac{1}{3} & \frac{2}{3} e^{-\gamma_1 l_2} & \frac{2}{3} e^{-\gamma_1 l_3} \\ \hline \frac{2}{3} e^{-\gamma_1 l_2} & -\frac{1}{3} e^{-2\gamma_1 l_2} & \frac{2}{3} e^{-\gamma_1 (l_2 + l_3)} \\ \frac{2}{3} e^{-\gamma_1 l_3} & \frac{2}{3} e^{-\gamma_1 (l_2 + l_3)} & -\frac{1}{3} e^{-2\gamma_1 l_3} \end{array} \right] \quad (3.70)$$

and

$$\underline{S}_\gamma = \begin{bmatrix} \underline{S}_{pp\gamma} & \underline{S}_{pq} \\ \underline{S}_{qp} & \underline{S}_{qq\gamma} \end{bmatrix}$$

$$= \left[ \begin{array}{c|cc} -\frac{1}{3} e^{-2\gamma_1 l_1} & \frac{2}{3} e^{-\gamma_1 (l_1 + l_2)} & \frac{2}{3} e^{-\gamma_1 (l_1 + l_3)} \\ \hline \frac{2}{3} e^{-\gamma_1 (l_1 + l_2)} & -\frac{1}{3} e^{-2\gamma_1 l_2} & \frac{2}{3} e^{-\gamma_1 (l_2 + l_3)} \\ \frac{2}{3} e^{-\gamma_1 (l_1 + l_3)} & \frac{2}{3} e^{-\gamma_1 (l_2 + l_3)} & -\frac{1}{3} e^{-2\gamma_1 l_3} \end{array} \right] \quad (3.71)$$

From the preceeding two equations we have

$$[\underline{S}_{qq\gamma} - \underline{S}_{qq\beta}] = \begin{bmatrix} 0 & 0 \\ 0 & 0 \end{bmatrix} \quad (3.72a)$$

$$[\underline{S}_{dq} \ \underline{S}_{dq}^t]^{-1} = \left[ \frac{4}{9} \left[ e^{-2\gamma_1 l_2} + e^{-2\gamma_1 l_3} \right] \right]^{-1} \quad (3.72b)$$

$$[S_{qd}^t \ S_{qd}]^{-1} = \left[ \frac{4}{9} \left[ e^{-2\gamma_1 l_2} + e^{-2\gamma_1 l_3} \right] \right]^{-1} \quad (3.72c)$$

Using (3.29), (3.36) - (3.40) and, (3.70) - (3.72c), we obtain

$$\underline{S}_1 = 0$$

$$\underline{M}_{12} = 1, \underline{M}_{21} = 1, \underline{M}_{11} = -\frac{1}{3}, \underline{M}_{22} = 0, \text{ and}$$

$$\underline{S}_\alpha = \begin{bmatrix} 0 & e^{-\gamma_1 l_1} \\ e^{-\gamma_1 l_1} & 0 \end{bmatrix} \quad (3.73)$$

which is identical to the  $\underline{S}_\alpha$  given by (3.69).

It may be recalled that Z-matrix formulation of the desegmentation method cannot be used when  $Z_{qq\gamma} = Z_{qq\beta}$ . In S-matrix formulation such a condition does not arise even if  $[S_{qq\gamma} - S_{qq\beta}]$  is a singular matrix (such as in 3.72(a)).

### 3.4.3 Planar circuit examples

#### A. Example 1

Consider the trapezoidal planar circuit configuration shown in Fig. 3.3(a). It is desired to evaluate the input impedance for this one port circuit at port  $p_1$ . This impedance has been evaluated using, both, the desegmentation method proposed in this chapter and the segmentation method known earlier [23].

For employing the desegmentation method, an equilateral triangle  $\beta$  is added to the trapezoidal ( $\alpha$ -segment) so that the

combination of  $\alpha$  and  $\beta$  is also an equilateral triangle  $\gamma$  as shown in Fig. 3.3(b). The Z-matrices for  $\beta$ - and  $\gamma$ -segments are computed using Green's function [21]. The number of the q-ports is decided by following the procedure outlined in the section 3.2.4 and is found to be 4. The width of the q-ports is chosen small enough so that the field variation, over a port width, can be assumed to be negligible. As there is no specified port, of the initial  $\alpha$ -circuit, corresponding to the c-ports, equation (3.15) yields the value of the input impedance needed. Fig. 3.9 shows the variation of this input impedance with frequency for the case when  $A = 3.1711$  cm.,  $a = 0.25$  A,  $\epsilon_r = 2.55$  and the thickness of the dielectric substrate  $d = 1.6$  mm.

For the analysis using the segmentation method, the trapezoidal circuit is divided in three segments, i.e., two  $30^\circ - 60^\circ$  right triangles and one rectangle as illustrated in Fig. 3.9 (inset). The Z-matrices for these segments are computed using Green's functions [21], [1].  $Z_{pp\alpha}$  is then computed using the segmentation method for Z-matrices [23]. It is found that the number of interconnecting ports (between the rectangle and two  $30^\circ - 60^\circ$  triangles) required for convergence of  $Z_{pp\alpha}$  is 16. The results obtained by this method are also plotted in Fig. 3.9 and agree very well with those obtained by the desegmentation method.

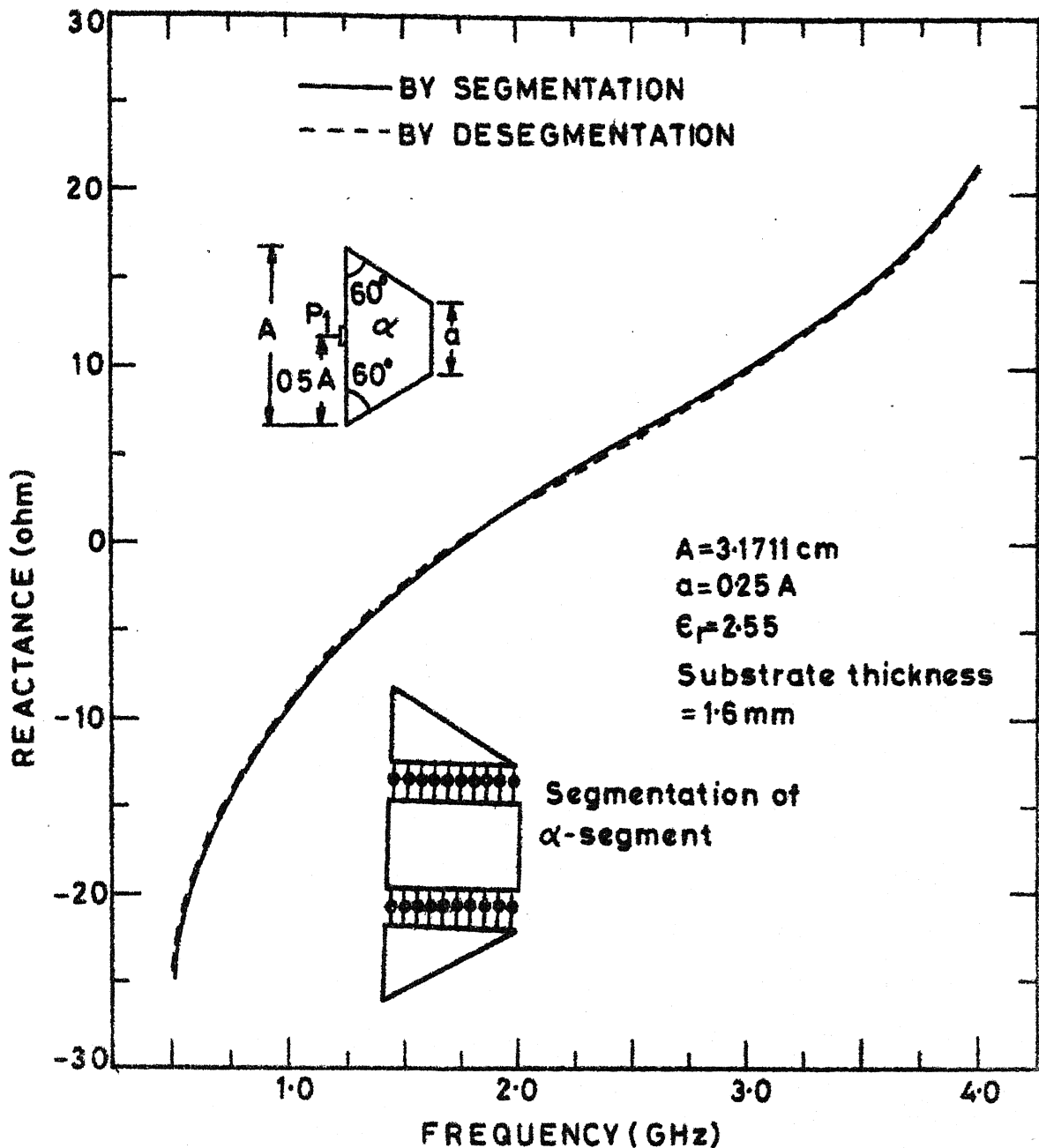


FIG.3.9 VARIATION OF INPUT REACTANCE AT PORT  $P_1$  OF THE TRAPEZOIDAL 2-d CIRCUIT WITH FREQUENCY AS EVALUATED BY SEGMENTATION AND DESEGMENTATION METHODS

## B. Example 2

Another example considered is a rectangular ring type planar circuit shown in Fig. 3.3(c). In this case also it is required to find out the input impedance at the port  $p_1$  of the  $\alpha$ -circuit. In this case  $\beta$ -segment is a rectangular element of length 'a' and width 'b' which when added to  $\alpha$ -segment of Fig. 3.3(c) results in a complete rectangular planar circuit  $\gamma$  as shown in Fig. 3.3(d). The characteristics of the small rectangle  $\beta$  and the outer (filled) rectangle  $\gamma$ , of dimensions  $A \times B$ , are computed using impedance Green's function for rectangular segments [1]. In this case the total periphery of the  $\beta$ -segment is common with the inner periphery of the  $\alpha$ -segment. The ports c and d are located along this interconnection. Thus there is no part of the periphery, of the  $\beta$ -segment, available for locating the q-ports. Since  $Q$  (the number of q-ports) can not be made zero, these ports are located inside the  $\beta$ -segment (i.e., inside the small rectangle). These are the fictitious ports, with port voltages measured between the port locations and the ground plane. As in the case of the ports on periphery, in this case also the voltages are averaged over each port width. The port current is considered to flow in the direction normal to the plane of the paper. The formulation presented in the preceeding sections of this chapter holds good for such a case also. The minimum number of q-ports is decided by following the same procedure

as used for Example 1 and is found to be 9. These q-ports are indicated by vertical bars in Fig. 3.3(d). The width of these ports have also been selected iteratively for fast convergence of numerical computations. The values of the input impedance obtained are plotted in Fig. 3.10, as a function of frequency, for the case when  $A = 5$  cm,  $B = 1$  cm.,  $a = 1$  cm.,  $b = 8$  mm,  $\epsilon_r = 2.54$  and thickness of substrate is 1.6 mm.

This circuit is analyzed using the segmentation method also. The  $\alpha$ -circuit is divided into four segments as shown in the Fig. 3.10 (inset). For this example, the number of interconnected ports required between the various segments is found to be 4. The results agree very well with those obtained from the desegmentation method as shown in Fig. 3.10.

### 3.5 COMPUTATIONAL EFFORT IN DESEGMENTATION AND SEGMENTATION

In this section we compare the computational efforts needed in segmentation and desegmentation methods for analyzing 2-d circuits. Two typical examples are presented for this comparison.

#### A. Example 1

Consider a planar square segment with one square patch removed from one of its corners as shown in Fig. 3.11(a). There are  $P$  number of p-ports specified on the  $\alpha$ -segment. It is required to evaluate  $Z_{pp\alpha}$ .



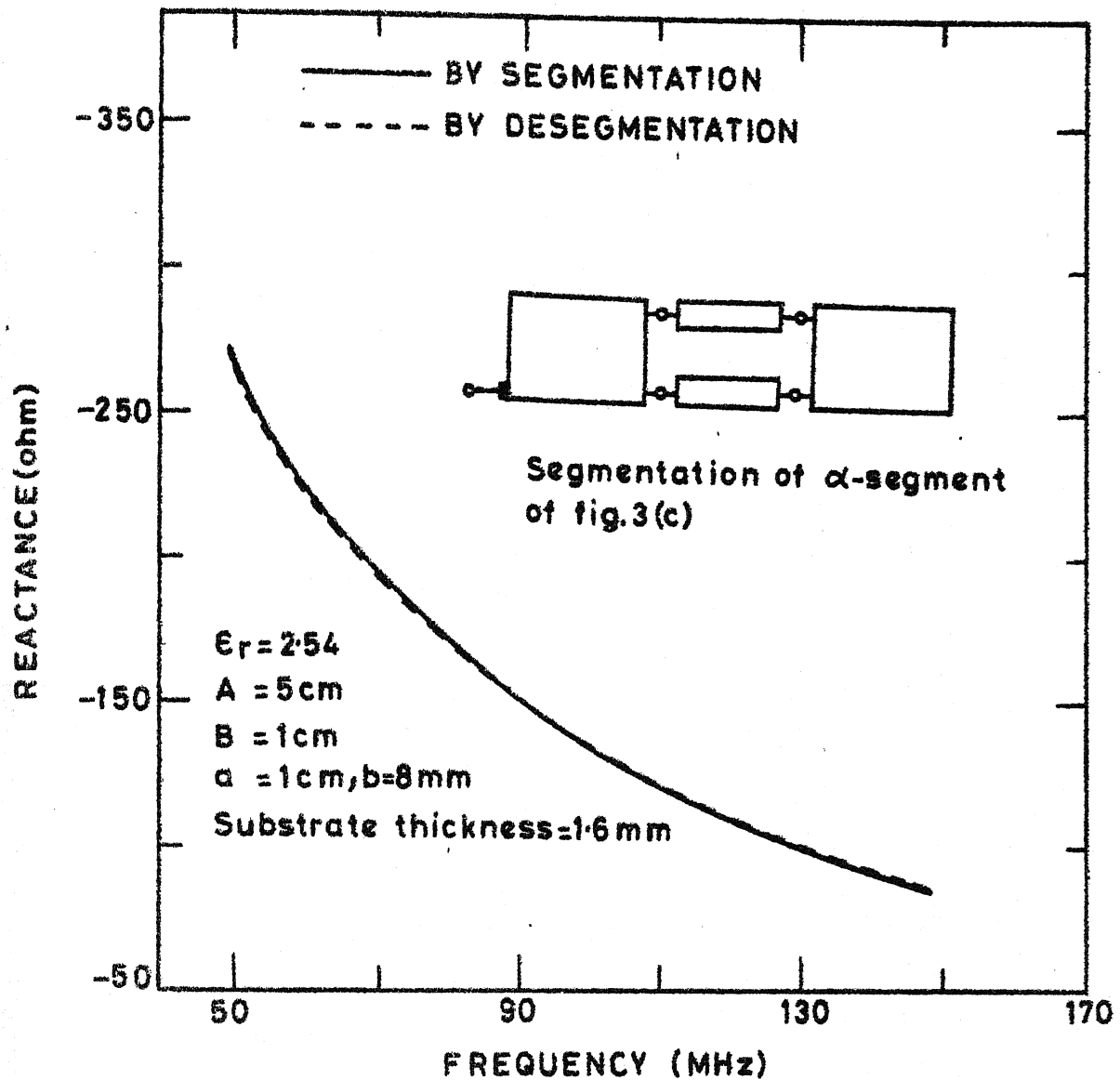


FIG.3.10 VARIATION OF INPUT REACTANCE (At port  $P_1$  of the rectangular ring 2-d circuit) WITH FREQUENCY AS EVALUATED BY SEGMENTATION AND DESEGMENTATION METHOD

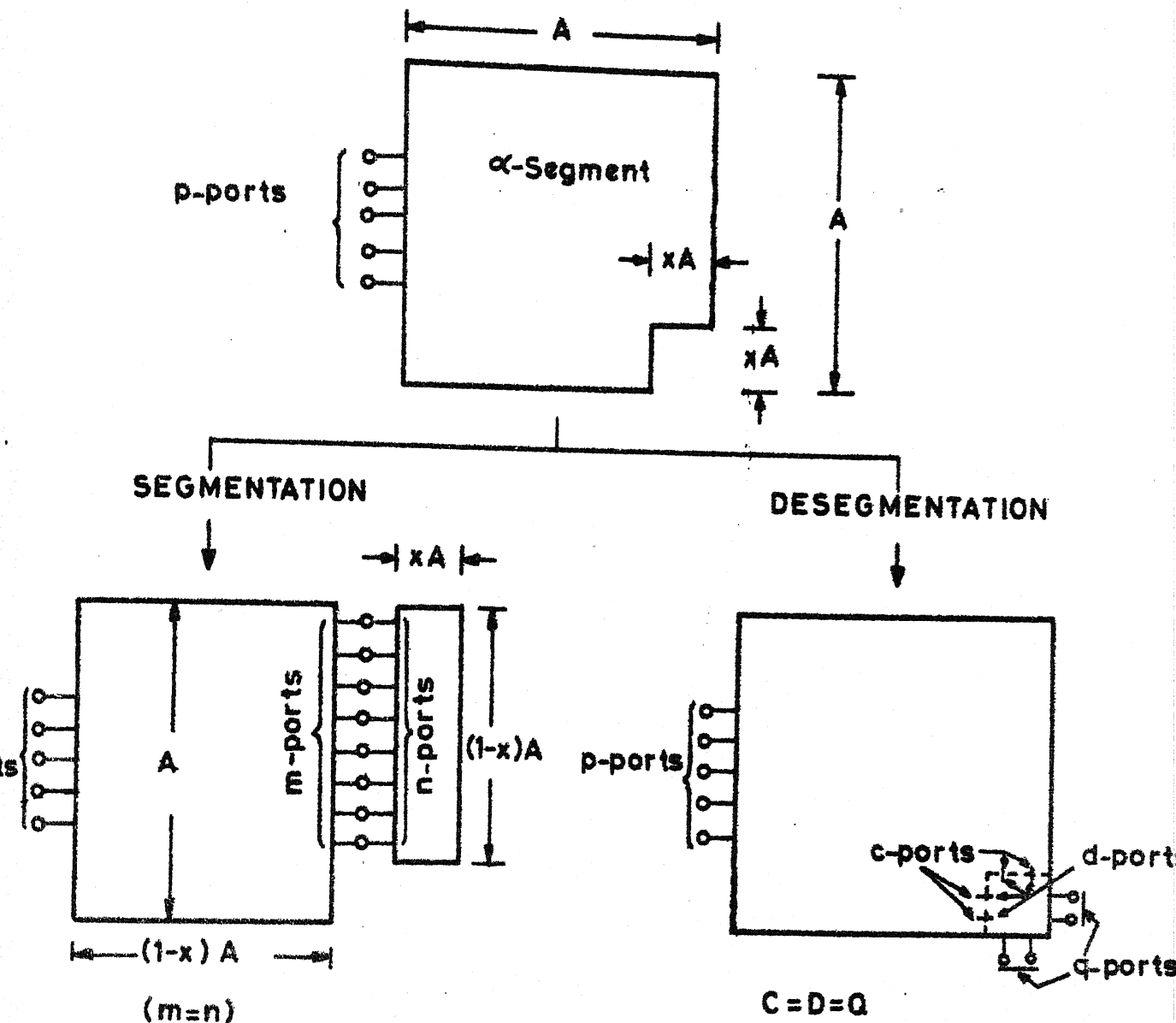


FIG. 3-11 (a) GIVEN  $\alpha$ -SEGMENT,  $Z_{pp\alpha}$  TO BE EVALUATED  
 (b) SEGMENTATION APPLIED TO  $\alpha$ -SEGMENT  
 (c) DESEGMENTATION APPLIED TO  $\alpha$ -SEGMENT

Let  $Q$  be the number of  $q$ -ports needed for convergence of  $\underline{Z}_{pp\alpha}$  while using desegmentation method. Since  $\beta$ - and  $\gamma$ -segments are both rectangular shapes (Fig. 3.11(c)), the computational effort in evaluating the integral function in the Green's function of  $\underline{Z}_{\beta}$  equals that in evaluating the integral function of  $\underline{Z}_{\gamma}$ . Hence,  $E(\beta) = E(\gamma) = 1$  (say). As only  $p$ -ports are specified on  $\alpha$ -segment, (3.15) can be used. Employing (3.17) with  $P = P_1$  and  $P_2 = 0$ , the computational effort in evaluating  $\underline{Z}_{\beta}$  and  $\underline{Z}_{\gamma}$  is,

$$E_{\text{deseg}} = Q + (P+Q) = P+2Q \text{ units} \quad (3.74)$$

It may be recalled here that (3.15) is a part of (3.14), which is valid for  $C = D = Q$ . Thus for removal of a square patch of dimensions ' $x A$  by  $x A$ ' from a larger square of dimensions ' $A$  by  $A$ ', the interface between  $\alpha$ - and  $\beta$ -segments is considered to have  $Q (= C = D)$  interconnections. The length of the interface is ' $2 x A$ ' units. Thus for ' $2 x A$ ' units long interface one needs  $Q$  number of  $q$ -ports.

In evaluating  $\underline{Z}_{pp\alpha}$  by segmentation method, the  $\alpha$ -segment is divided into two rectangular segments of dimensions ' $A$  by  $(1-x)A$ ' and ' $x A$  by  $(1-x)A$ ' as illustrated in Fig. 3.11(b). The interface, of length  $(1-x)A$  units, between the two segments is considered to be connected by  $m (= n)$  interconnections. The two  $Z$ -matrices to be evaluated are of order ' $P+m$  by  $P+m$ ' and ' $m$  by  $m$ '. The computational effort in evaluating these

matrices, with  $E(\beta) = E(\gamma) = 1$  unit, is

$$E_{\text{seg}} = m + (P+m) = P+2m \quad \text{units} \quad (3.75)$$

For given number of p-ports ( $=P$ ), the computational effort in (3.74) and in (3.75) depends upon  $Q$  and  $m(=n)$  respectively. At a given frequency, the number of interconnected ports in Figs. 3.11(b) and 3.11(c), can be assumed to be directly proportional to the length of the interface. Therefore, when the lengths of the interfaces in the two cases are equal we have  $m=n=Q$  and (3.74) and (3.75) are identical. Therefore, the condition for equal computational efforts in segmentation and desegmentation is

$$(1-x)A = 2xA \quad (3.76)$$

which yields  $x = 1/3$ . In such a situation, the orders of the matrices to be inverted in implementation of segmentation and of desegmentation are also equal.

Thus for the  $\alpha$ -segment of Fig. 3.11(a), the desegmentation is computationally more efficient than the segmentation method if  $x < 1/3$ . For  $x > 1/3$ , the reverse is true. These arguments can be extended to circuits of other configurations. Another example of Fig. 3.12(a) is considered for illustrating this.

## B. Example 2

Consider the  $\alpha$ -segment shown in Fig. 3.12(a). It is

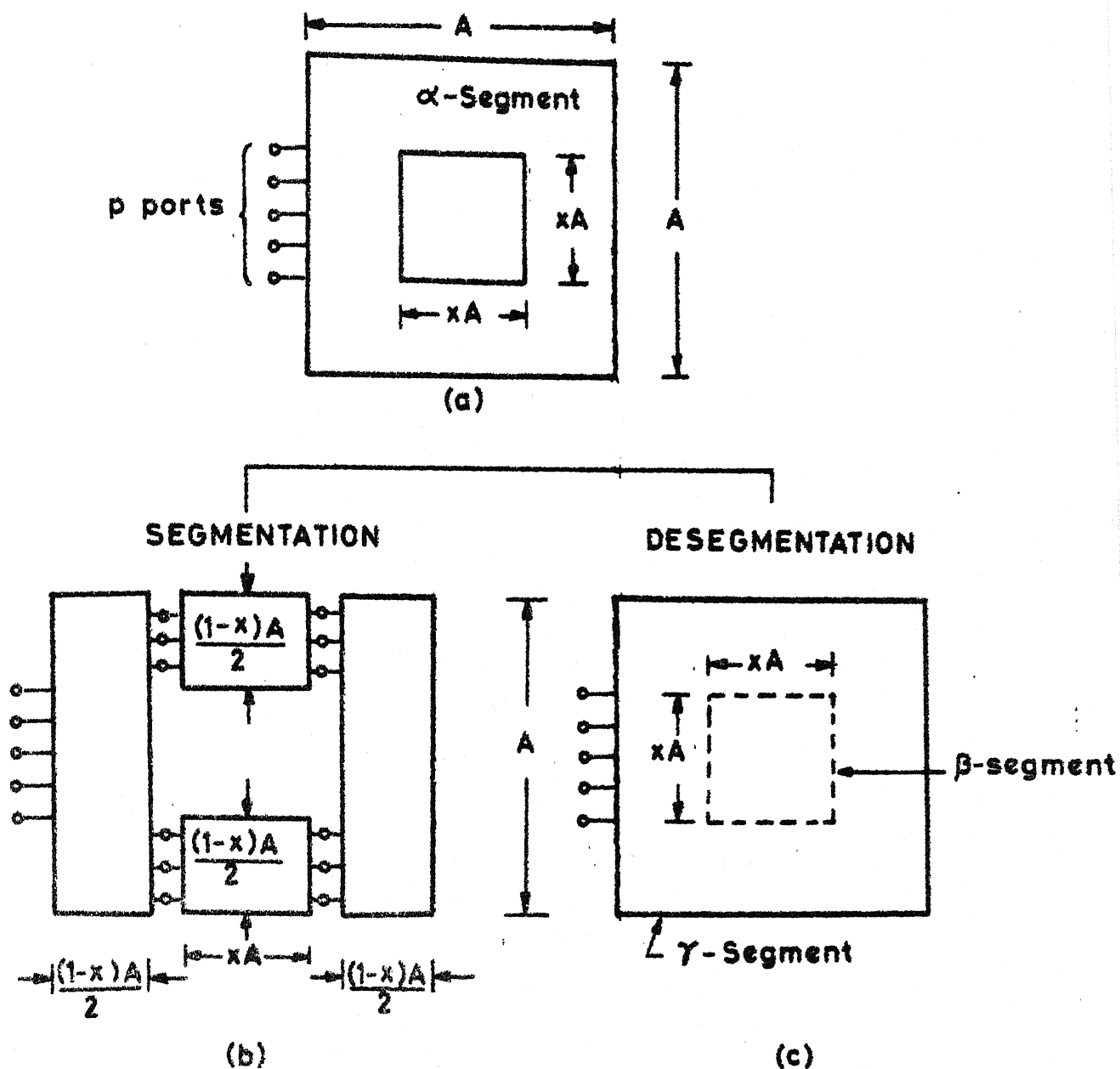


FIG. 3-12 (a)  $\alpha$ -SEGMENT TO BE ANALYZED ;

(b) SEGMENTATION APPLIED TO  $\alpha$ -SEGMENT

(c) DESEGMENTATION APPLIED TO  $\alpha$ -SEGMENT

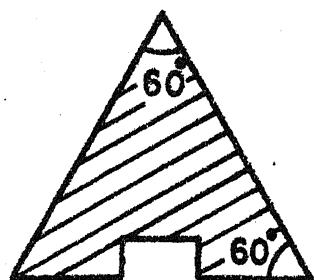
desired to evaluate the Z-matrix  $Z_{pp\alpha}$  with p-port (= P in number). The application of segmentation and desegmentation methods to the  $\alpha$ -segment is illustrated in Fig. 3.12(b) and in Fig. 3.12(c), respectively. As discussed in the preceeding paragraphs, the computational effort in the implementation of the two methods would be equal if the lengths of the interfaces are equal. The length of the interface in case of desegmentation (Fig. 3.12(c)) is '4xA'. In case of segmentation of the  $\alpha$ -segment, the total length of the interface is '2(1-x)A'. Since the two smaller and the two larger rectangles in Fig. 3.12(b) are identical, the effective interface. corresponding to which the Z-parameters of the rectangles should be evaluated using Green's function, reduces to (1-x)A. This is so because the Z-matrices for only two rectangles, one smaller and one larger, need evaluation. Thus for equal computational effort in the two methods we have

$$(1-x)A = 4xA$$

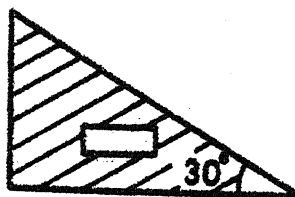
which gives  $x = 0.2$ .

Therefore, for the  $\alpha$ -segment of Fig. 3.12(a), the desegmentation method is computationally more efficient than the segmentation method if  $x < 0.2$ . At  $x = 0.2$ , the two methods need equal computational efforts.

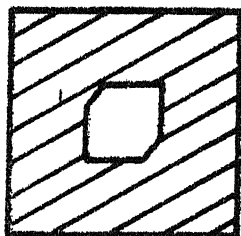
For circuit configurations such as shown in Fig. 3.13, the geometries of  $\beta$ - and  $\gamma$ -segments are not similar (i.e. both are



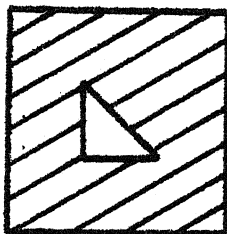
(a)



(b)



(c)



(d)

**FIG. 3-13 TWO DIMENSIONAL CIRCUIT CONFIGURATIONS WHERE DESEGMENTATION CAN BE MORE EFFICIENT THAN THE SEGMENTATION OR VICE VERSA DEPENDING UPON THE SIZE OF THE PATCH REMOVED FROM THE REGULAR SHAPES**

not rectangular or same type of triangles). Therefore, the computational efforts  $E(\beta)$  and  $E(\gamma)$ , needed in evaluating the integral functions in the Green's functions for  $\beta$ - and  $\gamma$ -segments, respectively, should be first determined. The computational efforts in the two methods can then be evaluated to determine the efficiency of one method over that of the other on the basis of preceeding discussion.

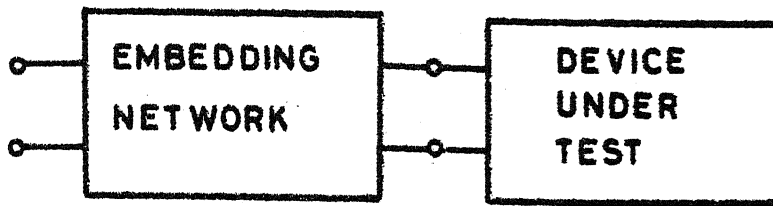
### 3.6 APPLICATION TO DE-EMBEDDING

#### 3.6.1 De-embedding

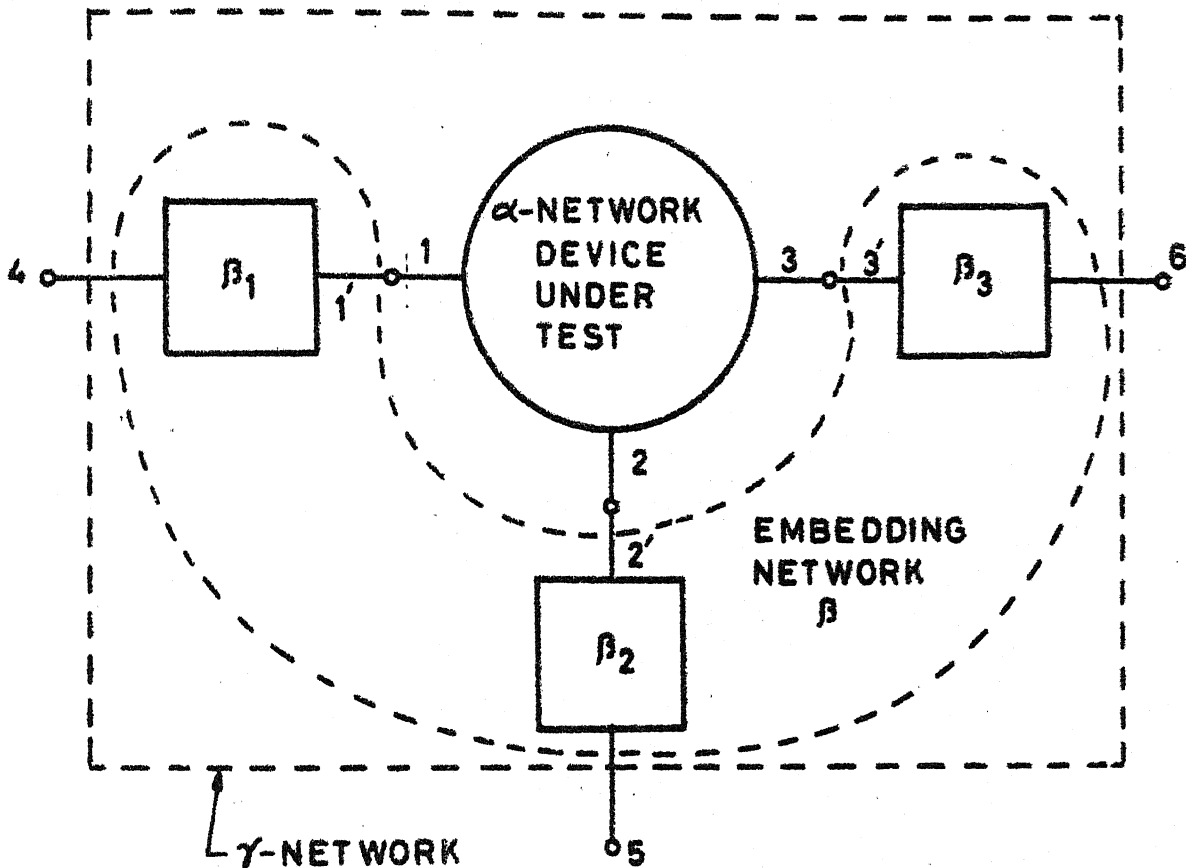
For measurement at microwave, or higher, frequencies it becomes necessary to take into account the effect of the intervening networks (connectors etc.) between the measurement system and the device under measurement. This process of separating the effect of the intervening structures from the measured parameters has been termed as de-embedding [53]. A procedure for de-embedding in terms of Z-parameters, for single port devices such as one shown in Fig. 3.14(a), has been reported earlier [53]. De-embedding for such a one-port circuit can be carried out using either the Z-parameters or the S-parameters since in such a case (Fig. 3.14(a)) the impedance parameters can be expressed in terms of the S-parameters or vice versa in a relatively simple way.

Formulas for the direct calculation of the scattering parameters of a linear two-port network, when measurements are





(a)



(b)

$\left. \begin{array}{l} \text{c-ports: } 1, 2, 3 \\ \text{d-ports: } 1', 2', 3' \\ \text{q-ports: } 4, 5, 6 \end{array} \right\} P=0, C=D=Q=3$

FIG.3-14(a) SINGLE PORT NETWORK EMBEDDED IN A TWO PORT NETWORK (b) THREE PORT NETWORK EMBEDDED IN A  $\beta$  NETWORK

made on an imperfect network analyzer, have also been reported [54]. Also the Through-Short-Delay (TSD) procedure [55] which provides a noniterative calibration procedure for two-port measurement has been extended for n-port scattering parameter measurements [56]. In the modified method [56], the system errors are separated by a 2n-port error model. The transfer-parameters (T-parameters) of the error model are expressed in terms of the S-parameters of three n-port standards which sequentially replace the n-port device under test. A detailed procedure of measurement is given in [56].

It may be pointed out here that for analyzing planar microwave circuits, the Z-matrix formulation is commonly used since the impedance Green's functions directly give the impedance matrices. On the other hand, in the case of measurements and de-embedding one deals with the scattering parameters. In this section, it is shown that the formulation of the desegmentation method in terms of S-matrices can be used as a solution of the generalized de-embedding problems.

### 3.6,2 De-embedding using desegmentation method

For using the formulation of the desegmentation method for de-embedding, the total system (i.e. the embedded system) is treated as the  $\gamma$ -segment. The embedding network (connectors etc.) becomes the  $\beta$ -segment (characterized by previous calibrations), and the device or the network under test is the

$\alpha$ -segment whose characteristics are to be found. This is illustrated by an example shown in Fig. 3.14(b) where a three-port  $\alpha$ -network is embedded in three connectors  $\beta_1, \beta_2$  and  $\beta_3$ . These three connectors form the entire  $\beta$ -network. In this case we have  $P = 0$  and  $C = D = Q = 3$ . In general, all the ports of the  $\alpha$ -network are embedded in  $\beta$ -network which makes  $P = 0$ . From (3.43) the S-parameters of the  $\alpha$ -network pertaining to c-ports are given by

$$\underline{S}_{cc} = [\underline{U} + \underline{S}_2 \underline{S}_{dd}]^{-1} \underline{S}_2 \quad (3.78)$$

where  $\underline{S}_2$ , given by (3.42), is

$$\underline{S}_2 = \underline{S}_{qd}^{-1} [\underline{S}_{qq\gamma} - \underline{S}_{qq\beta}] \underline{S}_{dq}^{-1} \quad (3.79)$$

For a single-port device ( $\alpha$ -network) when only one connector (with two-ports) is involved, the submatrices in (3.78) and (3.79) are just single elements. The  $\underline{S}_\alpha (= \underline{S}_{cc})$  in (3.78), in this case, is then given by

$$\underline{S}_\alpha = S_{cc} = \frac{S_{qq\gamma} - S_{qq\beta}}{S_{dq} S_{qd} + S_{dd} (S_{qq\gamma} - S_{qq\beta})} \quad (3.80)$$

It may be pointed out here, that to evaluate  $\underline{S}_{cc}$  from (3.78) we require  $\underline{S}_{qq\gamma}$  and all the submatrices of  $\underline{S}_\beta$ . The scattering matrix  $\underline{S}_\gamma$  is obtained by measurements on the embedded network and  $\underline{S}_\beta$  is known from previous calibrations of connectors, etc.

### 3.6.3 Illustrative example

For illustrating the de-embedding procedure, discussed in the preceeding section, we consider an example of a three-port circulator, with identical connectors at three-ports, as shown in Fig. 3.14(b). The measured S-parameters (i.e.  $\underline{S}_Y$  with  $p = 0$  and ports numbered as in Fig. 3.14(b)) are

$$\left. \begin{aligned} S_{44} &= S_{55} = S_{66} = 0.0148 + j0.0493 \\ S_{45} &= S_{56} = S_{64} = -0.1339 + j0.0624 \\ S_{46} &= S_{65} = S_{54} = -0.8975 + j0.1854 \end{aligned} \right\} \quad (3.81)$$

The S-matrices for the connectors, known from previous calibrations, are

$$\underline{S}_{\beta 1} = \underline{S}_{\beta 2} = \underline{S}_{\beta 3} = \left[ \begin{array}{c|c} 0.0568 - j0.0374 & -0.0966 - j0.9543 \\ \hline -0.0966 - j0.9543 & 0.0245 + j0.0364 \end{array} \right] \quad (3.82)$$

The scattering matrices of the three connectors can be grouped together to obtain the block diagonal scattering matrix  $\underline{S}_\beta$  (of order 6 by 6) as in (3.20).

Employing (3.78), (3.79), (3.81) and (3.82), the scattering-matrix for the  $\alpha$ -network (the three-port circulator) after de-embedding is found to have various components as

listed below.

$$\begin{aligned}
 S_{11} &= (-0.523 - j0.232)10^{-9} && \approx 0.0 \\
 S_{12} &= (0.1 - j0.186 \times 10^{-8}) && \approx 0.1 \\
 S_{13} &= (0.995 + j0.625 \times 10^{-9}) && \approx 0.995 \\
 S_{21} &= (0.995 + j0.160 \times 10^{-8}) && \approx 0.995 \\
 S_{22} &= (-0.465 + j0.116)10^{-9} && \approx 0.0 \\
 S_{23} &= (0.1 + j0.184 \times 10^{-8}) && \approx 0.1 \\
 S_{31} &= (0.1 + j0.139 \times 10^{-8}) && \approx 0.1 \\
 S_{32} &= (0.995 + j0.160 \times 10^{-8}) && \approx 0.995 \\
 S_{33} &= (-0.465 + j0.232)10^{-9} && \approx 0.0 .
 \end{aligned}$$

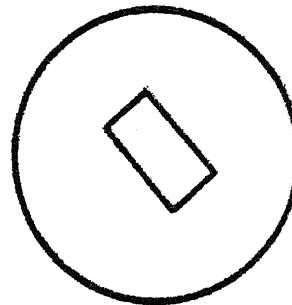
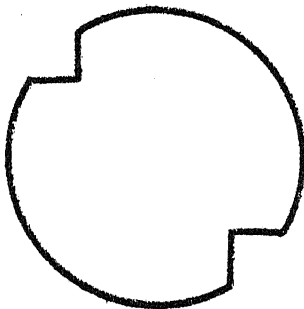
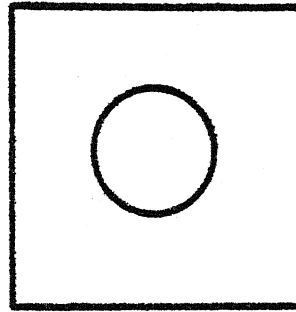
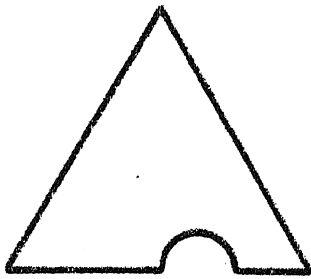
Correctness of these values have been verified by recalculating  $\underline{S}_Y$  by the segmentation method for S-matrices.

### 3.7 DISCUSSIONS

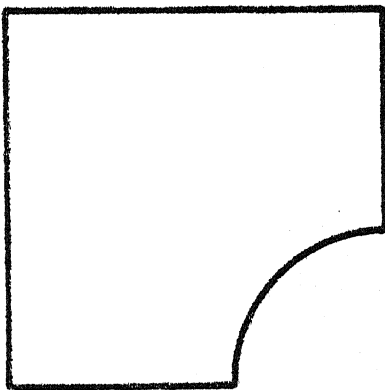
A method called 'desegmentation' for analysis of 2-d circuits has been proposed. Formulations of the method in terms of Z-matrices and in terms of S-matrices have been developed. The validity of the method is illustrated by several examples of lumped circuits and transmission line circuits. Two planar circuit examples, choosen such that the segmentation method is also applicable, have been included. The results obtained by using desegmentation method are compared with those obtained by implementation of segmentation

method and are found to agree precisely. An alternative scheme for implementing the desegmentation method is discussed in Section 3.2.5 which sometimes results in saving in computational effort and storage requirements because of reduced order of the matrices involved. Two typical examples have been included to compare the computational efficiencies of segmentation and desegmentation methods. In general, the desegmentation is more efficient than the segmentation method when the size of the  $\beta$ -segment (needed to convert the  $\alpha$ -segment into a regular shape  $\gamma$ ) is small as compared to the  $\alpha$ - and  $\gamma$ -segments.

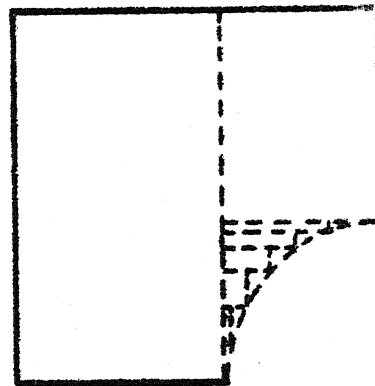
There are several situations where desegmentation method can be applied but segmentation method is not applicable. Some such configurations are shown in Fig. 3.15(a). One may think of using segmentation method in these cases also by approximating the curved boundary by piece wise linear approximations and dividing the pattern in number of triangles and rectangles as illustrated in Fig. 3.15(b). However, this method becomes difficult since Green's functions are known for only three types of triangles and it may not be possible to fit even the piece wise linear boundary within these three types of triangles. Also, computational effort increases enormously as number of segments is likely to become very large.



(a)



Approximate  
segmentation



(b)

**FIG.3-15 (a) CIRCUIT CONFIGURATIONS WHERE  
DESEGMENTATION CAN BE USED BUT  
SEGMENTATION IS NOT POSSIBLE (b)  
APPROXIMATE SEGMENTATION OF ONE  
OF THE CIRCUITS OF TYPE (a)**

The formulation of the method in terms of S-matrices is used to evolve a generalized method for de-embedding of multi-port networks. This is illustrated by a typical example of a three port circulator.

The desegmentation method extends the applicability of the Green's function approach of 2-d circuit analysis. Also, the method finds applications in the analysis and design of planar microstrip antennas and has been used for analysis and design of corners chopped square patch antennas and a square patch antenna with a diagonal slot reported in Chapters Five and Six, respectively.



## CHAPTER FOUR

### DIAGONAL FED NEARLY SQUARE PATCH ANTENNA

As mentioned in Section 1.2.3, a rectangular patch antenna with nearly equal sides yields circular polarization (CP) when input is at one of the corners [31], [42]. It has been pointed out [42] that the length to width ratio of the rectangle should be equal to 1.029 for obtaining CP. The corresponding experimental value of axial ratio has been reported to be nearly 1.4 dB. In this study [42] the modal expansion method has been used for analyzing the antenna.

This chapter gives the details of the investigations carried out on this type of antennas using the Green's function approach with magnetic wall boundary as discussed in Chapter Two.

Antenna configuration has been optimized for improving axial ratio and input VSWR and the results are confirmed experimentally. The feed location is optimized for the best input VSWR without using any external impedance matching network.

#### 4.1 OPTIMIZATION AND ANALYSIS

##### 4.1.1 Optimization of length to width ratio

The antenna shown in Fig. 4.1(a) is considered as a

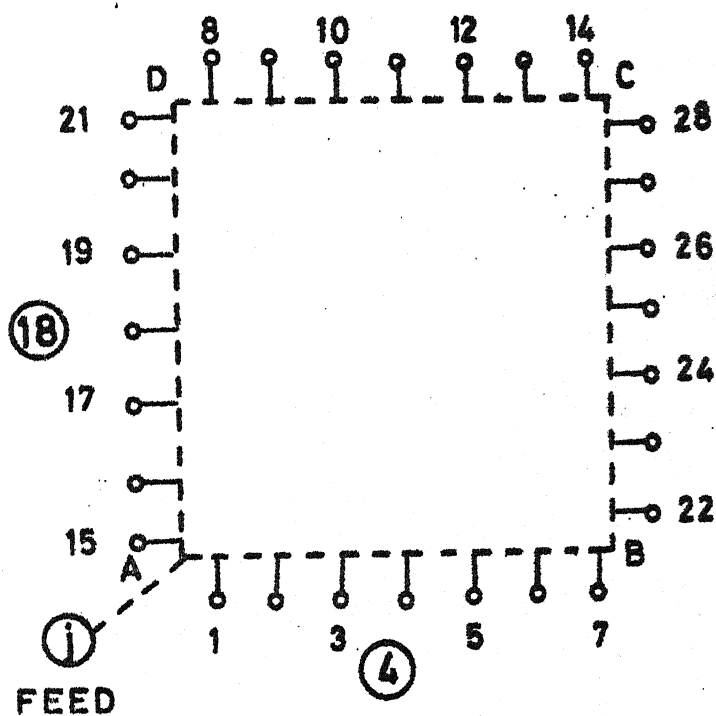
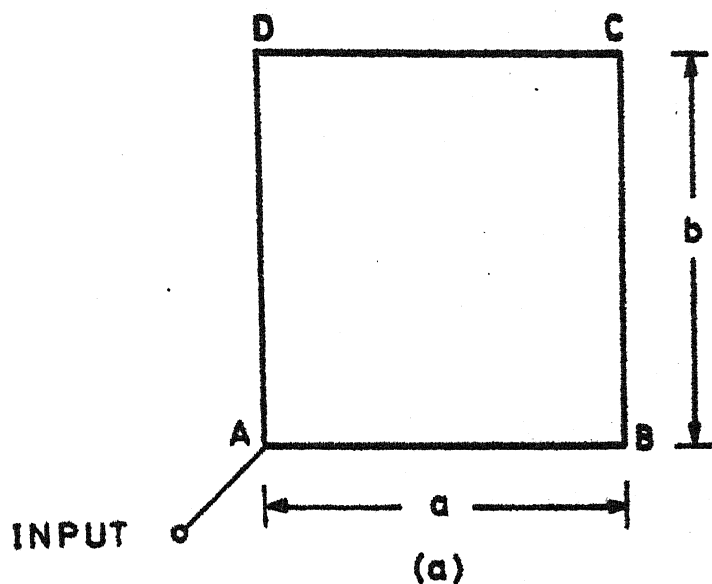


FIG. 4.1(a) A CORNER FED NEARLY SQUARE CP MICROSTRIP PATCH ANTENNA (b) THE CAVITY MODEL CONSIDERED AS MULTI-PORT CIRCUIT

cavity model with multiple ports along the magnetic wall boundary as shown in Fig. 4.1(b). The entire boundary is divided into several sections and each section is considered as a port. The widths of these ports are considered small enough so that the variations of field over each of these port widths are negligibly small. The voltage at each port is the average value of the voltage over the portwidth. The port number 1 (or 15) can be considered to be located at the corner A and therefore can be considered as the input port. Alternatively an additional port can be located at  $(x/a, y/b) = (0.0, 0.0)$  and considered to be the input port. When the width of the port 1 (or 15) is small enough the results of analysis are in exact agreement with those obtained when an additional port at the corner represents the input port.

The impedance Green's function for rectangle [1] is used to evaluate the Z-matrix of the multiport cavity model shown in Fig. 4.1(b). To take into account the loading effect of the radiated power, all the ports along the periphery are considered to be terminated in radiation resistances [50] as discussed earlier in Section 2.1.1. The Z-matrix of the multiport cavity with radiation resistances taken into account is evaluated using the segmentation method discussed in Section 2.2.2. For a unit current input at the  $i$ th port, the  $i$ th column of the Z-matrix yields the voltages at various ports along the periphery of the antenna.

The electric vector potential is evaluated using (2.4) and the far-field is calculated from (2.5). The axial ratio is calculated from the polarization ellipse of the E-component of the far-field.

The axial ratio is calculated as a function of frequency, for various values of the ratio of length to width of the rectangle. The results obtained for a S-band antenna, on a  $1/8''$  thick polystyrene substrate with  $\epsilon_r = 2.52$ , are shown in Fig. 4.2. In this case the periphery was divided into 28 ports. For optimizing axial ratio, the length of one of the sides 'a' is kept constant whereas that of the other side is varied. It has been found that (for  $\epsilon_r = 2.52$ , and substrate thickness =  $1/8''$ ) for  $a = 2.66$  cm, the best circular polarization (CP) is observed at a frequency 3.101 GHz for  $b/a = 1.05263$ . The corresponding axial ratio is found to be 0.45 dB. If CP at any other frequency is desired, the length of the side 'a' can be varied and the  $b/a$  ratio can be optimized. The curves in Fig. 4.3 show the variation of axial ratio as a function of physical and effective length to width ratios for the rectangle. It is observed that the axial ratio is quite sensitive to variations in  $b/a$  ratio and for achieving the best axial ratio one needs to fix the  $b/a$  ratio very accurately.

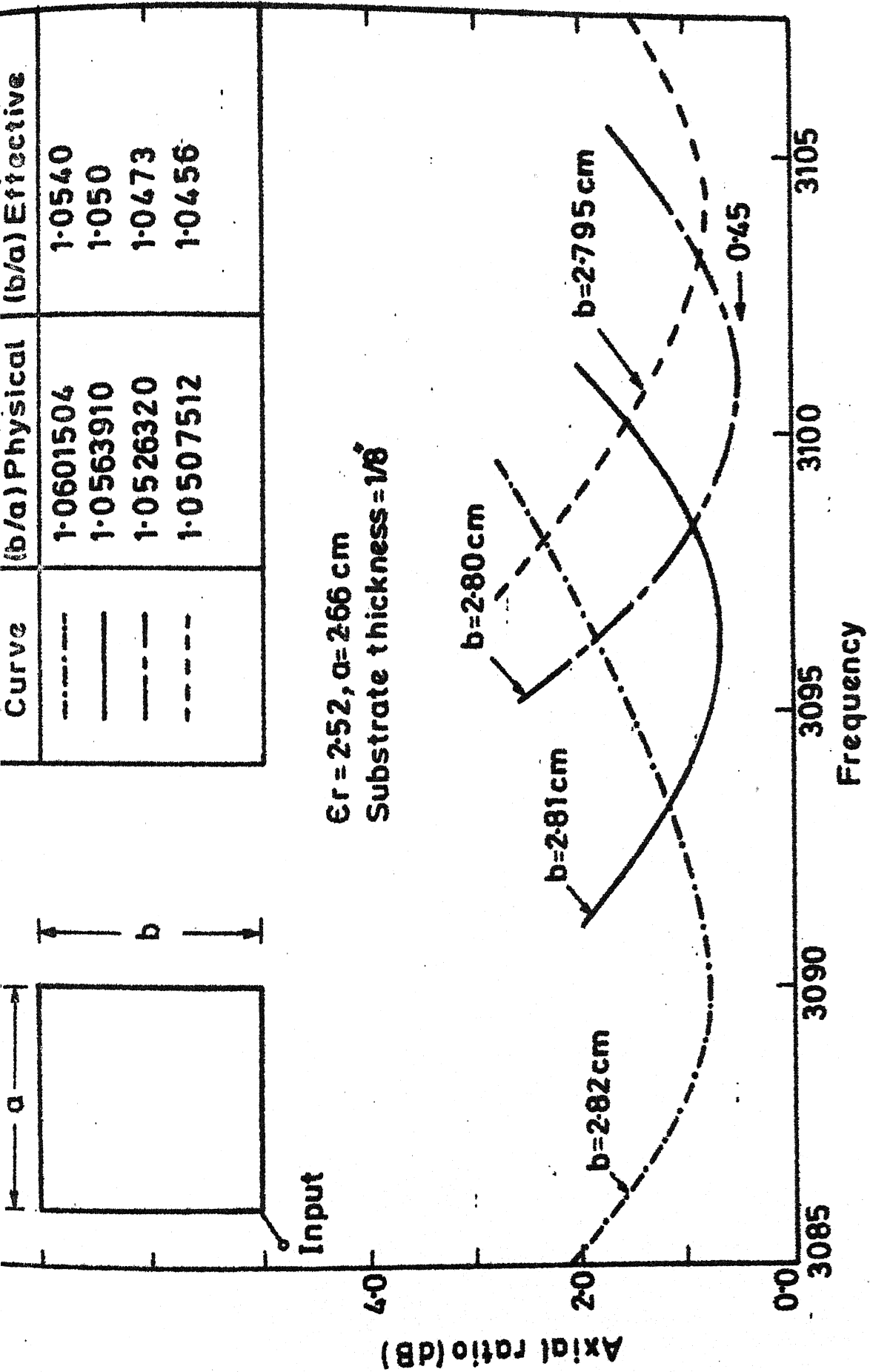


FIG. 4.2 VARIATION OF AXIAL RATIO WITH FREQUENCY FOR DIFFERENT VALUES OF THE RATIO (b/a)

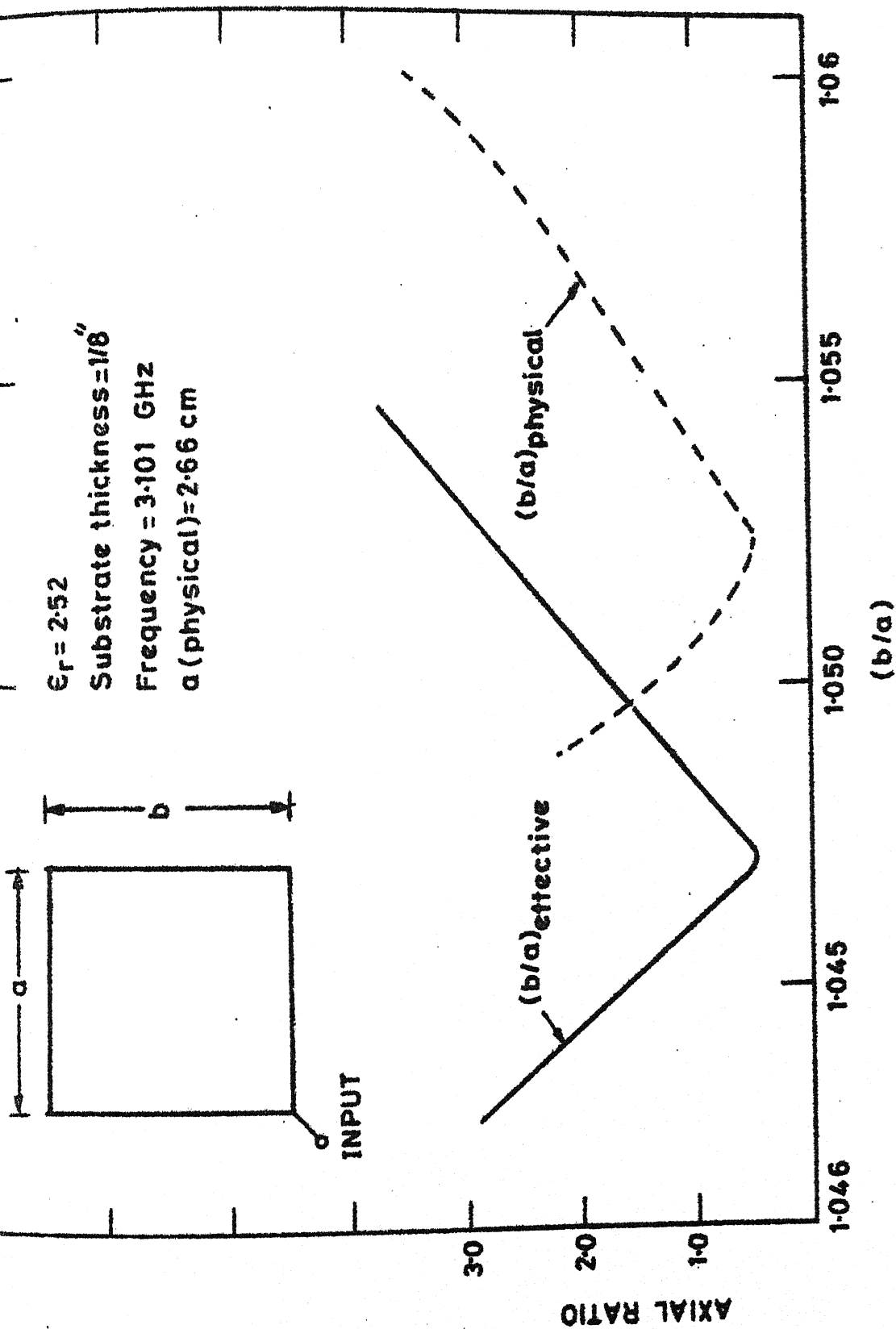


FIG.4.3 VARIATION OF AXIAL RATIO WITH  $b/a$  RATIO AT 3101 MHz

#### 4.1.2 Voltage and magnetic current distribution

The voltage distribution along the periphery of the antenna, for the best axial ratio (0.45 dB) and input port located right at the corner 'A' of the antenna, is shown in Fig. 4.4. The existence of circular polarization is indicated by the presence of two components of the voltage in phase-quadrature. The magnetic current moments along the four edges and the resultant moment vectors are shown in Fig. 4.5. It may be recalled here that  $\bar{K}'$  in (2.1) is the magnetic current density in volts/meter and  $\bar{K}$  in (2.2) is the integration of  $\bar{K}'$  over the thickness of the substrate and is therefore in volts. Hence,  $\bar{K}$  can be termed as linear magnetic current density. The value  $\bar{K}$  obtained from (2.2) is the value of the linear magnetic current density at one of the ports. Since voltage  $V$  is the average value over the width of the port,  $\bar{K}$  is also the average value. The term magnetic current moment (or current moment) as used in this thesis is the integration of the linear magnetic current density with distance along the periphery of the antenna. For example, when the voltage (and therefore the linear magnetic current density  $\bar{K}_i$ ) over the width of the  $i$ th port is considered to be constant, the product of  $\bar{K}_i$  and the width of the  $i$ th port gives the value of magnetic current moment over the width of the  $i$ th port.

Substrate thickness =  $1/8''$   
 $\epsilon_r = 2.52$ ,  $a = 2.66$  cm  
 $(b/a) = 1.052632$ ,  $f = 3101$  MHz  
 $(b/a)_{\text{effective}} = 1.043$

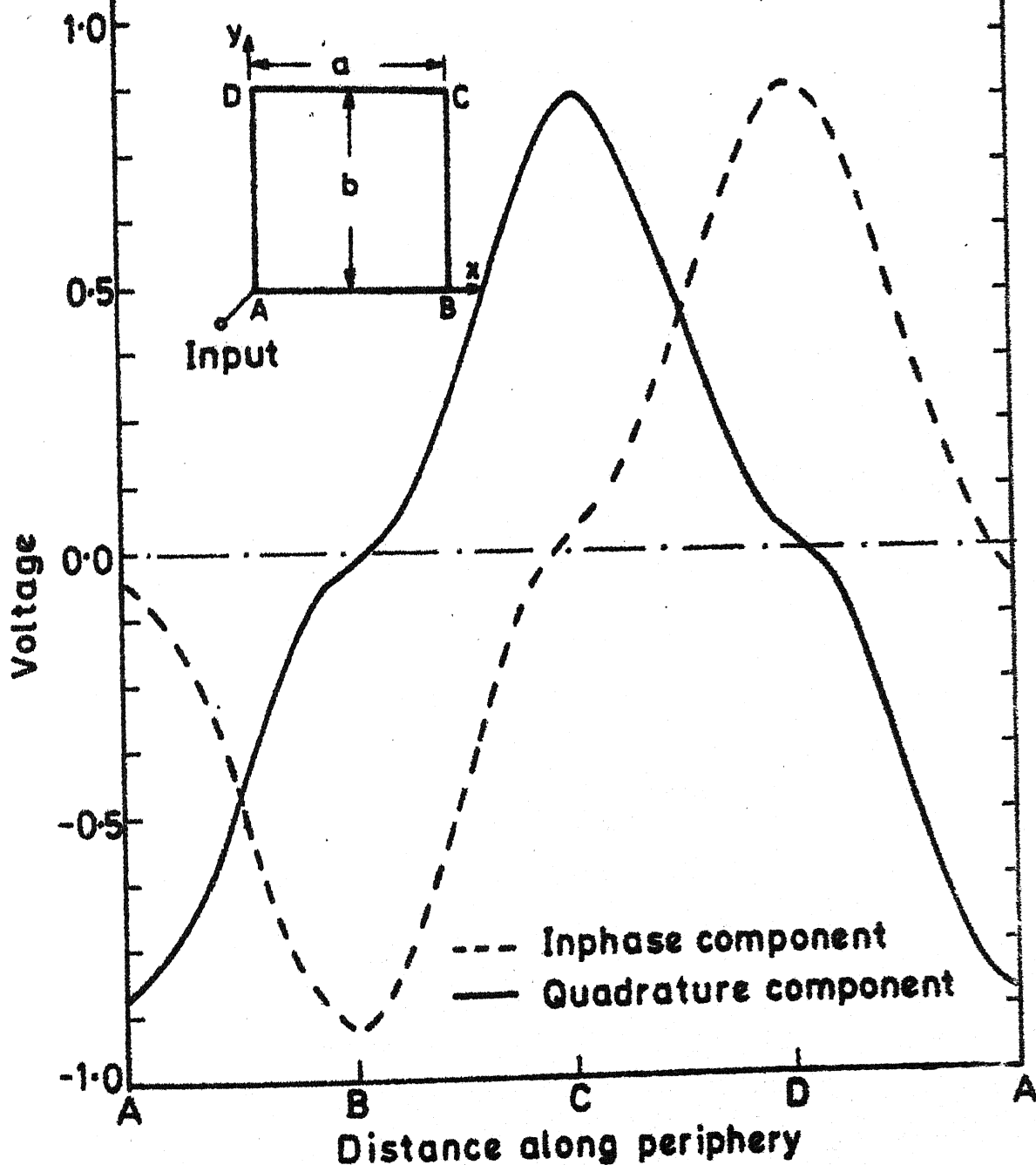
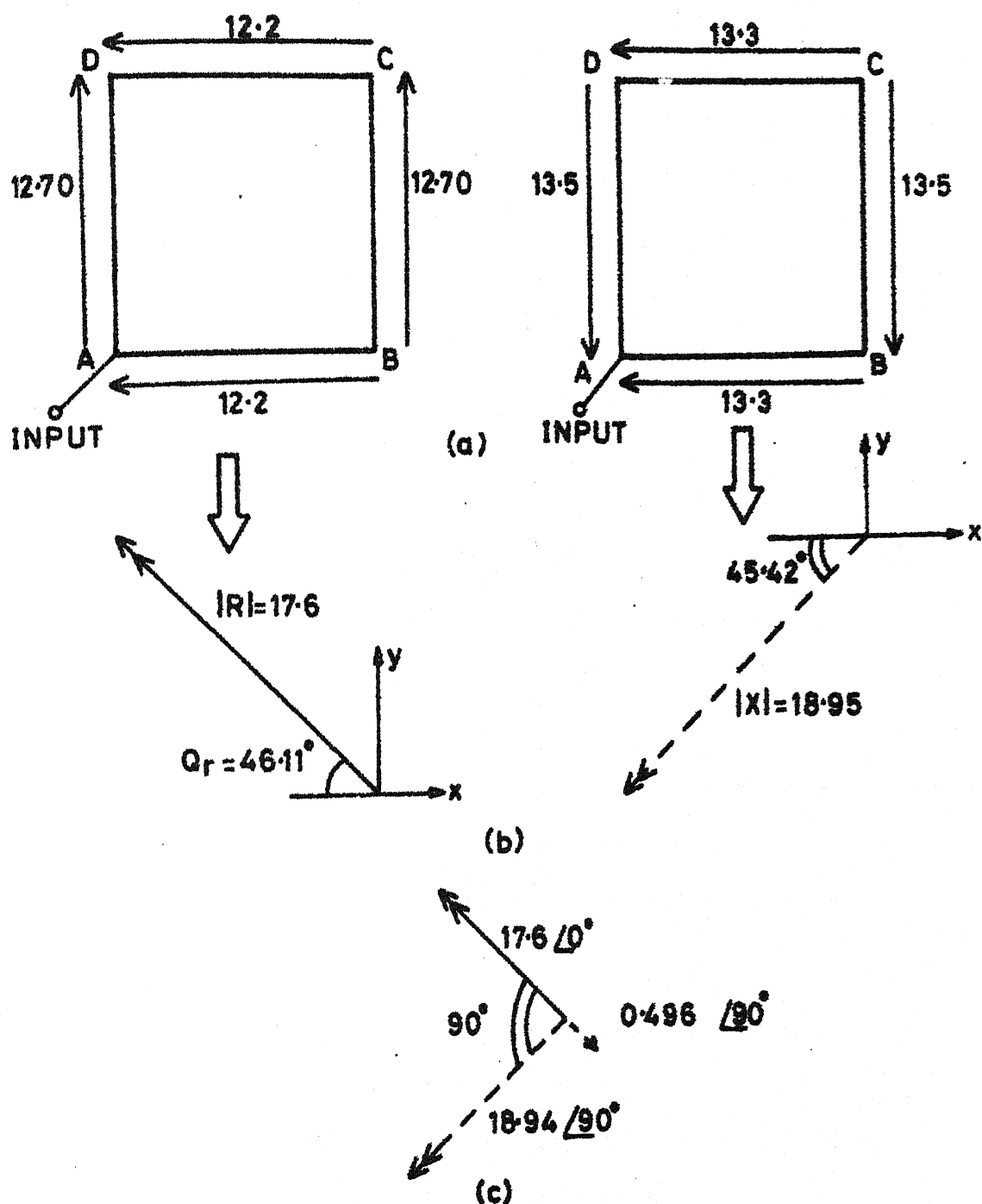


FIG. 4.4 VOLTAGE DISTRIBUTION ALONG PERIPHERY FOR INPUT AT  $(x/a, y/b) = (0, 0)$





**FIG. 4.5 MAGNETIC CURRENT MOMENT DISTRIBUTION AND ORIENTATION OF RESULTANT MOMENT VECTORS FOR THE VOLTAGE DISTRIBUTION SHOWN IN FIG. 4.4**

The resultant components of the magnetic current moments are evaluated by vector addition of the components along the four edges. These resultant components are oriented at  $91.53^\circ$  angle with respect to each other and are in phase-quadrature. This explains the existence of circular polarization, the value of axial ratio being determined by the relative amplitudes of the two vectors and the space angle between the two vectors. The components (in phase-quadrature) of the resultant magnetic current moments can be resolved along two orthogonal axes as shown in Fig. 4.5(c). The axial ratio for the polarization ellipse of the magnetic current moment calculated from Fig. 4.5(c) is found to be  $\approx 0.4$  dB. This value of axial ratio corresponds to the axial ratio ( $= 0.45$  dB) for the far-field (in broad-side direction) as expected from the discussion in Section 2.1.4. The difference of 0.05 dB is expected to be because of the reason that the magnitudes of the line currents in Fig. 4.5 have been obtained graphically from Fig. 4.4.

It may be noted that the physical lengths of the sides of the rectangle are  $0.4672\lambda_d$  and  $0.48\lambda_d$ , respectively, where  $\lambda_d = \lambda_0/\sqrt{\epsilon_r}$  and  $\lambda_0$  is the free-space wavelength at the frequency (3.101 GHz) where the best axial ratio is obtained. The corresponding effective lengths of the sides of the rectangle are  $0.494\lambda_d$  and  $0.50606\lambda_d$ . Thus one of the effective lengths ( $0.494\lambda_d$  is less than  $0.5\lambda_d$ ) is less

than half wavelength where as the other value is slightly greater than half wavelength. This could be expected from the discussions in Section 1.2.3 on the mechanism of operation of single feed circularly polarized patch antennas.

It has been pointed out by Lo [39] that for circular polarization, the ratio  $b/a$  should be equal to  $(1+1/Q)$ . In the present case the value of  $(1+1/Q)$ , calculated as explained in Appendix A, is found to be 1.0654 which is slightly greater than the values (1.05263 and 1.04727) of the ratio of physical lengths ( $b/a$ ) and of effective lengths ( $b_e/a_e$ ), respectively. The ratio ( $b/a$ ), and therefore ratio  $b_e/a_e$ , has been found to depend upon the  $\epsilon_r$  and the thickness of substrate. Various parameters and a summary of the results for the antennas investigated are included in Tables 4.1 and 4.2 on pages 169 and 170 respectively.

## 4.2 ORTHOGONAL MODES

### 4.2.1 Orthogonal modes and their resonance frequencies

The discussion in the preceeding section explains why corner feeding of the antenna results in circular polarization. There are two voltage components in phase-quadrature (Fig.4.4), for which the resultant magnetic current moment vectors are in phase-quadrature and very nearly in space-quadrature (Fig. 4.5). This results from the existence of two orthogonal modes. These orthogonal modes can be excited by feeding the antenna at mid-points of the sides AB and AC, that is at the

port number 4 and at the port number 18 shown in Fig. 4.1. The distributions of voltage and magnetic current moments along the edges of the antenna for input at port 4 and 18 are shown in Fig. 4.6 to Fig. 4.9.

The orientations of magnetic current moments in Fig. 4.7 and in Fig. 4.9 show that the antenna, when fed at port 4 or port 18, is linearly polarized. The polarization of the antenna at resonance frequencies of these two orthogonal modes has been verified experimentally. Fig. 4.10 illustrates the variation of amplitudes of the two orthogonal components of the far-field with frequency. It may be noted from Fig. 4.10 that at the resonance frequency of the mode when the larger dimension of the rectangle is resonant, amplitude of  $E_\phi$  is measured to be 20 dB below the amplitude of  $E_\theta$ . At the resonance frequency of the other mode, we have  $|E_\theta|$  20 dB below  $|E_\phi|$ . The calculated values of  $|E_\theta|$  and  $|E_\phi|$  as functions of frequency are also plotted in Fig. 4.10. The measured values of resonance frequencies of the two orthogonal modes are 3.032 GHz and 3.169 GHz. The respective theoretical values are 3.035 GHz and 3.175 GHz. At resonance frequencies of the two orthogonal modes, even for feed location on the diagonal, only one mode is excited dominantly. The polarization is, therefore, linear and one of the far-field components becomes maximum. The curves in Fig. 4.10 have been obtained for feed location on one of the

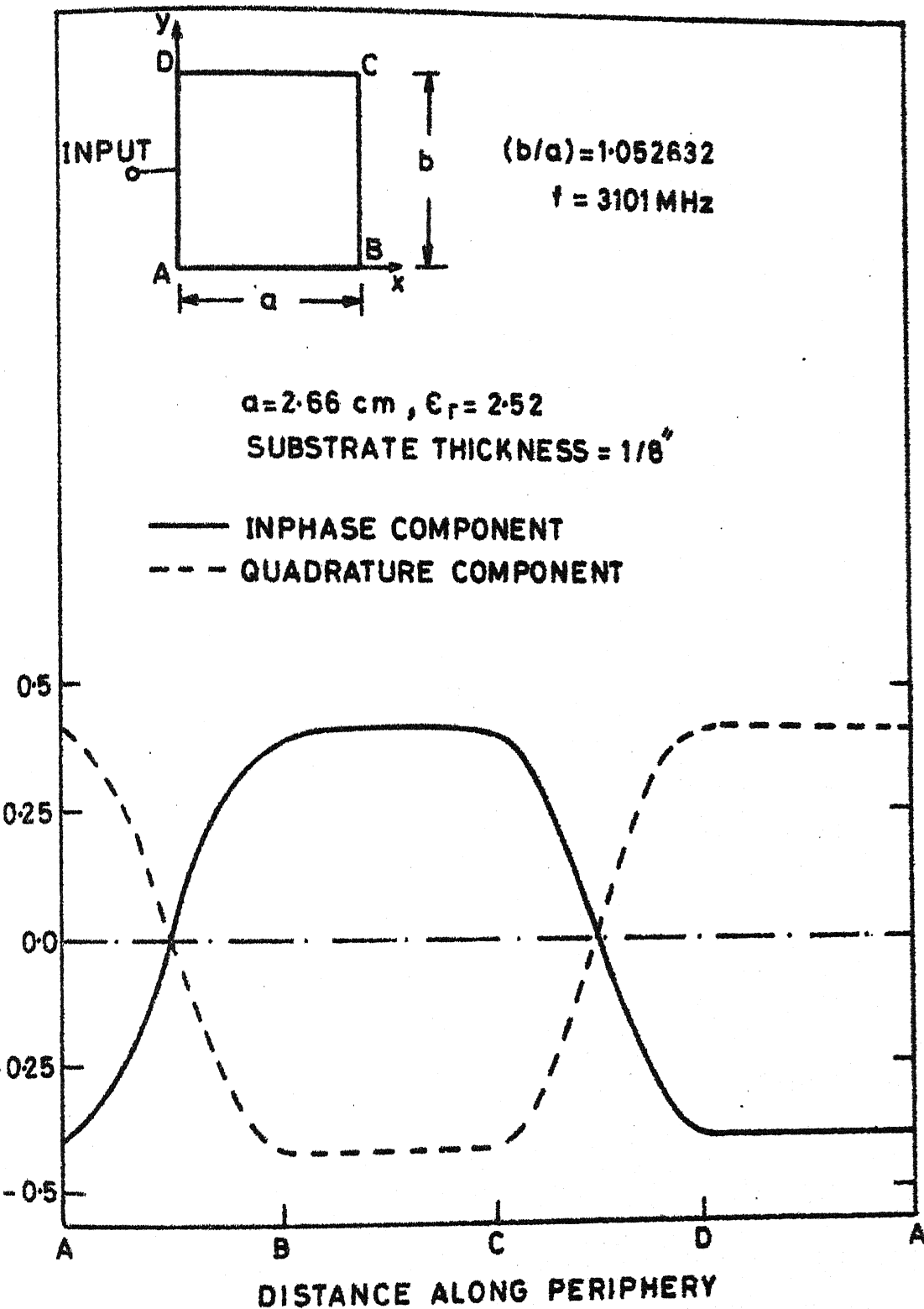


FIG. 4.6 VOLTAGE DISTRIBUTION ALONG PERIPHERY  
 FOR INPUT AT  $(x/a, y/b) = (0.0, 0.5)$

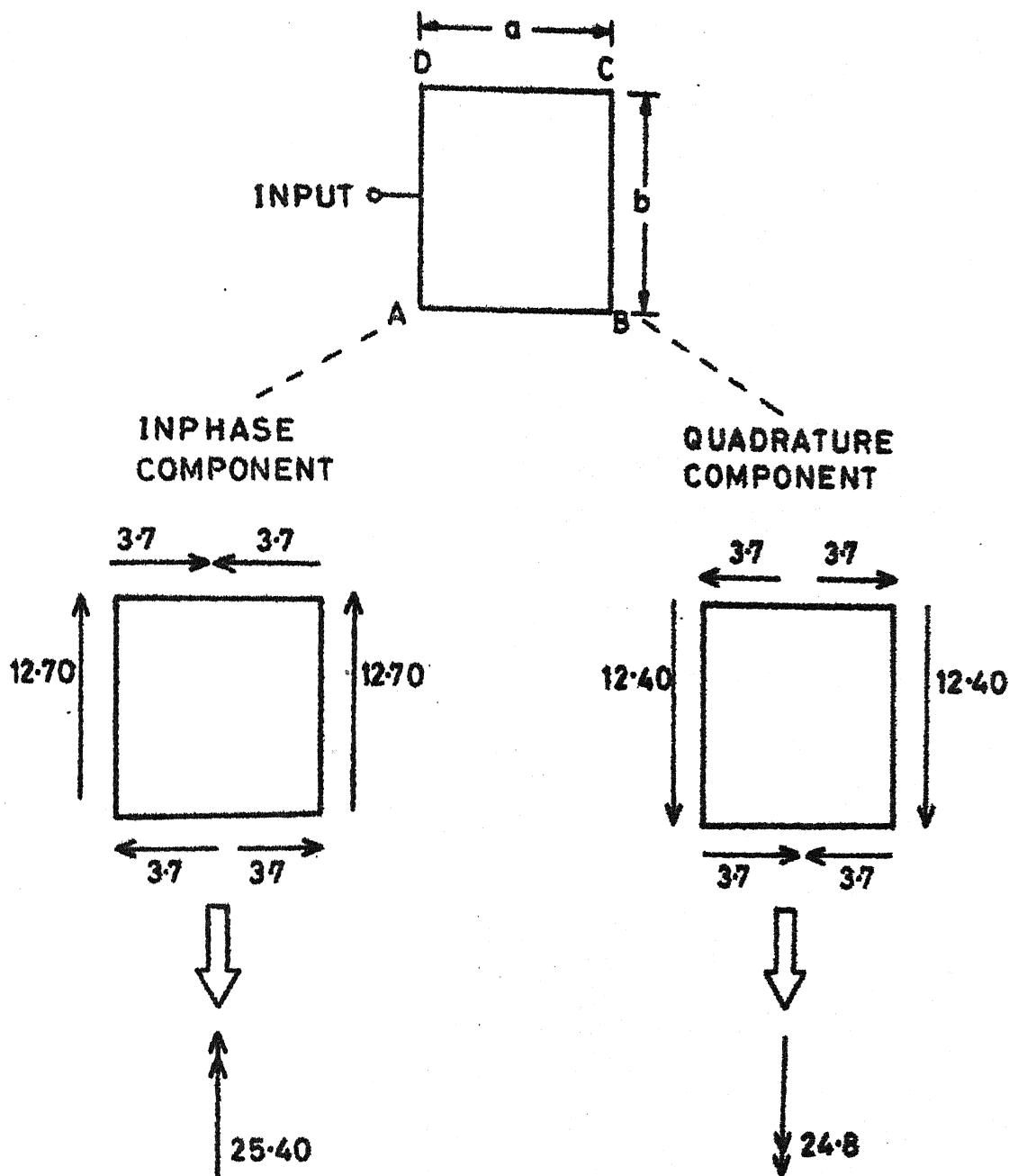


FIG. 4.7 DISTRIBUTION OF MAGNETIC CURRENT MOMENTS AND ORIENTATION OF RESULTANT MOMENT VECTORS FOR VOLTAGE DISTRIBUTION OF FIG. 4.6

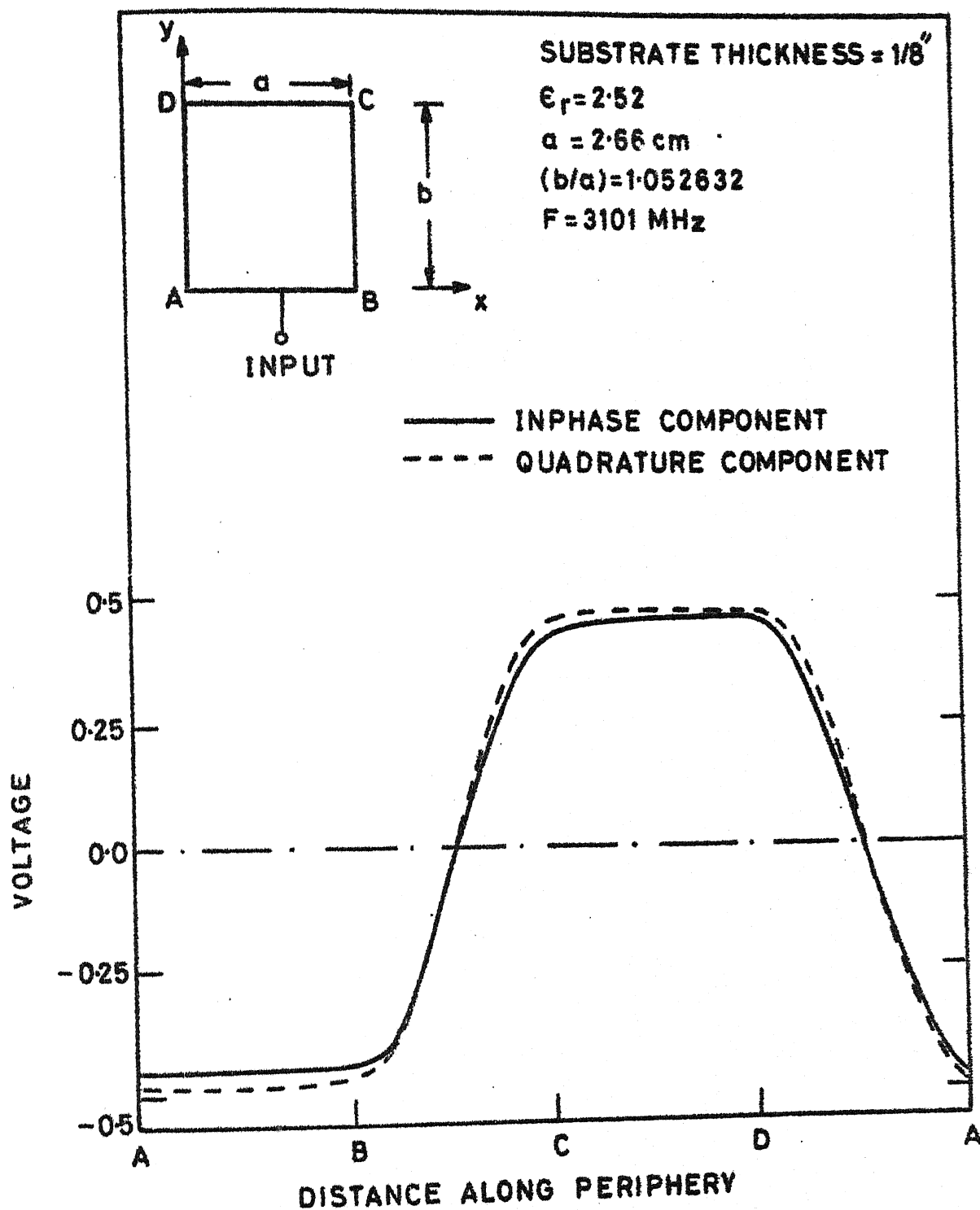
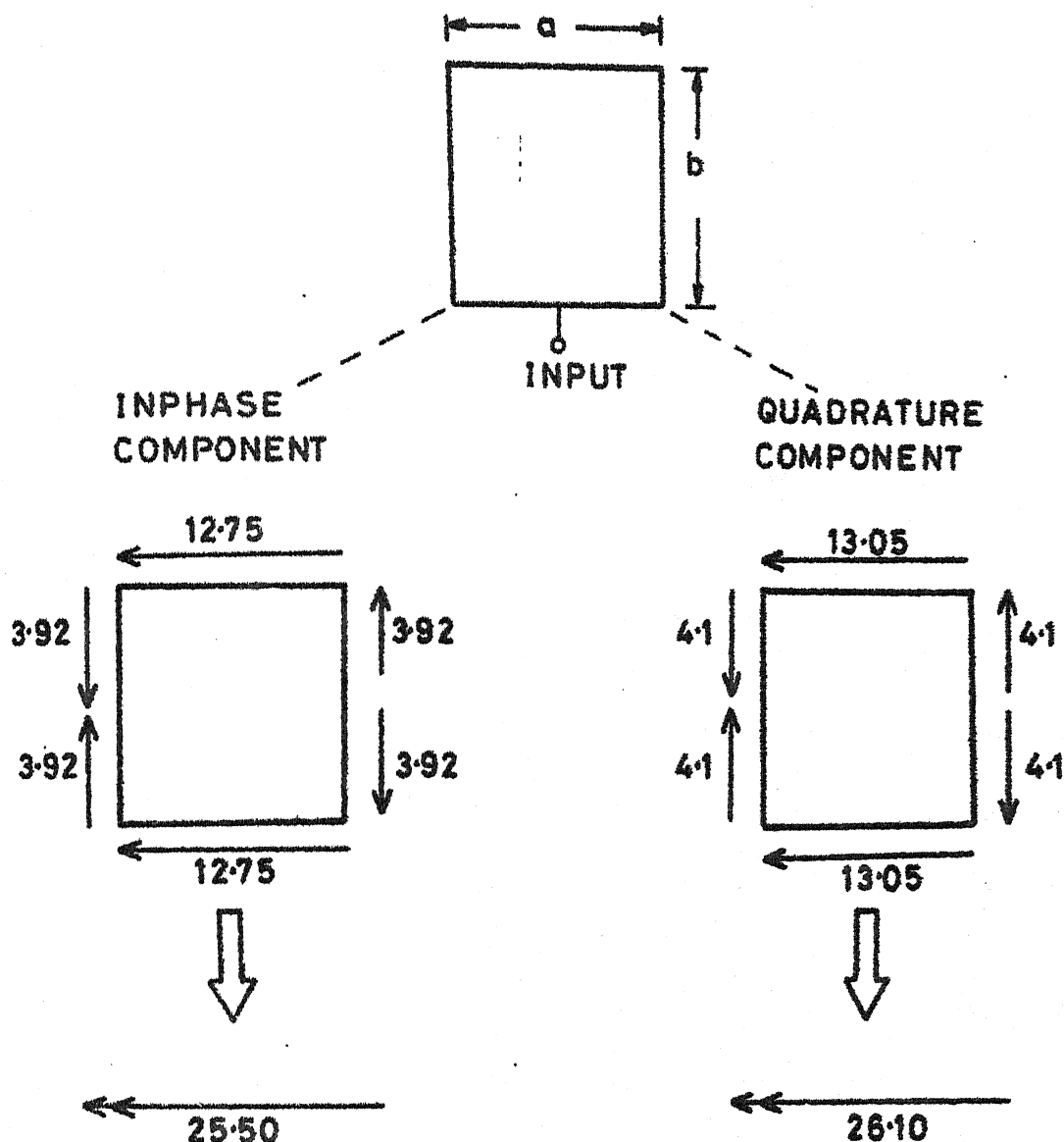
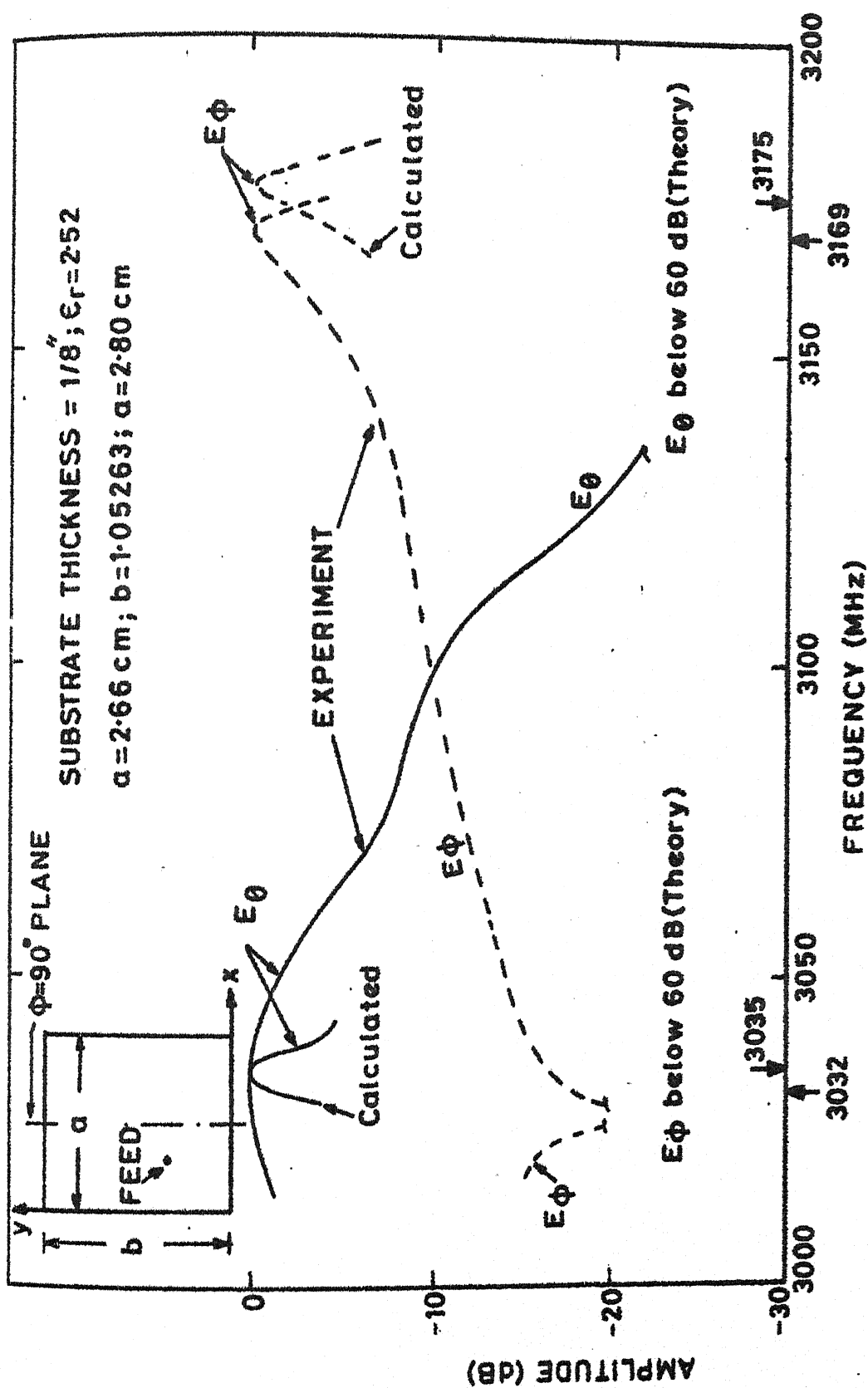


FIG. 4-8 VOLTAGE ALONG PERIPHERY OF THE ANTENNA FOR INPUT AT  $(x/a, y/b) = (0.5, 0.0)$



**FIG. 4.9 MAGNETIC CURRENT MOMENT DISTRIBUTION AND ORIENTATION OF RESULTANT MOMENT VECTORS EQUIVALENT TO VOLTAGE DISTRIBUTION OF FIG. 4.8**





**FIG. 4-10 VARIATION OF AMPLITUDES OF FAR-FIELD COMPONENTS  
(In  $\phi = 90^\circ$  plane) WITH FREQUENCY FOR A DIAGONAL FED  
ANTENNA**

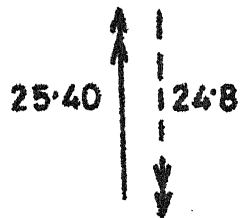
diagonals as shown in Fig. 4.10 (inset). Thus the antenna fabricated for studying circular polarization, can also be used for measuring resonance frequencies of two linearly polarized orthogonal modes. This property has also been employed in Chapters Five and Six for studying the corners chopped antennas and a square patch antenna with a diagonal slot.

#### 4.2.2 Superimposition of orthogonal modes

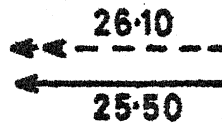
Consider the vector sum of the components of the magnetic current moments for the two orthogonal modes (of Figs. 4.7 and 4.9) as illustrated in Fig. 4.11. The sum of the magnetic current moments for these two modes, as in Fig. 4.11, correspond to the magnetic current moment which results if the antenna is excited at one of the corners of the rectangle (Fig. 4.5). The two resultant magnetic current moment vectors in Fig. 4.11 are in phase-quadrature and are oriented at  $88.44^\circ$  with respect to each other. Corner feeding of the antenna thus excites two orthogonal modes in phase-quadrature which results into circular polarization of the antenna.

It may be noted that if the feed is located at corner 'D' (Fig. 4.4) instead of being at corner 'A', reversal of the relative phase difference between  $E_\theta$  and  $E_\phi$  (the far-field components) takes place. Thus, the sense of polarization is reversed when the feed port is shifted from corner 'A' to corner 'D'.

—— INPHASE COMPONENT  
 ---- QUADRATURE COMPONENT



FROM FIG. 4.7



FROM FIG. 4.9

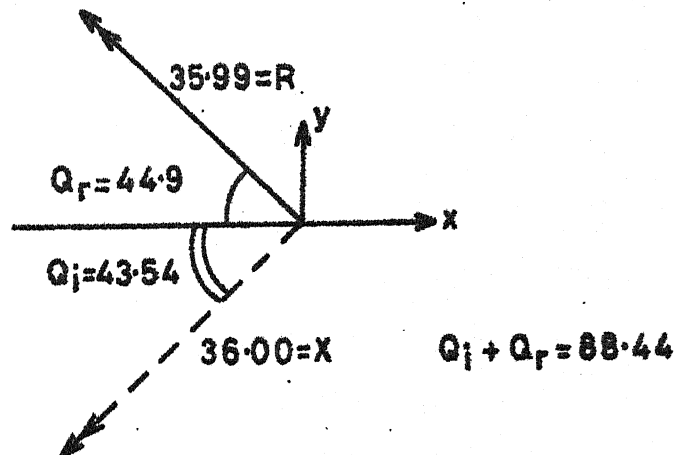


FIG. 4.11 VECTOR SUM OF MAGNETIC CURRENT MOMENTS OF FIG. 4.7 AND FIG. 4.9. THE TWO RESULTANT VECTORS ARE NEARLY PERPENDICULAR TO EACH OTHER

Since the location of a corner feed is symmetrical with respect to the mid-points of the two sides which meet at that corner (i.e. the location of corner A with respect to the mid-points of sides AB and AD in Fig. 4.1), it is expected that the polarization characteristics should remain unchanged if the feed is located on the diagonal. The variations of axial ratio and input VSWR with feed location (coaxial feed) along one of the diagonals is discussed in the next section.

#### 4.3 INPUT VSWR AND FEED LOCATION

The variation of axial ratio and input VSWR (at 3.101 GHz where the axial ratio of 0.45 dB occurs for corner feeding) with feed location on one of the diagonals of the patch is illustrated in Fig. 4.12. The axial ratio degrades from 0.45 dB to 0.79 dB and improves again as the feed is moved along the diagonal AC. The input VSWR decreases from 8.1 to 1.73 as the feed is moved from corner 'A' to a point '0.36 AC' on the diagonal AC. For feed location at a distance  $r$  greater than '0.36 AC' the input VSWR starts increasing again. The distance of the optimum location of the feed (for the minimum input VSWR = 1.73) in terms of electrical length is  $0.2575\lambda_d$ . Thus for optimum feed port location ('0.36 AC' from the corner 'A' as in Fig. 4.12) the axial ratio of 0.77 dB is obtained as against the 0.45 dB when the antenna is fed at corner 'A'.

SUBSTRATE THICKNESS =  $1/8"$

$\epsilon_r = 2.52$

$a = 2.66 \text{ cm}, b = 1.052632, a = 2.80 \text{ cm}$

FREQUENCY = 3.101 GHz

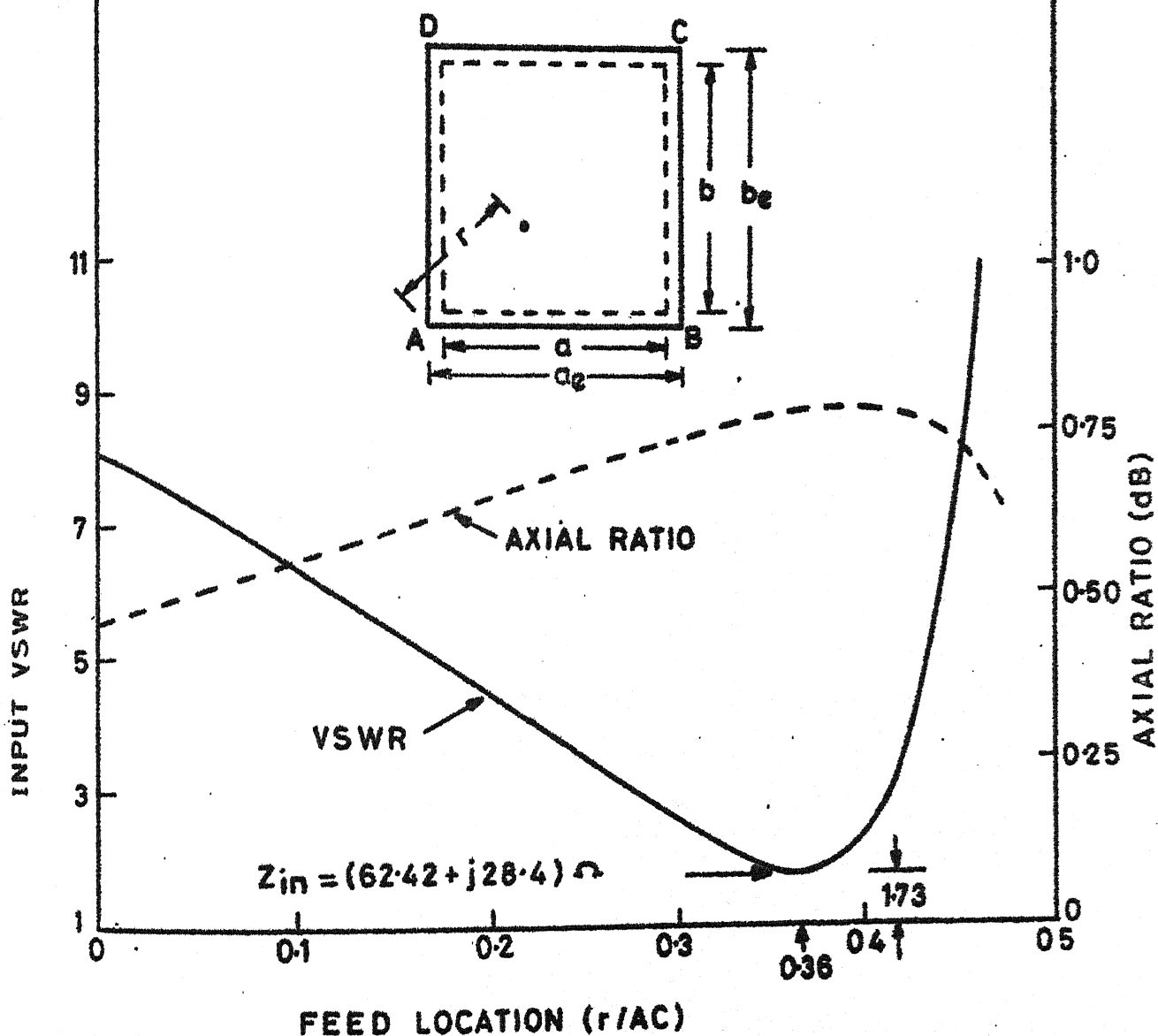


FIG. 4.12 VARIATION OF INPUT VSWR AND AXIAL RATIO WITH FEED LOCATION ALONG THE DIAGONAL A

It has been found that the axial ratio equal to 0.45 dB with feed location on the diagonal (for best input VSWR) is obtained again if the frequency is shifted to 3.103 GHz which is 2 MHz higher than the 3.101 GHz at which the best value of axial ratio (0.45 dB) is obtained for feed location at corner 'A'. Thus the original low value of axial ratio can be obtained even when the feed is located on the diagonal. There is of course a small shift in frequency.

The measured and calculated values of input VSWR over a frequency band for which axial ratio  $< 6$  dB, for the antenna on  $1/8$ " thick substrate having  $\epsilon_r = 2.52$ , are plotted in Fig. 4.13. The VSWR is thus found to vary only by small amount over the frequency range within which the axial ratio remains less than 6 dB.

Input VSWR of the antenna described above is about 1.73. From calculation it is observed the  $Z_{in}$  ( $62.42 + j28.4$ ) is higher than the feed line impedance of 50 Ohms. Thus VSWR could be improved by decreasing  $Z_{in}$ . Since for the same effective dimensions of a microstrip circuit the impedance level (reactive component) reduces to half the original value if the thickness is reduced to half, another antenna on  $1/16$ " substrate (with  $\epsilon_r = 2.52$  as in the preceeding case) was designed. For this antenna, the variation of input VSWR with feed location is shown in Fig. 4.14. The optimum value of input VSWR is found to be 1.33 and occurs again for a feed

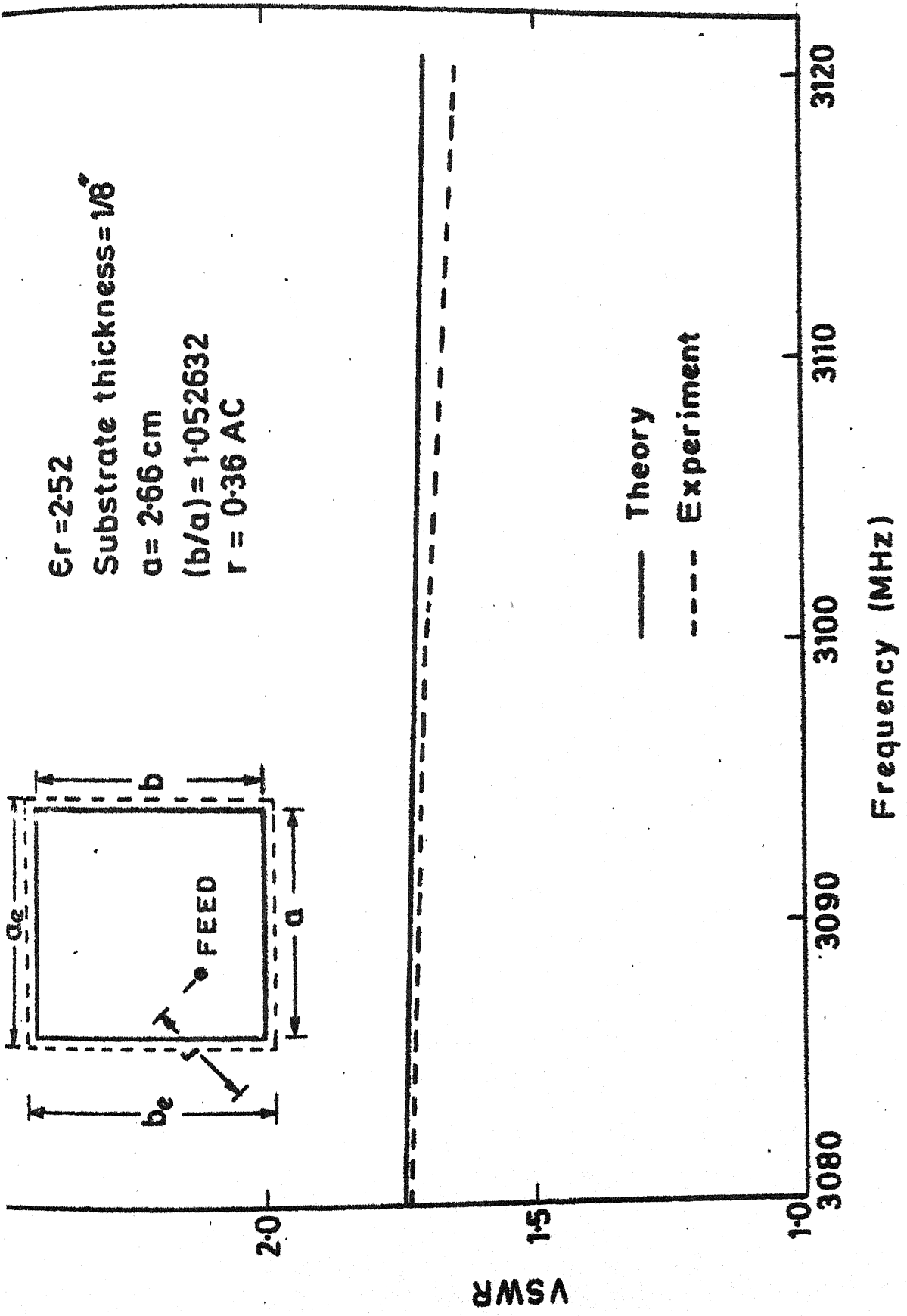


FIG.4.13 VARIATION OF INPUT VSWR WITH FREQUENCY

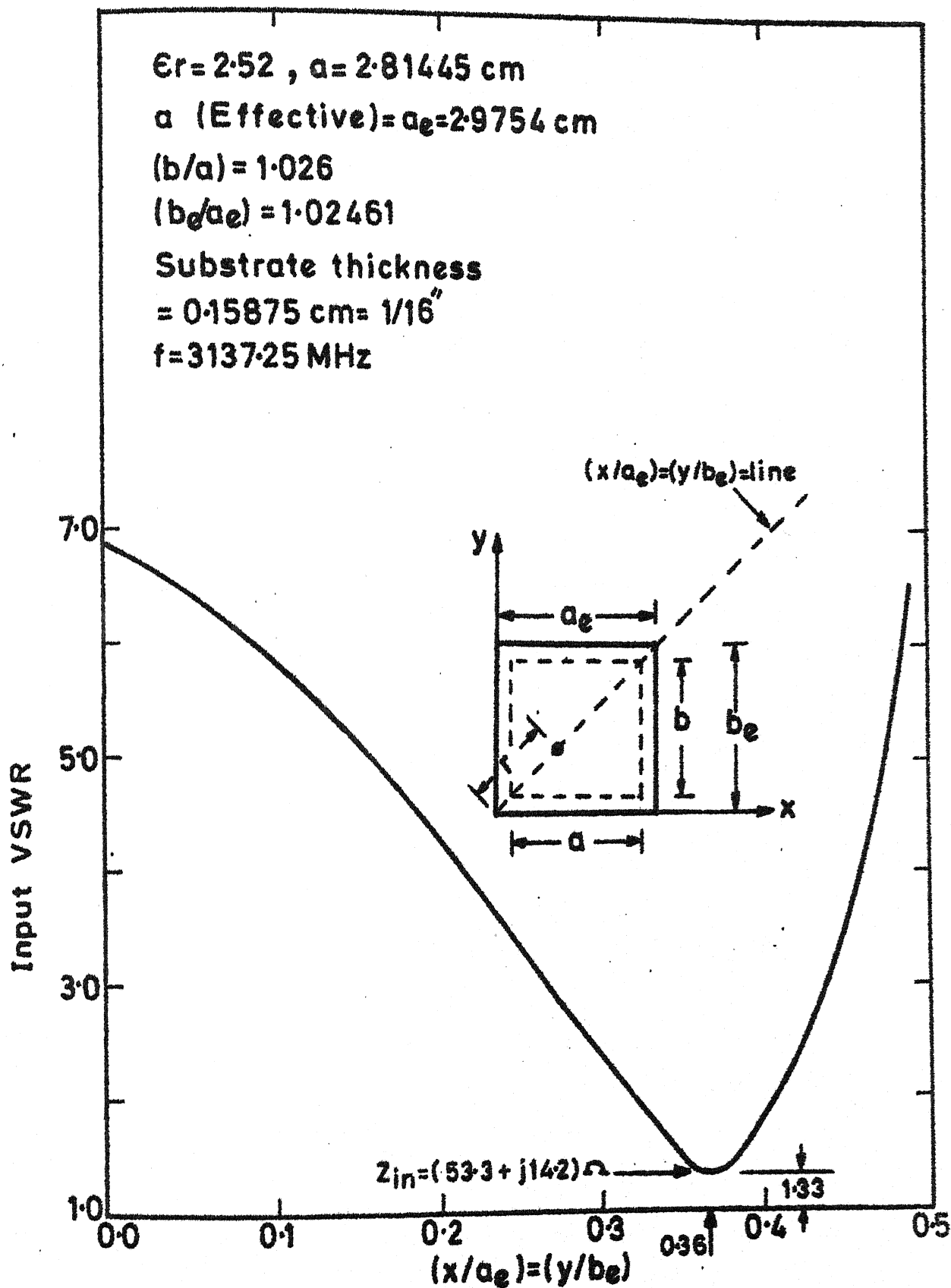


FIG. 4.14 VARIATION OF INPUT VSWR WITH INPUT PORT LOCATION ON THE DIAGONAL  $x/a_e = y/b_e$



location which is at a distance  $r$  equal to 0.36 times the effective diagonal length from one of the corners as shown in Fig. 4.14. The ratio of the lengths of sides ( $b/a$ ) for the best axial ratio (0.17 dB) is found to be 1.026 for  $a = 2.81445$  cm. The dimension ' $a$ ' is chosen such that the effective length ' $a_e$ ' is equal to the corresponding effective length for the antenna, with  $1/8$ " substrate, discussed in the preceding section. The best axial ratio is found to occur at 3.13725 GHz. As the dielectric constant for the substrate with thickness  $1/16$ " was slightly different ( $\epsilon_r = 2.49$ ), the design was optimized again for  $\epsilon_r = 2.49$  and thickness =  $1/16$ " to confirm the results experimentally.

For this design the dimension ' $a$ ' is 2.80 cm. The best circular polarization occurs when ' $b$ ' = 1.02964 $a$ . The value of the best axial ratio is 0.17 dB and occurs at 3.1658 GHz. The input VSWR at this frequency is found to be minimum ( $= 1.33$ ) when the feed is located at a point, on the diagonal, 0.36 times the effective diagonal length from one of the corners. The variation of input VSWR with feed location is illustrated in Fig. 4.15. The measured and calculated values of input VSWR over a band of frequencies, for which axial ratio remains less than 6 dB, is plotted in Fig. 4.16. In this case also the input VSWR variation over the entire frequency range of interest is small. The input impedance values at the center frequencies for the three antennas are :

$\epsilon_r = 2.49$ ,  $f = 3.165$  GHz

SUBSTRATE THICKNESS  $= 1/16$ "

$a = 2.80$  cm,  $a_{eff} = 2.9613815$  cm

$(b/a) = 1.0296429$  cm

$(b/a)_{effective} = 1.02805340$

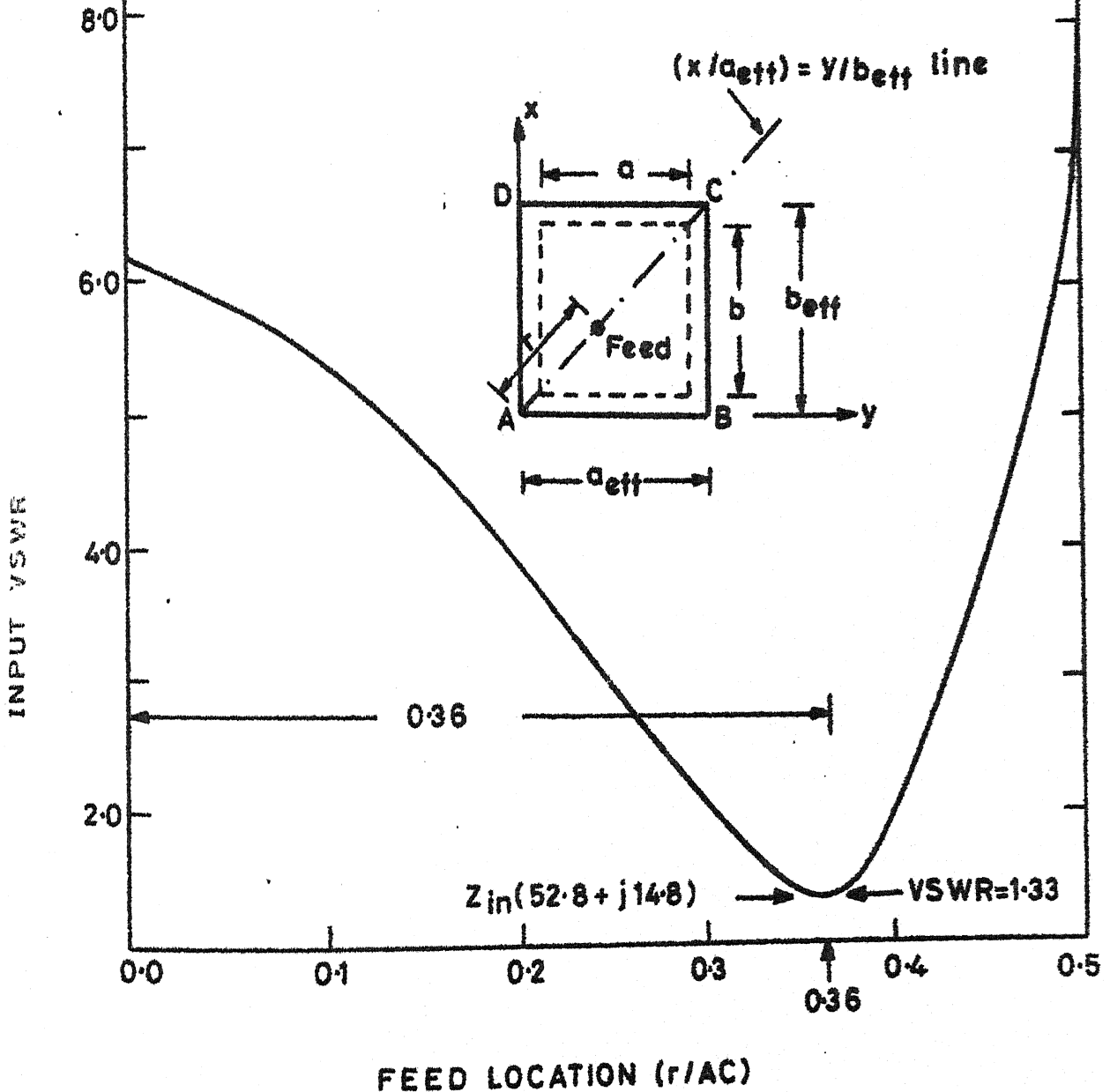
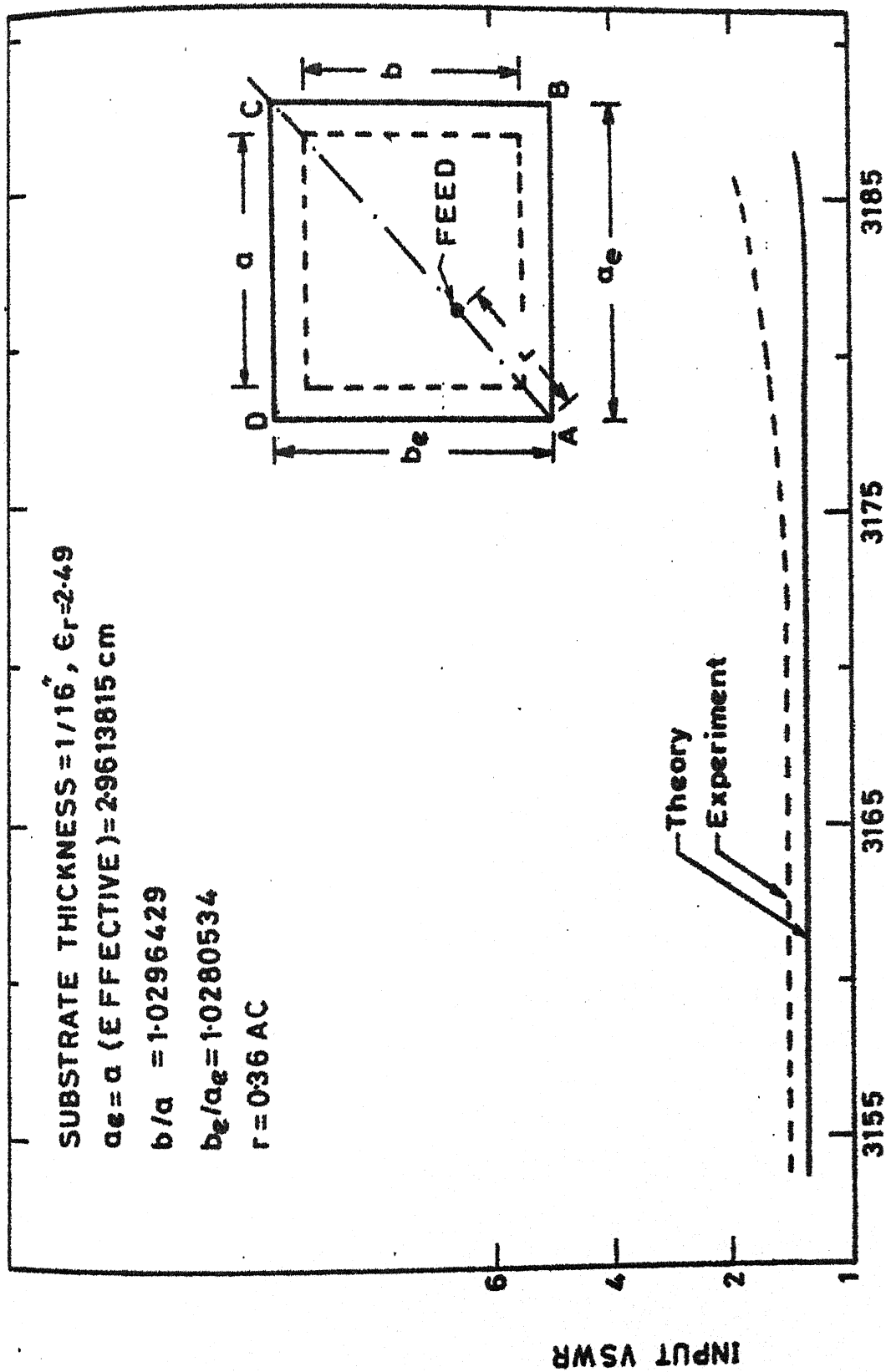


FIG. 4.15 VARIATION OF INPUT VSWR WITH FEED LOCATION ON THE DIAGONAL AC



SUBSTRATE THICKNESS =  $1/16"$ ,  $\epsilon_r = 2.49$   
 $a_e = a$  (EFFECTIVE) = 2.9613815 cm  
 $b/a = 1.0296429$   
 $b_e/a_e = 1.0280534$   
 $r = 0.36$  AC

FIG. 4-16 VARIATION OF INPUT VSWR WITH FREQUENCY FOR DIAGONAL FED ANTENNA

- i)  $(62.42 + j28.4) \Omega$  for substrate thickness =  $1/8"$ ,  $\epsilon_r = 2.52$ ;
- ii)  $(53.3 + j14.2) \Omega$  for substrate thickness =  $1/16"$ ,  $\epsilon_r = 2.52$ ,  
and
- iii)  $(52.8 + j14.8) \Omega$  for substrate thickness =  $1/16"$ ,  $\epsilon_r = 2.49$ .

Thus the reduction of substrate thickness to half reduces the reactive part of the input impedance to half which results into better input VSWR.

The input VSWR can be reduced further if a  $1/32"$  thick substrate is used. Extrapolating the results, we expect  $Z_{in}$  to be around  $(50 + j7)$  ohm and the VSWR is likely to be about 1.15. Although the input VSWR improves with the reduction in the thickness of the substrate, it has been observed that the axial ratio limited bandwidth decreases. However, there is a definite improvement observed in the value of the best axial ratio when the substrate height is reduced from  $1/8"$  to  $1/16"$ .

#### 4.4 BANDWIDTH AND BEAMWIDTH

The variations of axial ratio with frequency for the two antennas (fabricated on, (i) polystyrene substrate of thickness  $1/8"$  and dielectric constant  $\epsilon_r = 2.52$ ; and (ii) polystyrene substrate of thickness =  $1/16"$  with  $\epsilon_r = 2.49$ ) are shown in Fig. 4.17 and Fig. 4.18 respectively. The theoretical value of bandwidth (for axial ratio less than 6 dB) for the  $1/8"$

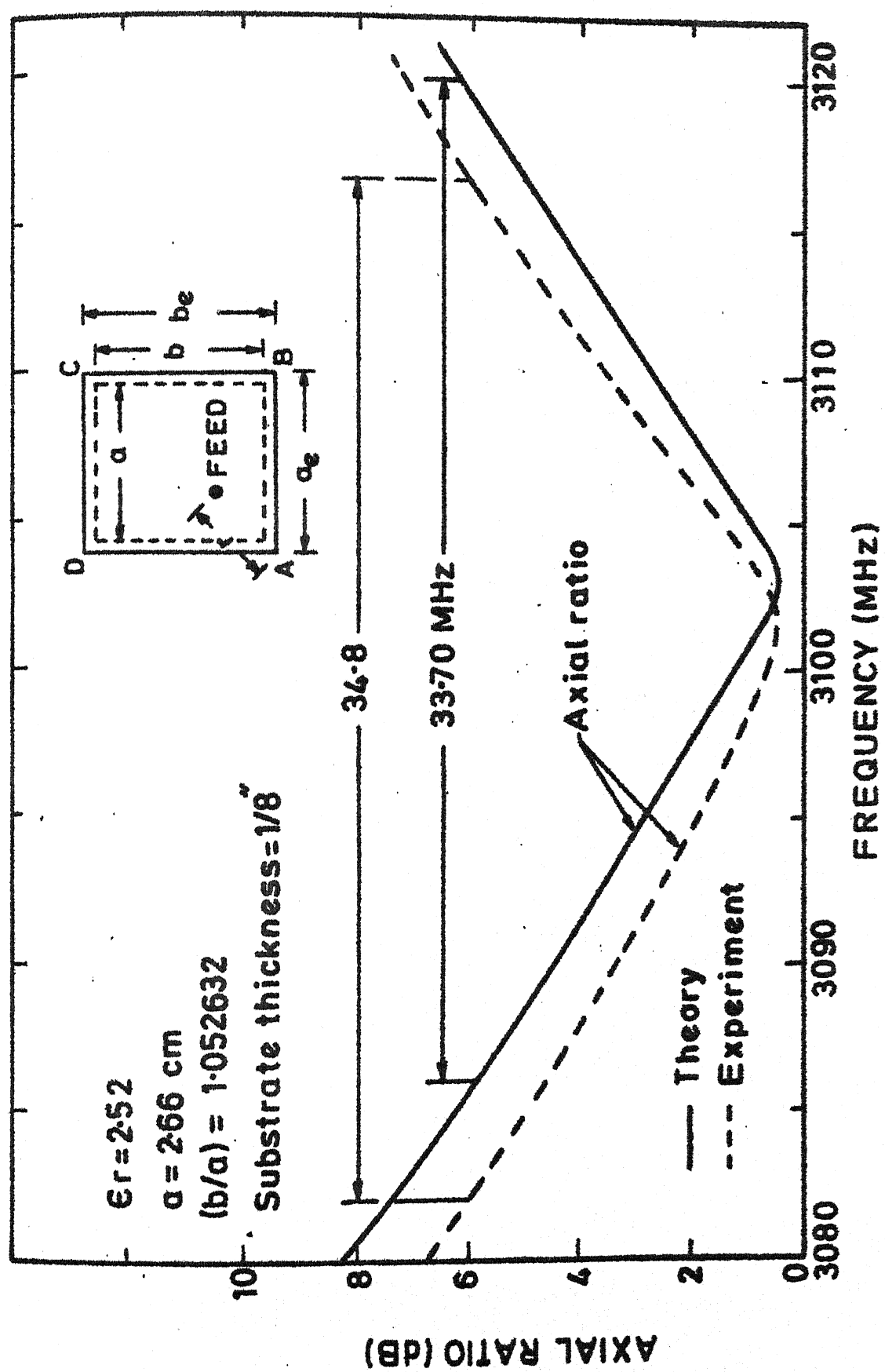


FIG.4.17 VARIATION OF AXIAL RATIO WITH FREQUENCY FOR INPUT PORT  
AT  $r = 0.36 \text{ AC}$

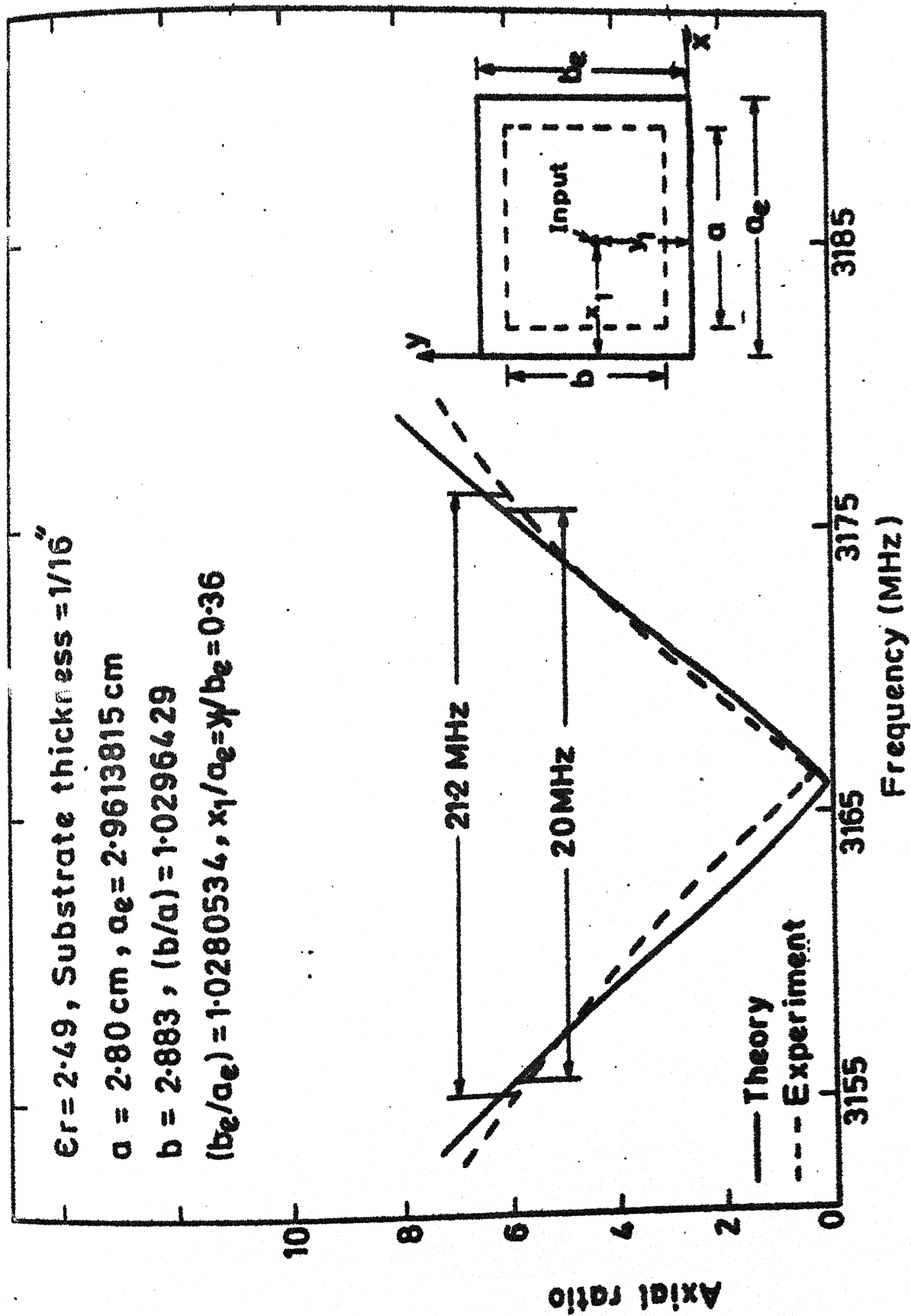


FIG. 4.18 VARIATION OF AXIAL RATIO WITH FREQUENCY FOR DIAGONAL

thick substrate ( $\epsilon_r = 2.52$ ) antenna is found to be 33.70 MHz which is 1.086 percent for the center frequency 3.103 GHz. The corresponding values of the bandwidths for antenna on 1/16" thick substrate ( $\epsilon_r = 2.49$ ) are 20 MHz and 0.632 percent (center frequency = 3.1658 GHz) respectively. The reduction in substrate thickness to half thus reduces the axial ratio bandwidth by about 41 percent.

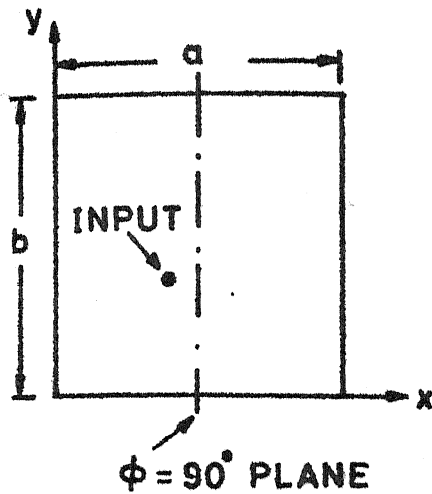
The radiation patterns, in  $\phi = 90^\circ$  plane, for the two antennas ( $\epsilon_r = 2.52$ , thickness of substrate = 1/8" ; and  $\epsilon_r = 2.49$ , thickness of substrate = 1/16" ) at frequencies where the axial ratio is the best obtainable are shown in Fig. 4.19 and Fig. 4.20 respectively. The difference between  $|E_\theta|$  and  $|E_\phi|$  remains within 3 dB for  $-55^\circ < \theta < +55^\circ$  and is within 6 dB for  $-68^\circ < \theta < +68^\circ$  for the antenna on 1/8" thick substrate with  $\epsilon_r = 2.52$ . The corresponding beamwidth for the 1/16" thick substrate antenna ( $\epsilon_r = 2.49$ ) for 3 dB difference between  $|E_\theta|$  and  $|E_\phi|$  is  $-58^\circ < \theta < 58^\circ$  and that for 6 dB difference between  $|E_\theta|$  and  $|E_\phi|$  is  $-69^\circ < \theta < 69^\circ$ . The experimental results on radiation pattern are discussed in the next section.

#### 4.5 EXPERIMENTAL RESULTS

Experiments have been carried out on 1/8" polystyrene substrate ( $\epsilon_r = 2.52$ )\* antenna and 1/16" polystyrene substrate ( $\epsilon_r = 2.49$ )\* antenna. The photographs of the two antennas are shown in Fig. 4.21(a) and (b). The experimental set-up is

---

\*Because of variation of  $\epsilon_r$  from sample to sample, values of  $\epsilon_r$  of the substrates were measured before designing the antennas. The measurement method used is described in Appendix B.



$f = 3.103 \text{ GHz}$

$\epsilon_r = 2.52$

SUBSTRATE THICKNESS  $= 0.3175 \text{ cm} = 1/8''$

$a = 2.66 \text{ cm}$

$b/a = 1.052632$

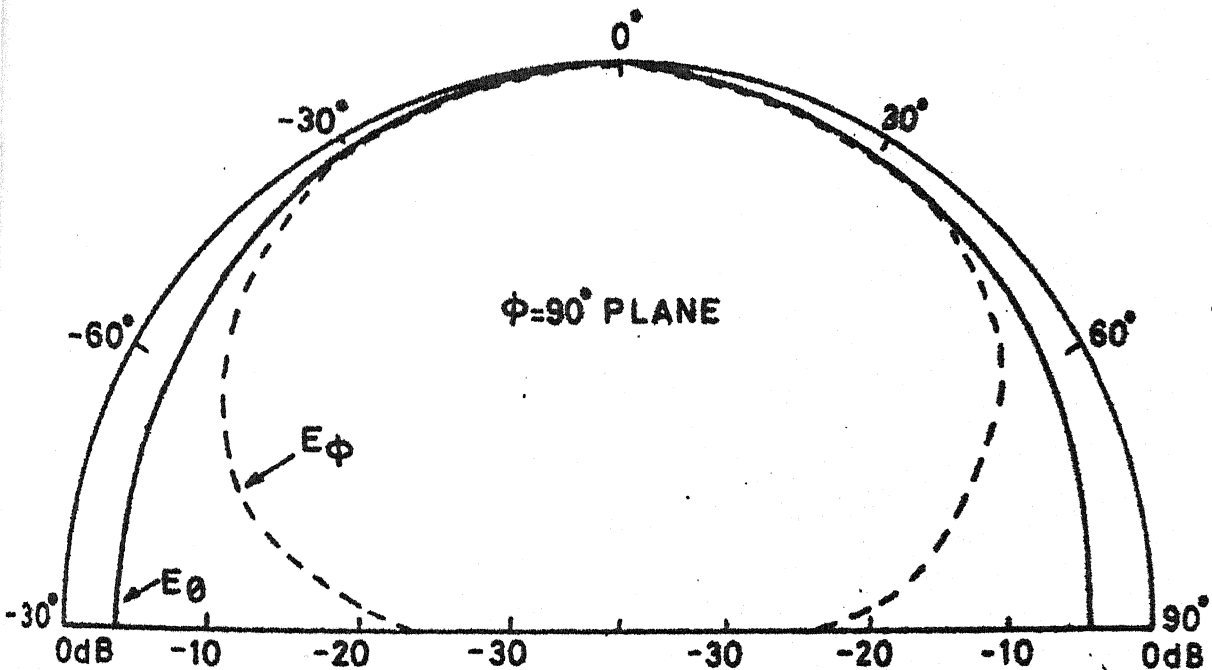
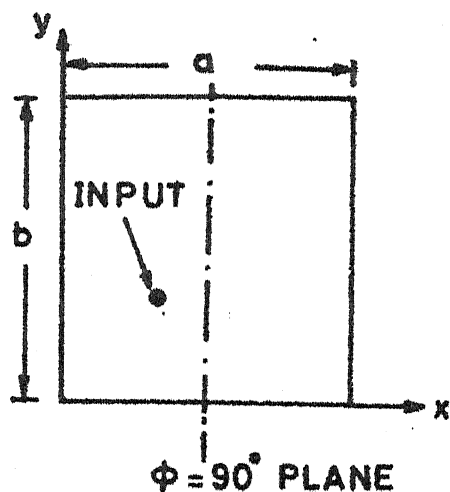


FIG. 4.19 ANTENNA CONFIGURATION AND ITS RADIATION PATTERN (Theoretical) IN  $\phi = 90^\circ$  PLANE FOR FEED LOCATED ON THE DIAGONAL AS SHOWN IN FIG. 4.13 (inset). Substrate thickness  $= 1/8''$





$$a = 2.80 \text{ cm}$$

$$b/a = 1.0296429$$

$$\text{SUBSTRATE THICKNESS} = 1/16''$$

$$\epsilon_r = 2.49$$

$$f = 3.1658 \text{ GHz}$$

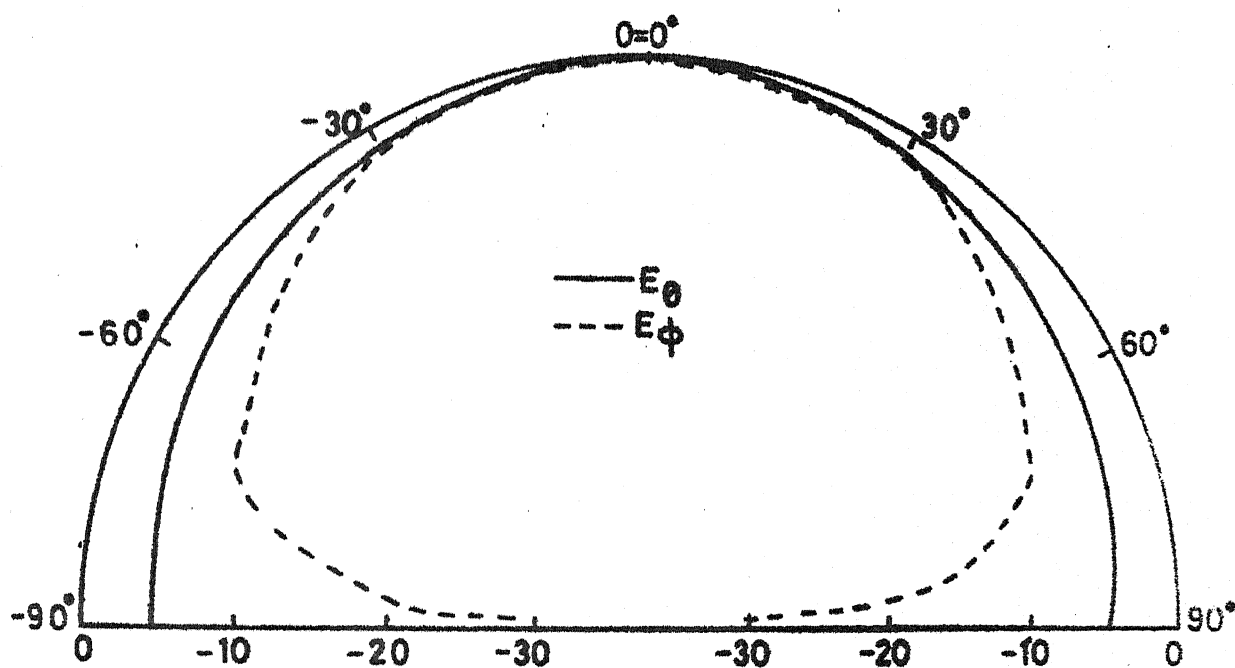


FIG. 4.20 RADIATION PATTERN FOR THE DIAGONAL FED ANTENNA IN  $\Phi = 90^\circ$  PLANE AS OBTAINED THEORETICALLY. THE FEED IS ON THE DIAGONAL AS SHOWN IN FIG. 4.16 (inset). Substrate thickness =  $1/16''$

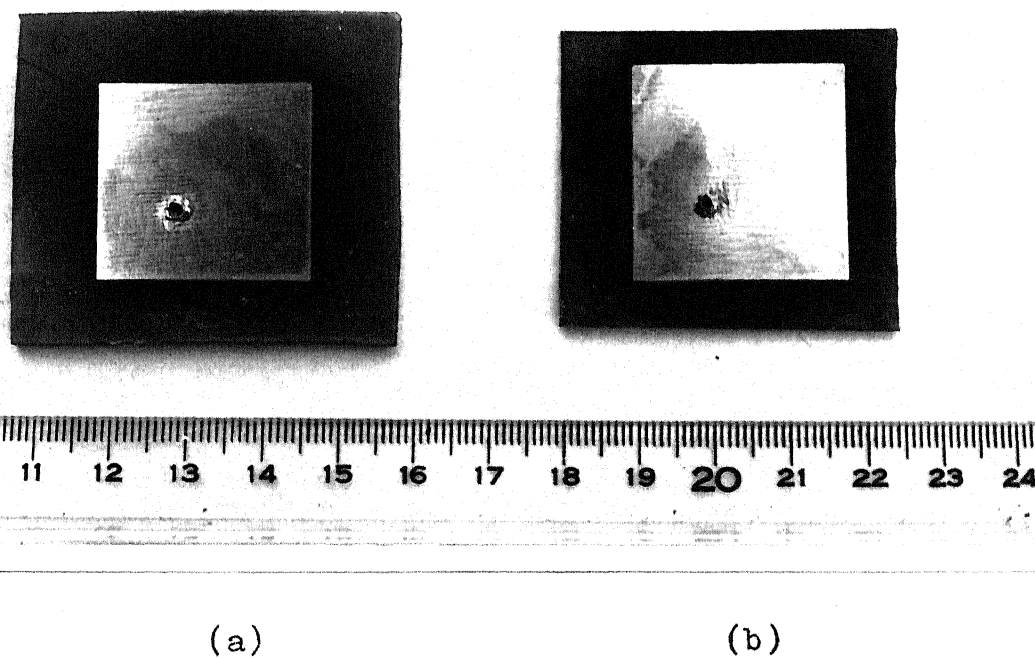


Fig. 4.21 Photograph of diagonal fed antennas fabricated on  
(a)  $1/8$ " thick substrate with  $\epsilon_r = 2.52$   
(b)  $1/16$ " thick substrate with  $\epsilon_r = 2.49$

shown in Fig. 4.22. The axial ratio is measured by turning the linearly polarized horn antenna by  $90^\circ$  to receive the other component.

The variation of axial ratio with frequency, for the two antennas, are plotted in Figs. 4.17 and 4.18. The experimental bandwidths for the two antennas are found to be 34.8 MHz (1.12 percent) for  $1/8$ " substrate antenna and 21.2 MHz (0.67 percent) for  $1/16$ " substrate antenna. The corresponding theoretical values of bandwidths are 1.086 percent and 0.632 percent. For the two antennas, the variation of input VSWR with frequency over the bandwidth for which axial ratio remains less than 6 dB, are shown in Fig. 4.13 and in Fig. 4.16.

The theoretical and experimental values of far-field components, for the two antennas, in  $\phi = 90^\circ$  plane are plotted in Fig. 4.23 to Fig. 4.26. It is found that the experimental and theoretical results for input VSWR, axial ratio and radiation patterns are in good agreement.

Parameters and results of the antennas investigated are summarized in Tables 4.1 and 4.2.

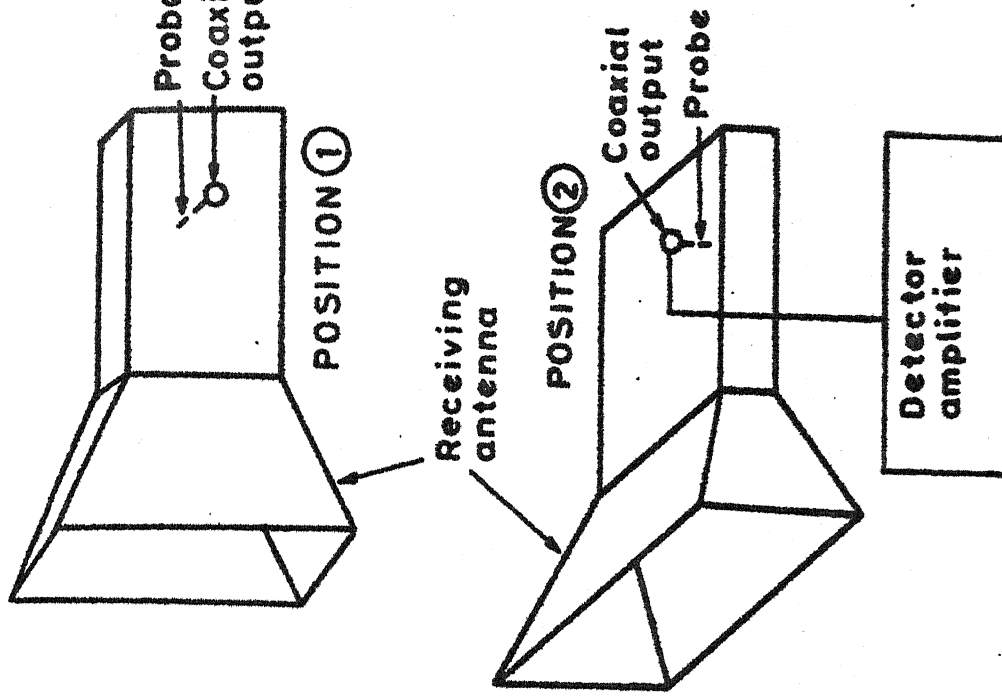
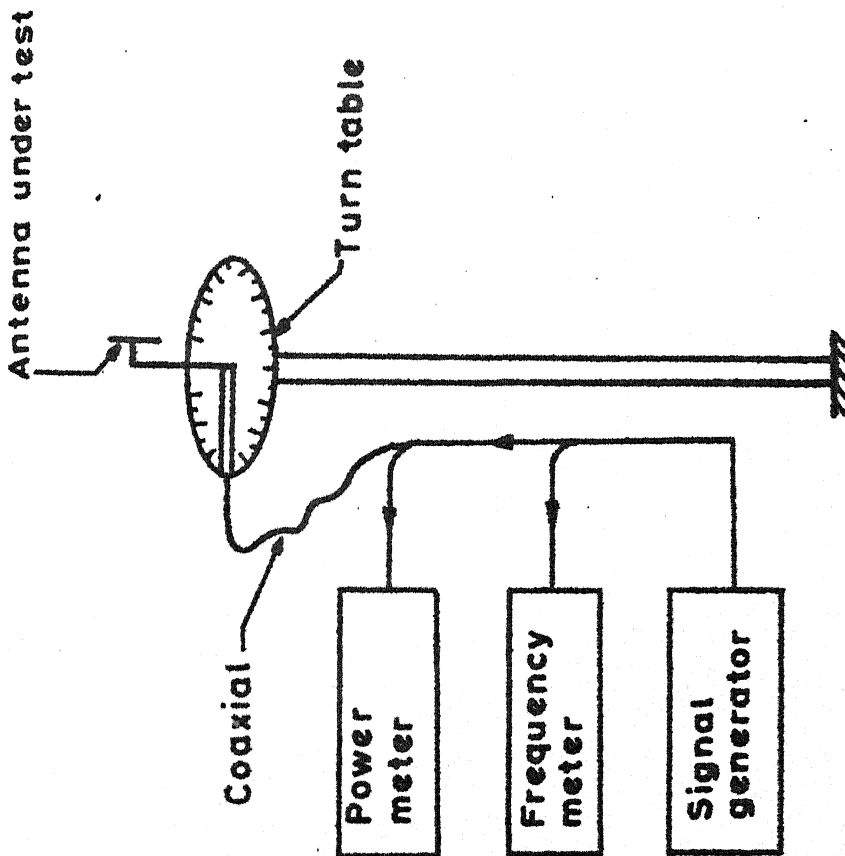
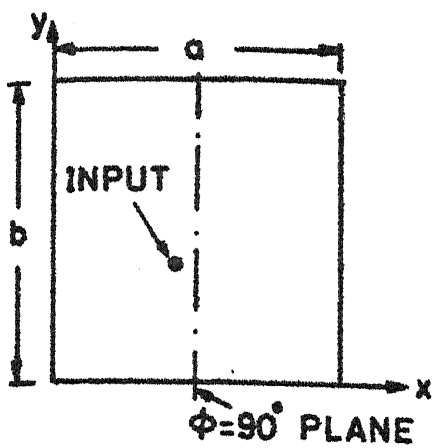


**FIG-4-22 EXPERIMENTAL SETUP FOR RADIATION PATTERN AND AXIAL RATIO MEASUREMENT**



$f = 3103 \text{ MHz}$

$\epsilon_r = 2.52$

SUBSTRATE THICKNESS  $= 1/8$

$a = 2.66 \text{ cm}$

$b/a = 1.052632$

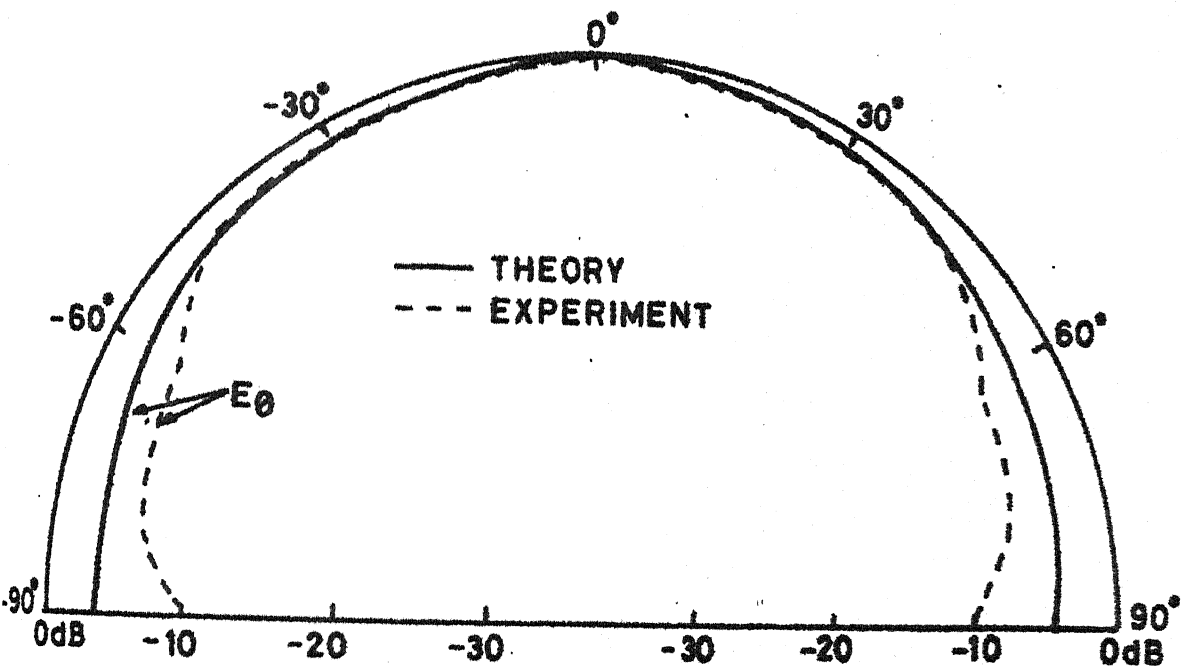
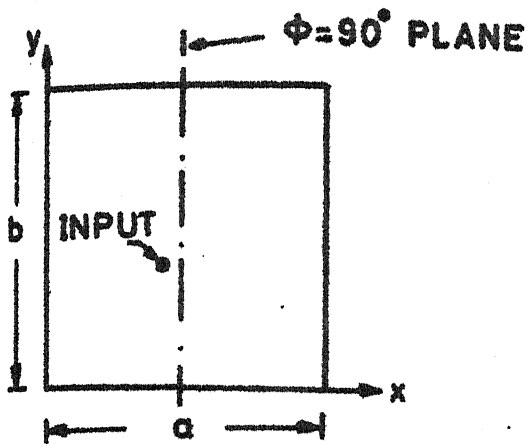


FIG. 4.23 COMPARISON OF THEORETICAL AND EXPERIMENTAL VALUES OF  $E_\theta$  IN  $\phi = 90^\circ$  PLANE FOR A DIAGONAL FED ANTENNA. FEED LOCATION IS AS SHOWN IN FIG. 4.13 (inset)



$f = 3103 \text{ MHz}$

$\epsilon_r = 2.52$

SUBSTRATE THICKNESS  $= 1/8$

$a = 2.66$

$b/a = 1.052632$

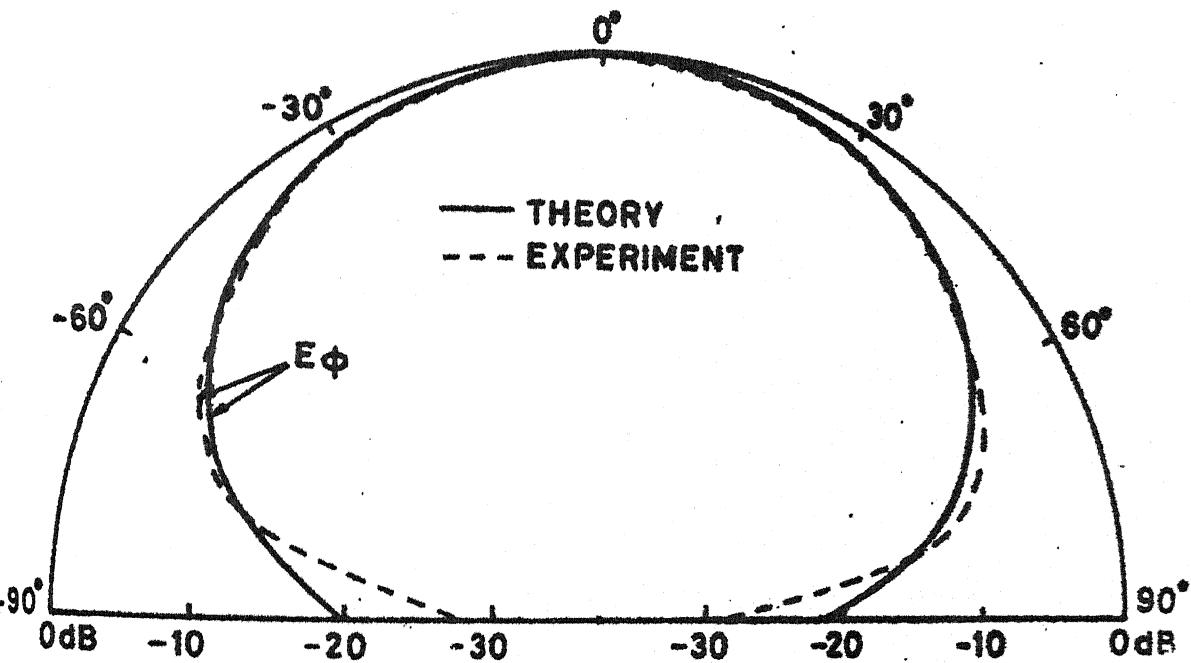
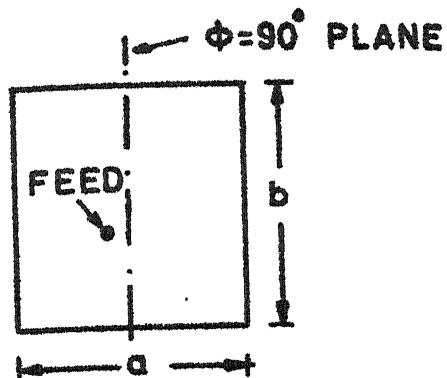


FIG. 4.24 COMPARISON OF THEORETICAL AND EXPERIMENTAL VALUES OF  $E_\phi$  IN  $\Phi = 90^\circ$  PLANE FOR A DIAGONAL FED ANTENNA. FEED LOCATION AS IN FIG. 4.13(inset)



$$\epsilon_r = 2.49, a = 2.80 \text{ cm}$$

$$b/a = 1.0296429$$

$$\text{SUBSTRATE THICKNESS} = 1/16''$$

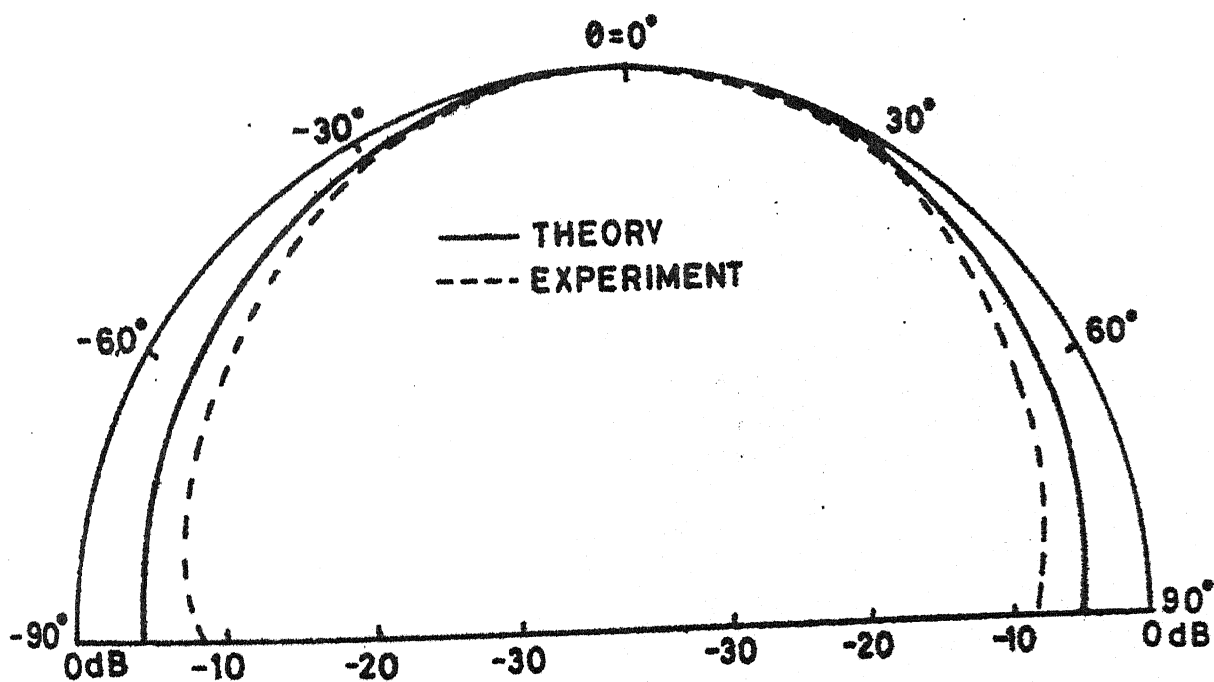
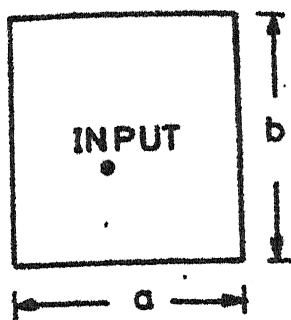


FIG. 4.25 COMPARISON OF THEORETICAL AND EXPERIMENTAL VALUES OF  $E_\theta$  FOR A DIAGONAL FED ANTENNA. FEED LOCATION IS AS IN FIG. 4.16 (inset)



$\epsilon_r = 2.49$ ,  $a = 2.80$  cm

$b/a = 1.0296429$

SUBSTRATE THICKNESS =  $1/16$ "

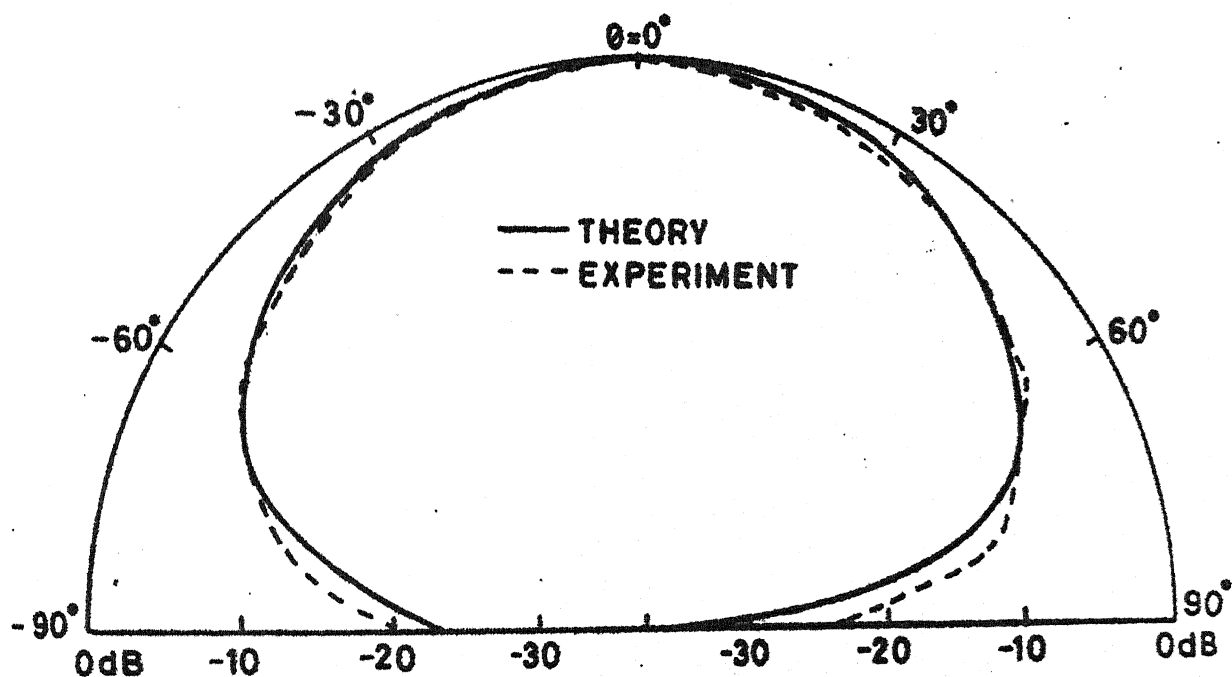


FIG. 4.26 COMPARISON OF VALUES  $E_\phi$  AS OBTAINED THEORETICALLY AND EXPERIMENTALLY. FEED LOCATION IS AS IN FIG. 4.16 (inset)



Table 4.1

Parameters for the diagonal fed antennas investigated

	ANTENNA I	ANTENNA II	ANTENNA III
1. Substrate thickness	1/8"	1/16"	1/16"
2. Dielectric constant	2.52	2.52	2.49
3. Side length 'a' (cm)	2.66	2.81445	2.80
4. Side length 'b' (cm)	2.80	2.8877	2.8830
5. $(b/a)_{\text{physical}}$	1.05263	1.0260	1.02964
6. $(b/a)_{\text{effective}} = (b_e/a_e)$	1.04727	1.02461	1.02805
7. $(1 + \frac{1}{Q})$	1.0654	1.03708	1.0416
8. Electrical lengths			
i) $a_e$	$0.4928 \lambda_d$	$0.4939 \lambda_d$	$0.493 \lambda_d$
ii) $b_e$	$0.5178 \lambda_d$	$0.5060 \lambda_d$	$0.50683 \lambda_d$

Table 4.2

Results of investigations on diagonal fed antennas having parameters as in Table 4.1

	ANTENNA I		ANTENNA II		ANTENNA III	
	Theory	Experiment	Theory	Experiment	Theory	Experiment
1. Best axial ratio (dB)	0.45	0.5	0.17	-	0.17	0.25
2. Center frequency $F_c$ (GHz)	3.1030	3.1015	3.1372	-	3.1658	3.1664
3. Resonance frequencies of orthogonal modes (GHz)	3.035 3.175	3.032 3.169	3.099 3.175	-	3.122 3.210	3.116 3.203
4. Input VSWR at $F_c$	1.73	1.72	1.33	-	1.33	1.55
5. Bandwidth (MHz) for axial ratio $< 6$ dB	33.7 (1.086%)	34.8 (1.12%)	19.6 (0.625%)	-	20.0 (0.632%)	21.2 (0.670%)
6. Beamwidth for difference between $ E_\theta $ and $ E_\phi $						
i) $< 3$ dB	110°	140°	114°	-	116°	140°
ii) $< 6$ dB	136°	160°	135°	-	138°	161°

#### 4.6 DISCUSSIONS

Investigations have been carried out on three diagonal fed S-band antennas on substrates having different values of thickness and of dielectric constant. The ratio of length to width of the rectangular patch is optimized for obtaining the best circular polarization. The length to width ratio is found to depend upon the value of the dielectric constant and thickness of the substrate. The feed port is located on one of the diagonals to obtain the minimum input VSWR. In all the three cases investigated, the distance of the feed location from one of the end points of the diagonal is found to be 0.36 times the effective diagonal length. It is observed that better input VSWR can be obtained by using thinner substrates but reduction in the thickness of the substrate to half reduces the axial ratio limited bandwidth by nearly 41 percent. The VSWR remains practically constant over the range of frequencies for which axial ratio remains less than 6 dB.

The beamwidths for three antennas, defined for 3 dB and 6 dB difference between  $|E_\theta|$  and  $|E_\phi|$ , are given in Table 4.2. The theoretical values of beamwidths for the three antennas are nearly equal. The measured values are greater than the respective theoretical values (Table 4.2). This difference between measured and theoretical values can be explained from the nature of variations of the far-field

components with  $\theta$ . The theoretical and experimental values of  $E_\phi$  in Figs. 4.24 and 4.26 are in agreement for  $0 < \theta < 90^\circ$ . But in case of  $E_\theta$ , it is observed that for  $\theta > 60^\circ$  the experimental values decrease faster as compared to the values obtained theoretically (Figs. 4.23 and 4.25). (Such difference between measured and theoretical values of  $E_\theta$  has been observed by Dereryd [57] also). Also, from Figs. 4.19 and 4.20 it is found that  $|E_\phi| < |E_\theta|$  for  $\theta > 30^\circ$ . Thus the faster rate of decrease in experimental  $|E_\theta|$  with  $\theta$  reduces the difference between  $|E_\theta|$  and  $|E_\phi|$ . Thus the experimental beamwidth is increased. The decrease in experimental values of  $E_\theta$  near  $\theta = 90^\circ$  can perhaps be attributed to the excitation of surface waves which cause flow of power along the surface of the substrate.

The values of  $(1 + \frac{1}{Q})$  are found to be slightly greater than the ratios  $(b/a)$  physical and  $(b/a)$  effective.

Experimental results are in good agreement with those evaluated theoretically. It is thus found that the Green's function approach, as proposed in Chapter Two, can be used for analysis and design of microstrip antennas.

The next chapter describes the details of investigations carried out on corners chopped square patch antennas using the Green's function approach and the desegmentation method.

## CHAPTER FIVE

### CORNERS CHOPPED SQUARE PATCH ANTENNA

#### 5.1 ANALYSIS AND OPTIMIZATION

##### 5.1.1 Analysis

The configuration of a corners chopped patch antenna is shown in Fig. 5.1. For analysis, the antenna configuration ( $\alpha$ -segment) is considered as obtained by chopping off two diagonally opposite corners of a regular square patch ( $\gamma$ -segment) and the desegmentation method, as illustrated in Fig. 5.2, is used. The separated corners, which are isosceles right-angled triangles, are designated as segments  $\beta_1$  and  $\beta_2$ .

The antenna ( $\alpha$ -segment) to be analyzed is considered as multiport circuit as shown in Fig. 5.3(a). For the typical circuit chosen for illustration, the periphery (magnetic wall boundary) of this multiport circuit is divided into 32 ports (2 to 33). An additional port (corresponding to the feed point) is considered to be located at mid-point of port number 5. The width of this port is taken equal to the width of the feed line in case of microstrip feed or equal to the diameter of the pin of coaxial feed line as the case may be. This additional port is numbered as 1. Thus following the nomenclature of Chapter Three, there are 25 p-ports (1 to 25) and 8 c-ports (26 to 33). For the configuration

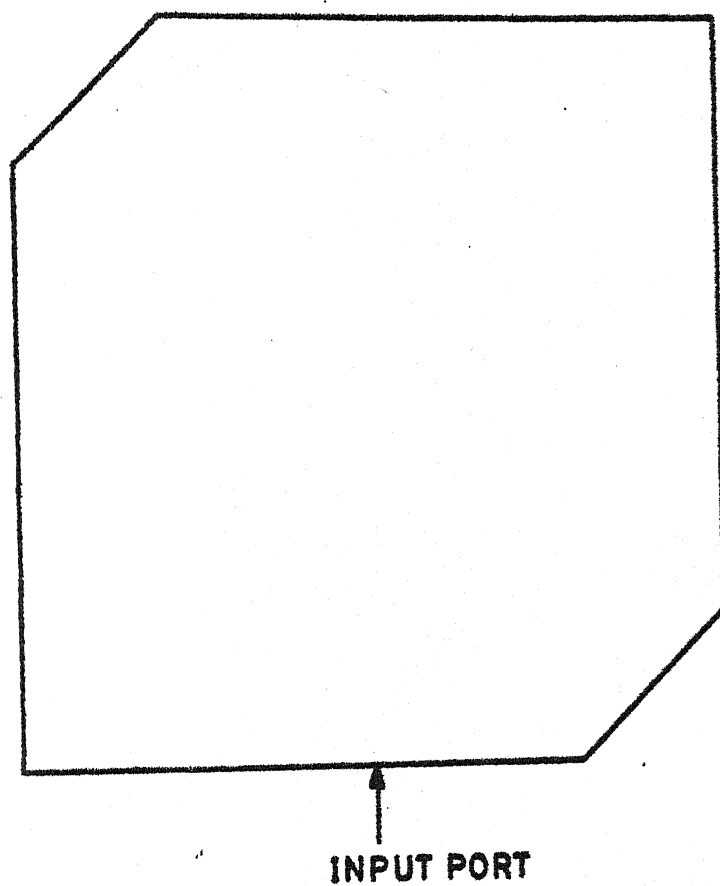


**FIG. 5.1 CORNERS CHOPPED SQUARE PATCH ANTENNA FOR CIRCULAR POLARIZATION**

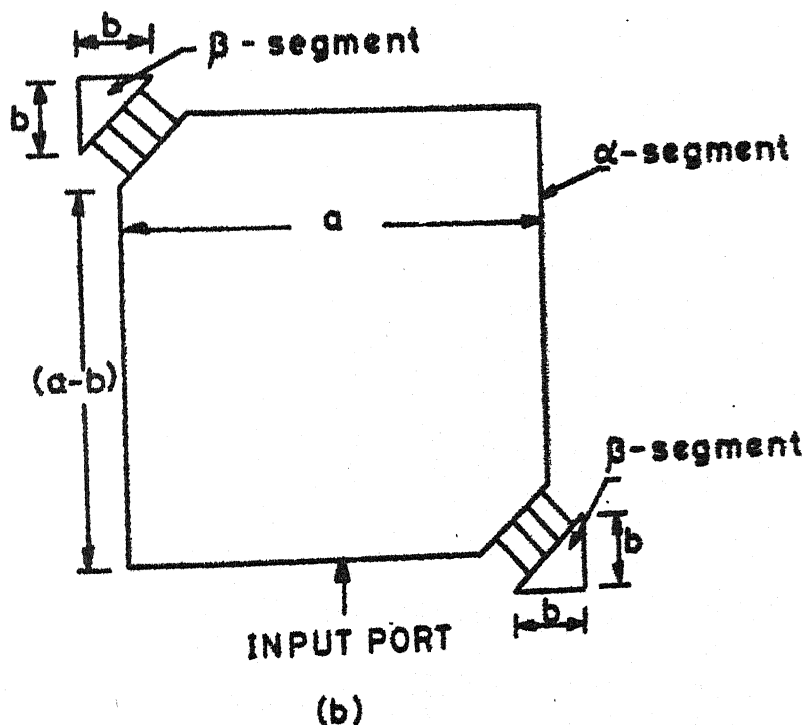
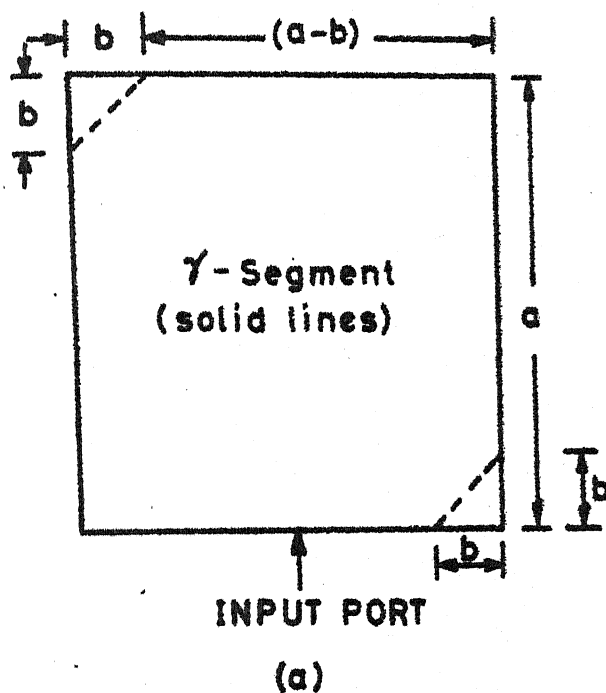
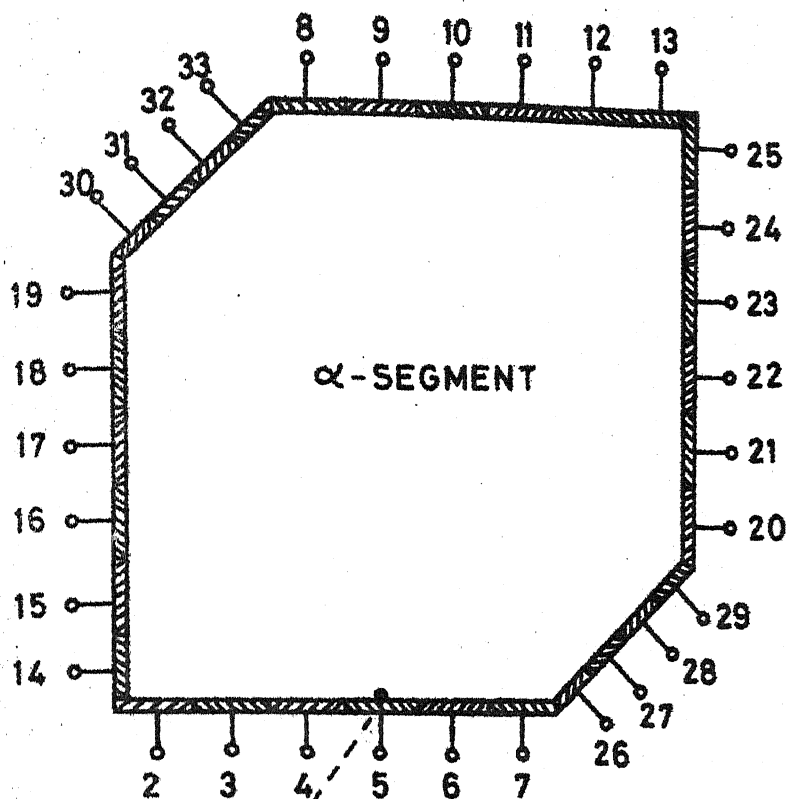
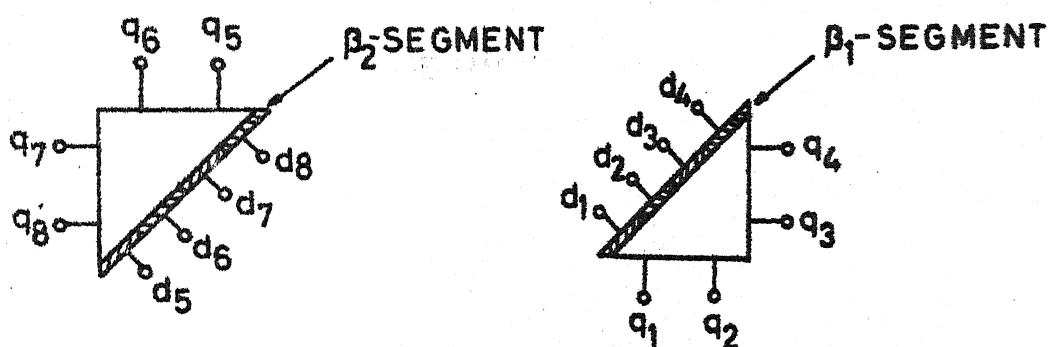


FIG. 5.2 (a) THE REGULAR SQUARE  $\gamma$ -SEGMENT;  
 (b) REMOVAL OF  $\beta_1$ - AND  $\beta_2$ - SEGMENTS  
 FROM  $\gamma$ - SEGMENT YIELDS  $\alpha$ - SEGMENT  
 OF FIG. 5.1



(a)



(b)

FIG. 5-3(a) THE ANTENNA STRUCTURE CONSIDERED AS MULTI-PORT CIRCUIT; p-PORTS: 1 TO 25 ; c-PORTS: 26 TO 33; (b) THE  $\beta$ -SEGMENTS WITH 4 d-PORTS AND 4 q-PORTS ON EACH OF THEM



considered, it turns out that 4 q-ports on each of the  $\beta$ -segments (Fig. 5.3(b)) are sufficient for accurate evaluation of the Z-matrix of the  $\alpha$ -segment. As there are 4 q-ports on each of the  $\beta$ -segments 4 c-ports at each of the truncated corners of the  $\alpha$ -segment and 4 d-ports on each of the  $\beta$ -segments are needed. The hypotenuse of each of the triangles is divided into 4 sections which form d-ports as shown in Fig. 5.3(b).

The Z-matrices of  $\gamma$ - and  $\beta$ -segments are evaluated using the Green's functions [1], [21]. The desegmentation method as formulated in (3.14) is then used to evaluate the Z-matrix of the multiport network model of Fig. 5.3(a). The Z-matrix so obtained pertains to an ideal cavity model with magnetic wall boundary. The Z-matrix of the multiport model with radiated power taken into account, is evaluated by considering the ports, 2 to 33 (Fig. 5.3), to be terminated by radiation resistances. However, as discussed in Section 2.2.2, the input port (numbered 1) is left unterminated.

The voltage distribution around the periphery of the antenna is obtained from (2.19). The magnetic current moment distribution (equivalent to the voltage distribution) is evaluated from (2.2), and the far-field is computed using (2.4) and (2.5). The axial ratio is evaluated over a band of frequencies for different values of the truncation. The variations of polarization characteristics with the truncation

and the frequency are discussed in the following section.

### 5.1.2 Optimum truncation

For the choosen dimensions ( $a = 2.73$  cm) of the square patch ( $\gamma$ -segment in Fig. 5.2(a)) with  $\epsilon_r = 2.52$  and substrate thickness =  $1/8$ ", the axial ratio is evaluated at several frequencies for each value of the truncation 'b'. The variation of axial ratio with frequency and with amount of truncation is illustrated in Fig. 5.4. It is found that for 'b' (effective) = 0.44 cm, the axial ratio is 0.12 dB at 3175.0 MHz. The ratio (b/a) is 0.04578 when evaluated in terms of physical dimensions and equal to 0.1444626 in terms of effective dimensions.

Voltage and magnetic current distributions, that are responsible for circular polarization of the antenna, are discussed in the following section.

### 5.1.3 Voltage and magnetic current distribution

The in-phase and quadrature components of the voltage around the periphery of the antenna, for feed location as shown in Fig. 5.5 (inset), are shown in Fig. 5.5. Comparison of this voltage distribution with that for the diagonal fed antenna, shown in Fig. 4.4, shows that they differ in nature of distribution along the periphery of the two antennas. In case of diagonal fed antenna, each of the radiating edges of the antenna has the in-phase and quadrature components of

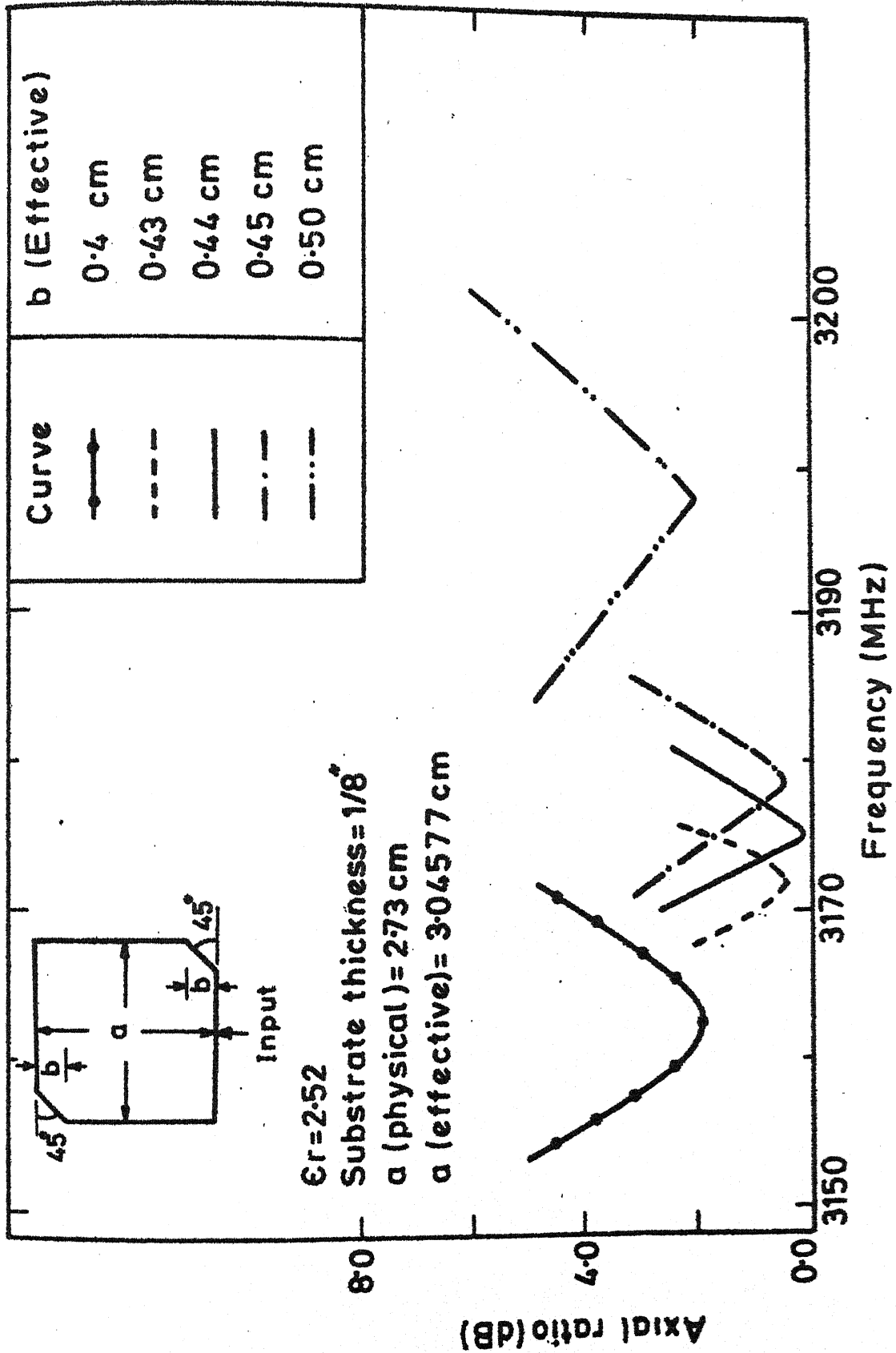
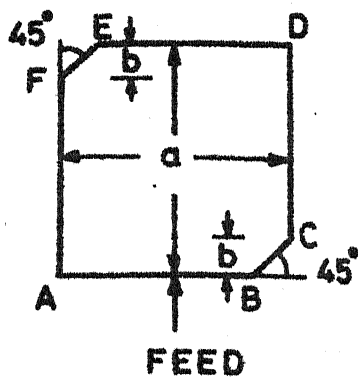


FIG. 5.4 VARIATION OF AXIAL RATIO WITH FREQUENCY FOR DIFFERENT VALUES OF TRUNCATION 'b'



$a$  (Physical) = 2.73 cm,  
 $a$  (Effective) = 3.04577 cm,  
 $b$  (Effective) = 0.44 cm,  
 $\epsilon_r = 2.52$ ,  
 Substrate thickness =  $1/8$ ",  
 $f = 3175.0$  MHz

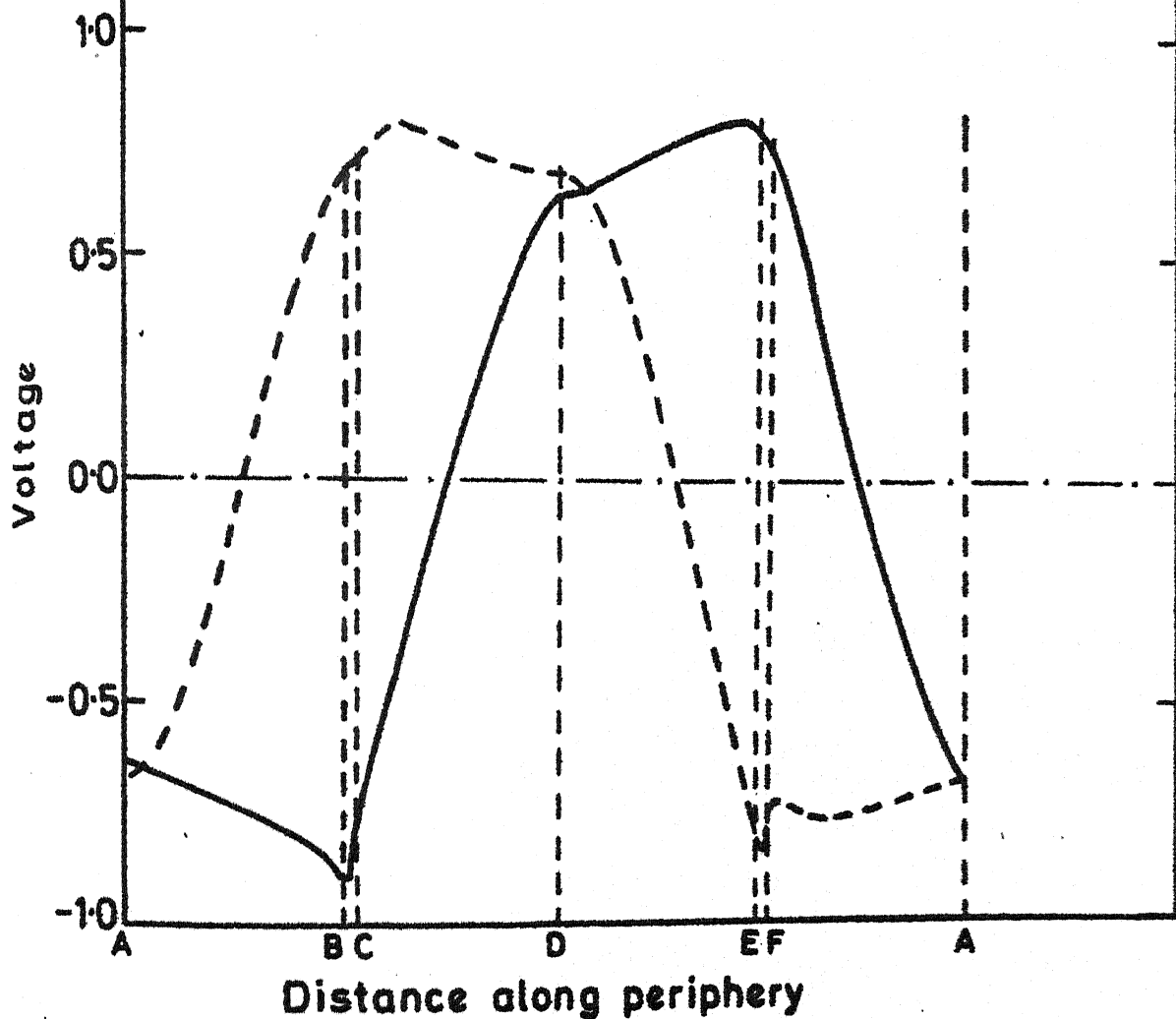
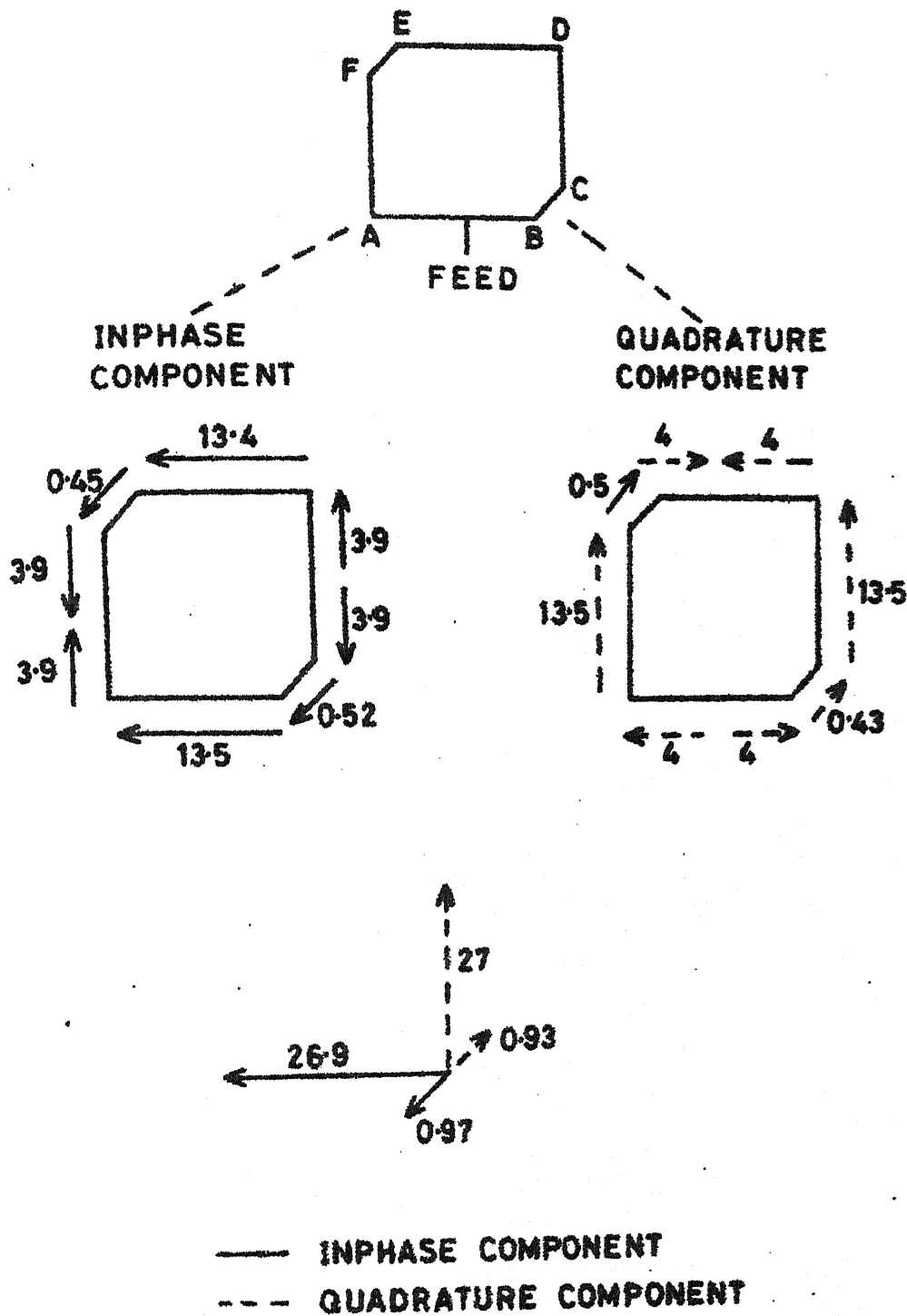


FIG. 5.5 DISTRIBUTION OF VOLTAGE ALONG THE PERIPHERY OF THE ANTENNA FOR FEED LOCATION AS SHOWN

voltage which contribute to net radiation. In case of the corners chopped square patch antenna (Fig. 5.5), the radiations from edges AB and DE are due to the inphase component of the voltage. The edges CD and FA radiate due to the quadrature component of the voltage along these edges.

This feature becomes more clear from the comparison of the magnetic current moment distributions shown in Fig. 4.5 (for diagonal fed antenna) and in Fig. 5.6, the latter illustrating the magnetic current moment and the orientation of the resultant magnetic current moment vectors for the corners chopped square patch antenna. Orientations of the resultant magnetic current vectors as illustrated in Fig. 5.6 reveal that the antenna is circularly polarized. The amplitude of the magnetic current moments in Fig. 5.6 are obtained from the voltage distribution of Fig. 5.5. The value of axial ratio for the magnetic current moments (Fig. 5.6) is found to be nearly 0.035 dB whereas the axial ratio evaluated for far-field is 0.12 dB. As discussed in Section 4.2 for a diagonal fed antenna, the voltage distribution of Fig. 5.5 that results into circular polarization of the corners chopped square patch antenna should be expressible as linear combination of two orthogonal modes. A discussion on these two constituent modes is presented in the next section.



**FIG. 5.6 MAGNETIC CURRENT MOMENT DISTRIBUTION AND ORIENTATION OF RESULTANT MOMENT VECTORS FOR VOLTAGE DISTRIBUTION OF FIG. 5.5**

## 5.2 ORTHOGONAL MODES

Consider the voltage distribution along the periphery of the antenna when the antenna is excited at one of the untruncated corners as shown in Fig. 5.7. The corresponding magnetic current moments are shown in Fig. 5.8. As the magnetic current moments along the edges of the truncated corners are equal in magnitude and opposite in direction, their contributions to the radiation field cancel out in the broadside direction. The orientations of the resultant components of magnetic current moments, as in Fig. 5.8, indicate that the antenna is linearly polarized. The theoretical and experimental values of the resonance frequency of this mode are 3.1340 GHz and 3.1325 GHz respectively. The measured amplitudes of the two far-field components (orthogonal to each other) are shown in Fig. 5.9 as functions of frequency. At resonance frequency, the amplitudes differ by more than 19 dB and the antenna is therefore linearly polarized.

Now consider the distribution of the voltage (Fig. 5.10) and of the equivalent magnetic moments (Fig. 5.11) along the edges of the antenna when fed at one of the truncated corners. It is found that the magnetic current moments along truncated corners of the antenna are additive (contrary to the situation shown in Fig. 5.8). The polarization of the antenna is again linear (Fig. 5.11) but is in space quadrature with that

$\epsilon_r = 2.52$ ,  $F = 3175.0$  MHz  
 SUBSTRATE THICKNESS  $= 1/8"$   
 $a$  (Effective)  $= 3.04577$  cm  
 $b$  (Effective)  $= 0.44$  cm  
 $a$  (physical)  $= 2.73$  cm

— INPHASE COMPONENT  
 --- QUADRATURE COMPONENT

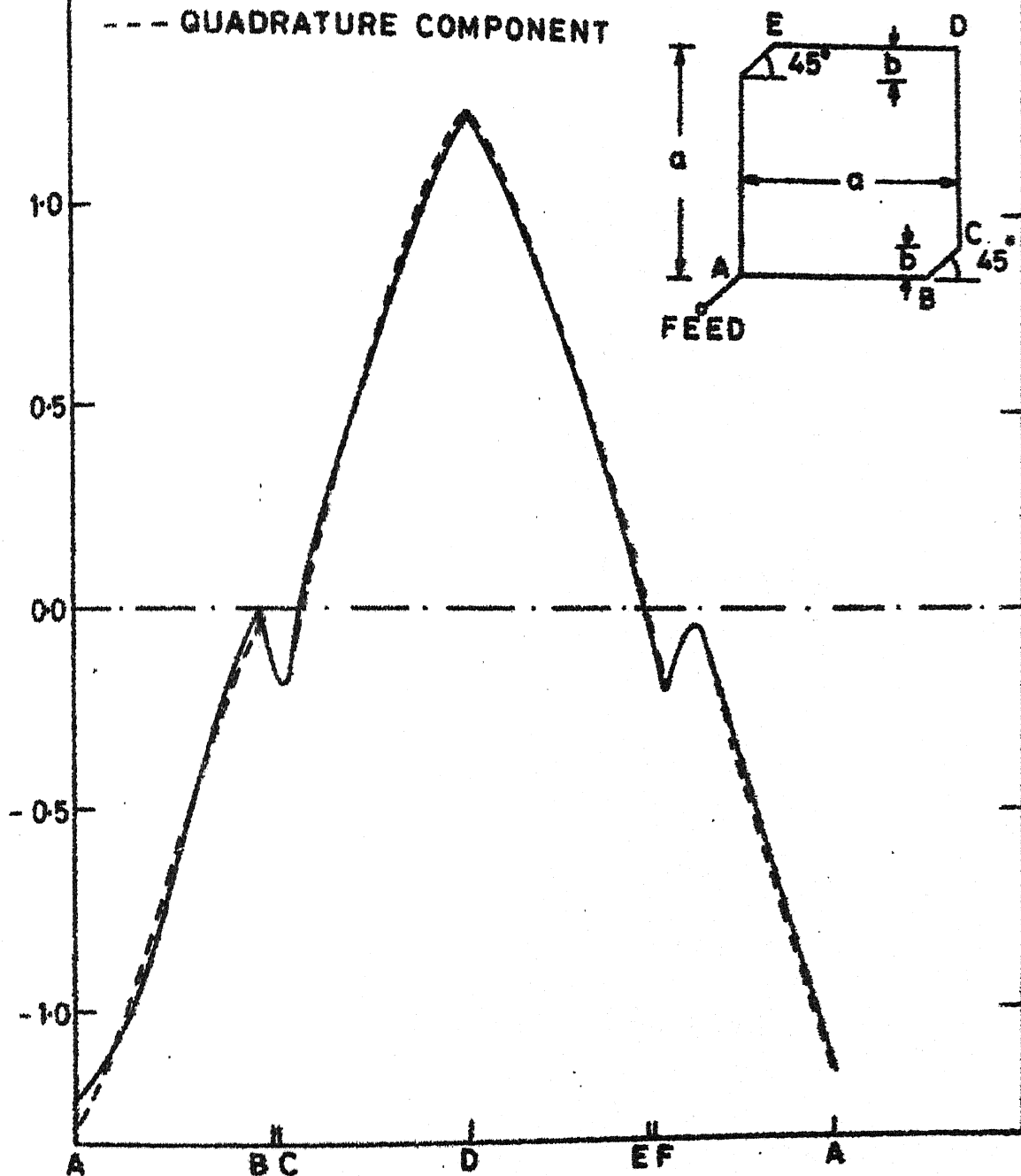
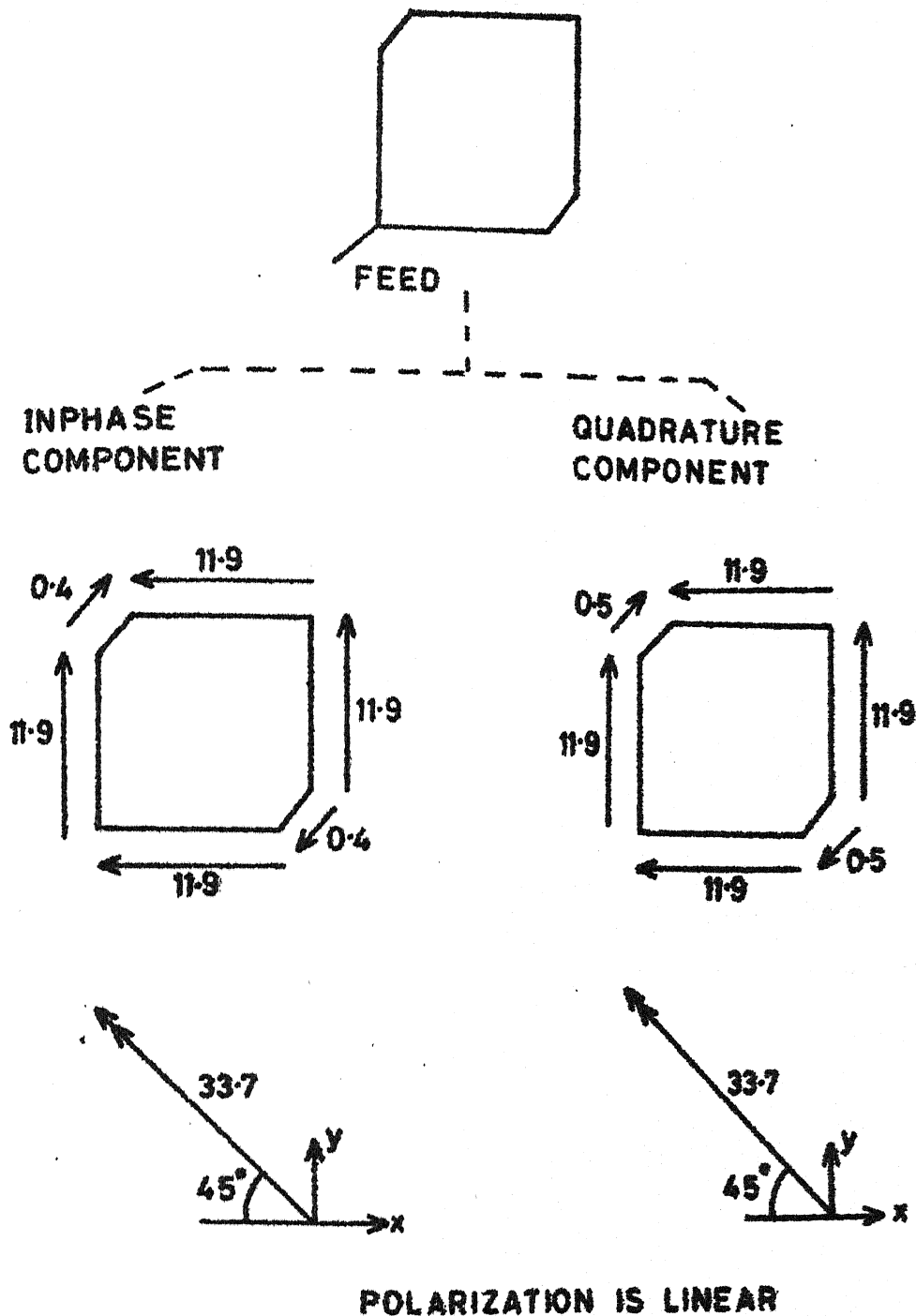


FIG.5-7 VARIATION OF VOLTAGE ALONG PERIPHERY  
 OF THE ANTENNA FOR FEED LOCATION AT  
 CORNER A





**FIG. 5.8 MAGNETIC CURRENT MOMENT DISTRIBUTION AND ORIENTATION OF RESULTANT MOMENT VECTORS FOR VOLTAGE DISTRIBUTION OF FIG. 5.7**

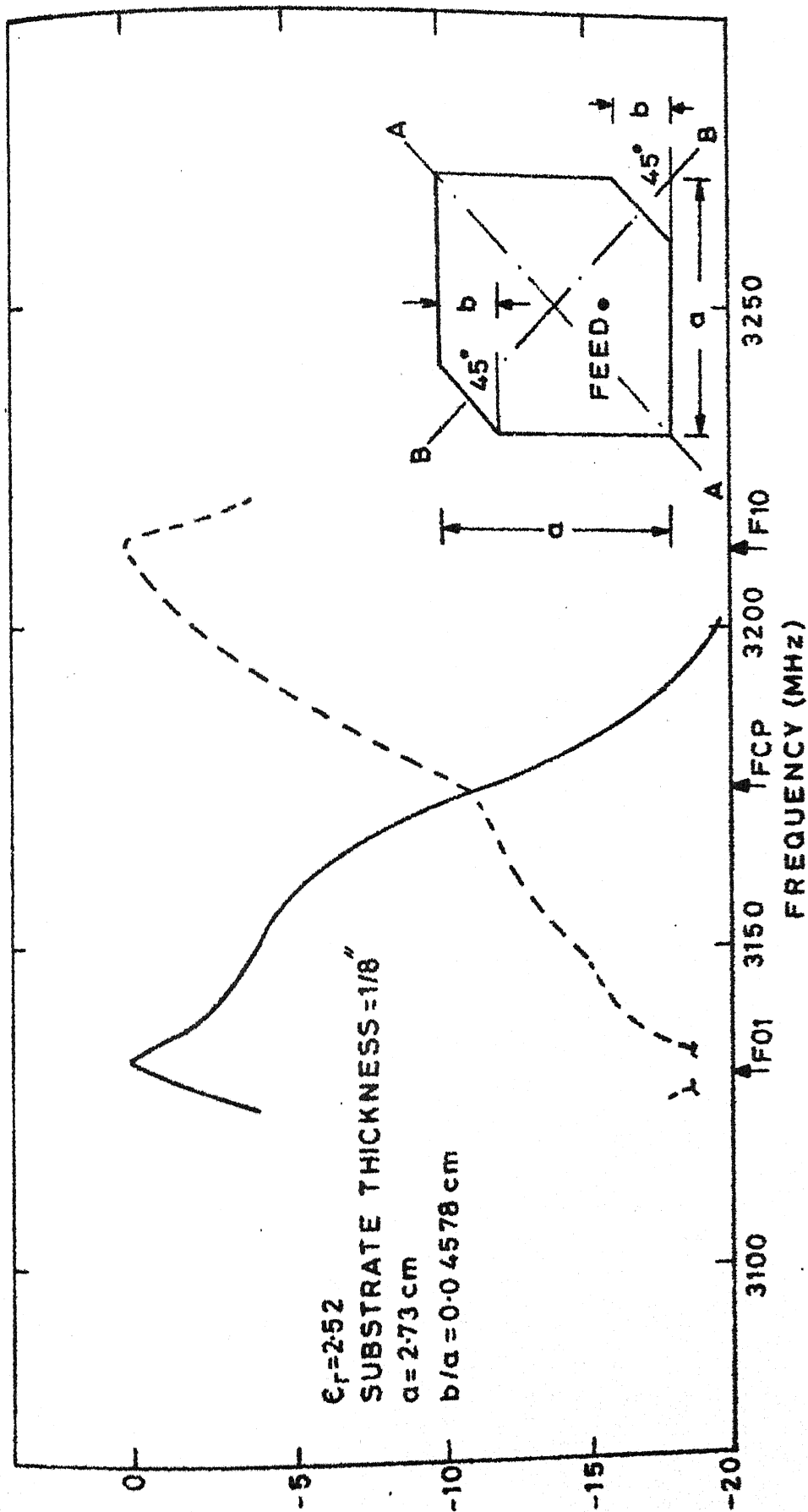


FIG.5.9 VARIATION OF AMPLITUDES OF THE TWO ORTHOGONAL COMPONENTS  
 OF FAR-FIELD WITH FREQUENCY IN BROAD-SIDE DIRECTION IN  
 PLANES A-A AND B-B

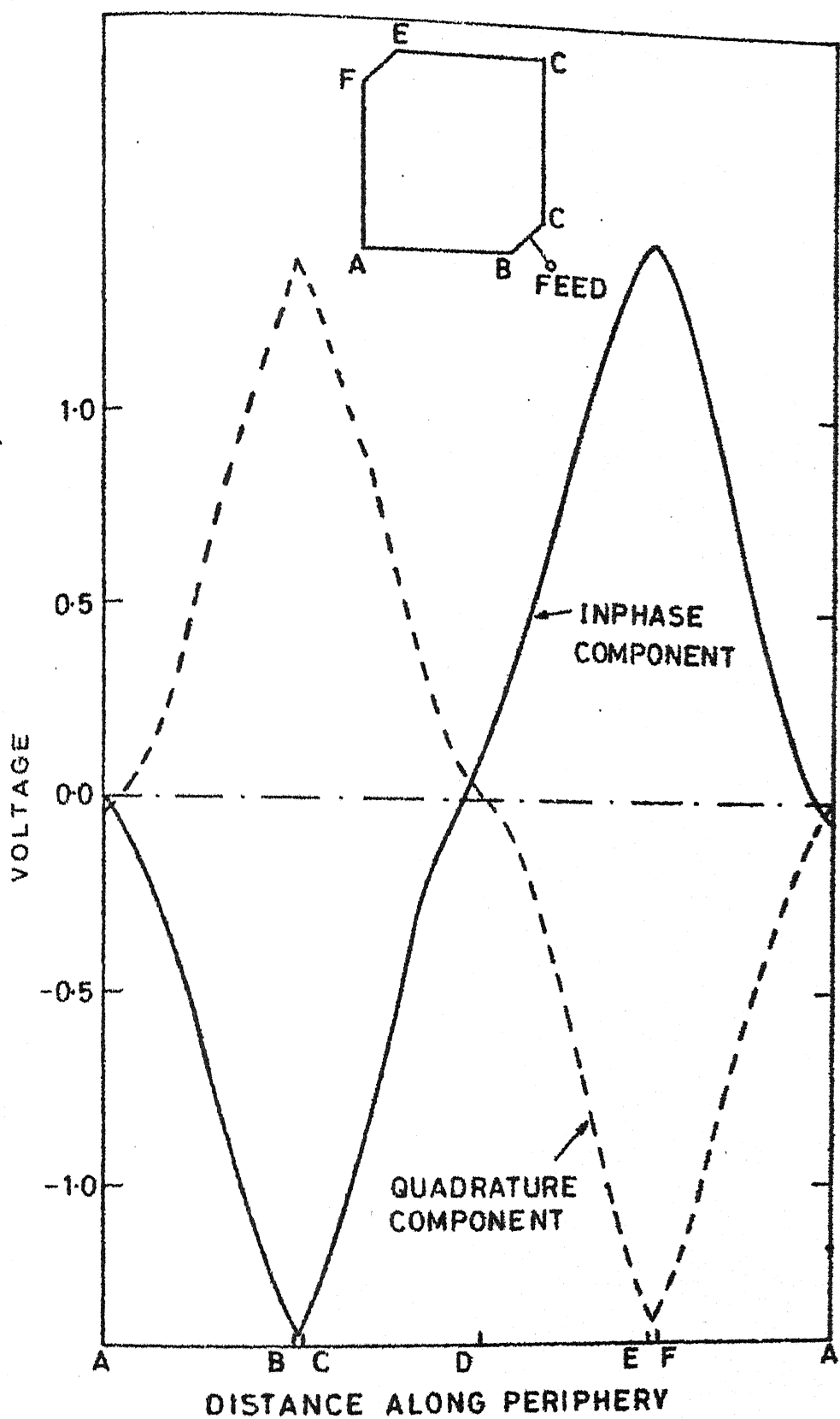


FIG. 5-10 VOLTAGE DISTRIBUTION ALONG THE PERIPHERY OF THE ANTENNA FOR FEED LOCATION AS SHOWN (inset)

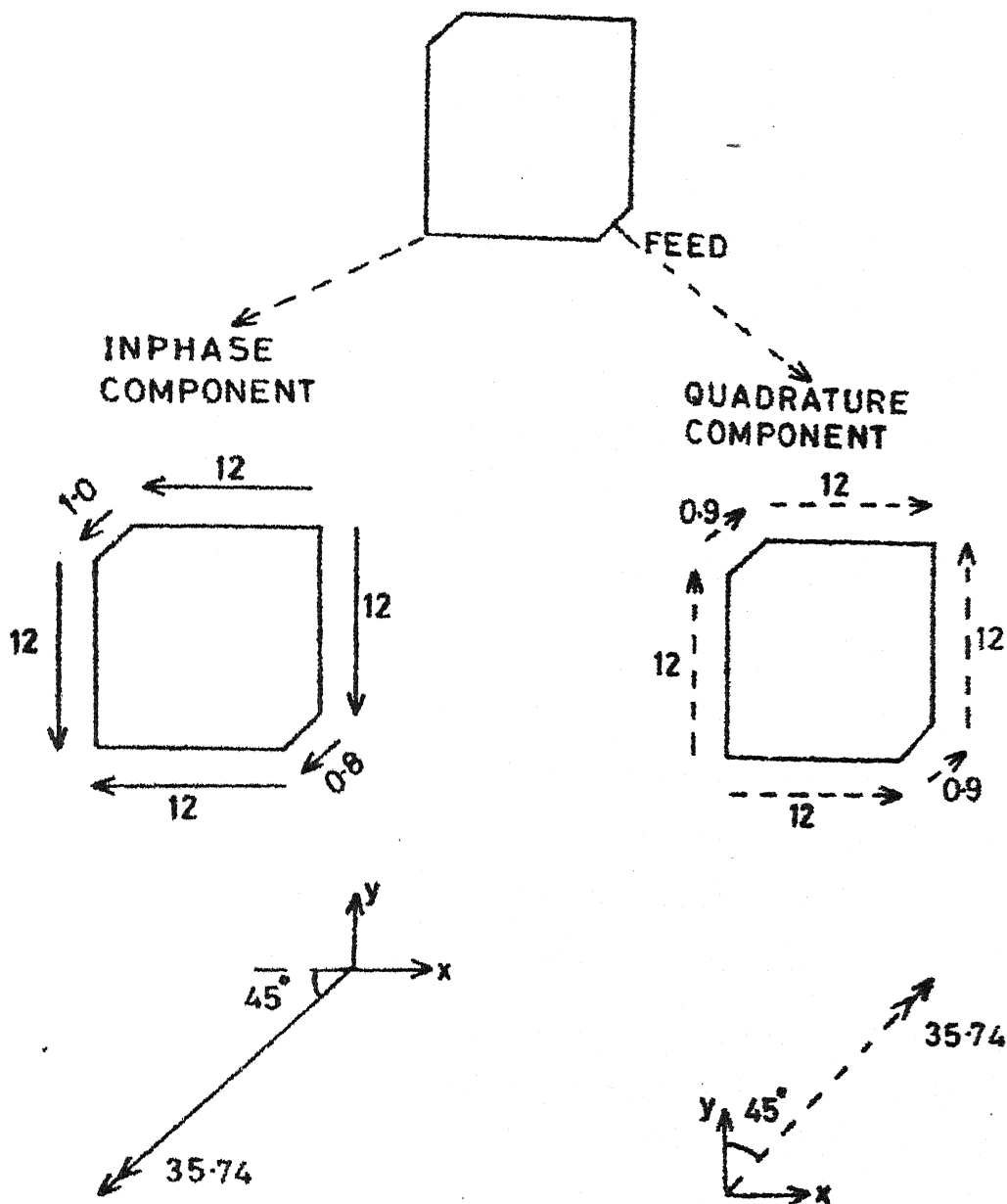


FIG.5-11 MAGNETIC CURRENT MOMENT DISTRIBUTION AND ORIENTATION OF RESULTANT MOMENT VECTORS FOR VOLTAGE DISTRIBUTION OF FIG.5-1

obtained when the antenna is excited at one of the untruncated corners. The calculated and measured values of resonance frequency of this mode are 3.2155 GHz and 3.2125 GHz. At the measured value of the resonance frequency the amplitudes of the two orthogonal components of far-field differ by more than 19 dB and the antenna is thus linearly polarized (Fig. 5.9).

The superimposition of the resultant magnetic current moments shown in Figs. 5.8 and 5.11 is illustrated in Fig. 5.12. From the comparison of the resultant vectors in Figs. 5.6 and 5.12, it may be concluded that excitation of the antenna for feed location as in Fig. 5.6 excites two orthogonal modes which results into circular polarization. The input VSWR for feed location as shown in Fig. 5.6 (inset) is found to be 5.9. In order to investigate the possibility of improving the input VSWR without using any external impedance matching network, feed port locations on the line  $x/a_e = 0.5$  (Fig. 5.13 inset) have been considered. Discussion of this aspect follows in the next section.

### 5.3 FEED LOCATION AND INPUT VSWR

As pointed out in the preceeding section, the input VSWR at the periphery of the antenna is 5.9. From the relative location of the feed in Fig. 5.5 (inset) with respect to the feed locations (for the two orthogonal modes) shown in Figs. 5.7 and 5.10 it can be argued that the feed

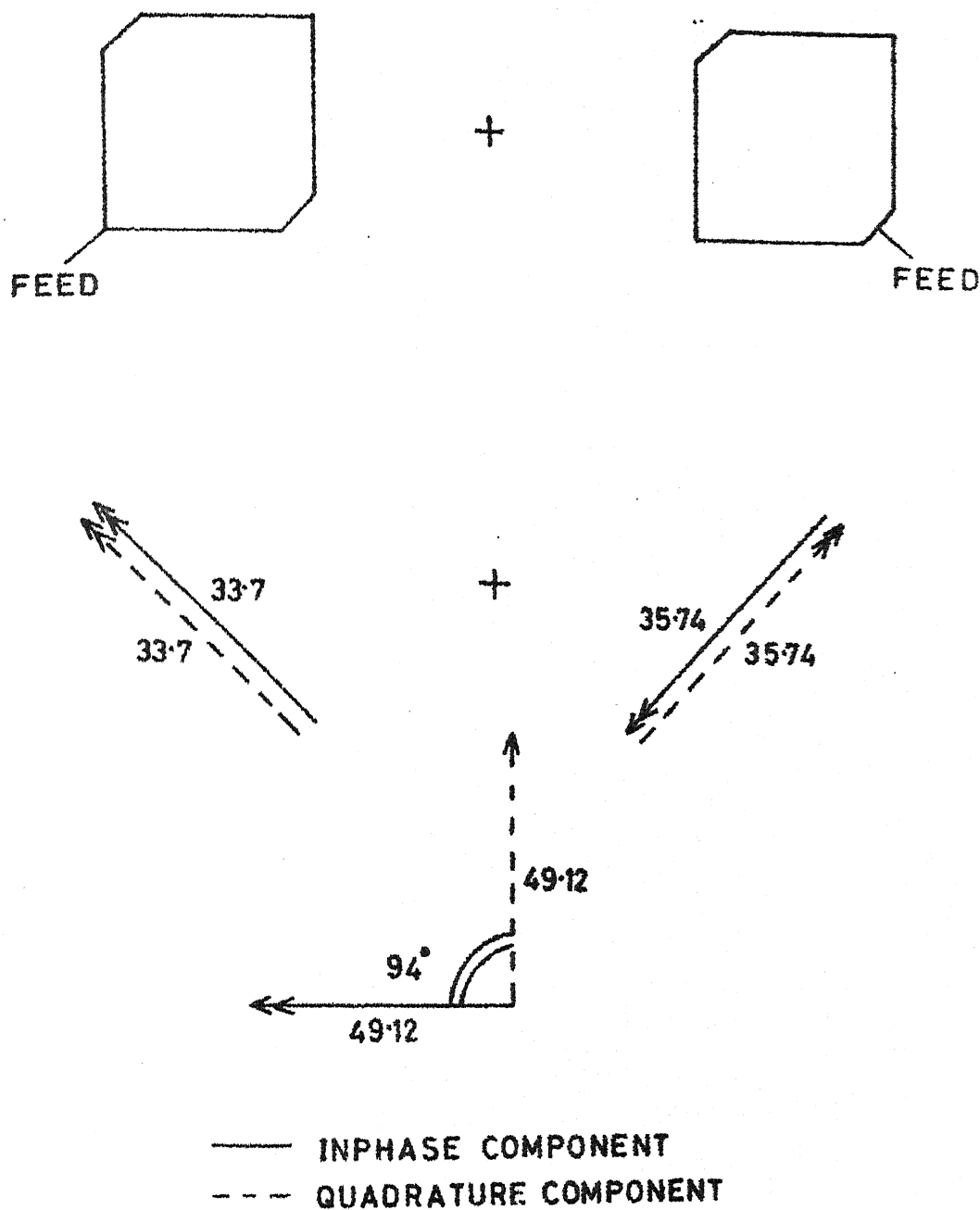


FIG. 5.12 VECTOR ADDITION OF MAGNETIC CURRENT  
MOMENT VECTORS OF FIG. 5.8 AND OF  
FIG. 5.11

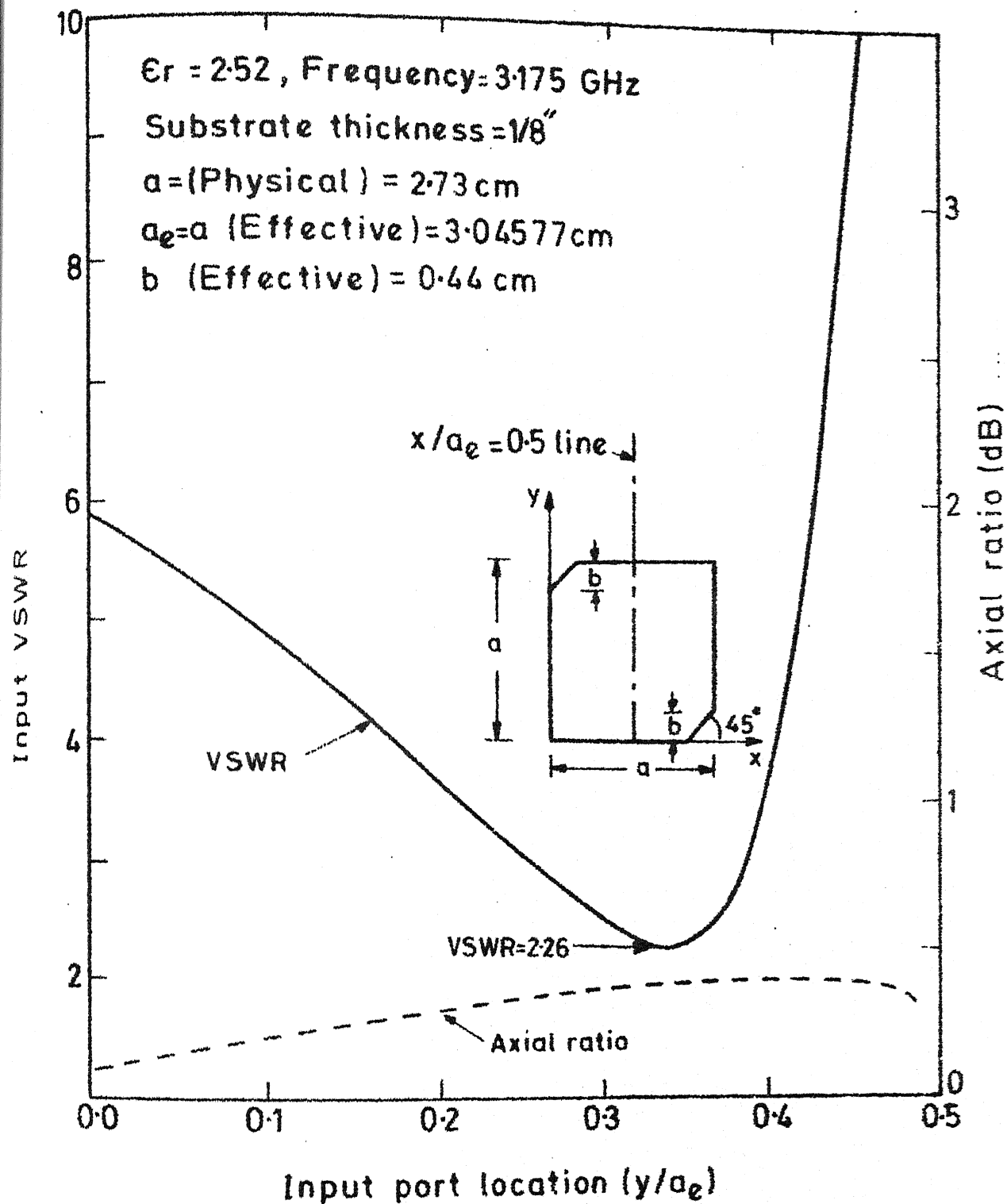


FIG. 5-13 VARIATION OF INPUT VSWR WITH FEED LOCATION ON  $x/a_e = 0.5$  LINE. Substrate thickness =  $1/8''$

location on the line  $x/a_e = 0.5$  (Fig. 5.13) should also yield circular polarization. The variation of input VSWR and axial ratio (at 3.175 GHz) with feed location is illustrated in Fig. 5.13. The input VSWR reduces from 5.9 for feed location at  $(x/a_e, y/a_e) = (0.5, 0.0)$  to 2.26 when the feed is located at  $(x/a_e, y/a_e) = (0.5, 0.345)$ . For  $y/a_e > 0.345$  on the line  $x/a_e = 0.5$ , the input VSWR starts increasing until at  $y/a_e = 0.5$  the input impedance ( $Z_{in} = 0.511 + j32.41$ ) tends to be purely reactive and the input VSWR becomes very large.

As illustrated in Fig. 5.13, the axial ratio degrades from 0.12 dB for feed at  $(x/a_e, y/a_e) = (0.5, 0.0)$  to a maxima of 0.4 dB for feed at  $(x/a_e, y/a_e) = (0.5, 0.45)$ . The value of axial ratio for the feed location at  $(x/a_e, y/a_e) = (0.5, 0.345)$ , where the input VSWR is minimum, is 0.36 dB. For the optimum location of the feed port, the best axial ratio (0.02 dB) occurs at 3.1758 GHz. This frequency is 0.8 MHz above the frequency at which the best circular polarization (axial ratio = 0.12 dB) is obtained when the antenna is fed at  $(x/a_e, y/a_e) = (0.5, 0.0)$ . Such a shift in frequency has been observed in case of diagonal fed antennas also as discussed in Section 4.3. Thus it is found that the feed can be located on the line  $x/a_e = 0.5$  to realize better input VSWR without affecting the polarization characteristics. Also the feed can be located on the line  $y/a_e = 0.5$  to realize



the same input VSWR values, as for feed locations on the line  $x/a_e = 0.5$ , but the relative phase difference between  $E_\theta$  and  $E_\phi$  changes sign and the sense of polarization is reversed. For the antenna discussed in the preceeding sections, the values of dielectric constant and thickness of the substrate were taken to be 2.52 and  $1/8$ " respectively.

Another antenna on  $1/16$ " substrate having  $\epsilon_r = 2.51$  has been designed for S-band operation. The dimension 'a' of the square patch was choosen equal to 2.86 cm and the optimum truncation for the best axial ratio (0.12 dB) is  $'0.0573a'$ . The variation of input VSWR with feed location is shown in Fig. 5.14. In this case the best input VSWR ( $= 1.6$ ) is obtained when the feed is located at  $(x/a_e, y/a_e) = (0.5, 0.33)$ . The optimum value of axial ratio (0.12 dB) for this feed location occurs at 3.1756 GHz. The calculated values of resonance frequencies of the two orthogonal modes for this antenna are 3.1370 GHz and 3.234 GHz. The corresponding measured values are 3.1343 GHz and 3.2298 GHz respectively.

For both the antennas the axial ratio and input VSWR are calculated at several frequencies. The beamwidths for the antennas are obtained from the radiation patterns at the frequencies where the best <sup>axial</sup> ratio is observed. These aspects are discussed in the following section.

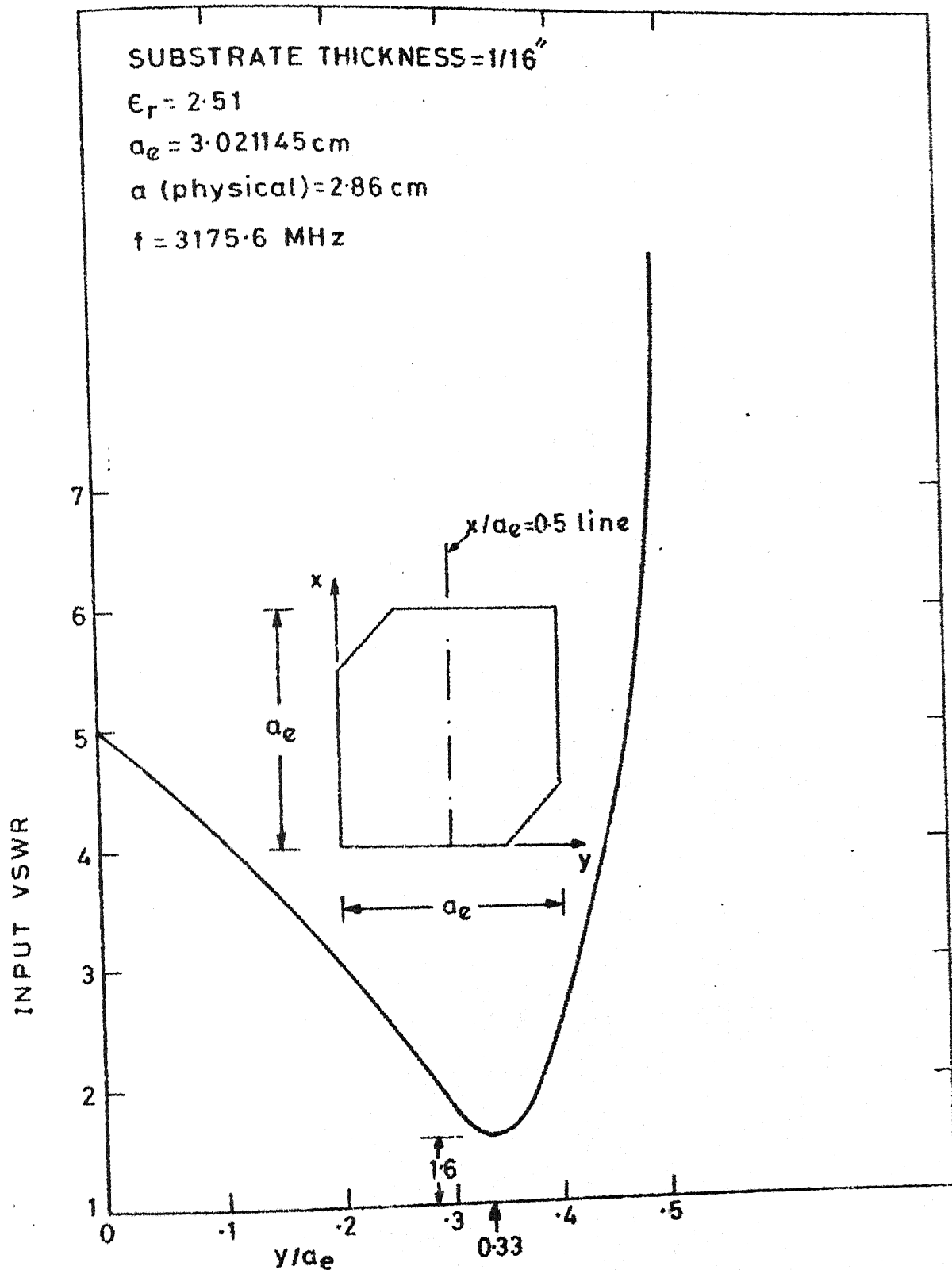


FIG. 5-14 VARIATION OF INPUT VSWR WITH FEED LOCATION ON  $x/a_e = 0.5$  LINE FOR A  $1/16''$  SUBSTRATE ANTENNA

## 5.4 BANDWIDTH AND BEAMWIDTH

### 5.4.1 Variation of input VSWR with frequency

The calculated values of input VSWR as a function of frequency (in the frequency range over which the axial ratio remains less than 6 dB) for the two antennas investigated are plotted in Figs. 5.15 and 5.16. For the 1/8" thick substrate ( $\epsilon_r = 2.52$ ) antenna the input VSWR variation (theoretically) over the entire band of frequencies of interest remains practically constant as illustrated in Fig. 5.15. The value of input VSWR at center frequency (3.1758 GHz at which the best axial ratio is = 0.02 dB) is 2.26. At 3.169 GHz the input VSWR is 2.15 and at 3.190 GHz the value of input VSWR is 2.2. The measured values of input VSWR are also plotted in Fig. 5.15.

For the antenna on thinner substrate (thickness = 1/16",  $\epsilon_r = 2.51$ ) the input VSWR (1.6) is found to remain practically constant from 3.167 GHz to 3.183 GHz as shown in Fig. 5.16. Experimental results are also illustrated in the figure. The center frequency for this antenna is 3.1756 GHz and the axial ratio at this frequency is 0.12 dB. It is thus observed that by using thinner substrates, better values of input VSWR may be realized. A discussion on variation of axial ratio with frequency for the two antennas is given in the following paragraphs.

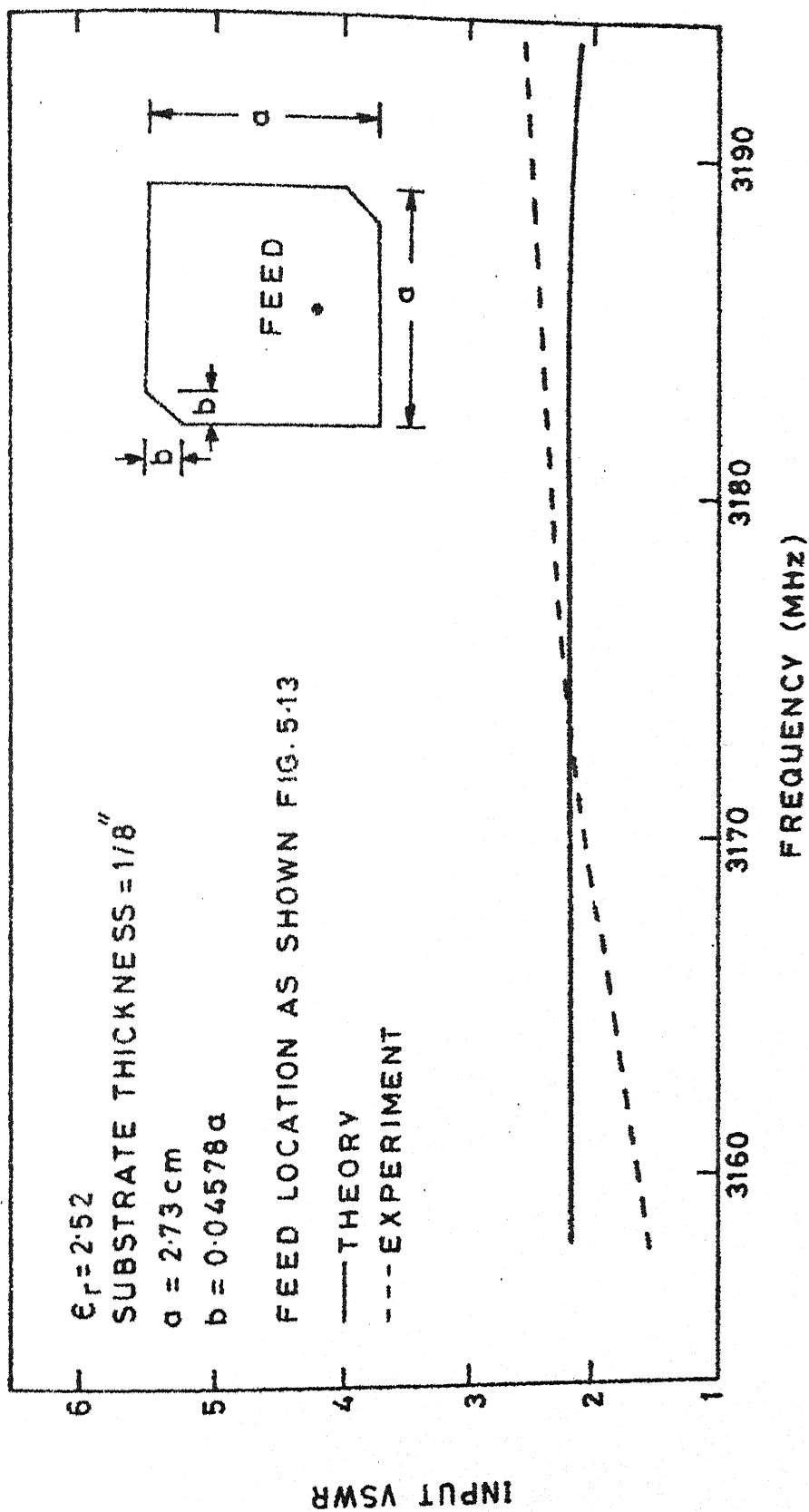


FIG.5-15 VARIATION OF INPUT VSWR WITH FREQUENCY FOR A  
CORNERS CHOPPED SQUARE PATCH ANTENNA

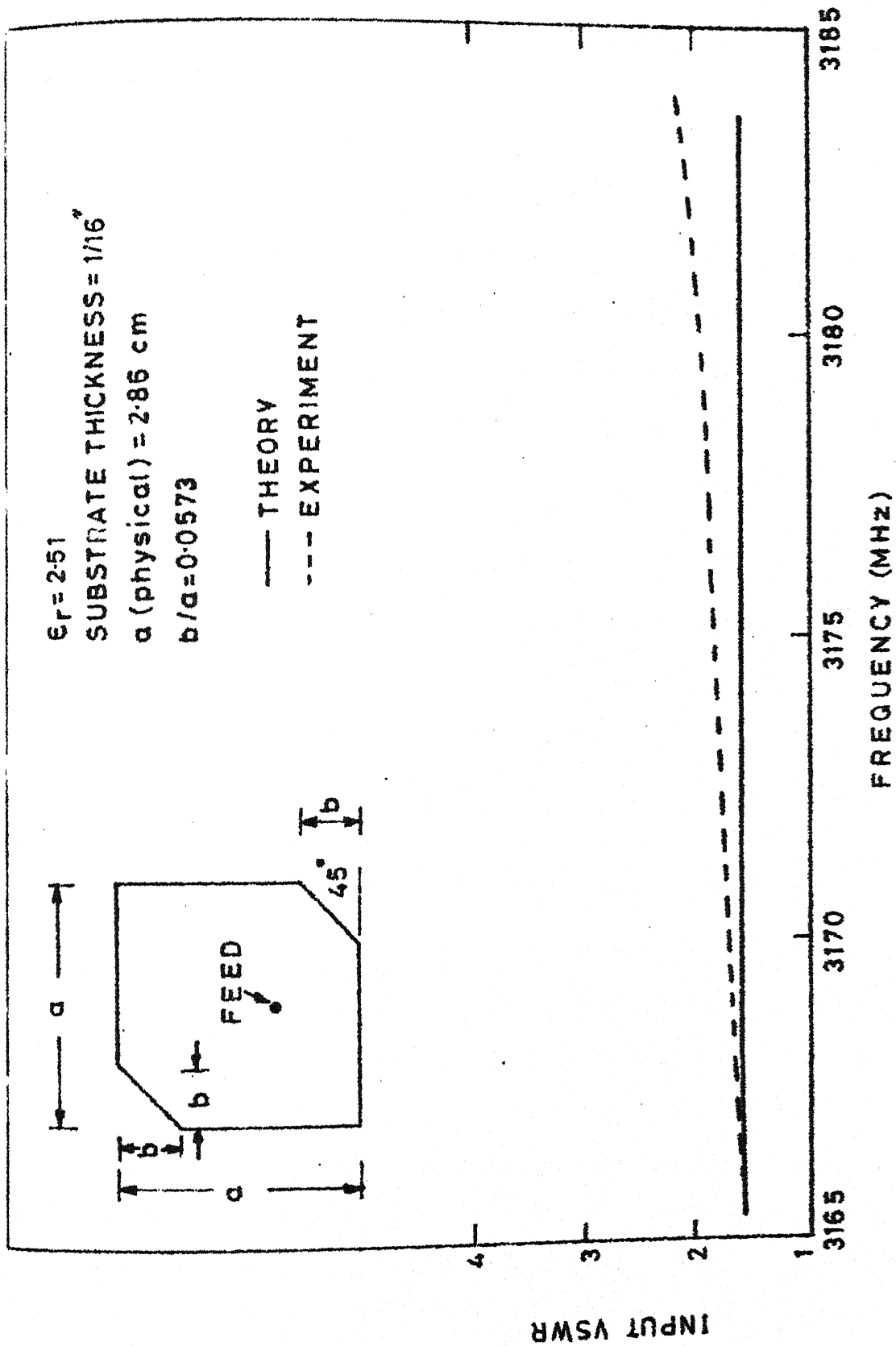


FIG. 5.16 VARIATION OF INPUT VSWR WITH FREQUENCY FOR A  $1/16"$  SUBSTRATE CORNERS CHOPPED ANTENNA. FEED LOCATION IS AS OPTIMIZED IN FIG. 5.14

#### 5.4.2 Variation of axial ratio with frequency

For the two antennas, designed on polystyrene substrates of thickness  $1/8"$  and  $1/16"$  (with  $\epsilon_r = 2.52$  and  $2.51$  respectively) the variations of axial ratio with frequency are shown in Figs. 5.17 and 5.18.

For the  $1/8"$  thick antenna the best value of axial ratio ( $= 0.02$  dB) is found (theoretically) to occur at  $3.1758$  GHz. The feed location is at  $(x/a_e, y/a_e) = (0.5, 0.345)$  where the input VSWR is found to be minimum (Fig. 5.13). It may be recalled that for feed at  $(x/a_e, y/a_e) = (0.5, 0.0)$ , the best value of axial ratio equal to  $0.12$  dB is obtained at  $3.175$  GHz. Thus there is a shift in center frequency by an amount equal to  $0.8$  MHz and also the axial ratio improves (becomes  $0.02$  dB) when the feed is located at  $(x/a_e, y/a_e) = (0.5, 0.345)$ . The bandwidth, for axial ratio  $< 6$  dB, is found to be  $26.4$  MHz (theoretically) and  $29.4$  MHz (experimentally). These values correspond to  $0.831$  percent and  $0.925$  percent.

The corresponding value of bandwidth for an S-band antenna on a substrate of thickness  $= 1/16"$  and  $\epsilon_r = 2.51$  is found to be  $14$  MHz (theoretically) which corresponds to  $0.4408$  percent. The best axial ratio ( $0.12$  dB) is found to occur at  $3175.6$  MHz (Fig. 5.18). The axial ratio limited bandwidth for the  $1/16"$  substrate antenna is nearly  $47$  percent less than that for the  $1/8"$  substrate antenna. It may be

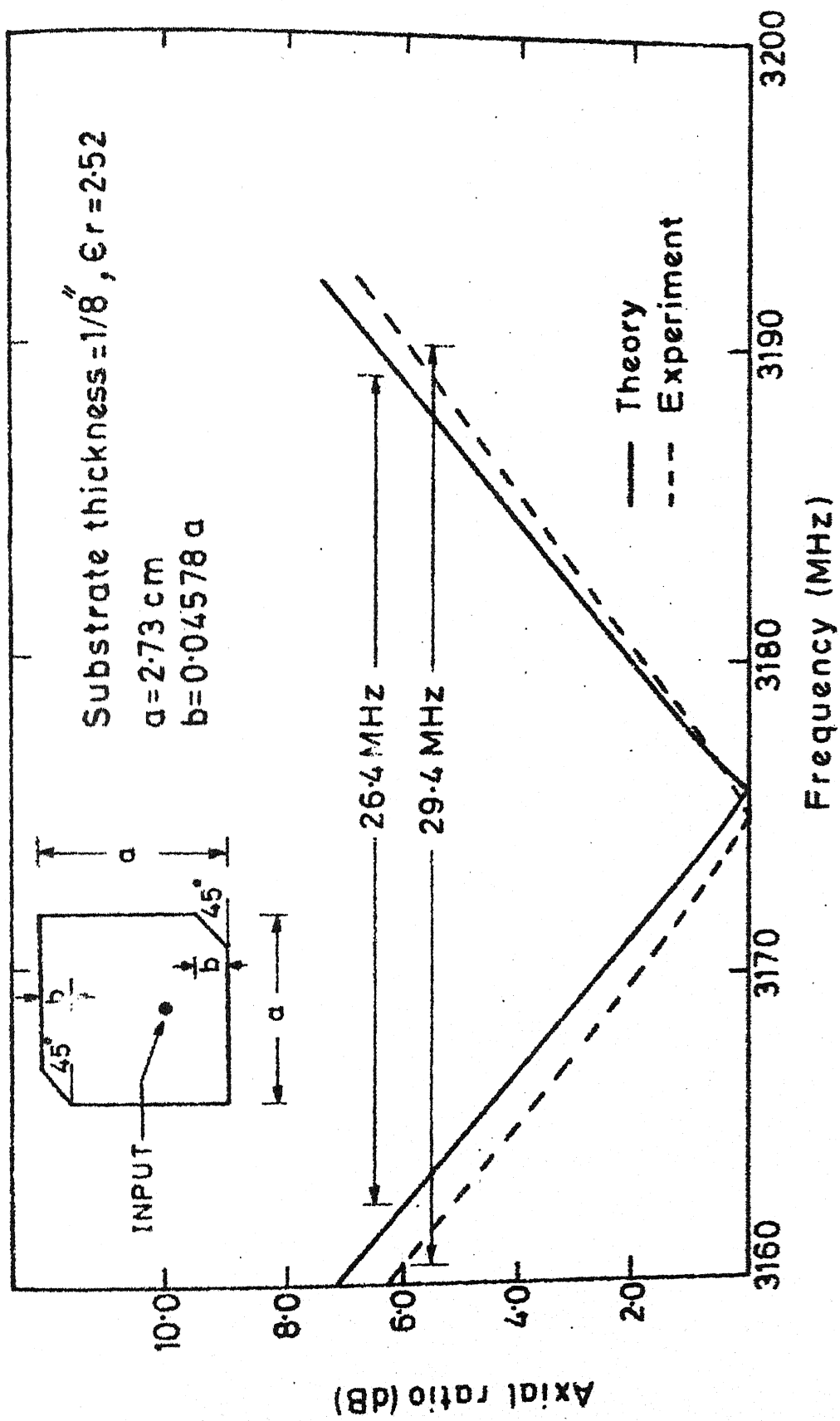


FIG.5.17 VARIATION OF AXIAL RATIO WITH FREQUENCY FOR CORNERS  
 CHOPPED ANTENNA ON  $1/8$ " THICK SUBSTRATE

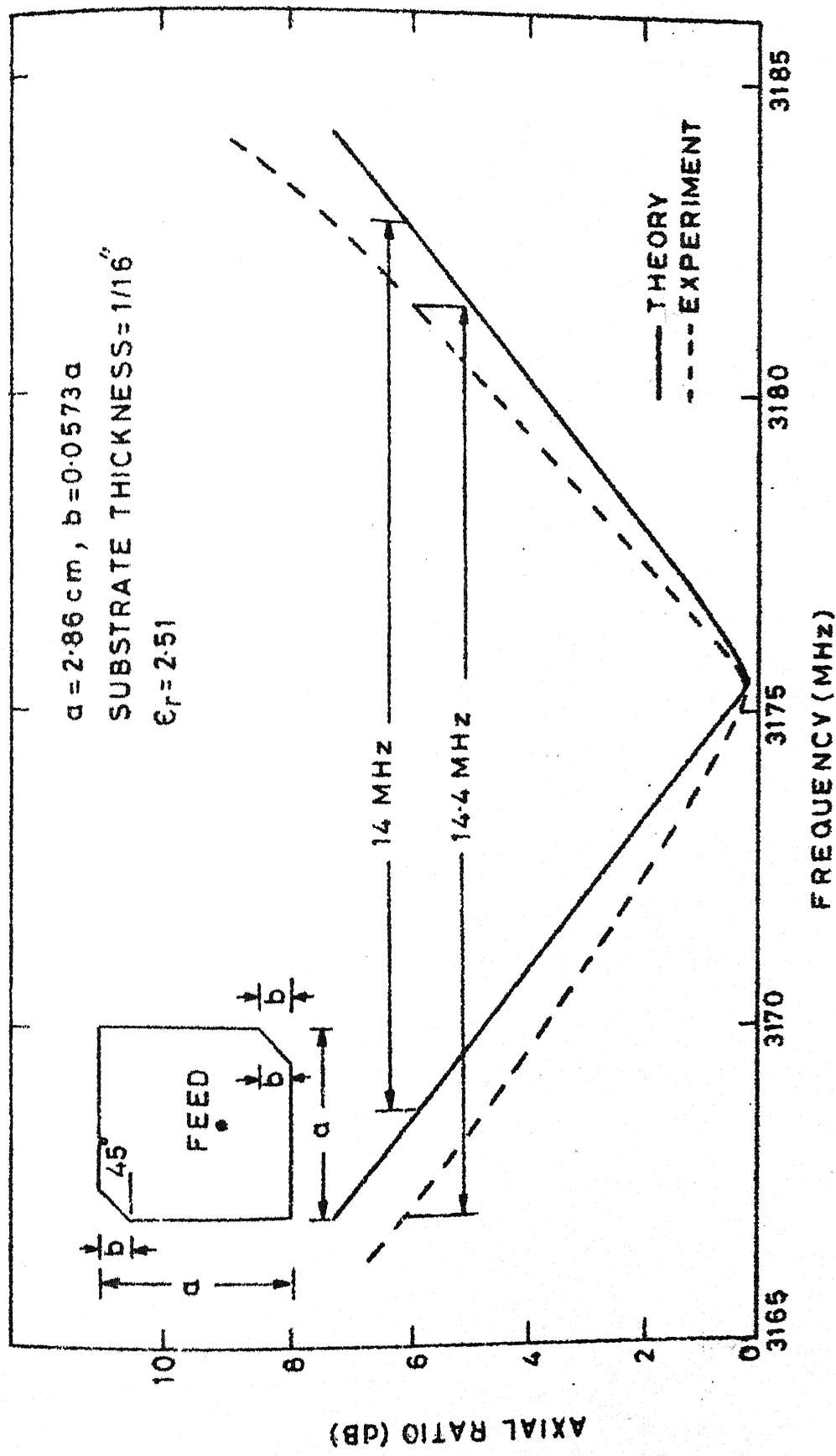


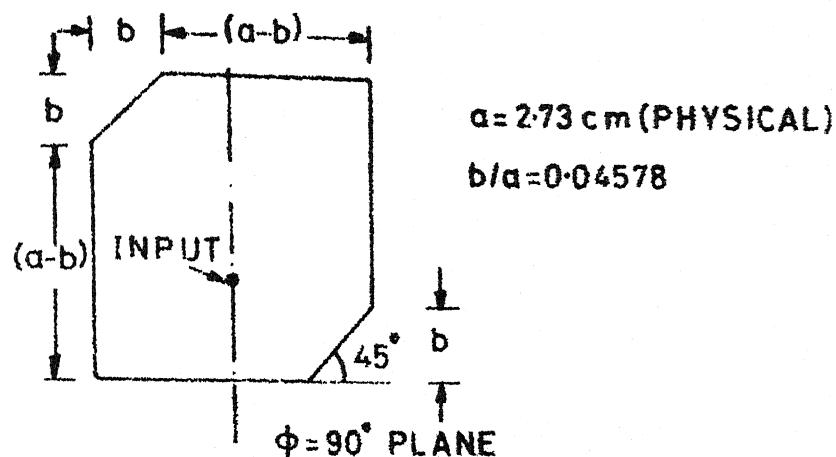
FIG. 5-18 VARIATION OF AXIAL RATIO WITH FREQUENCY FOR A CORNERS  
CHOPPED SQUARE PATCH ANTENNA ON  $1/16"$  THICK SUBSTRATE



noted that since the values of  $\epsilon_r$  in the two cases are nearly equal, the reduction in bandwidth is mainly due to the reduction in thickness of the antenna. Such a reduction (41 percent) in bandwidth has been observed in the case of diagonal fed antenna also, as discussed in Section 4.4. Also from Figs. 5.15 - 5.18, it is observed that the bandwidth is limited by axial ratio in case of both the corners chopped antennas. The input VSWR variation is very small over the frequency range over which the axial ratio remains less than 6 dB.

#### 5.4.3 Radiation pattern

The radiation pattern for the antenna, in  $\varphi = 90^\circ$  plane and at frequency 3.1758 GHz, designed on a substrate of thickness  $1/8"$  with  $\epsilon_r = 2.52$ , is shown in Fig. 5.19. The beamwidth for 3 dB difference between  $E_\theta$  and  $E_\varphi$  is  $129^\circ$  ( $-64.5^\circ < \theta < 64.5^\circ$ ) and that for 6 dB difference between  $E_\theta$  and  $E_\varphi$  is  $142^\circ$  ( $-71^\circ < \theta < 71^\circ$ ). For the  $1/16"$  substrate antenna ( $\epsilon_r = 2.51$ ) the radiation pattern, at frequency (3.1752 GHz) where the best axial ratio is obtained, is shown in Fig. 5.20. The beamwidth for 3 dB and 6 dB difference between  $E_\theta$  and  $E_\varphi$  are found to be  $129^\circ$  and  $142^\circ$  respectively. Thus the beamwidths for the corners chopped antennas on  $1/8"$  and  $1/16"$  thick substrate antennas are found to be equal.



SUBSTRATE THICKNESS  $= 1/8''$ ;  $\epsilon_r = 2.52$

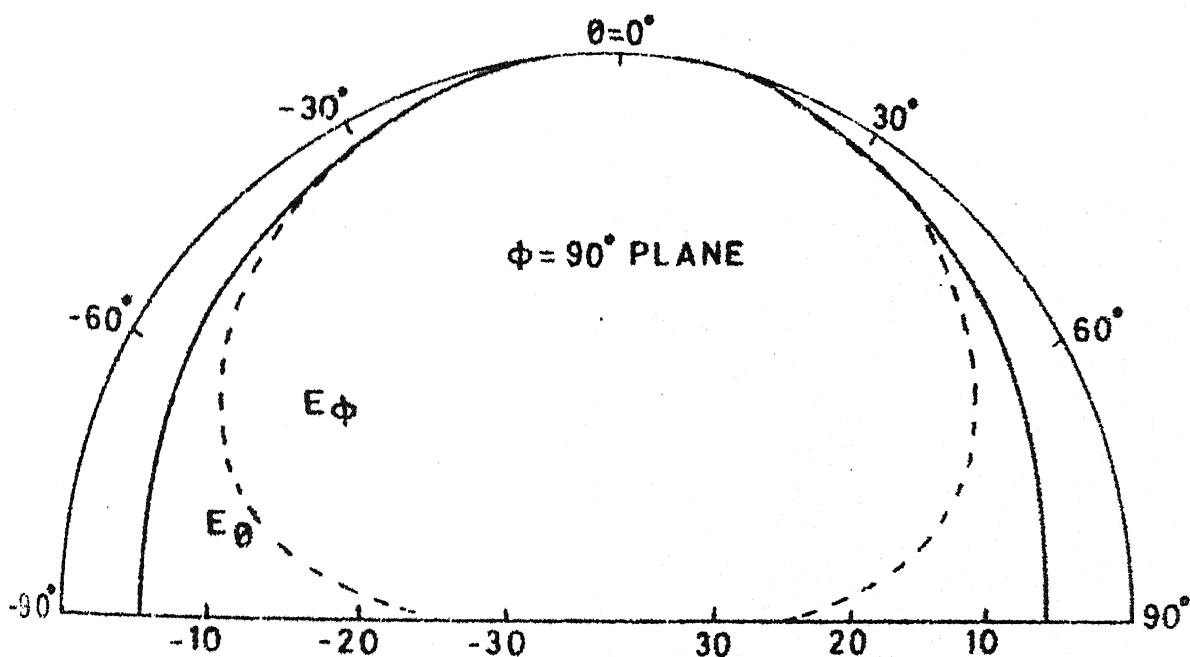
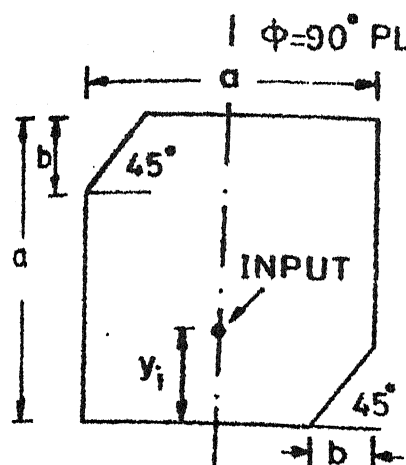


FIG-5-19 THE CORNERS CHOPPED SQUARE PATCH ANTENNA AND ITS RADIATION PATTERN IN  $\phi = 90^\circ$  PLANE AT 3175.8 MHz



$$a = 2.86 \text{ cm}$$

$$b/a = 0.0573$$

$$f = 3.1752 \text{ GHz}$$

$$y_i = 0.33 a_e$$

$$a_e = a \text{ (EFFECTIVE)}$$

$$\epsilon_r = 2.51$$

SUBSTRATE THICKNESS =  $1/16''$

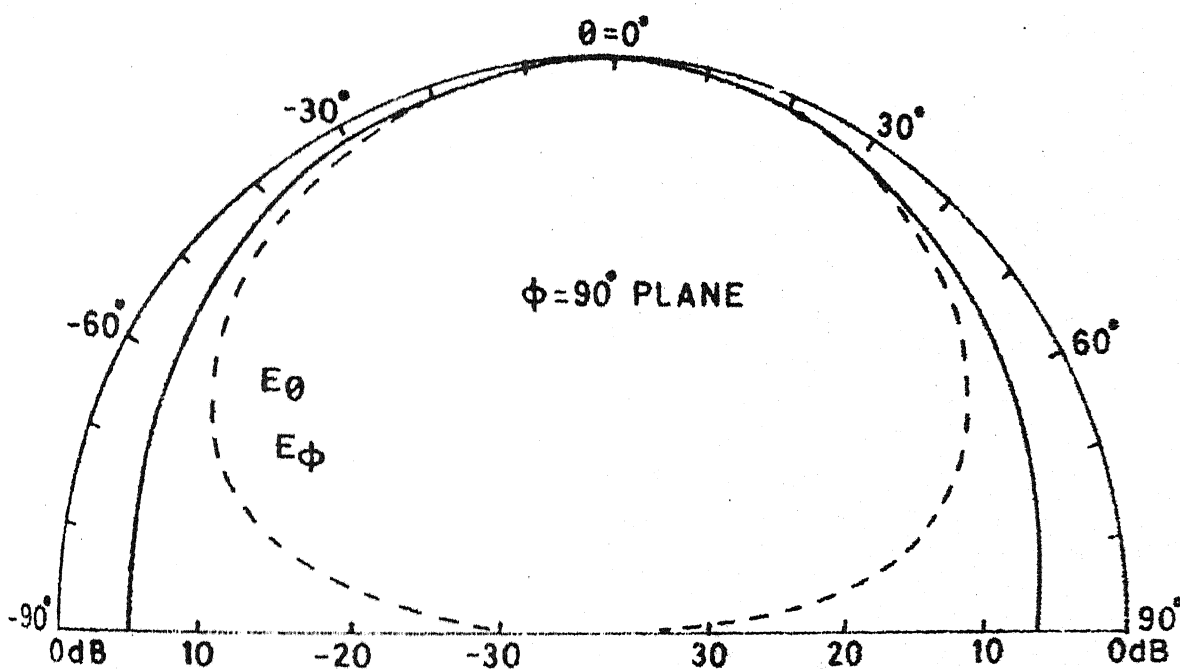


FIG. 5.20 RADIATION PATTERN (in  $\phi = 90^\circ$  plane) FOR CORNERS CHOPPED ANTENNA ON A POLYSTYREN SUBSTRATE OF THICKNESS =  $1/16''$

## 5.5 EXPERIMENTAL RESULTS

The photographs of the fabricated antennas are shown in Fig. 5.21. The experimental set up is shown in Fig. 4.22. The variations of axial ratio with frequency for the two antennas ( $1/8$ " thick substrate with  $\epsilon_r = 2.52$  and  $1/16$ " thick substrate with  $\epsilon_r = 2.51$ ) are shown in Fig. 5.17 and in Fig. 5.18. The measured values of bandwidths for the two antennas are 29.4 MHz (0.925 percent) and 14.4 MHz (0.4535 percent). The input VSWR variations with frequency for the two antennas are illustrated in Figs. 5.15 and 5.16. It is observed from these figures that the input VSWR ( $=1.8$ ) for antenna on a substrate of  $1/16$ " is better than the input VSWR ( $=2.26$ ) for  $1/8$ " substrate antenna. The measured value of axial ratio bandwidth is, of course, 51 percent less for the  $1/16$ " substrate as compared to that for  $1/8$ " substrate antenna.

For comparison the theoretical and experimental values of far-field components are shown in Figs. 5.22 and 5.23. The results of the study of the two antennas are summarized in Table 5.1 and in Table 5.2.

## 5.6 DISCUSSIONS

Two corners chopped square antennas fabricated on polystyrene substrates having substrate thickness  $1/8$ " ( $\epsilon_r = 2.52$ ) and  $1/16$ " ( $\epsilon_r = 2.51$ ) have been investigated. The

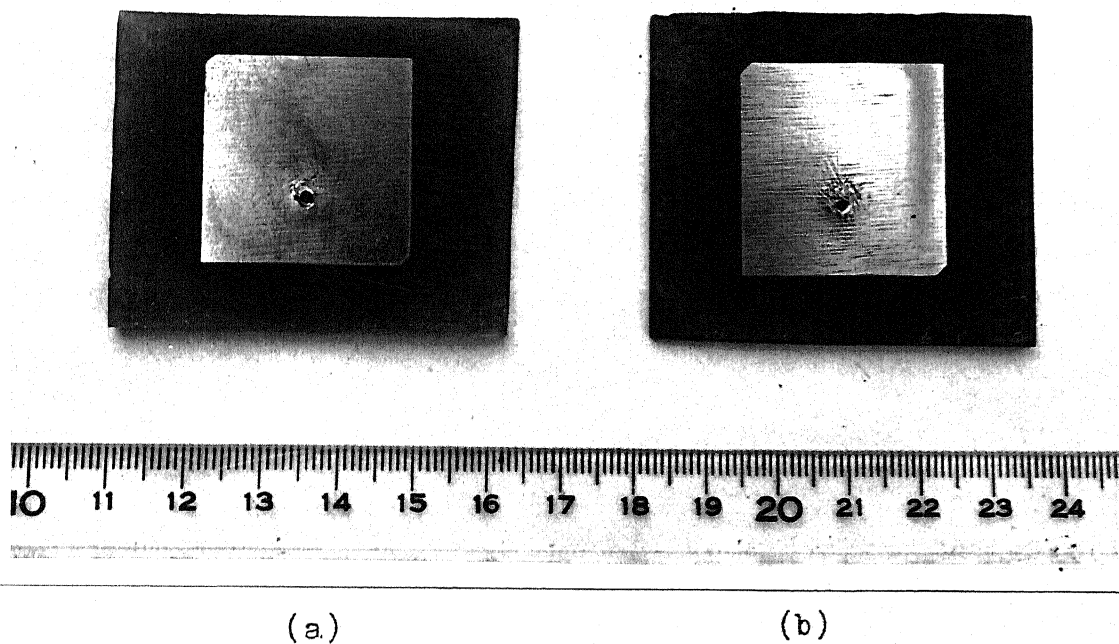


Fig. 5.21 Photograph of the corners chopped antennas  
a) substrate thickness =  $1/8"$ ,  $\epsilon_r = 2.52$   
b) substrate thickness =  $1/16"$ ,  $\epsilon_r = 2.51$

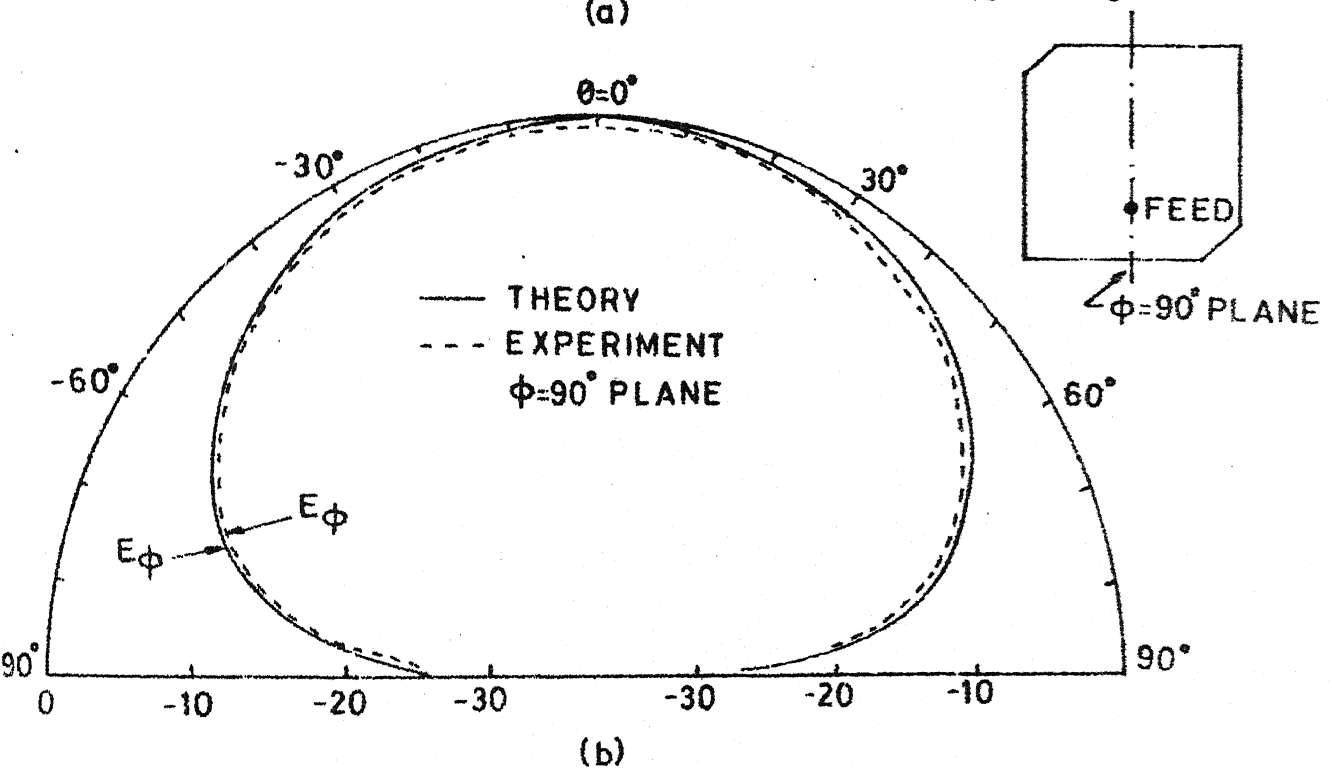
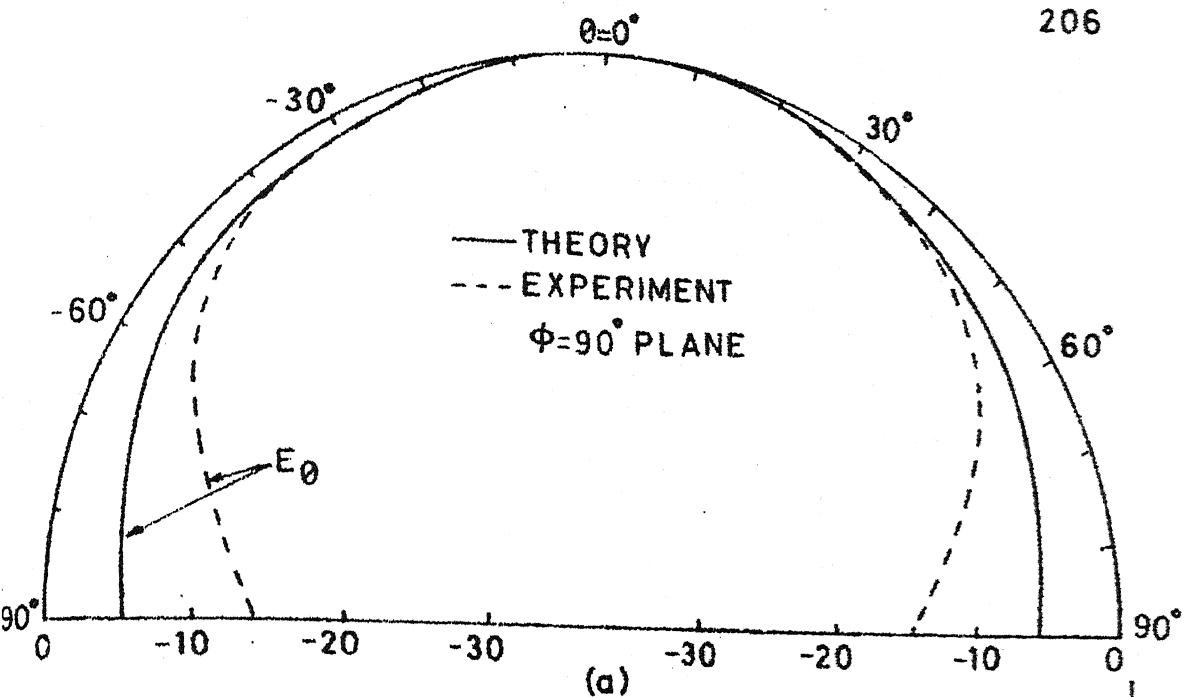


FIG. 5-22 THEORETICAL AND MEASURED VALUES OF  $E_\theta$  AND  $E_\phi$  (in  $\phi=90^\circ$  plane) FOR CORNERS CHOPPED ANTENNA SHOWN IN PHOTOGRAPH 5-21(a)  
Substrate thickness =  $1/8''$ ,  $\epsilon_r = 2.52$

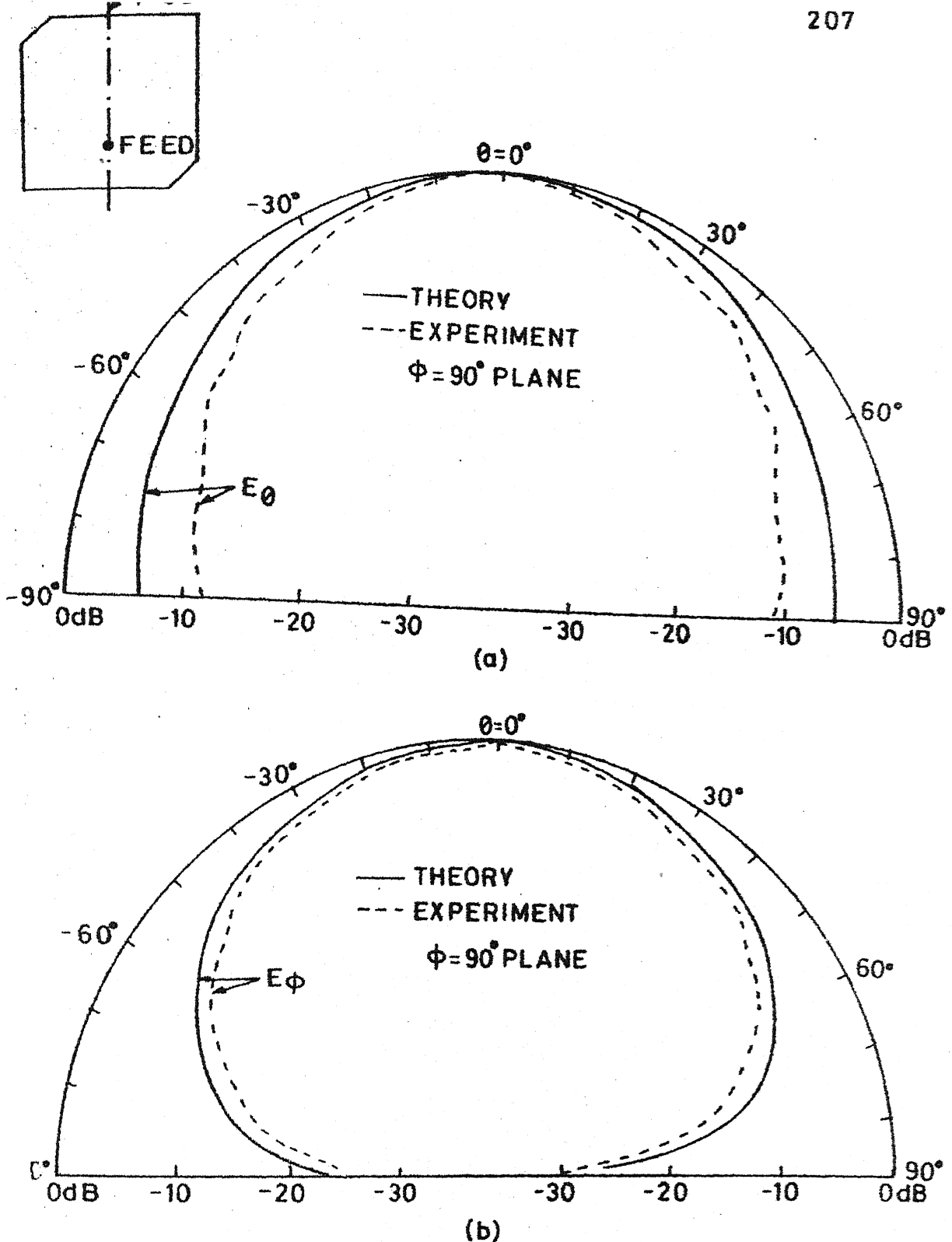


FIG.5-23 RADIATION PATTERN FOR A CORNERS CHOPPED ANTENNA (on 1/16" polystyrene substrate with  $\epsilon_r=251$ ) SHOWN IN PHOTOGRAPH 521(b)

Table 5.1 Summary of results for a corners chopped antenna fabricated on a substrate of thickness equal to  $1/8''$  with  $\epsilon_r = 2.52$ .  
 Dimensions of the square patch  $= 2.73 \times 2.73 \text{ cm}^2$ ,  
 Truncation of corners  $= 0.04578 \text{ a cm}$

	Theoretical value	Experimental value
1. Center frequency (GHz)	3.1758	3.1750
2. Resonance frequencies of orthogonal modes (GHz)	3.1340 3.2155	3.1325 3.2125
3. Axial ratio at center frequency (dB)	0.02	$\approx 0.0$
4. Bandwidth (MHz) for axial ratio $< 6 \text{ dB}$	26.4 (0.831%)	29.4 (0.925%)
5. Input VSWR at center frequency	2.26	2.26
6. Beamwidth for difference between $ E_\theta $ and $ E_\phi $		
i) $< 3 \text{ dB}$	$-64.5^\circ < \theta < 64.5^\circ$	$-76^\circ < \theta < 76^\circ$
ii) $< 6 \text{ dB}$	$-71^\circ < \theta < 71^\circ$	$-81^\circ < \theta < 81^\circ$



Table 5.2 Summary of results for a corners chopped antenna fabricated on a substrate of thickness equal to  $1/16''$  with  $\epsilon_r = 2.51$ .  
 Dimensions of the square patch =  $2.86 \times 2.86 \text{ cm}^2$   
 Truncation =  $0.0573a \text{ cm}$

	Theoretical value	Experimental value
1. Center frequency (GHz) (GHz)	3.1756	3.1753
2. Resonance frequency of orthogonal modes (GHz)	3.1370 3.2340	3.1343 3.2298
3. Axial ratio (dB) at center frequency	0.12	0.15
4. Bandwidth (MHz) for axial ratio $< 6 \text{ dB}$	14.0 (0.44%)	14.4 (0.4535%)
5. Input VSWR at center frequency	1.6	1.8
6. Beamwidth for difference between $ E_\theta $ and $ E_\phi $		
i) $< 3 \text{ dB}$	$-64.5^\circ < \theta < 64.5^\circ$	$-69^\circ < \theta < 69^\circ$
ii) $< 6 \text{ dB}$	$-71^\circ < \theta < 71^\circ$	$-80^\circ < \theta < 80^\circ$

theoretical analysis has been carried out employing the desegmentation method. Axial ratio as good as 0.02 dB and 0.12 dB have been realized. The location of the feed, in both the cases, is determined for minimum obtainable input VSWR (with respect to a 50 Ohms coaxial line). It is observed that change in feed location on the line joining the mid-points of two opposite sides of the antenna causes a small shift in frequency at which the best circular polarization is observed. Also, as in the case of diagonal fed antenna discussed in Chapter Four, the bandwidth of the corners chopped antennas is limited by axial ratio and not by input VSWR.

The effects of thickness of the substrate on axial ratio bandwidth and VSWR bandwidth are studied. It is found that reduction in the thickness of the substrate to half the value reduces the axial ratio bandwidth by 51 percent as measured and by nearly 47 percent as evaluated theoretically. Thinner substrates of course yield better values of input VSWR. The beamwidths for both the substrates thicknesses are equal. The measured values of beamwidths are found to be greater than the respective theoretical values as in case of diagonal fed antennas discussed in Chapter Four.

The theoretical and experimental results are found to be in good agreement. The experimental values of axial ratio bandwidth are, of course, slightly greater (by 3 MHz for  $1/8''$

substrate antenna and by 0.4 MHz for 1/16" substrate antenna) than the respective theoretical values. This difference is expected because losses in the dielectric and those in the conductors have been ignored in the analysis. These losses decrease the Q-factor and thus increase the bandwidth.

## CHAPTER SIX

### SQUARE PATCH ANTENNA WITH A DIAGONAL SLOT

As pointed out in Chapter One, a square patch antenna with a diagonal slot is capable of producing circular polarization. Some experimental results on the performance of this antenna have been reported earlier [33]. However, no theoretical procedure for analysis and design have been available so far. This chapter presents a detailed account of investigations carried out on this type of antenna employing the Green's function approach and the desegmentation method as proposed in Chapters Two and Three respectively. The results of theoretical investigations are verified experimentally.

#### 6.1 ANALYSIS AND OPTIMIZATION

A square patch antenna with a diagonal slot is shown in Fig. 6.1(a). For analysis and design, the antenna configuration is considered as a square patch ( $\gamma$ -segment) of dimensions 'a by a' from which a rectangular patch ( $\beta$ -segment) of dimensions 'p by w', located along the diagonal of the square, has been removed. In other words, if a rectangular patch ( $\beta$ -segment) is added to the antenna configuration ( $\alpha$ -segment) of Fig. 6.1(a), a regular square patch ( $\gamma$ -segment) is obtained. This is illustrated in Fig. 6.1(b). The desegmentation method can therefore be used for evaluating the Z-

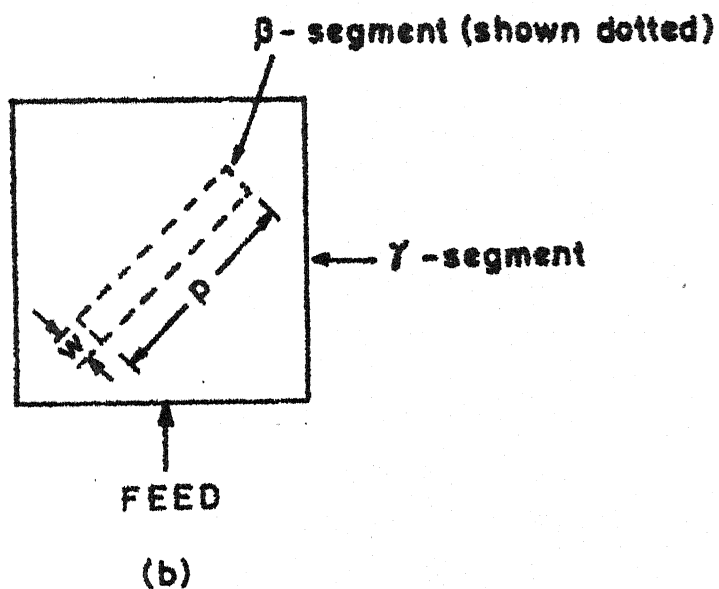
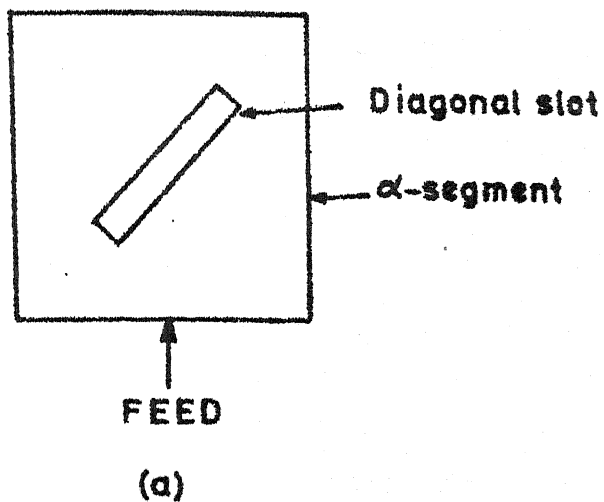


FIG.6.1 (a) A SQUARE PATCH WITH A DIAGONAL SLOT ;  
 (b)  $\gamma$ - SEGMENT AS COMBINATION OF  $\alpha$ - AND  $\beta$ -  
 SEGMENTS

parameters of the  $\alpha$ -segment of Fig. 6.1(a) by using the procedure illustrated for planar circuit example 2 discussed in Section 3.4.4. The Z-matrices for  $\beta$ - and  $\gamma$ -segments (Fig. 6.1) are evaluated employing the Green's function for rectangular planar segment [1]. A detailed discussion on analysis and optimization of the dimensions of the slot for obtaining the best axial ratio is given in this section.

#### 6.1.1 Evaluation of Z-matrix for multiport model

For analyzing the antenna configuration of Fig. 6.1(a), the outer boundary of the planar model, after outward extension to account for fringing field, is considered to be divided into a discrete number of ports as shown in Fig. 6.2. The input port is considered to be located at mid-point of one of the sides as in Fig. 6.2. The periphery of the diagonal slot which constitutes the interface between  $\beta$ - and  $\gamma$ -segments is also divided into discrete number of ports. The locations of c- and d-ports are shown in Fig. 6.2. The q-ports are located on the surface of the  $\beta$ -segment as in the case of planar circuit example 2 in Section 3.4.4. It is found in the present case that 27 q-ports are sufficient for the convergence of the values of the Z-parameters of the  $\alpha$ -segment over the frequency range of interest. In order that formulation (3.14) can be used for evaluating the Z-matrix, it is required that the number of c-ports (= that of d-ports) should also be equal to 27 (= number of q-ports). This

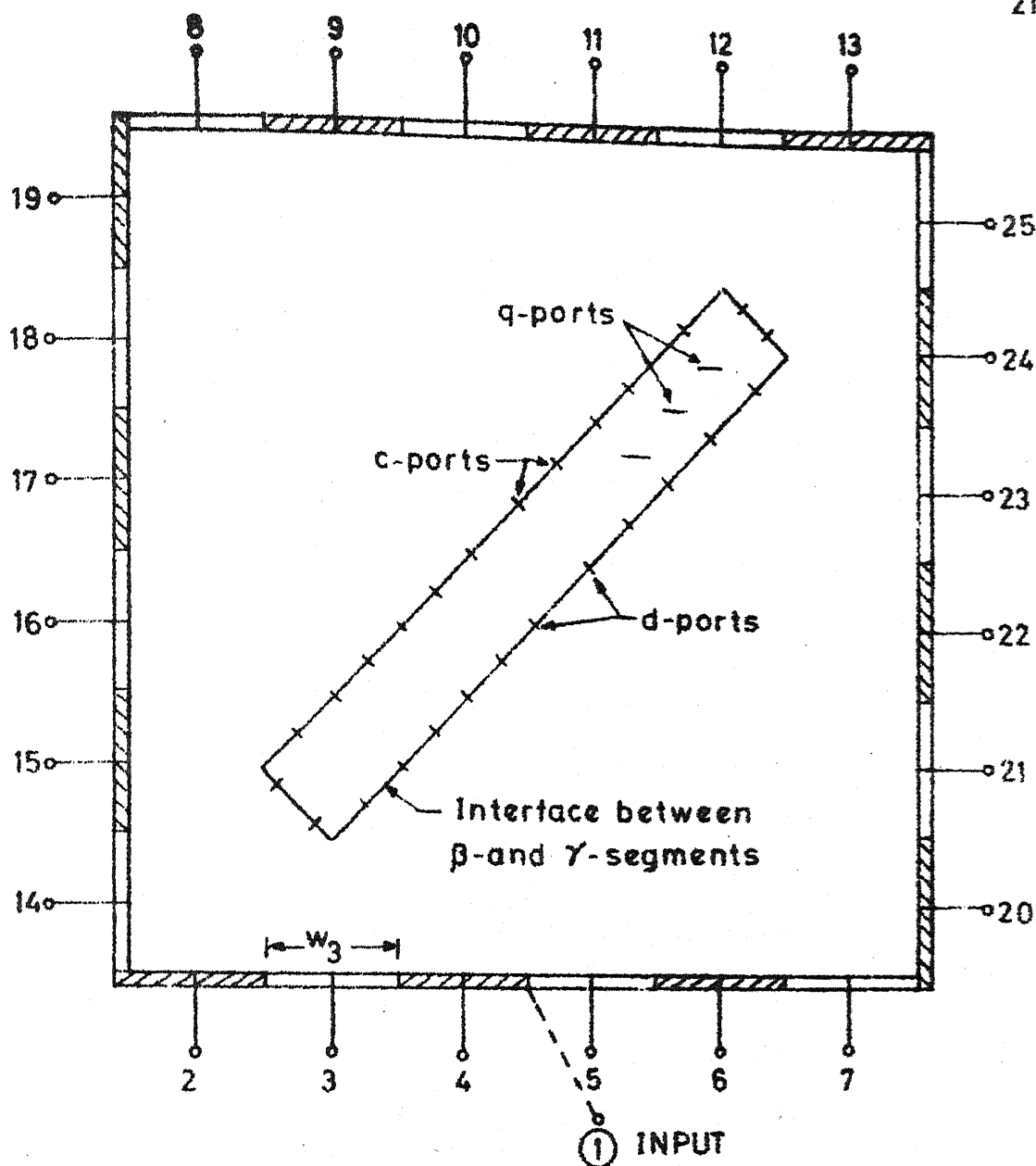


FIG. 6.2 LOCATION OF VARIOUS PORTS ON  $\gamma$ - AND  $\beta$ -SEGMENTS;  $P=25$ ;  $Q=C=D=27$ ; ONLY A FEW q-PORTS ARE SHOWN FOR CLARITY

implies that the periphery of the  $\beta$ -segment should be divided in 27 ports which constitute d-ports. Correspondingly, the periphery of the diagonal slot in the  $\alpha$ -segment should also be divided in 27 ports.

Experience with the analysis of a number of antenna configurations reveals that the portwidths at the radiating edges should be of the order of  $1/10$  of the wavelength, or smaller, for accurate analysis. This fact has been used to reduce the computational effort required for evaluating the Z-matrix of the multiport network model of Fig. 6.2 as explained below.

First consider the case when the outer periphery of the planar model ( $\alpha$ -segment) is divided in 24 ports (ports 2 to 25 in Fig. 6.2). An additional port is considered, on the periphery of the antenna, which represents the input port. The additionally incorporated port (numbered 1) overlaps the widths of two ports (numbered 4 and 5) in Fig. 6.2. This can always be done in theoretical analysis, since the voltages at only 2 to 25 on the periphery are used for evaluating the antenna performance. The ports 1 to 25 constitute the p-ports and correspond to  $P_1 = 25$  in reference with equation (3.16).

When  $C = D = Q = 27$ , it is required to evaluate all the submatrices of  $\underline{Z}_\beta$  and  $\underline{Z}_\gamma$  in order to employ (3.14). The matrix  $\underline{Z}_\beta$  is, therefore, of the order  $(D+Q) \times (D+Q) = 54 \times 54$ .



The Z-matrix of the  $\gamma$ -segment ( $\underline{Z}_\gamma$ ) is of the order  $52 \times 52$ , that is  $(P_1+Q) \times (P_1+Q)$ . Since  $\beta$ - and  $\gamma$ -segments are, both, rectangular, the computational efforts in evaluating the integral function (in the Green's function expression) at one port of  $\beta$ -segment and at one port of  $\gamma$ -segment are equal. That is  $E(\beta) = E(\gamma)$ . Hence, the total computational effort in evaluating  $\underline{Z}_\beta$  and  $\underline{Z}_\gamma$ , when procedure described in Section 3.2.3 is used, is obtained from (3.16) as

$$E_1 = 2Q + (P_1+Q) = 54 + 52 = 106 \text{ units.} \quad (6.1)$$

where it has been assumed that  $E(\beta) = E(\gamma) = 1$  unit.

Now consider the situation when 12-ports (numbered 26 to 37 in Fig. 6.3) are considered to be located around the radiating edges of the diagonal slot. These ports are treated as unconnected ports as explained in Section 3.2.5. Thus in reference with the nomenclature used in Sections 3.2.5 and 3.2.6, we have  $P_2 = 12$ . Total number of p-ports is thus  $P = P_1 + P_2 = 37$ . Since the additionally incorporated p-ports (12 in number) are located right at the radiating edges of the diagonal slot, the voltage distribution along the slot periphery can be evaluated from the Z-parameters corresponding to these ports. The validity of this procedure has been demonstrated by a lumped circuit example in Section 3.4.4 and the theoretical concept has been discussed in Section 3.2.5. In the present case we have  $P_1 = 25$ ,  $P_2 = 12$  and  $Q = 27$ . Since we may now employ (3.15), the orders of

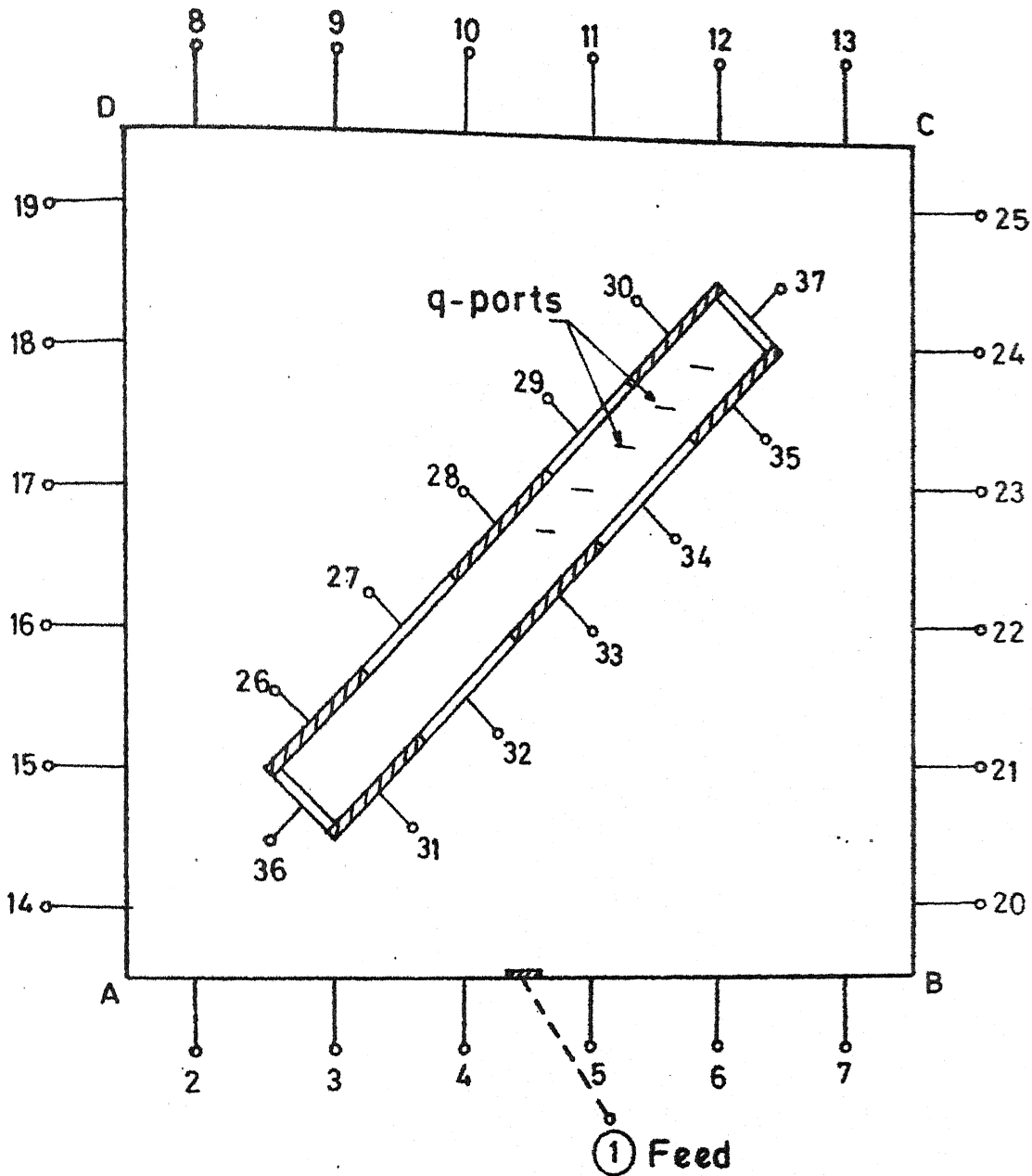


FIG-6-3 INCORPORATION OF ADDITIONAL p-PORTS(26to 37)  
 AROUND THE PERIPHERY OF THE SLOT;  $P=37, Q=27$   
 THIS SCHEME REDUCES COMPUTATIONAL EFFORT  
 AND COMPUTER STORAGE REQUIREMENT

the matrices  $\underline{Z}_\beta (= \underline{Z}_{qq\beta})$ , and  $\underline{Z}_\gamma$  are  $Q \times Q (= 27 \times 27)$  and  $(P_1+P_2+Q) \times (P_1+P_2+Q) = 64 \times 64$ , respectively. Assuming again  $E(\beta) = E(\gamma) = 1$ , the total computational effort in evaluating  $\underline{Z}_\beta (= \underline{Z}_{qq\beta})$  and  $\underline{Z}_\gamma$  is given by (3.17) as

$$E_2 = Q + (P_1+P_2+Q) = 27 + (25+12+27) = 91 \text{ units} \quad (6.2)$$

The orders of the matrices  $\underline{Z}_\beta$  and  $\underline{Z}_\gamma$  and the total computational efforts in evaluating these two matrices in the two schemes discussed above are summarized in Table 6.1.

Table 6.1 Orders of  $\underline{Z}_\beta$  and  $\underline{Z}_\gamma$  and total computational effort in evaluating these matrices

	Scheme of Fig. 6.2	Scheme of Fig. 6.3
1. Procedure employed	Section 3.2.3	Section 3.2.5
2. Orders matrices		
i) $\underline{Z}_\beta$	54 x 54	27 x 27
ii) $\underline{Z}_\gamma$	52 x 52	64 x 64
3. Computational effort	106 units	91 units

From Table 6.1 it is observed that the procedure discussed in Section 3.2.5 reduces the order of the matrix  $\underline{Z}_\beta$ . This reduces the total computational effort and computer storage requirements.

Both the schemes, discussed above, have been tried and it is found that the results for axial ratio and input VSWR agree exactly. It was then decided to employ the second scheme for detailed analysis of the antenna, the Z-matrix of the multiport equivalent of the planar model  $\alpha$ -segment being evaluated employing (3.15). The Z-matrix so obtained is that of an ideal multiport resonator model wherein the losses due to radiation have not been considered so far.

The radiated power is accounted for by terminating all the ports, except the input port, by radiation resistances [50] as explained in Section 2.1.1. The input impedance of the resultant network, loaded with radiation resistances, is evaluated employing the formulation (2.18a). The voltage along the periphery of the antenna is evaluated using (2.19) as explained in Section 2.1.2.

#### 6.1.2 Voltage along the radiating edges

The variations of voltage components (in-phase and quadrature components with respect to the input current phasor) along the (outer) periphery of the antenna and that along the periphery of the slot, for input port marked as 1 in Fig. 6.3, are shown in Figs. 6.4 and 6.5. These voltage distributions are for optimum dimensions of the antenna which result in the best axial ratio ( $= 0.198$  dB) at 3.130 GHz (for  $\epsilon_r = 2.52$  and substrate thickness  $= 1/8''$ ). The

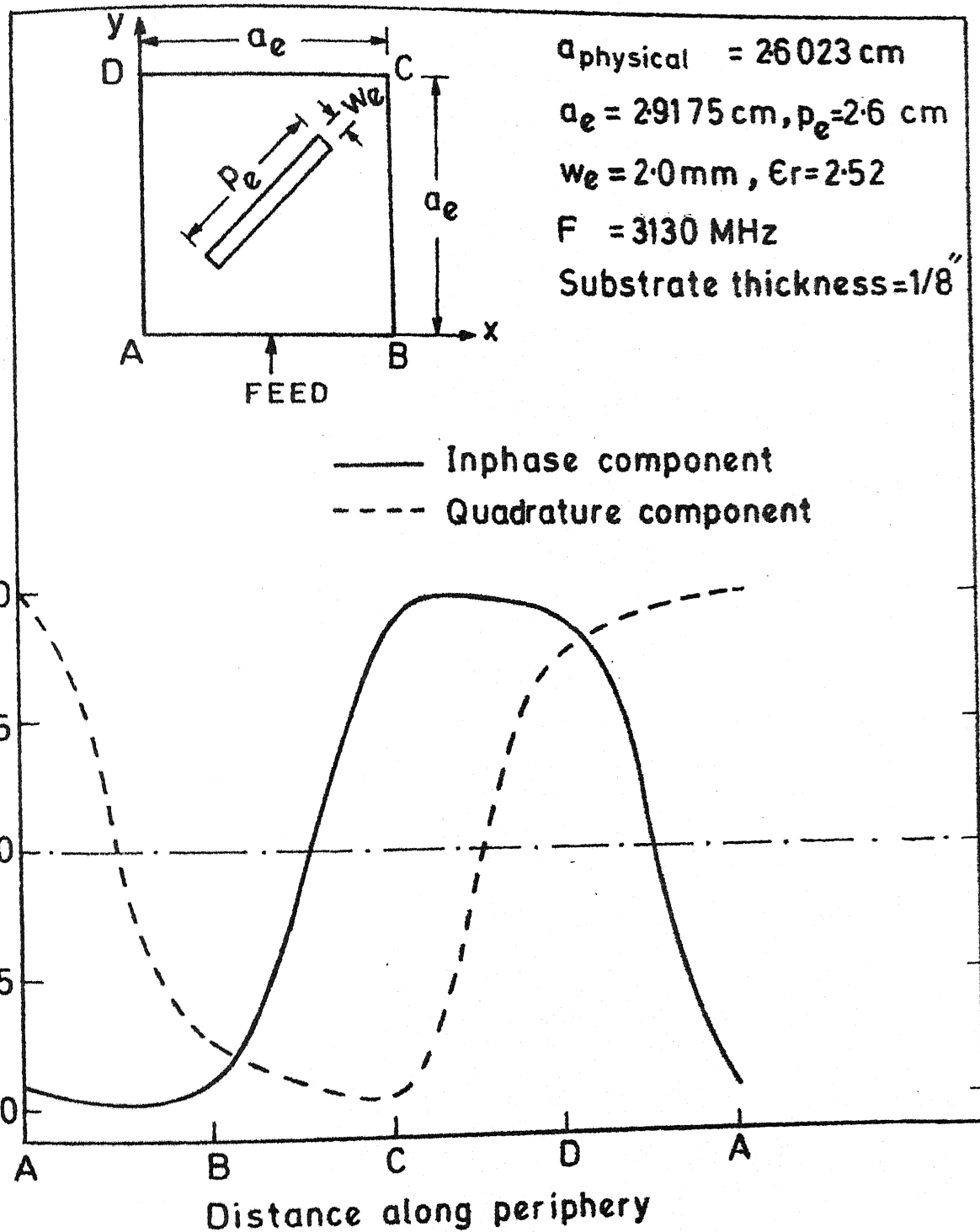


FIG. 6.4 VOLTAGE ALONG OUTER PERIPHERY OF THE ANTENNA

$\epsilon_r = 2.52$ ,  $p_e = 2.60 \text{ cm}$ ,  $w_e = 2.0 \text{ mm}$ ,  
 $a = 2.9175 \text{ cm}$ ,  $f = 3130 \text{ MHz}$   
 Substrate thickness  $= 1/8''$

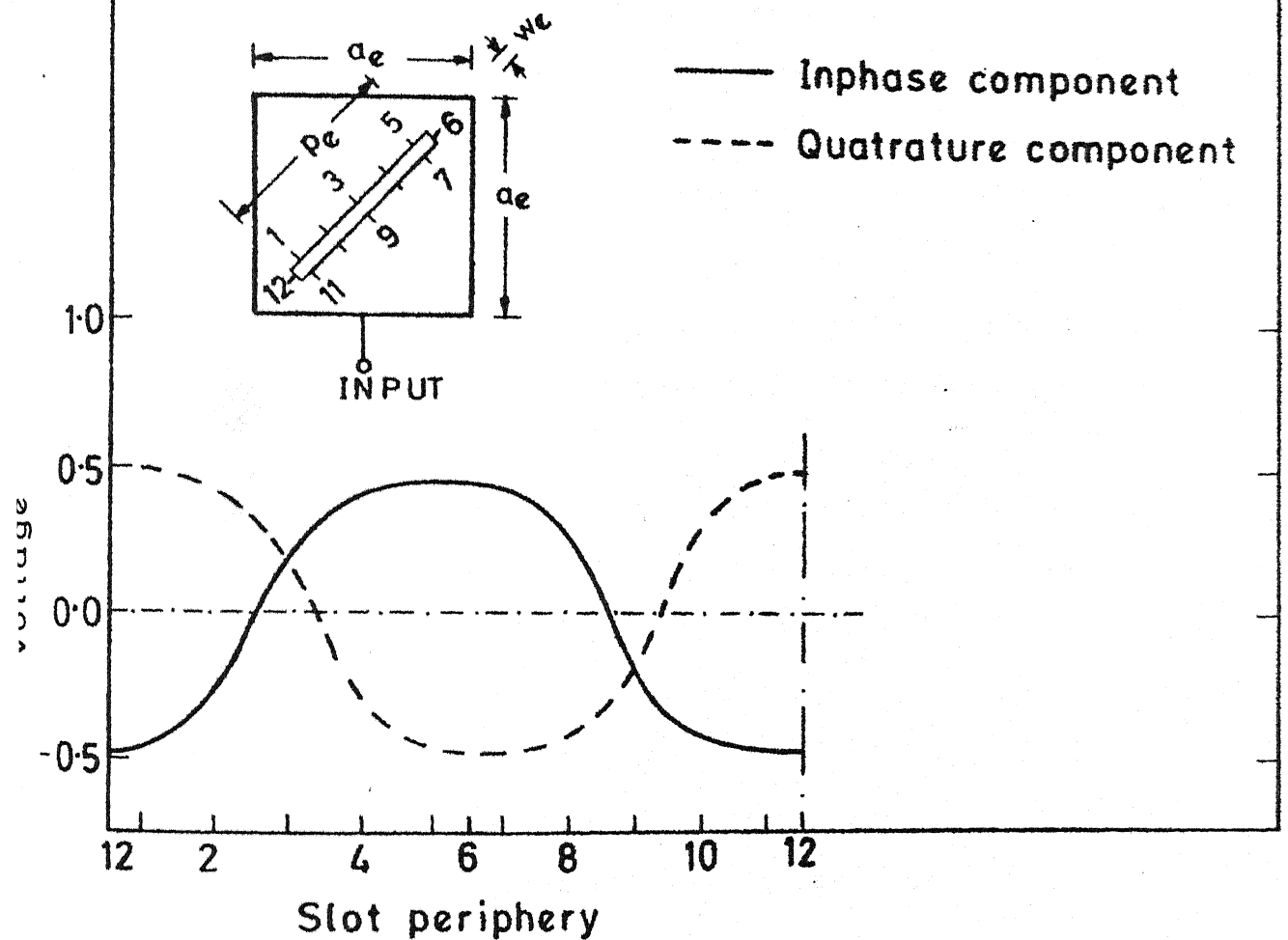


FIG. 6.5 VOLTAGE VARIATION ALONG THE PERIPHERY OF THE SLOT

effective dimensions of the antenna are :  $a_e = 2.9175$  cm,  $p_e = 2.6$  cm,  $w_e = 2.0$  mm. These voltage distributions (Figs. 6.4 and 6.5) are expressed as equivalent magnetic currents for evaluating the radiation characteristics of the antenna.

### 6.1.3 Magnetic current distribution

The linear magnetic current density ( $V$ ), equivalent to the voltage at a port is evaluated from (2.2). The magnetic current moment distribution, equivalent to the voltage distributions shown in Figs. 6.4 and 6.5, is shown in Fig. 6.6. The components of the magnetic current moments (the inphase and quadrature components) along the radiating edges of the antenna are added vectorially to obtain the resultant magnetic current moments as shown in Fig. 6.6. The two resultant component vectors, in phase-quadrature, are separated by an angle  $90.003^\circ$  in space. The normalized amplitudes of the two resultant moment vectors are 20.7188 and 20.2367 volts. The existence of two orthogonal magnetic moment vectors in phase-quadrature clearly indicates the circular polarization characteristic of the antenna. The ratio of amplitudes of the two resultant orthogonal vectors (Fig. 6.6) is 0.205 dB. The axial ratio (in broadside direction) of the polarization ellipse of the far-field, corresponding to the magnetic current moment distribution shown in Fig. 6.6, has been found to be 0.198 dB ( $\approx 0.2$  dB).

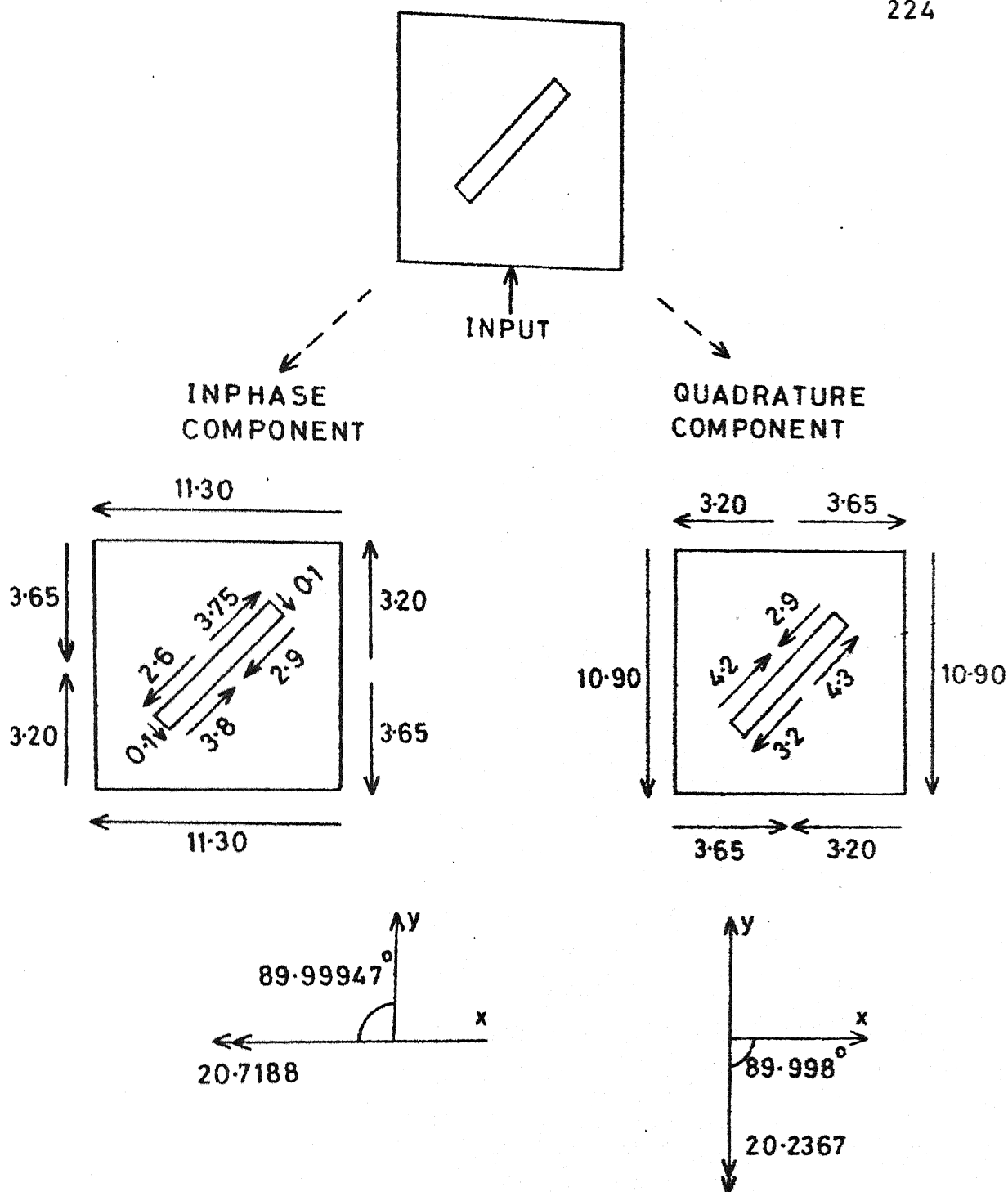


FIG. 6.6 MAGNETIC CURRENT MOMENT DISTRIBUTION AND ORIENTATION OF THE TWO RESULTANT VECTORS. THE TWO RESULTANT VECTORS ARE IN SPACE-QUADRATURE WITH RESPECT TO EACH OTHER



Thus the axial ratio of the polarization ellipse of the wave radiated by the antenna, in the broadside direction, can be evaluated from the polarization ellipse of the magnetic current moments as has been pointed out in Section 2.1.4. For evaluating the radiation characteristics in other directions, the electric vector potential is evaluated from (2.4) and the far-field is calculated using equations (2.5a) and (2.5b). The polarization performance (axial ratio) of the antenna as a function of slot dimensions is discussed in the following section.

#### 6.1.4 Optimum dimensions of the slot

For the chosen dimensions of the square patch, the optimum dimensions of the slot which yield best circular polarization (axial ratio = 0.198 dB at 3.130 GHz) are determined by evaluating the axial ratio at several frequencies for different values of length and width of the slot. The feed point is considered to be located at mid-point of one the sides as shown in Figs. 6.7 and 6.8 (insets). At 3.130 GHz the variation of axial ratio with slot length, for effective slot width equal to 2 mm, is shown in Fig. 6.7. The corresponding variation with slot width, for effective slot length  $p_e = 2.6$  cm, is illustrated in Fig. 6.8. It is observed from Fig. 6.7 that for +0.2 mm and -0.2 mm change in the width of the slot from the optimum value (2.00 mm) the axial ratio degrades to 1.7 dB and 1.0 dB respectively.

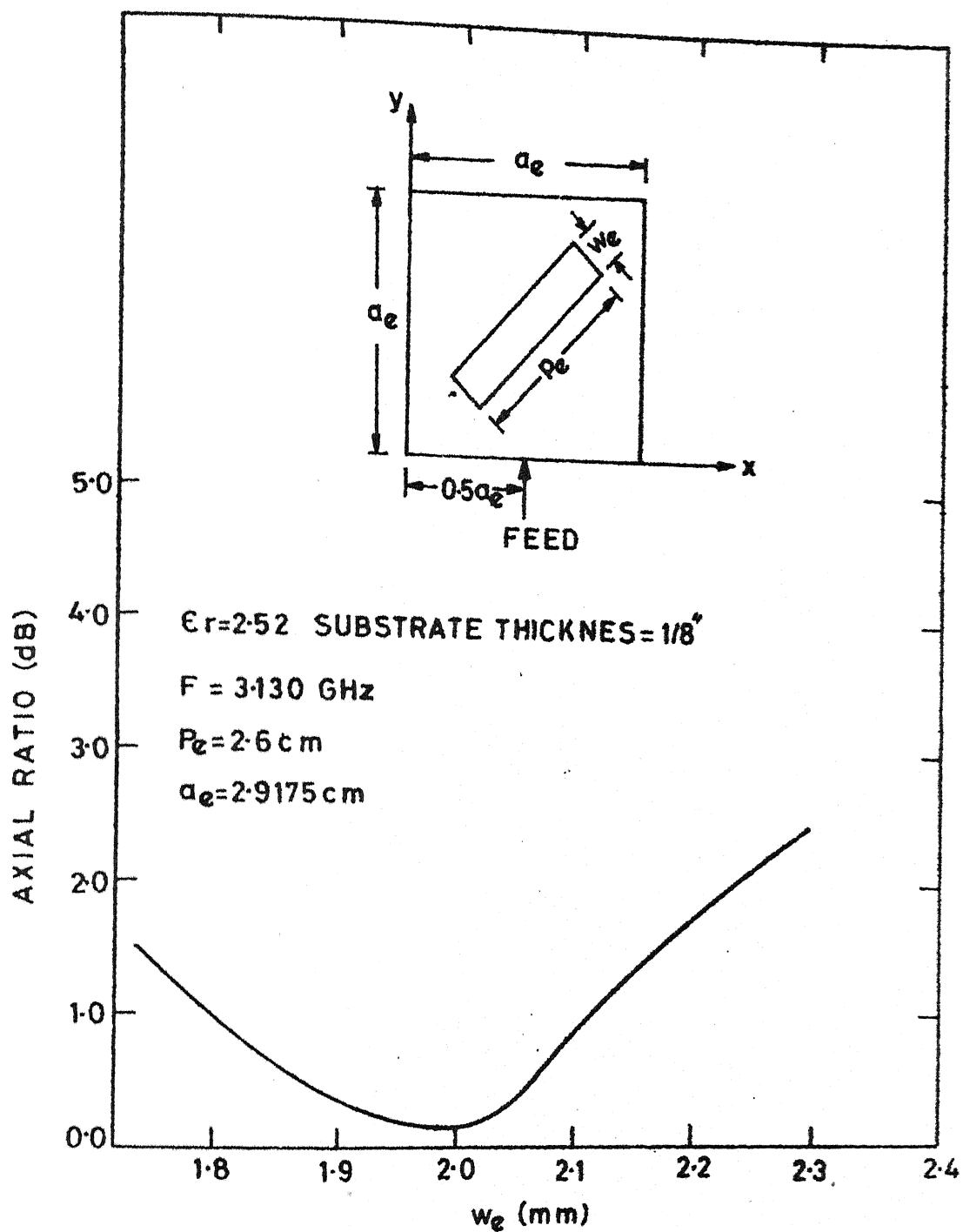


FIG.6-7 VARIATION OF AXIAL RATIO WITH SLOT WIDTH( $w$ )

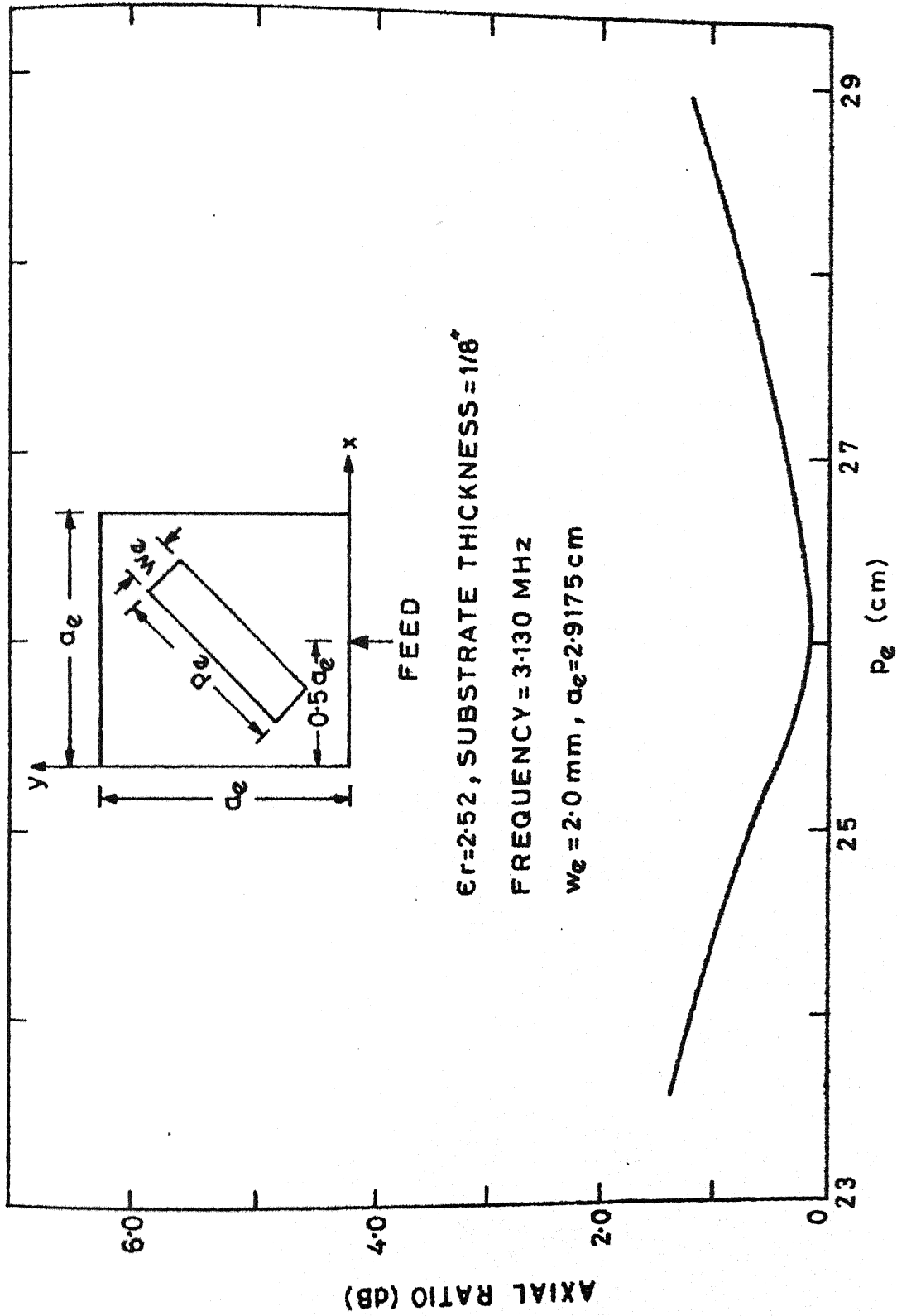


FIG.6-8 VARIATION OF AXIAL RATIO WITH SLOT LENGTH

Thus the axial ratio is quite sensitive to the width of the slot. From Fig. 6.8 it is observed that for +2.00 mm and -2.00 mm deviation from the optimum length of the slot the axial ratio degrades to 1.0 dB and 1.15 dB. The sensitivity of axial ratio degradation to slot length is thus nearly 1/10 of the corresponding sensitivity to the slot width variation. The optimum dimensions of the slot (from Figs. 6.7 and 6.8) are thus  $p_e = 2.6$  cm and  $w_e = 2.0$  mm which give the best axial ratio = 0.198 dB at 3.130 GHz for  $a_e = 2.9175$  cm.

A discussion on the two orthogonal modes, a linear combination of which yield the voltage distribution such as shown in Fig. 6.4 (and therefore circular polarization), is given in the following section.

## 6.2 ORTHOGONAL MODES OF RESONANCE

From the discussion in the preceeding section it is concluded that circular polarization is obtained for feed location at  $(x/a, y/b) = (0.5, 0.0)$ , that is at mid-point of one of the sides of the diagonal slot square patch antenna. This, in fact, is the result of two orthogonal modes that are excited for such a location of the feed. The two orthogonal modes can be excited by feeding the antenna at the two extreme ends of one of the sides, say at corners A and B of the antenna in Fig. 6.3. The polarization characteristics of the antenna can be explained in terms of the linear combination of these two modes.

Consider the voltage distributions along the radiating edges of the antenna that result for feed location at corner 'A' (frequency = 3.130 GHz) as shown in Fig. 6.9 and Fig. 6.10. The equivalent magnetic current moment distributions and the orientations of the resultant magnetic current moments are illustrated in Fig. 6.11. It is observed from the magnetic current moment distribution (Fig. 6.11) and the corresponding voltage distribution (Fig. 6.10) around the radiating edges of the diagonal slot, that the net radiation from the slot is zero. The radiations from only the outer periphery of the antenna contribute to the far-field. The polarization of the antenna is linear as can be expected from the orientation of the resultant components of the magnetic current moments in Fig. 6.11. The amplitude of each of the two component vectors in phase-quadrature is 16.5463 volts. These amplitudes are to the same scale as the amplitudes of the vectors in Fig. 6.6 and at the same frequency (= 3.130 GHz). As these vectors are collinear in space, the polarization is evidently linear. The calculated value of resonance frequency of this mode is 3.212 GHz, the measured value being 3.210 GHz.

Now consider the voltage distribution along the radiating edges of the antenna when feed is located at corner B as shown in Fig. 6.12 and Fig. 6.13. The calculated resonance frequency of this mode is 3.063 GHz and the measured value is

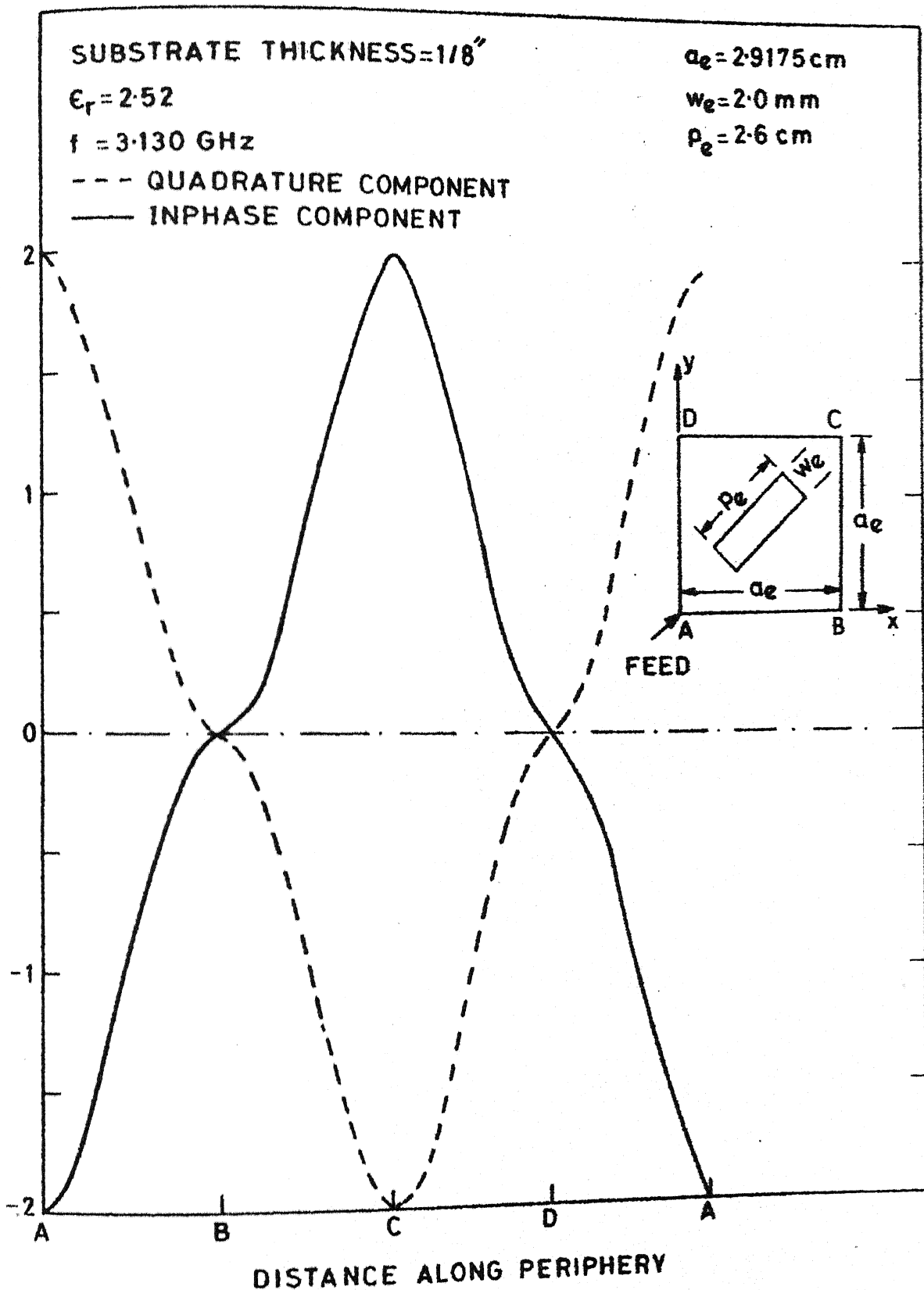


FIG.6.9 VARIATION OF VOLTAGE ALONG PERIPHERY  
FOR FEED AT CORNER A

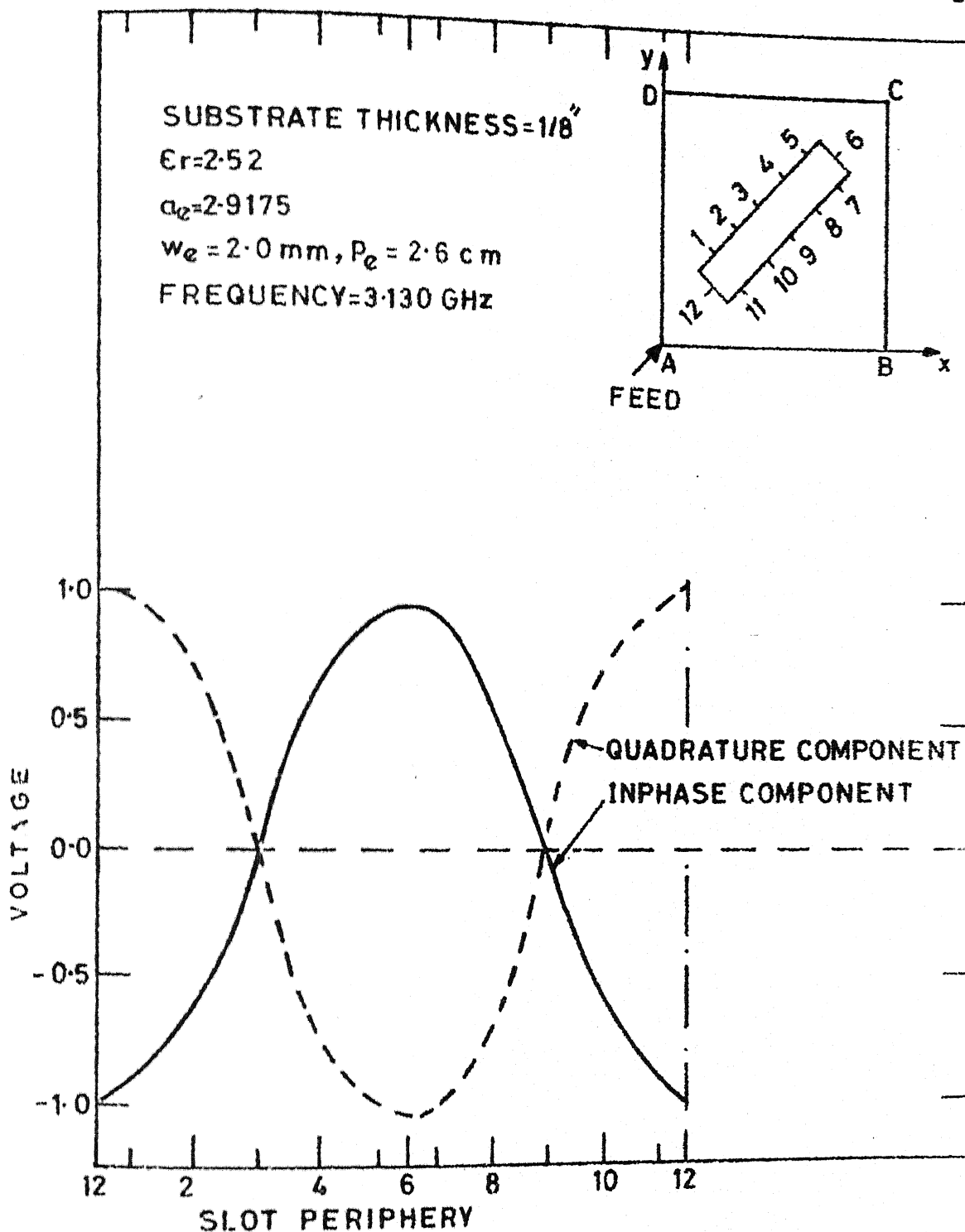
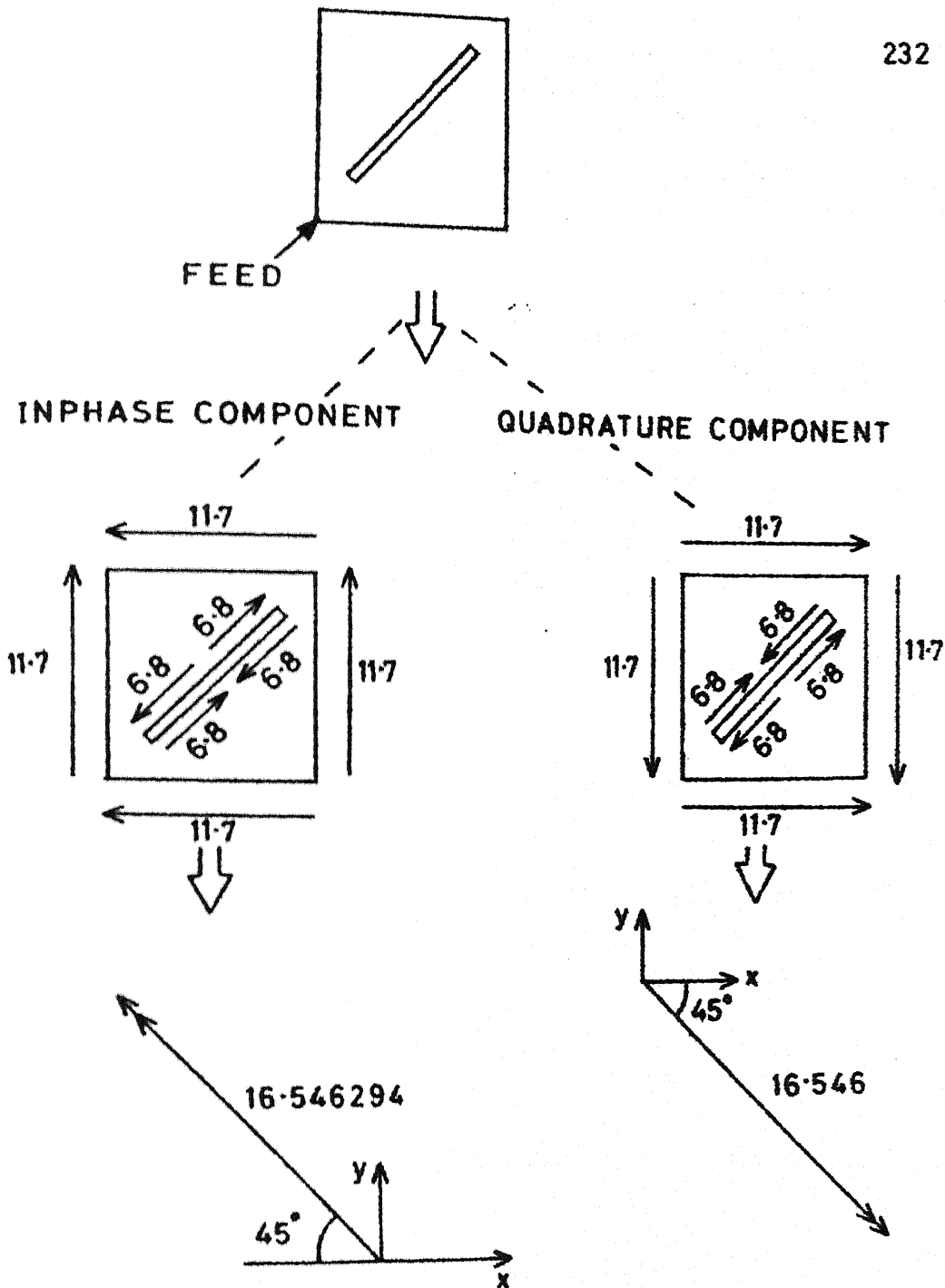


FIG.6.10 VARIATION OF VOLTAGE ALONG THE PERIPHERY OF THE SLOT FOR FEED AT CORNER A



**FIG.6-11 MAGNETIC CURRENT MOMENT DISTRIBUTIONS AND ORIENTATION OF RESULTANT MAGNETIC CURRENT MOMENTS; SLOT RADIATION EFFECT CANCELLS OUT**



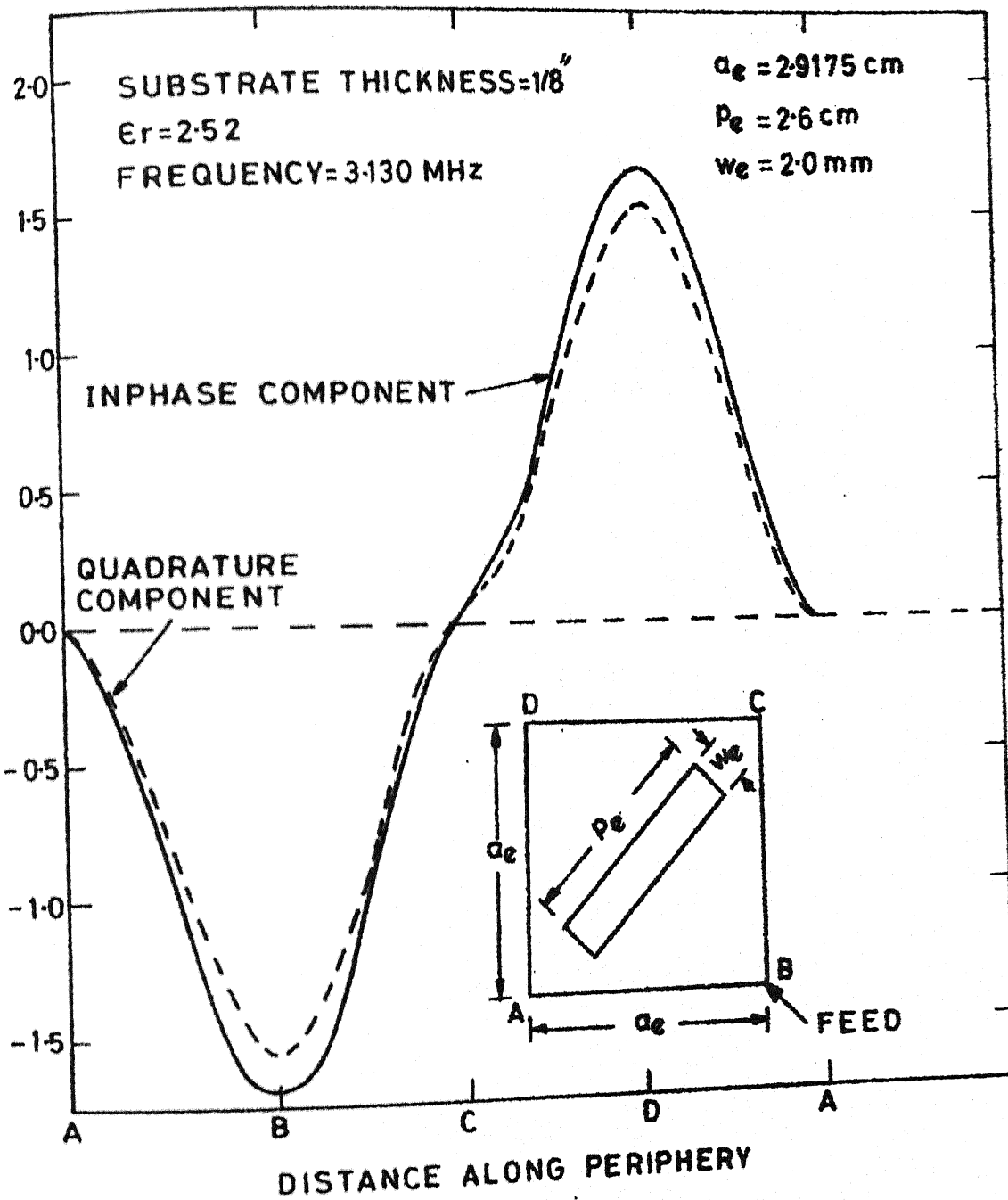


FIG. 6-12 VOLTAGE DISTRIBUTION ALONG THE OUTER PERIPHERY OF THE ANTENNA FOR FEED AT CORNER B

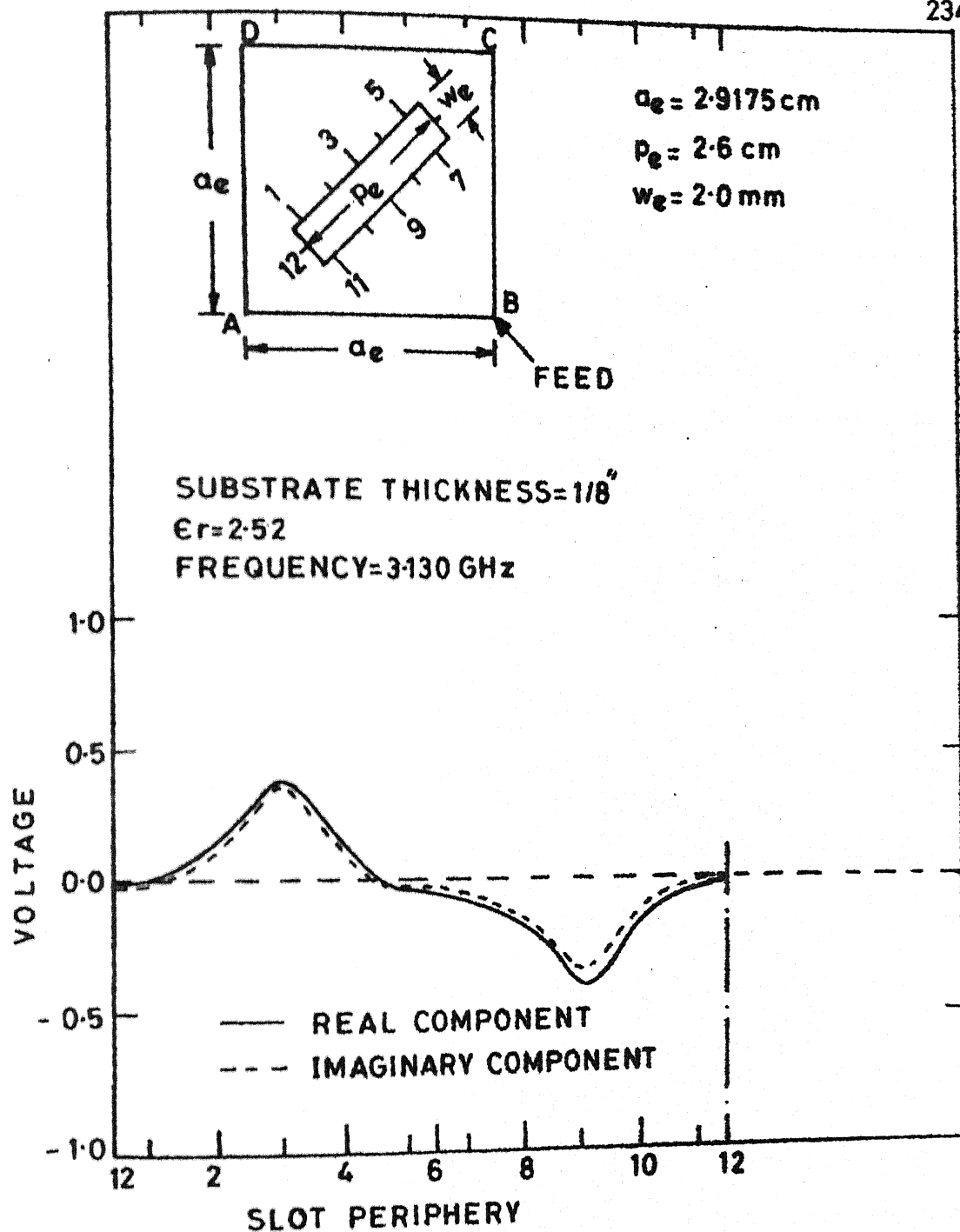


FIG. 6-13 DISTRIBUTION OF VOLTAGE ALONG THE PERIPHERY OF THE SLOT FOR FEED AT CORNER B

3.060 GHz. The magnetic current moment distribution and the orientations of the resultant current moment component vectors are illustrated in Fig. 6.14. The amplitudes of the two resultant components of magnetic current moment (in phase-quadrature and collinear in space) are 16.8664 and 15.17. The amplitudes of these vectors are to the same scale as those of the magnetic current vectors in Fig. 6.6 and Fig. 6.11. It may be noted from Fig. 6.14 that the polarization of the radiated wave is again linear and is orthogonal to that for the case when feed point is at the corner A. That is for feed port location at corner A (Fig. 6.11) the magnetic current moment is polarized along the line  $y = -x$  whereas the polarization of the resultant magnetic current moment for input port location at corner B (Fig. 6.14) is along the line  $y = x$ . Thus the two polarizations are orthogonal to each other.

Fig. 6.15 illustrates the measured values of the two orthogonal components of the far-field as functions of frequencies. It is observed that at resonance frequencies of the two modes, the amplitudes differ by more than 16 dB. The antenna is thus linearly polarized at resonance frequencies of the two modes shown in Figs. 6.11 and 6.14. Also, at resonance frequencies one of the far-field components becomes maximum. These observations are consistent with the similar results for diagonal fed antenna and the corners chopped antenna reported in Sections 4.2.1 and 5.2 respectively.

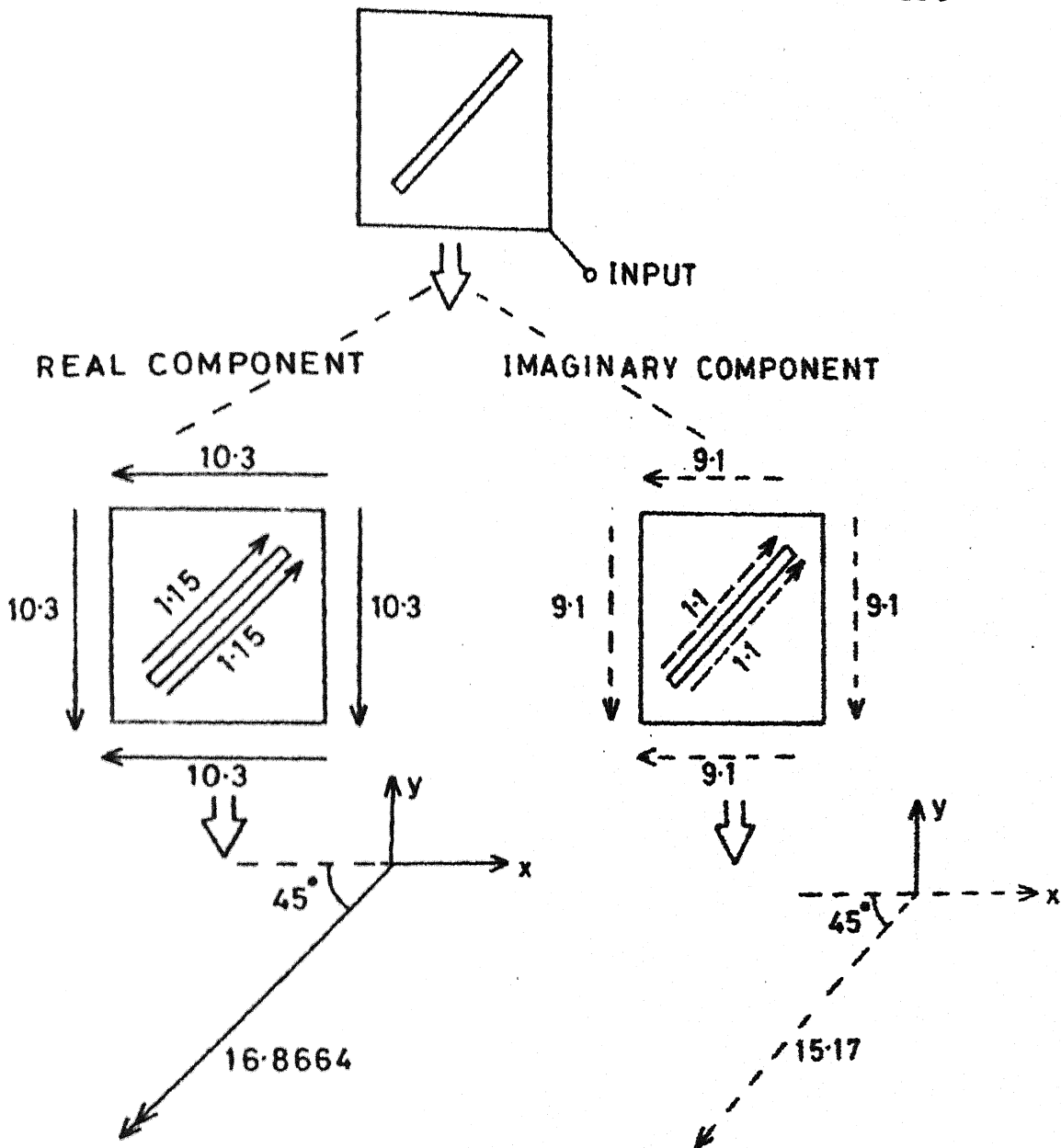


FIG. 6-14 MAGNETIC CURRENT MOMENT DISTRIBUTIONS AND ORIENTATION OF RESULTANT CURRENT MOMENTS; SLOT RADIATION EFFECT IS IN OPPOSITION TO THAT DUE TO PERIPHERAL MAGNETIC CURRENT

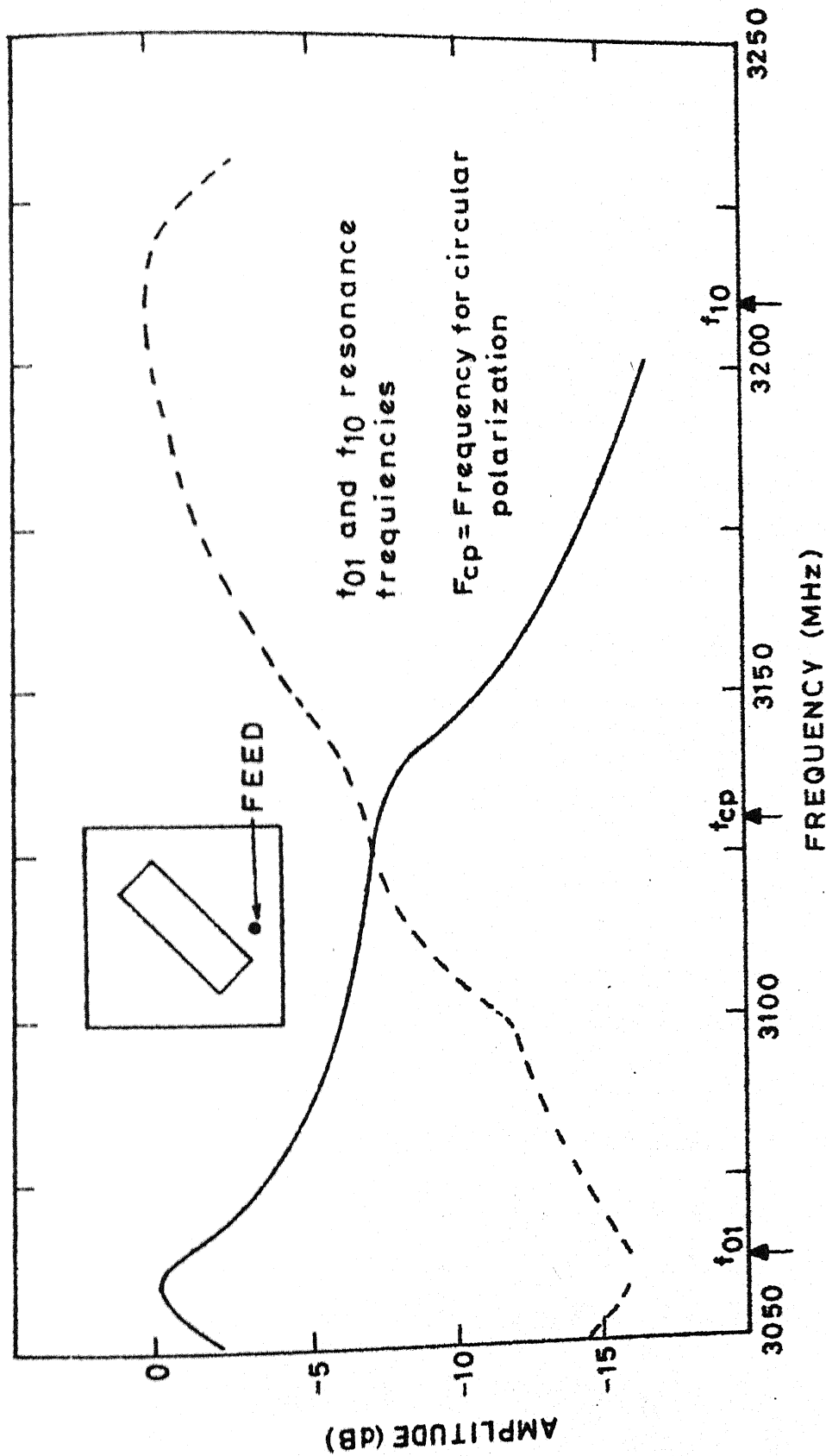
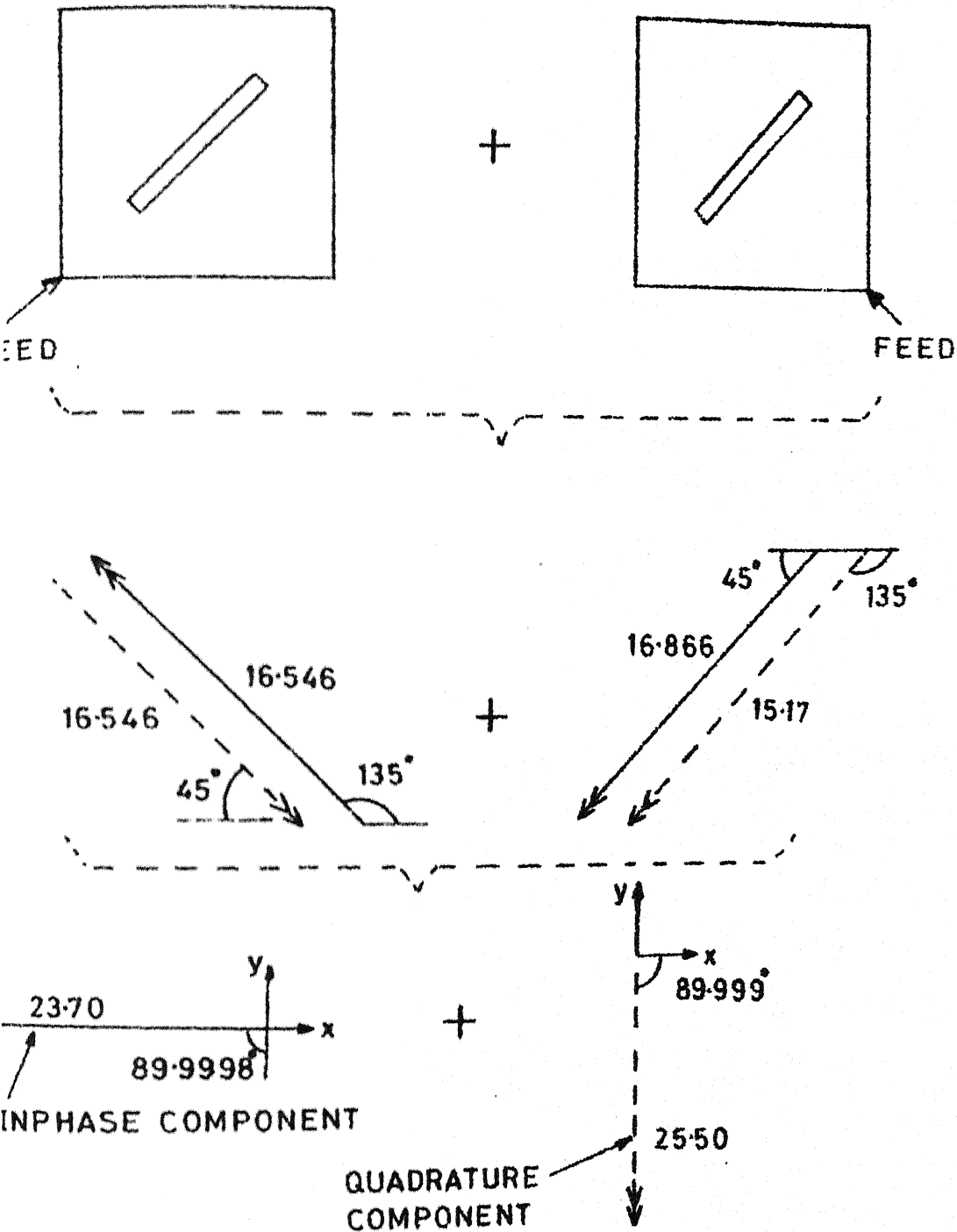


FIG.6.15 VARIATION OF AMPLITUDES OF THE TWO ORTHOGONAL COMPONENTS OF FAR-FIELD WITH FREQUENCY FOR THE DIAGONAL SLOT ANTENNA

The combination of two orthogonal modes discussed above produces circular polarization. Fig. 6.16 illustrates the vector sum of the resultant components of magnetic current moments of the two orthogonal modes shown in Fig. 6.11 and in Fig. 6.14 respectively. The resultant component vectors in Fig. 6.16 are in phase-quadrature and are at  $90^\circ$  to each other in space. The axial ratio for the magnetic current moment of Fig. 6.16 is 0.635 dB.

Comparison of the orientation and of the amplitudes of the resultant components of magnetic current moment of Fig. 6.16 with those of the corresponding component vectors of Fig. 6.6 shows that the orientations of the vectors in the two situations are identical. The absolute amplitudes of the components of magnetic current moment in Fig. 6.6 differ from the amplitudes of the corresponding components in Fig. 6.16. Thus feed at mid-point of one of the sides of the antenna results in partial excitation of two orthogonal modes in phase-quadrature which results into circular polarization at a frequency decided by the parameters of the dielectric substrate and the dimensions of the antenna.

The input VSWR with respect to a  $50\ \Omega$ -line, at 3.130 GHz where the best axial ratio ( $= 0.198$  dB) is obtained, is found to be 3.5 for feed location at mid-point of one of the sides as shown in Fig. 6.6. The optimization of feed location for minimum input VSWR is discussed in the following section.



6-16 SUMMATION OF COMPONENTS OF MAGNETIC CURRENT MOMENTS FOR THE TWO ORTHOGONAL MODES SHOWN IN FIG. 6-11 AND FIG. 6-14

### 6.3 MINIMUM VSWR AND OPTIMUM FEED LOCATION

As pointed out in the preceeding discussions the feed location at mid-point of one of the sides of the diagonal slot antenna yields best circular polarization. This location is symmetrical with respect to the two diagonals of the antenna structure. Investigations have been carried out to determine the optimum location of the feed for minimum input VSWR on the line joining the mid-points of two opposite sides of the antenna. It has been decided so because the line  $x/a_e = 0.5$  (as in Fig. 6.17) is also located symmetrically with respect to the two diagonals. The variation of input VSWR and of axial ratio with feed location is illustrated in Fig. 6.17. The axial ratio remains constant at about 0.2 dB for  $y/a_e \leq 0.175$  but degrades thereafter.

The input VSWR improves to 1.25 for location at  $y/a_e = 0.35$ . For values of  $y/a_e > 0.35$  the input VSWR degrades. At  $y/a_e = 0.35$  where the input VSWR is minimum ( $= 1.25$ ) the axial ratio is 2.5 dB. For axial ratio to remain at 0.2 dB, the optimum value of input VSWR is 2.5 that corresponds to the feed location  $(x/a_e, y/a_e) = (0.5, 0.175)$ . Thus in the present case the input VSWR cannot be improved further if the axial ratio is to be maintained at 0.2 dB (which is the best obtainable for the antenna investigated).

Similar variations of VSWR and axial ratio are obtained when the feed is located on the line  $y/a_e = 0.5$  line for



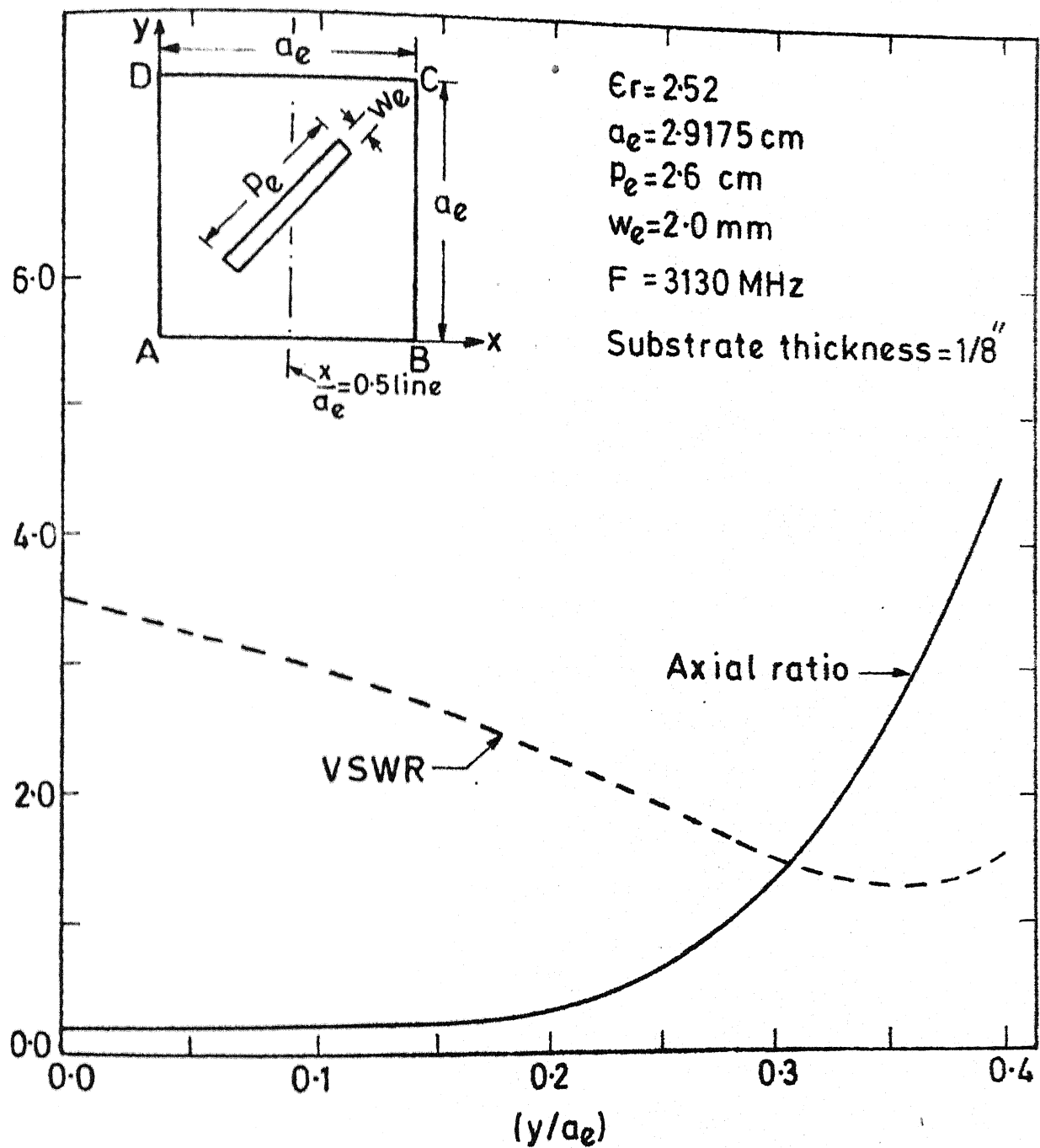


FIG.6.17 VARIATION OF AXIAL RATIO AND INPUT VSWR WITH FEED LOCATION ON  $x/a_e = 0.5$  LINE

$0 < x/a_e < 0.5$  except that the sense of polarization is reversed. The results on radiation characteristics of the antenna are reported in the next section.

#### 6.4 BANDWIDTH AND BEAMWIDTH

Axial ratio and input VSWR are evaluated at several frequencies and the corresponding bandwidths are evaluated therefrom. The radiation pattern is evaluated at frequency (3.130 GHz) where the axial ratio is the best obtainable. The beamwidth is evaluated from the radiation pattern.

##### 6.4.1 Variation of input VSWR and axial ratio with frequency

The input VSWR as a function of frequency is evaluated for two different locations of feed port (Fig. 6.18). The choosen locations are  $(x/a_e, y/a_e) = (0.5, 0.112)$  and  $(x/a_e, y/a_e) = (0.5, 0.2)$ . The variation of input VSWR with frequency (over the band of frequencies for which axial ratio remains less than 6 dB), for the two feed port locations is illustrated in Fig. 6.18. The input VSWR (theoretical) varies from 3.1 at 20 MHz below the center frequency ( $= 3.130$  GHz) to 2.8 at 20 MHz above the center frequency for feed location at  $(x/a_e, y/a_e) = (0.5, 0.112)$ . The corresponding variation of input VSWR for location at  $(x/a_e, y/a_e) = (0.5, 0.2)$  is from 2.4 to 2.2. The experimental values of input VSWR for one of the feed locations are also shown in Fig. 6.18.

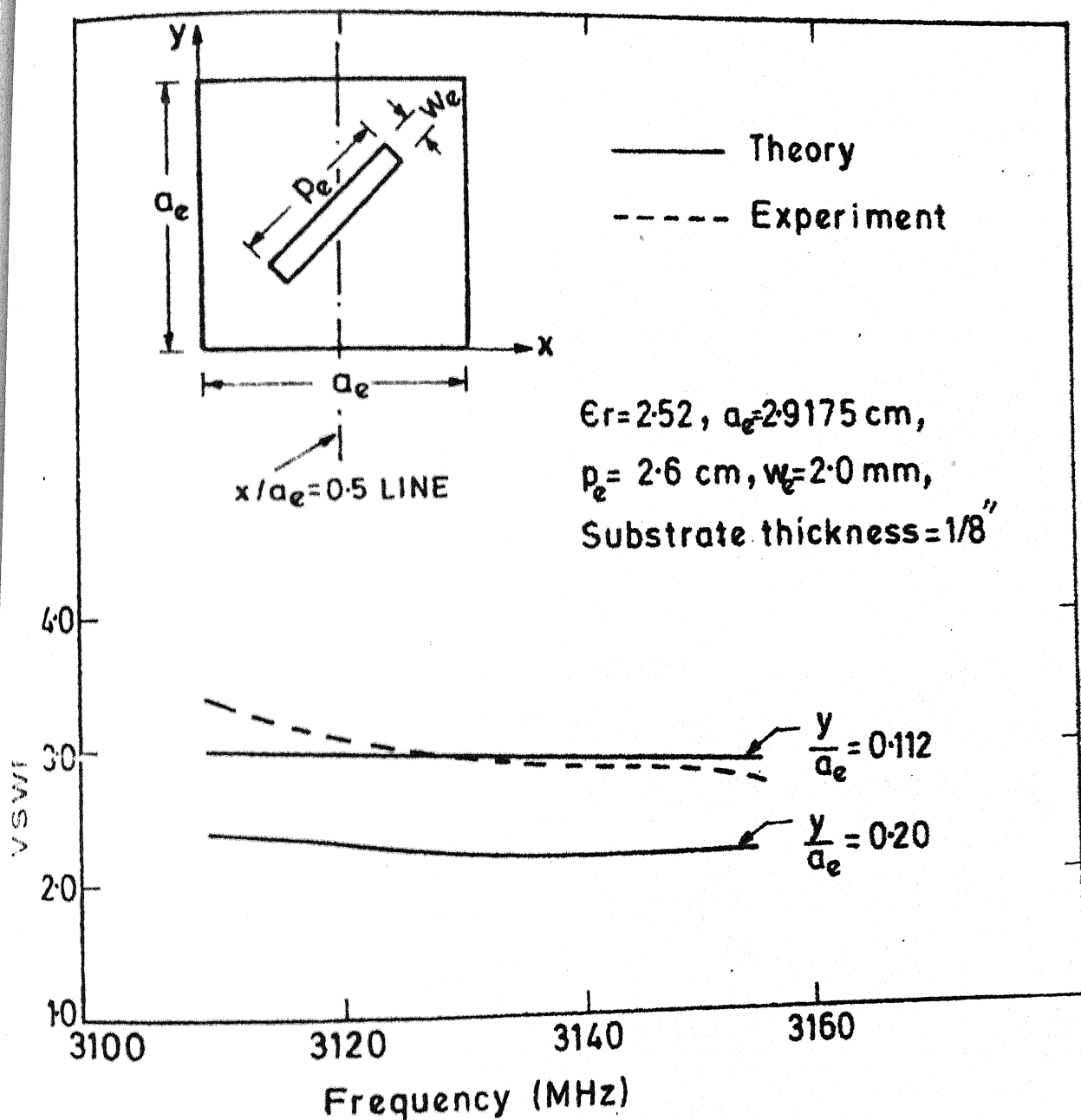


FIG. 6.18 VARIATION OF INPUT VSWR WITH FREQUENCY FOR TWO DIFFERENT LOCATIONS OF INPUT PORT ON  $x/a_e = 0.5$  LINE (COAXIAL FEEDING)

The variation of axial ratio with frequency is illustrated in Fig. 6.19. The bandwidth (for axial ratio less than 6 dB) is 35.5 MHz which corresponds to 1.134 percent for center frequency 3.130 GHz. The experimental results are also plotted in Fig. 6.19. The measured value of axial ratio bandwidth is 38.0 MHz (= 1.214 percent).

From Figs. 6.18 and 6.19, it is found that the antenna bandwidth is limited by axial ratio and not by input VSWR, the input VSWR remaining practically constant over this bandwidth.

#### 6.4.2 Radiation pattern and beamwidth

The radiation pattern is evaluated at the center frequency (3.130 GHz) where the axial ratio is the best obtainable ( $\approx 0.2$  dB). The feed port is considered to be located at  $(x/a_e, y/a_e) = (0.5, 0.112)$ . The radiation pattern in  $\varphi = 90^\circ$  plane is shown in Fig. 6.20. The difference between the amplitudes of  $E_\theta$  and  $E_\varphi$  remains less than 3 dB for  $-58^\circ < \theta < 58^\circ$  and less than 6 dB for  $-69^\circ < \theta < 69^\circ$ . The beamwidth is thus  $116^\circ$  for 3 dB difference between  $|E_\theta|$  and  $|E_\varphi|$  and is  $138^\circ$  for 6 dB difference between  $|E_\theta|$  and  $|E_\varphi|$ .

### 6.5 EXPERIMENTAL RESULTS

A photograph of the fabricated antenna is shown in Fig. 6.21. The experimental set up is shown in Fig. 4.22.

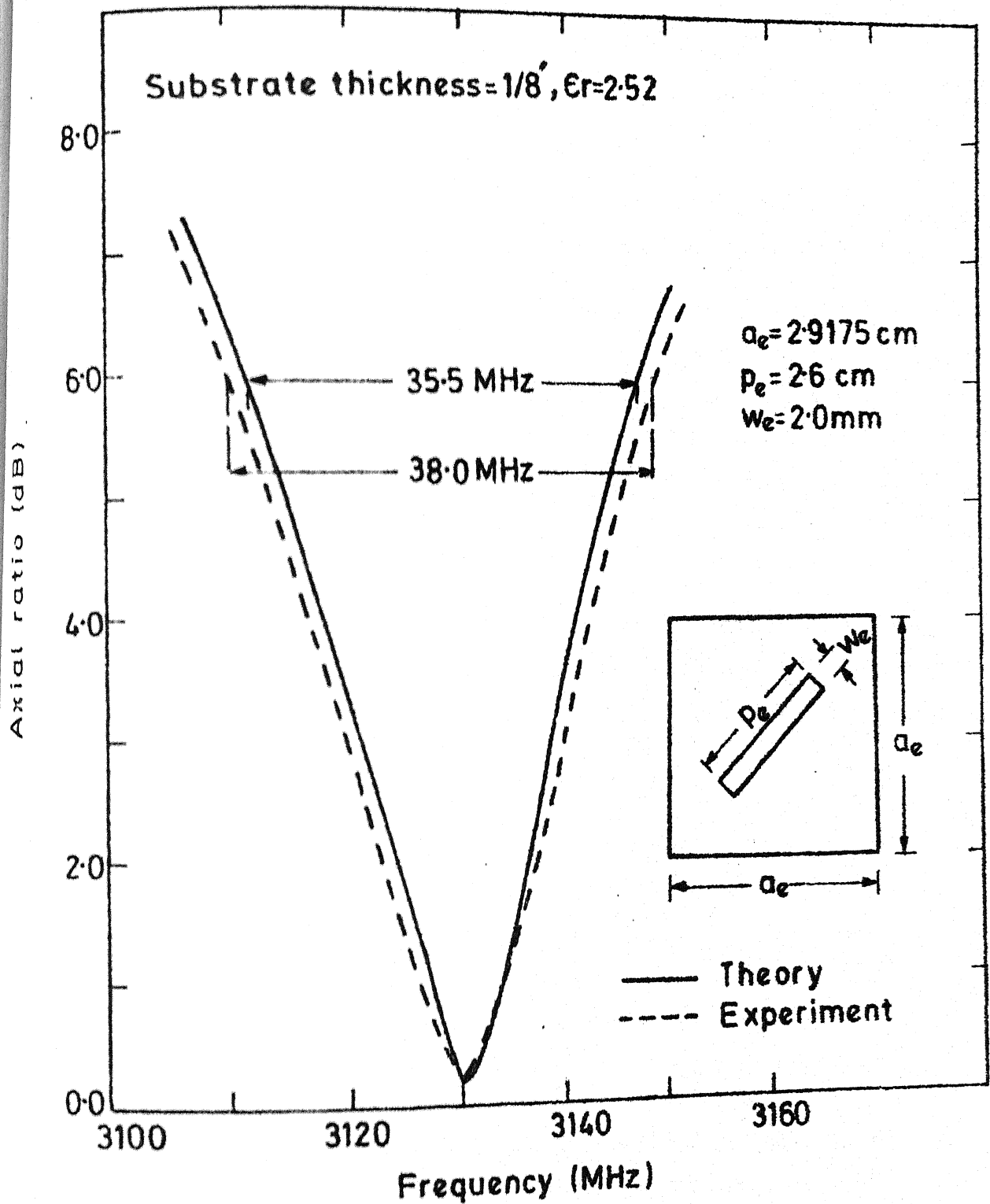
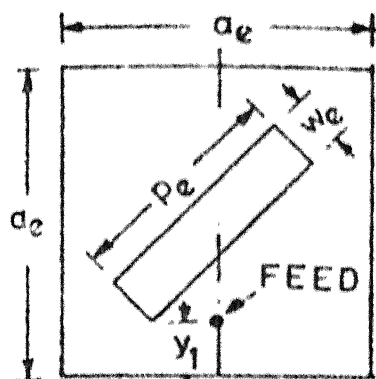


FIG. 6-19 VARIATION OF AXIAL RATIO WITH FREQUENCY



SUBSTRATE THICKNESS =  $1/8''$

$\epsilon_r = 2.52$

$a_e = 2.9175 \text{ cm}$

$p_e = 2.6 \text{ cm}, w_e = 2.0 \text{ mm}$

$y_1 = 0.112 a_e$ , Frequency = 3130 GHz

$\phi = 90^\circ$  PLANE

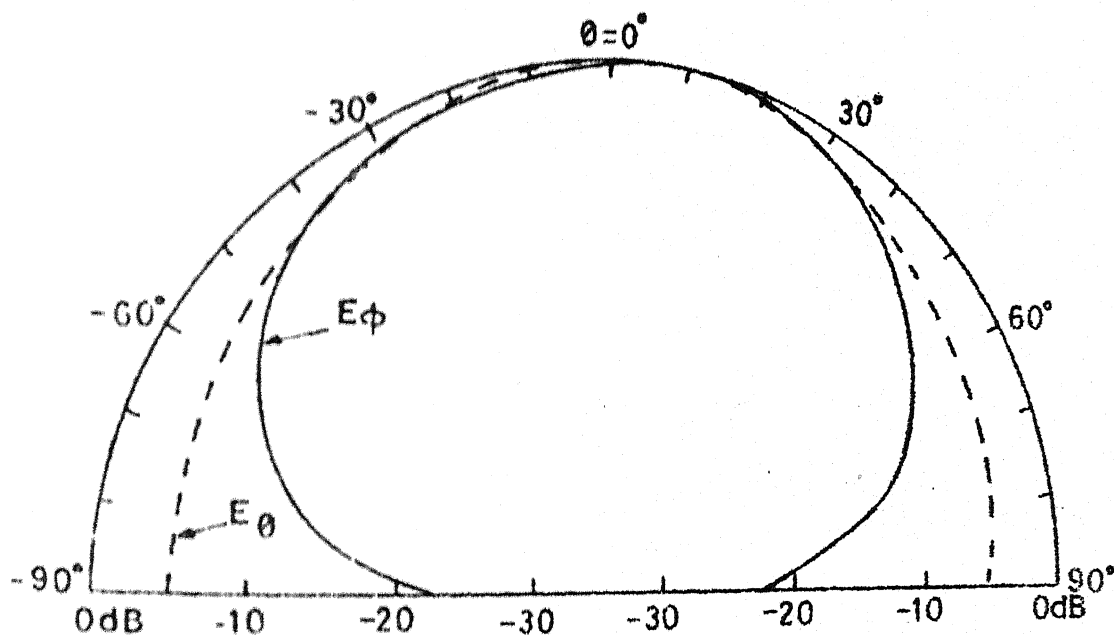


FIG. 6.20 RADIATION PATTERN (in  $\phi = 90^\circ$  plane) FOR A SQUARE PATCH ANTENNA WITH A DIAGONAL SLOT

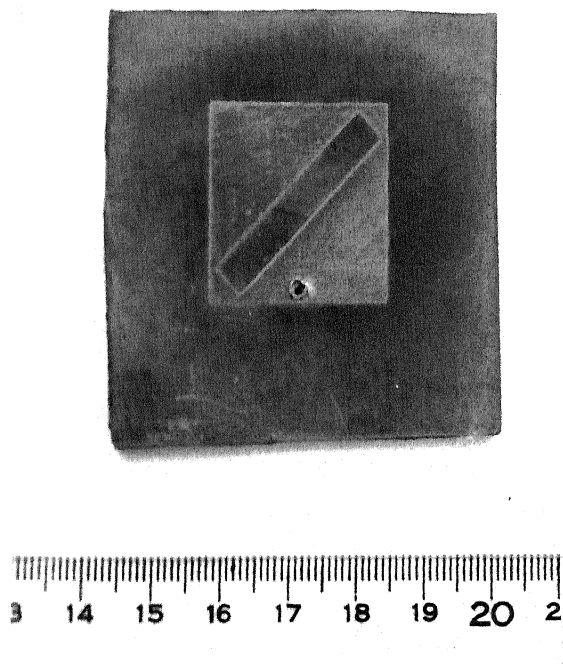


Fig. 6.21 Photograph of the square patch antenna with a diagonal slot

The measurements were carried out with feed location at  $(x/a_e, y/a_e) = (0.5, 0.112)$  as shown in Fig. 6.18. The measured values of input VSWR and axial ratio are plotted in Figs. 6.18 and 6.19 respectively. The theoretical and measured values are found to be in agreement. Fig. 6.22 illustrates the experimental and theoretical values of  $E_\theta$  and  $E_\phi$  in  $\phi = 90^\circ$  plane. The agreement between measured and theoretical values of  $E_\theta$  is very good for  $-40^\circ < \theta < 40^\circ$ . The measured values of  $E_\phi$  agree precisely with the respective theoretical values.

Table 6.2 gives a summary of the results of investigations carried out on the square patch antenna with a diagonal slot.

## 6.6 DISCUSSIONS

A square patch with a diagonal slot is analyzed and optimized (for S-band operation) using the desegmentation method. The mechanism of operation of the antenna is explained in terms of the voltage and the magnetic current moment distributions of two orthogonal modes. The resonance frequencies of these modes are calculated and verified experimentally. The effect of slot dimensions on the axial ratio is studied. The feed location is optimized for minimum input VSWR. Lower values of input VSWR can be obtained if thinner substrate is used as observed in the cases of diagonal fed antennas reported in Chapter Four, and the corners chopped antennas discussed in Chapter Five.



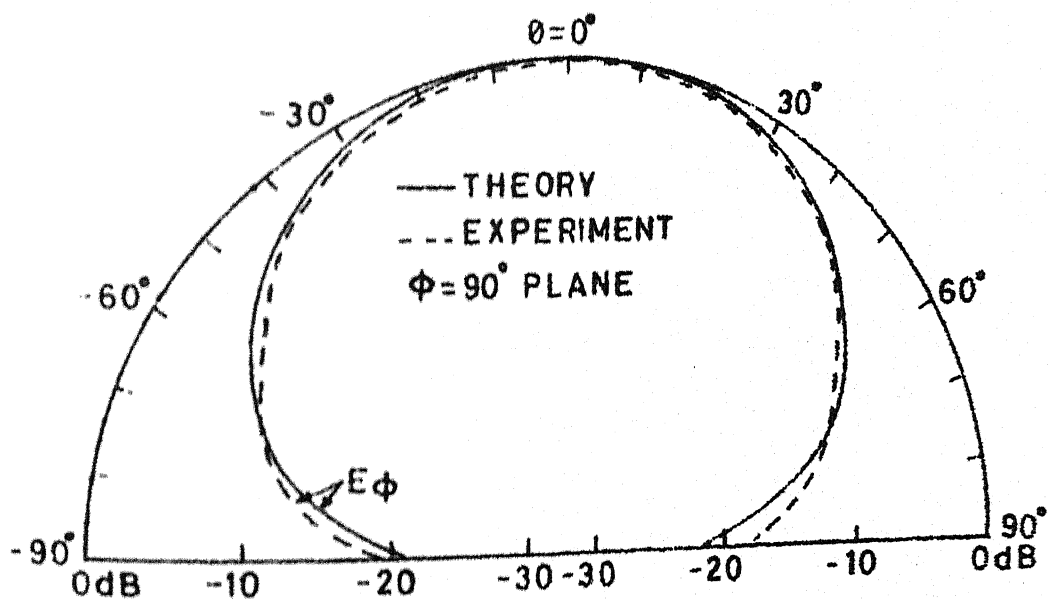
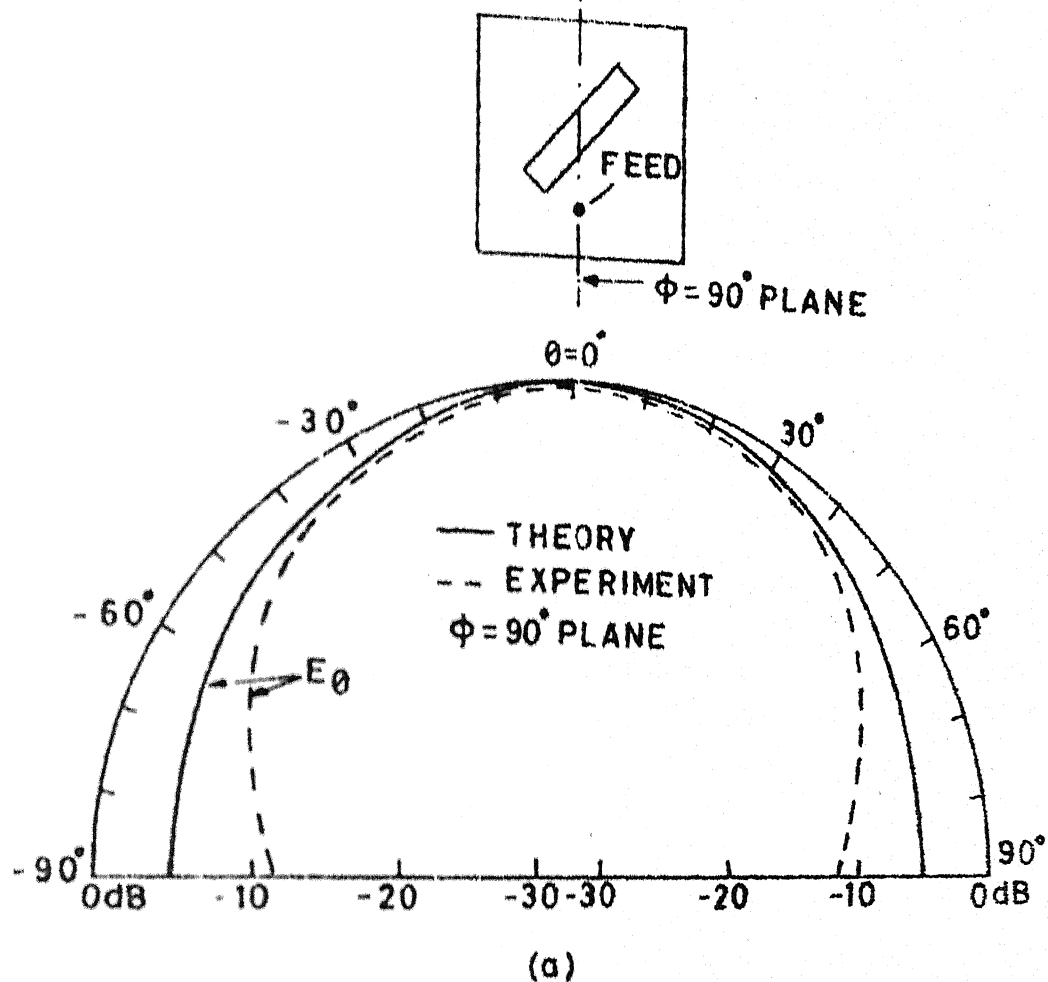


FIG.6.22 THEORETICAL AND EXPERIMENTAL  
VALUES OF FARE FIELD COMPONENTS

Table 6.2 Performance of a square patch antenna with a diagonal slot (Substrate thickness =  $1/8"$ ,  $\epsilon_r = 2.52$ , Effective dimensions of the slot =  $2.6 \times 0.2 \text{ cm}^2$ , Effective dimensions of the square patch =  $2.9175 \times 2.9175 \text{ cm}^2$ )  
Physical dimension  $pxw = 2.89 \times 0.47 \text{ cm}^2$ ;  
 $axa = 2.602 \times 2.602 \text{ cm}^2$

	Theoretical	Experimental
1. Center frequency	3.130 GHz	3.130 GHz
2. Resonance frequencies of orthogonal modes	3.063 GHz; 3.212 GHz	3.060 GHz; 3.210 GHz
3. Axial ratio at center frequency	0.198 dB	0.2 dB
4. Bandwidth for axial ratio < 6 dB	35.5 MHz (1.134 percent)	38.0 MHz (1.214 percent)
5. Input VSWR at the chosen feed location	2.9	2.9
6. Beamwidth for difference between $ E_\theta $ and $ E_\phi $		
i) < 3 dB	$-58^\circ < \theta < 58^\circ$	$-62^\circ < \theta < 62^\circ$
ii) < 6 dB	$-69^\circ < \theta < 69^\circ$	$-75^\circ < \theta < 75^\circ$

The axial ratio limited bandwidth of the diagonal slot square patch antenna is found to be 38 MHz which is larger than that for the other two types of antennas investigated. The radiation pattern and beamwidths are evaluated. The theoretical and experimental results are found to be in good agreement. Thus it is demonstrated again that the desegmentation method, proposed in Chapter Three, along with the Green's function approach proposed in Chapter Two can be used for analysis and design of microstrip antennas.

## CHAPTER SEVEN

### CONCLUDING REMARKS

The work reported in this thesis can be broadly categorized as : (i) extension of the Green's function approach of 2-d circuit analysis to the analysis and design of microstrip antennas, (ii) proposal of a new technique for analysis of 2-d components, and (iii) applications of the proposed techniques to single feed circularly polarized microstrip antennas.

#### 7.1 ANALYTICAL TECHNIQUES

The Green's function approach with magnetic wall boundary conditions, a technique often used for analysis and design of 2-d components, has been extended to the analysis and design of microstrip patch antennas. In the proposed technique, the antenna is treated as a multiport lossless resonator. For a regular shaped antenna, the Z-matrix of the multiport network model is evaluated using the appropriate Green's function. For antennas having irregular shapes, use of the segmentation and/or desegmentation is proposed for evaluation of the Z-matrix. Since the multiport network is considered lossless, the elements of the Z-matrix are purely reactive. Therefore, taking the 'j' operator common, the Z-matrix is evaluated treating the entire matrix as real. This results in saving of computational time and computer storage required.

The radiated power is taken into account by terminating the ports of the multiport network by radiation resistances [50]. It is at this stage of computation process that the elements of Z-matrix of the lossless multiport model are treated as reactive, those of the radiation resistance network being purely resistive, and the elements of the resultant Z-matrix for loaded multiport network become complex. The input impedance (and therefore input VSWR), the voltage along periphery, the equivalent magnetic current, and radiation characteristics are evaluated consequently. For microstrip feed, the width of the input port is considered equal to that of the feed line. In case of coaxial feed, the width of the input port is taken equal to the diameter of the pin of the coaxial connector. This is an approximation to the actual physical situation. Also the losses in the dielectric substrate and in the conductors of the patch have been ignored. The contribution of surface waves is also not taken into account. These approximations are likely to contribute to the difference between the theoretical and experimental values of input VSWR. However, the theoretical and experimental values of axial ratio are found to be in good agreement over the entire band of frequencies of interest. At and near the center frequencies the agreement has been found to be precise.

A new technique called 'desegmentation method' has been proposed for analysis of 2-d components. In this method one or more regular segments ( $\beta$ ) are added to the given irregular shaped  $\alpha$ -segment such that the combination, called  $\gamma$ -segment, is either a regular shaped segment or a combination of regular shaped segments. Characterizations of  $\alpha$ -segment in terms of either Z- or S-parameters are obtained from those of the  $\beta$ - and  $\gamma$ -segments. The  $\beta$ - and  $\gamma$ -segments are analyzed using Green's function(s) and segmentation method if needed. The applicability of the method has been illustrated by examples of lumped circuits, of transmission line circuits and those of planar circuits. It has been pointed out that the desegmentation method is expected to be more efficient than the segmentation method in situations wherein the  $\beta$ -segment is much smaller than  $\alpha$ - and  $\gamma$ -segments. Also in some situations the segmentation method is not applicable whereas the desegmentation method can be used for analysis.

An alternative procedure for efficient evaluation of Z-matrices using desegmentation method has also been proposed in Chapter Three and has been used in Chapter Six for analyzing antenna with a diagonal slot. It has been pointed out that for 2-d components the procedure for evaluation of Z-matrices is more efficient than that in terms of S-matrices. The formulation of the desegmentation method in terms of S-matrices has been employed to evolve a generalized method for de-embedding of multiport networks.

### 7.1.1 Applications

Green's function approach and the desegmentation method proposed in this thesis have been used to analyze and optimize three types of single feed circularly polarized microstrip antennas. The Green's function approach has been used to design diagonal fed nearly square patch antennas for circular polarization in S-band. The mechanism of operation of this type of antennas has been explained in terms of the voltage distribution of two orthogonal modes. The length to width ratio of the rectangle for best axial ratio has been found to depend upon the dielectric constant and the thickness of the substrate. Optimum feed location for minimum VSWR has been determined. Effect of substrate thickness on axial ratio bandwidth and input VSWR have been investigated. It has been observed that better input VSWR values are realized for antennas on thinner substrates but the axial ratio bandwidth reduces by nearly 40 percent for 50 percent reduction in the thickness of the substrate. The study of the three diagonal fed antennas reveals that perfect impedance matching with 50 ohm coaxial feed line is not possible for this type of antennas. The reason for this is that two modes are to be excited simultaneously, with a single feed and this restricts the locations of the feed so that polarization characteristics are not affected. The antennas have been found to have axial ratio limited bandwidths, the input VSWR variations being very small over the bands of frequencies for which axial

ratio remains less than 6 dB. The beamwidths for the three antennas studied are found to be nearly equal. The theoretical results have been verified experimentally in two cases of the antennas.

S-band corners chopped square patch antennas have been analyzed, designed and optimized using desegmentation method. Two different designs on substrates having thickness equal to  $1/8$ " and  $1/16$ " are reported. The principle of operation of the antenna for circular-polarization is explained in terms of existence of two orthogonal modes. The resonance frequencies of these modes are evaluated. The polarization characteristics, input VSWR, and radiation patterns have been evaluated. It has been observed that the axial ratio bandwidth and the input VSWR reduce when substrate thickness is reduced as found in the case of diagonal fed antennas also. The theoretical results have been verified experimentally. Compared to diagonal fed antennas, these antennas are found to have poorer axial ratio bandwidths and input VSWR values.

A circularly polarized square patch antenna with a diagonal slot has been optimized. The desegmentation method has been employed for analysis and design. Again the operation is explained in terms of two orthogonal modes. The thickness and dielectric constant of the substrate chosen are  $1/8$ " and 2.52 respectively. Axial ratio and input VSWR are evaluated as functions of frequencies. The radiation



patterns and beamwidths are reported. The theoretical results have been verified experimentally.

A comparison of the performances of the three types of antennas (for substrate thickness  $= 1/8"$  and  $\epsilon_r = 2.52$ ) is given in Table 7.1.

Table 7.1 Performance parameters of three types of antennas (experimental)  
(Substrate thickness  $= 1/8"$ ,  $\epsilon_r = 2.52$ )

	Diagonal fed antenna	Corners chopped antenna	Square with diagonal slot
1. Center frequency (GHz)	3.015	3.175	3.130
2. The best axial ratio (dB)	0.5	$\approx 0.0$	0.2
3. Bandwidth (MHz) for axial ratio $< 6$ dB	34.8 (1.086%)	29.4 (0.925%)	38.0 (1.214%)
4. Minimum input VSWR at center frequency	1.72	2.26	2.3*

\*The location of the feed choosen in experimental studies was not the optimum and the experimental value of VSWR is 2.9.

The square patch antenna with a diagonal slot is thus found to have the largest bandwidth whereas the minimum input VSWR is obtainable with a diagonal fed antenna. The corners chopped antenna has the best axial ratio ( $\approx 0.0$  dB) but has the minimum axial ratio bandwidth.

## 7.2 SUGGESTIONS FOR FURTHER INVESTIGATIONS

Desegmentation method proposed in this thesis can be used for analysis and design of variety of microstrip antennas and circuits. Some further applications are suggested below.

### Antenna analysis and design

In addition to the three types of antennas discussed in this thesis, there are other antenna configurations proposed for obtaining circular polarization. These have been mentioned in Section 1.2.3 and one such configuration is shown in Fig. 3.13(c). Desegmentation method can be used for analysis and optimization of these configurations also.

For the pentagon antenna [28], the shape of Fig. 1.10(f) can be obtained by removing one  $30^\circ$ - $60^\circ$  triangle ( $\beta_1$ ) and one equilateral triangle ( $\beta_2$ ) from a larger  $30^\circ$ - $60^\circ$  triangular shape ( $\gamma_1$ ) as shown in Fig. 7.1(a). The desegmentation method can, therefore, be used. An alternative procedure is to employ, both, the segmentation and desegmentation methods. The segmentation method is used to combine two  $30^\circ$ - $60^\circ$  triangles to obtain a kite shaped configuration ( $\gamma_2$ ) as illustrated in Fig. 7.1(b). To obtain the pentagon shape from the kite, an equilateral triangular segment ( $\beta$ ) is chopped off from the kite by using desegmentation.

The circular disk antenna with a slot [43], shown in Fig. 7.1(c), is obtained when a rectangular patch is removed

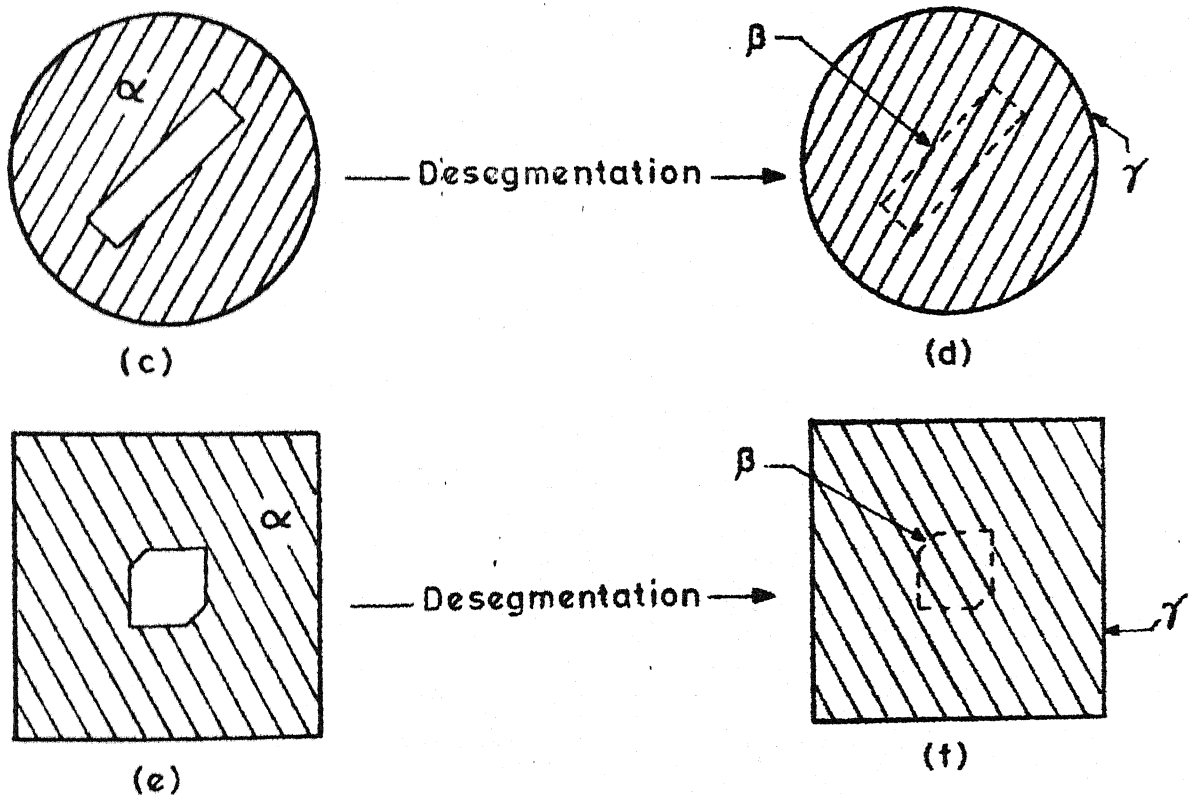
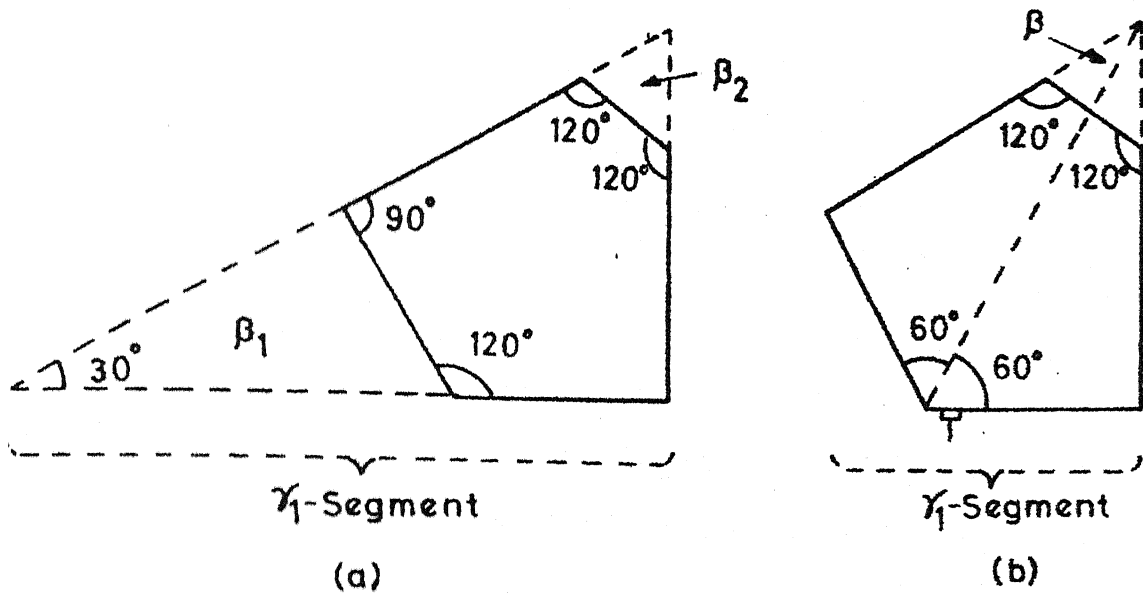


FIG. 7-1 (a) DESEGMENTATION APPLIED TO PENTAGON  
 (b) SEGMENTATION AND DESEGMENTATION  
 APPLIED TO PENTAGON (c) DESEGMENTATION  
 OF A SQUARE WITH A CORNERS CHOPPED  
 SQUARE REMOVED

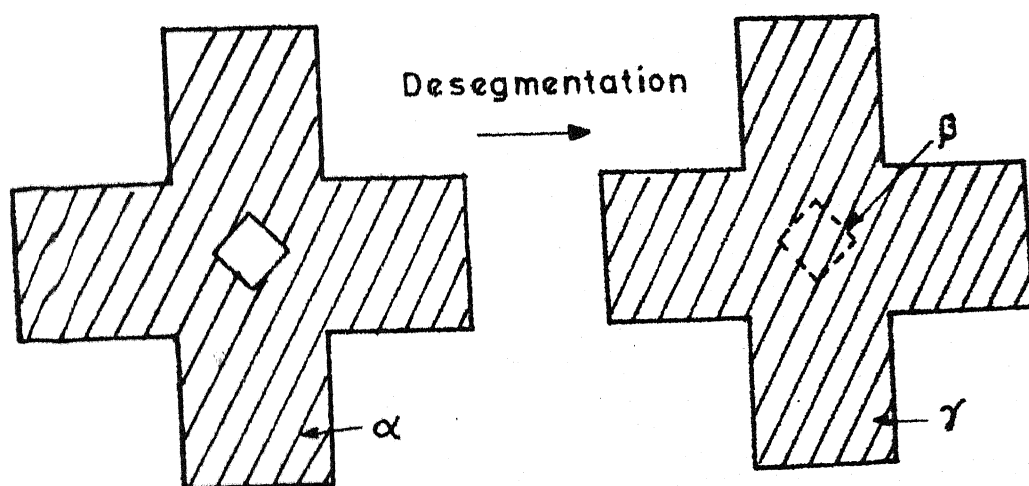
from a circular disk. The regular circular shape of Fig. 7.1(d) forms the  $\gamma$ -segment and the rectangular patch removed is the  $\beta$ -segment. The segments  $\beta$  and  $\gamma$  can be analyzed by using Green's functions [1],[5]. The desegmentation method can, therefore, be used.

For the antenna shape [43] of Fig. 7.1(e) the  $\gamma$ -segment (Fig. 7.1(f)) is obtained when a corners chopped square patch ( $\beta$ -segment) is added to the given shape. The  $\beta$ -segment can be analyzed by employing desegmentation method using the procedure described in Chapter Five. Green's function for rectangle [1] is used for analyzing the  $\gamma$ -segment. Thus in this analysis the desegmentation is used twice.

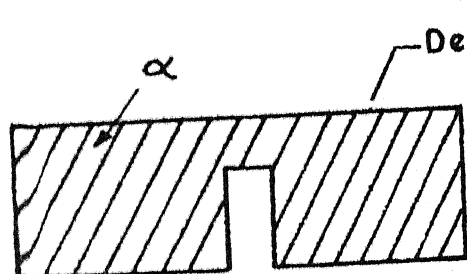
#### Circuit analysis and design

Desegmentation method is suitable for analysis and compensation of discontinuities in stripline and microstrip circuits. This method has already been used by colleagues in the group [59] for compensation of microstrip bends, steps and T-junctions. The technique can be extended to other types of discontinuities also. Some such discontinuity configurations which could be investigated are shown in Fig. 7.2.

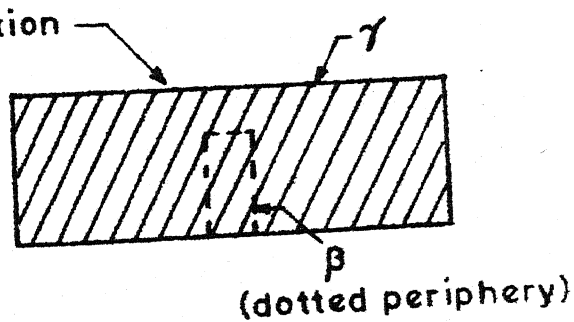
For a cross-junction discontinuity, the reactances may be compensated by removing a square patch from the junction as shown in Fig. 7.2(a). This is speculated on the basis of the fact that a T-junction (which is half of the cross-



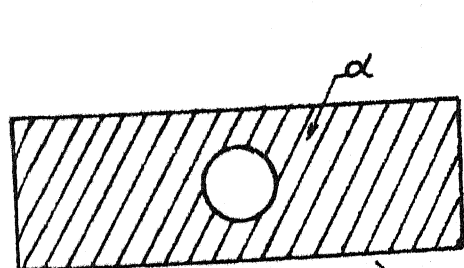
(a)



(b)



(dotted periphery)



(c)

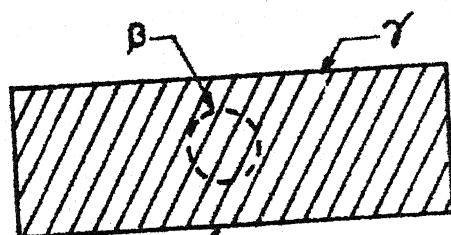


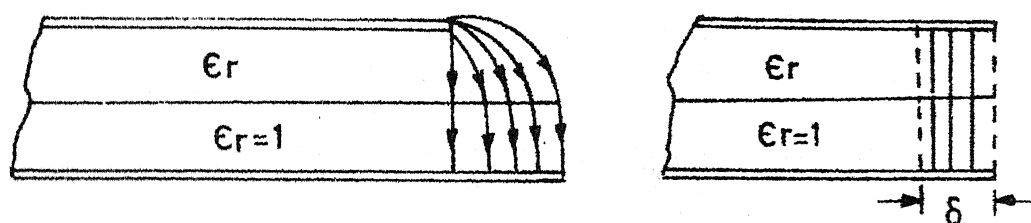
FIG.7.2 DESEGMENTATION APPLIED TO THREE DISCONTINUITY CONFIGURATIONS

junction) is compensated by removing a triangle and a bend (which can be considered as one fourth of the cross-junction) is compensated by chopping off the corner. Cross-junction with a square slot removed can be analyzed by desegmentation method. In this case, the  $\beta$ -segment is a square and the  $\gamma$ -segment is a combination of rectangular segments. Green's function for rectangle [1] can be used to characterize the  $\beta$ -segment. The segmentation method [4],[23] can be employed for evaluating the S- or Z-parameters for the  $\gamma$ -segment.

Other two discontinuities, i.e. notch (Fig. 7.2(b)) and a circular hole (Fig. 7.2(c)), are introduced intentionally for obtaining inductive reactances in the circuits. In these cases we need only characterization (and not compensation). For the notch discontinuity, the  $\alpha$ -segment of Fig. 7.2(b) is obtained by removal of a rectangular patch ( $\beta$ ) from another rectangular patch ( $\gamma$ ). Thus the method of desegmentation can be employed for characterization of the notch.

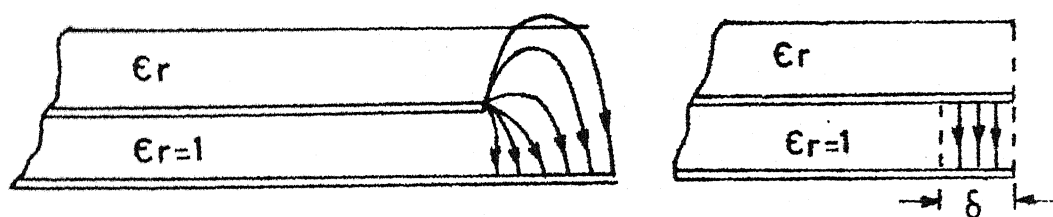
In case of circular hole discontinuity, a circular patch ( $\beta$ ) is added to the  $\alpha$ -segment (Fig. 7.2(c)) for obtaining the rectangular  $\gamma$ -segment. As  $\beta$ - and  $\gamma$ -segments are both regular shapes, these can be characterized by Green's functions [5],[1]. The  $\alpha$ -segment can be characterized in terms of the characterizations for  $\beta$ - and  $\gamma$ -segments employing desegmentation method.

Green's function approach and segmentation-desegmentation techniques can also be employed for analysis of MICs employing suspended and inverted microstrip configurations shown in Fig. 7.3. A planar waveguide model for such circuits is necessary for this purpose. As in the case microstrip and stripline circuits, fringing field can be accounted for by extending the physical boundary outwards. The formulas for extension of the physical boundaries (Fig. 7.3(a) and (b)) and for effective dielectric constants for such circuits would be needed.



(a)

$\delta$  = Extension of boundary



(b)

FIG. 7.3 (a) A SUSPENDED MICROSTRIP CIRCUIT  
AND THE EXTENSION OF BOUNDARY  
(b) AN INVERTED MICROSTRIP CIRCUIT  
AND EXTENSION OF BOUNDARY



## APPENDIX A

### CALCULATION OF Q FACTOR FOR RECTANGULAR PATCH ANTENNA

The quality factors of the two orthogonal modes of the rectangular patch of Fig. 4.1(a) are defined as

$$Q_{10} = 2\pi f R_{10} C_{10}, \quad Q_{01} = 2\pi f R_{01} C_{01} \quad (A.1)$$

The values of the capacitances  $C_{01}$  and  $C_{10}$  are given by

$$C_{10} = C_{01} = \epsilon_0 \epsilon_r a b / 2d \quad (A.2)$$

where  $d$  and  $\epsilon_r$  denote the thickness and dielectric constant of the substrate,  $\epsilon_0$  is the permittivity of the free-space, and  $a$  and  $b$  are the length and width, respectively, of the rectangular patch as shown in Fig. 4.1(a).

The values of the resistances  $R_{01}$  and  $R_{10}$  (the radiation resistance values) for the two modes, corresponding to the lengths of the sides  $a$  and  $b$ , are calculated using the relation given in [50].

The quality factor  $Q$  for the antenna is expressed as

$$Q = \frac{Q_{10} Q_{01}}{Q_{10} + Q_{01}} \quad (A.3)$$

The preceding equation is used to calculate the value of the factor  $(1 + \frac{1}{Q})$  for the three diagonal fed antennas discussed in Chapter Four.

## APPENDIX B

### MEASUREMENT OF DIELECTRIC CONSTANT

The dielectric constant of the substrates used for fabricating the antennas was measured as follows.

A half-wave resonator in stripline configuration is fabricated. The resonator is excited by gap coupled feed line as shown in Fig. B.1. The extension in the length of the resonator to account for the fringing field at the ends is given by [13]

$$\delta = \frac{2d \ln 2}{\pi} \quad (\text{B.1})$$

where  $d$  is the thickness of the substrate. The widths ( $W$ ) of the feed line and the resonator are chosen equal to that of a 50 ohm stripline with an assumed value of  $\epsilon_r = 2.55$ . The resonance frequency is measured and the dielectric constant is calculated therefrom as

$$\epsilon_r = [\lambda_0 / 2(L + 2\delta)]^2 \quad (\text{B.2})$$

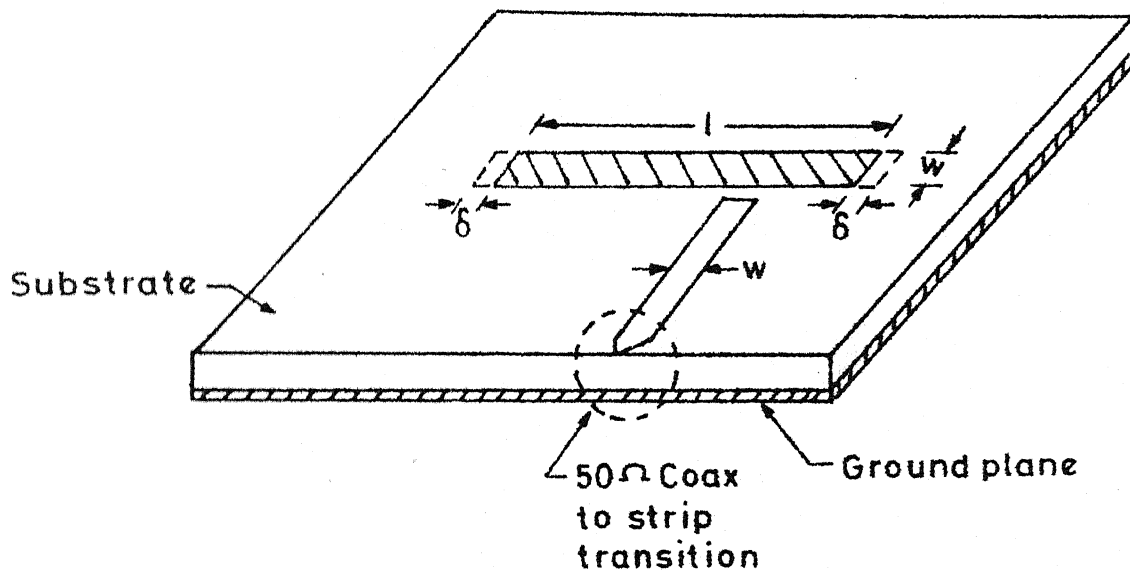


FIG. B.1 A STRIPLINE HALF-WAVE RESONATOR  
WITH UPPER PLANE REMOVED

## REFERENCES

- [1] T. Okoshi and T. Miyoshi, 'The planar circuit - an approach to microwave integrated circuitry', IEEE Trans. Microwave Theory Tech., vol. MTT-20, pp. 245-252, Apr. 1972.
- [2] P. Silvester, 'Finite element analysis of planar microwave networks', IEEE Trans. Microwave Theory Tech., vol. MTT-21, pp. 104-108, Feb. 1973.
- [3] T. Okoshi and T. Takeuchi, 'Analysis of planar circuits by segmentation method', Electron. Commun. Japan, vol. 58-B, no.8, pp. 71-79, 1975.
- [4] T. Okoshi, T. Uehara, and T. Takeuchi, 'The segmentation method - an approach to the analysis of planar microwave circuits', IEEE Trans. Microwave Theory Tech., vol. MTT-24, pp. 662-668, Oct. 1976.
- [5] T. Okoshi, T. Takeuchi, and J.P. Hsu, 'Planar 3-dB hybrid circuit', Electron. Commun. Japan, vol. 58-B, no.8, pp. 80-90, Aug. 1975.
- [6] J. Helszajn and D.S. James, 'Planar triangular resonators with magnetic walls', IEEE Trans. Microwave Theory Tech., vol. MTT-26, pp. 95-100, Feb. 1978.
- [7] J. Helszajn, D.S. James, and W.T. Nisbet, 'Circulators using planar triangular resonators', IEEE Trans. Microwave Theory Tech., vol. MTT-27, pp. 188-193, Feb. 1979.
- [8] R. Chadha, 'Triangular segments and two-dimensional analysis for microwave integrated circuits', Ph.D. thesis Department of Electrical Engineering, Indian Institute of Technology, Kanpur, India, May 1981.
- [9] R. Chadha and K.C. Gupta, 'Triangular, rhombic and hexagonal stripline resonators', to appear in AEU.
- [10] T. Miyoshi and T. Okoshi, 'Analysis of microwave planar circuits', Electron. Commun. Japan, vol. 55-B, no.8, pp. 24-31, Aug. 1972.
- [11] T. Miyoshi, S. Yamaguchi, and S. Goto, 'Ferrite planar circuits in microwave integrated circuits', IEEE Trans., Microwave Theory Tech., vol. MTT-25, pp. 593-600, July 1977.

- [12] T. Miyoshi and S. Miyauchi, 'The design of planar circulators for wideband operation', IEEE Trans. Microwave Theory Tech., vol. MTT-28, pp. 210-214, March 1980.
- [13] H.M. Altschuler and A.A. Oliner, 'Discontinuities in the center conductor of symmetric strip transmission line', IRE Trans. Microwave Theory Tech., vol. MTT-8, pp. 328-339, May 1960.
- [14] K.C. Gupta, R. Garg, and I.J. Bahl, Microstrip Lines and Slotlines, Dedham, MA: Artech House, 1979.
- [15] T. Miyoshi, 'Expansion of electromagnetic field in planar circuits', Electron. Commun. Japan, vol. 55-B, no.8, pp. 24-31, Aug. 1972.
- [16] T. Itoh and R. Mitra, 'A method for computing edge capacitance of finite and semi-infinite microstrip lines', IEEE Trans. Microwave Theory Tech., vol. MTT-20, pp. 847-849, Dec. 1972.
- [17] T. Itoh and R. Mitra, 'A new method for calculating the capacitance of a circular disk for microwave integrated circuits', IEEE Trans. Microwave Theory Tech., vol. MTT-21, pp. 431-432, June 1973.
- [18] Y. Rahmat-Samii, T. Itoh, and R. Mitra, 'A spectral domain analysis for solving microstrip discontinuity problems', IEEE Trans. Microwave Theory Tech., vol. MTT-22, pp. 372-378, April 1974.
- [19] A.K. Sharma, 'Spectral domain analysis of microstrip resonant structures', Ph.D. dissertation, Department of Electrical Engineering, Indian Institute of Technology, New Delhi, India, 1979.
- [20] O.C. Zienkiewicz, 'The Finite Element Method, London: McGraw-Hill, 1977.
- [21] R. Chadha and K.C. Gupta, 'Green's functions for triangular segments in planar microwave circuits', IEEE Trans. Microwave Theory Tech., vol. MTT-28, pp. 1139-1143, Oct. 1980.
- [22] R. Chadha and K.C. Gupta, 'Green's functions for circular sectors, annular rings and annular sectors in planar microwave circuits', IEEE Trans. Microwave Theory Tech., vol. MTT-29, pp. 68-71, Jan. 1981.

- [23] R. Chadha and K.C. Gupta, 'Segmentation method using impedance matrices for analysis of planar microwave circuits', IEEE Trans. Microwave Theory Tech., vol. MTT-29, pp. 71-74, Jan. 1981.
- [24] G.A. Deshchamps, 'Microstrip microwave antennas', 3rd USAP Symp. on Antennas, 1953.
- [25] J.Q. Howell, 'Microstrip antennas', 1972 G-APS Int. Symp., Williamsburg, VA, Dec. 1972.
- [26] R.E. Munson, 'Conformal microstrip antennas and arrays', IEEE Trans. Antennas propagat., vol. AP-22, pp. 74-78, Jan. 1974.
- [27] J.Q. Howell, 'Microstrip antennas', IEEE Trans. Antennas propagat., vol. AP-23, pp. 90-93, Jan. 1975.
- [28] H.D. Weinschel, 'A cylindrical array of circularly polarized microstrip antennas', 1975 APS Int. Symp. Digest, pp. 177-180.
- [29] L.C. Shen, S.A. Long, M.R. Allerding, and M.D. Walton, 'Resonant frequency of a circular disc printed-circuit antenna', IEEE Trans. Antennas propagat., vol. AP-25, pp. 595-596, July 1977.
- [30] M. Cuhai and D.S. James, 'Radiation from triangular and circular resonators in microstrip', G-MTT Int. Symp., June 1977.
- [31] C.M. Koloi, 'Corner fed electric microstrip dipole', Naval Missile Center, Pt. Mugu, California, March 1978.
- [32] Y.T. Lo, D. Solomon, and W.F. Richards, 'Theory and experiments on microstrip antennas', IEEE Trans. Antennas propagat., vol. AP-27, pp. 137-145, March 1979.
- [33] J.L. Kerr, 'Microstrip antenna developments', Proceedings of the Workshop on Printed Circuit Antennas, New Mexico State Univ., pp. 3.1 - 3.20, Oct. 1979.
- [34] K.R. Carver and E.L. Coffey, Theoretical investigations of microstrip antennas Tech. Report PT-00919, Jan. 1979.
- [35] L.C. Shen, 'Elliptical microstrip antenna with circular polarization', IEEE Trans. Antennas propagat., vol. AP-29, pp. 90-94, Jan. 1981.

- [36] S.A. Long, L.C. Shen, D.H. Schaubert, and F.G. Farrar, 'An experimental study of the circular -polarized elliptical printed circuit antenna', *Ibid*, pp. 95-99, Jan. 1981.
- [37] K.R. Carver and J.W. Mink, 'Microstrip antenna technology', *IEEE Trans. Antennas propagat.*, vol. AP-29, pp. 2-24, Jan. 1981.
- [38] I.J. Bahl and P. Bhartia, *Microstrip Antennas*, Dedham, MA: Artech House, 1981.
- [39] W.F. Richards, Y.T. Lo, and D.D. Harrison, 'An improved theory for microstrip antennas and applications', *IEEE Trans. Antennas propagat.*, vol. AP-29, pp. 38-46, Jan. 1981.
- [40] S. Yano and A. Ishimaru, 'A theoretical study of the input impedance of a circular microstrip disk antenna', *IEEE Trans. Antennas propagat.*, vol. AP-29, pp. 77-83, Jan. 1981.
- [41] *IEEE Trans. Antennas propagat.*, 'Special issue on Microstrip Antennas', vol. AP-29, Jan. 1981.
- [42] K.R. Carver and E.L. Coffey, 'Theoretical investigations of microstrip antennas', Tech. report PT-00929, pp. 60-66, Jan. 1979.
- [43] J.L. Kerr, 'Microstrip polarization technique', *Proc. 1978 Antenna Application Symp.*, Univ. of Illinois, Sept. 1978.
- [44] K.R. Carver and E.L. Coffey, 'Theoretical investigations of microstrip antennas', Tech. report No. PT-00929, pp. 73-79, Jan. 1979.
- [45] R.F. Harrington, 'Time-Harmonic Electromagnetic Fields', McGraw-Hill Book Co., NY 1961, p. 183.
- [46] E.O. Hammerstad, 'Equations for microstrip circuit design', 5th European Microwave Conf., digest, pp.268-272, Sept. 1975.
- [47] E.L. Newmann, 'Strip antenna in dielectric slab', *IEEE Trans. Antennas propagat.*, vol. AP-26, pp. 647-653, Sept. 1978.

- [48] J.H. Richmand, 'A wire-grid model for scattering by conducting bodies', IEEE Trans. Antennas propagat., vol. AP-14, pp. 782-786, Nov. 1966.
- [49] A.G. Derneryd, 'Linearly-polarized microstrip antennas', IEEE Trans. Antennas propagat., vol. AP-24, pp.846-851, Nov. 1976.
- [50] H. Pues and A. Van de Capelle, 'A simple accurate formula for the radiation conductance of a rectangular microstrip antenna', Int. IEEE APS-Symposium digest, pp. 23-26, June 1981.
- [51] T. Itoh and W. Menzel, 'A full-wave analysis method for microstrip structures', IEEE Trans. Antennas propagat., vol. AP-29, pp. 63-68, Jan. 1981.
- [52] K. Araki and T. Itoh, 'Hankel transform domain analysis of open circular microstrip radiating structures', IEEE Trans. Antennas propagat., vol. AP-29, pp. 84-89, Jan. 1981.
- [53] R.F. Bour and P. Penfield Jr., 'De-embedding and unterminating', IEEE Trans. Microwave Theory Tech., vol. MTT-22, pp. 282-288, March 1974.
- [54] S. Rehnmark, 'On the calibration process of an automatic network analyzer system', IEEE Trans. Microwave Theory Tech., vol. MTT-22, pp. 457-458, Apr. 1974.
- [55] N.R. Franzen and R.A. Speciale, 'A new procedure for system calibration and error removal in automated S-parameter measurements', Proc. 5th European Microwave Conf. (Hamburg Germany), pp. 69-73, Sept. 1975.
- [56] R.A. Speciale, 'A generalization of the TSD network-analyzer calibration procedure, covering n-port scattering parameter measurements affected by leakage errors', IEEE Trans. Microwave Theory Tech., vol. MTT-25, pp. 1100-1115, Dec. 1977.
- [57] A.G. Derneryd, 'A theoretical investigation of rectangular microstrip antenna element', IEEE Trans. Antennas propagat., vol. AP-26, pp. 532-535, July 1978.
- [58] V.A. Monaco and P. Tiberio, 'Automatic scattering matrix computation of microwave circuits', Alta. Freq. vol. 39, pp. 59-64, Feb. 1970.
- [59] R. Chadha and K.C. Gupta, 'Compensation of discontinuities in planar transmission lines', 1982 IEEE MTT-S International Symp. Dallas, Texas, June 15-17, 1982.